Semiconductors, Vol. 35, No. 7, 2001, pp. 735–761. Translated from Fizika i Tekhnika Poluprovodnikov, Vol. 35, No. 7, 2001, pp. 769–795.

REVIEWS

Doping of Semiconductors Using Radiation Defects Produced by Irradiation with Protons and Alpha Particles

V. A. Kozlov* and V. V. Kozlovski**

** Ioffe Physicotechnical Institute, Russian Academy of Sciences, Politekhnicheskaya ul. 26, St. Petersburg, 194021 Russia*

*** St. Petersburg State Technical University, Politekhnicheskaya ul. 29, St. Petersburg, 195251 Russia*

e-mail: kozlovski@tuexph.stu.neva.ru

Submitted November 8, 2000; accepted for publication December 19, 2000

Abstract—One of the modern methods for modifying semiconductors using beams of protons and alpha particles is analyzed; this modification is accomplished by the controlled introduction of radiation defects into the semiconductor. It is shown that doping semiconductors with radiation defects produced by irradiation with light ions opens up fresh opportunities for controlling the properties of semiconducting materials and for the development of new devices designed for optoelectronics, microelectronics, and nanoelectronics based on these materials; these devices differ favorably from those obtained by conventional doping methods, i.e., by diffusion, epitaxy, and ion implantation. © *2001 MAIK "Nauka/Interperiodica".*

1. INTRODUCTION

Modification of semiconducting materials (i.e., the controlled variation of their properties) using beams of light ions, in particular, of protons, has become one the most promising and actively developing physicotechnological methods in recent years. The interest in proton irradiation is caused by the wide and controlled range of the treated depths of the material (from 0.1 μm to 1 mm) and by the absence of complex radiation-defect clusters with high annealing temperatures. The three main factors influencing variation in the semiconductor properties as a result of proton irradiation are the formation of new impurities due to nuclear reactions, the radiation-induced formation of defects, and the accumulation of hydrogen atoms. The radiation-induced modification accomplished by the controlled introduction of defects (structural and compositional) into the material is referred to as radiation-induced doping. The classification of the modern lines in the radiation-induced modification of semiconductors using light-ion beams is illustrated in Table 1. Such classification of the lines in a radiation-induced modification can be recognized explicitly or implicitly in the majority of books, reviews, and collections of papers published in the past decade and devoted to the radiation physics of semiconductors and to radiation-induced defects, effects, and processes in semiconductors [1–13].

In contrast to an impurity atom (an impurity defect), which is typically a defect in the composition of the material, a radiation defect (vacancy, interstitial atom, divacancy, and the like) is, as a rule, a structural defect of the semiconductor material. However, the influence of both compositional and structural defects on semiconductor properties is similar. Typically, defect formation is accompanied with the emergence of local energy levels in the semiconductor band gap. Defects serve either as the sources or traps of electrons (donors or acceptors) or as the radiative (nonradiative) recombination centers for nonequilibrium charge carriers. The controlled introduction of radiation defects in combination with heat treatment makes it possible to significantly change the semiconductor electrical characteristics, such as the electrical conductivity; the type of conductivity; and the concentration, mobility, and lifetime of the charge carriers.

The development and wide use of radiation-related technologies in electronics [1–4] are indicative of the high efficiency of seemingly nontraditional methods and result from intensive studies of the physicochemical processes that underlie the radiation-related methods of doping.

At present, the employment of transmutation-induced doping of semiconductors under the effect of irradiation with light ions [11], proton-stimulated processes, and the introduction of hydrogen atoms [12] for modifying semiconductor properties have been the most widely represented in scientific publications. There are no analytical reviews concerned with the doping of semiconductors with radiation defects formed by irradiation with light ions. This review is directed at eliminating this gap.

The review consists of two parts devoted to the main materials of the modern semiconductor electronics, i.e., to silicon and the III–V compounds (gallium arsenide and indium phosphide). In each part of the review, we first consider the issues related to the radiation-defect production and then the issues related to the use of radiation defects in electronics. When analyzing radiation-

Table 1

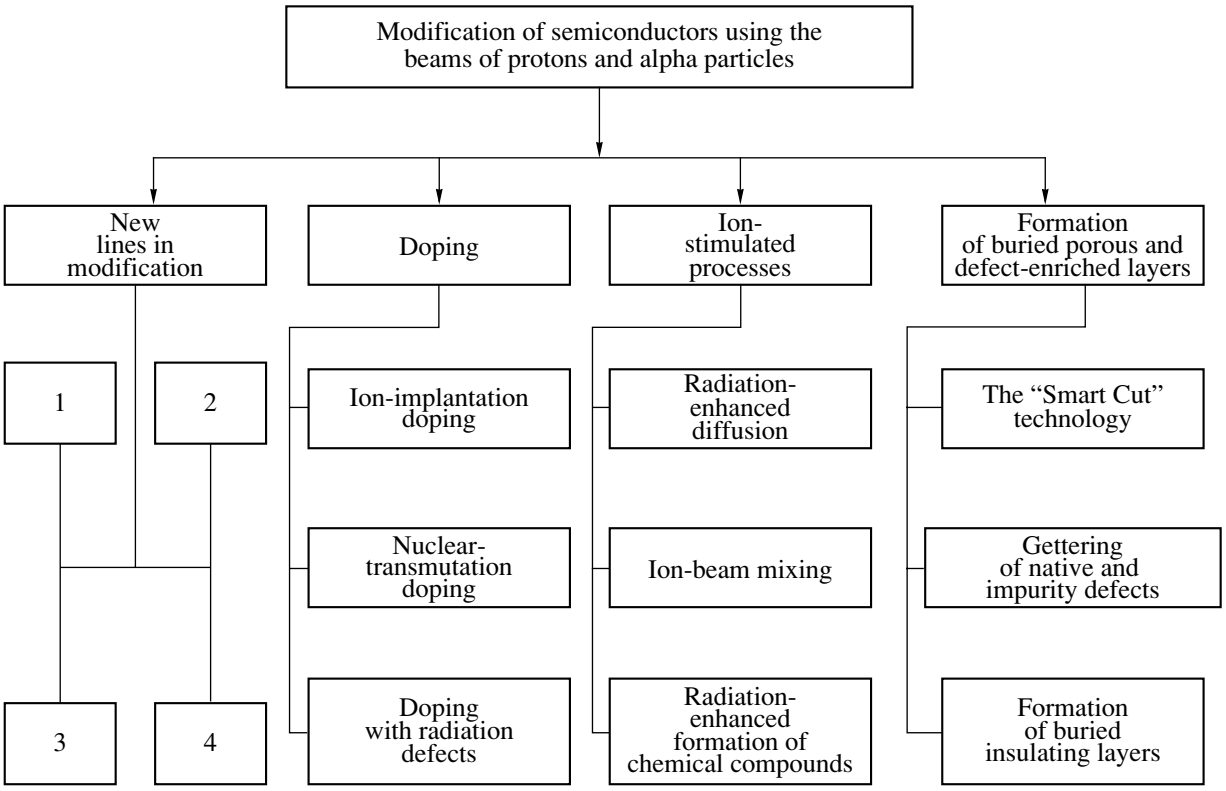

Notes: 1 stands for the formation of nanoblisters and nanopores acting as luminescence centers in the visible region of the spectrum for optoelectronic Si-based emitters; 2 stands for the formation of waveguides for electromagnetic waves, including solid-state radio-frequency coplanar transmission lines and optical waveguides; 3 stands for the formation of quantum-well structures for cryogenic electronics (quantum dots and single-electron transistors); and 4 stands for the formation of multilayer structures with heterojunctions (including optoelectronic integrated circuits, heterostructure bipolar transistors, and heterojunction complementary metal–oxide–semiconductor transistors) and three-dimensional very-large-scale integrated circuits.

defect formation in semiconductors subjected to irradiation with light ions and comparing this type of irradiation with other types, we chose electron irradiation (with an energy of ~1 MeV) as a reference; irradiation with electrons is most often used nowadays for radiation treatment of semiconductor crystals and devices. In view of the limitations imposed on the length of a paper in the journal, we are going to concentrate most attention (as was done in previous reviews [11, 12]) on the publications devoted not only to basic research but also to practical applications.

2. INTERACTION OF LIGHT IONS WITH SINGLE-CRYSTALLINE SEMICONDUCTORS

An incident particle is known to stop in a solid owing to its scattering by the electron subsystem of the matrix atoms (electronic stopping) and by the nuclei of these atoms (nuclear stopping). Electronic stopping results in the excitation and ionization of electron shells of the matrix atoms, whereas the interaction with nuclei of the matrix atoms is accompanied by the transfer of an appreciable energy to these atoms and leads to the formation of radiation defects (in the simplest case, Frenkel pairs). It follows from an analysis of the energy-loss curves according to the Lindhard–Scharff–Schiøtt theory [14] that defect production prevails for the reduced energy $\varepsilon < 2$, where

$$\varepsilon = (a/e^2)E_0M_2Z_1^{-1}Z_2^{-1}(M_1 + M_2)^{-1},$$
$$a = 0.8853r_B(Z_1^{2/3} + Z_2^{2/3})^{-1/2}. \quad (1)$$

Here, M_1, M_2, Z_1, and Z_2 are the masses and charges of the incident ion and the matrix ion, respectively; E_0 is the energy of the incident ion; r_B is the first Bohr radius; and e is the elementary charge. It can be seen from formula (1) that the energy below which the nuclear losses prevail is given by [15]

$$E_C = 2E_RZ_1Z_2(Z_1^{2/3} + Z_2^{2/3})^{1/2}(1 + M_1/M_2), \quad (2)$$

where E_R is the incident-particle energy corresponding to the Coulomb potential of two nucleons separated by a distance equal to the sum of their screened electron clouds; E_R = 13.6 eV for the system under consider-

ation. By introducing in (1) the values of the mass and charge (for example, for the hydrogen ion) and the effective mass and charge for GaAs, we obtain $E_C \approx 3$ keV (the effective mass for gallium arsenide is $M_{GaAs} \approx 73$, and the corresponding effective charge is $Z_{GaAs} \approx 32$); for interaction of a proton with a Si ion, we have $E_C \approx 1$ keV. Thus, only a few percent of the total ion energy (for example, amounting to hundreds of kiloelectronvolts) is spent on the production of radiation defects. The remaining portion of the energy is spent on the excitation and ionization of the matrix atoms (As and Ga atoms in the first case and Si atoms in the second case). Since the main generation of radiation defects occurs after the proton energy has been reduced to 1–3 keV, there is a pronounced nonuniformity in the radiation-defect generation along the particle track. Correspondingly, two terms appear in the formula for the total number of semiconductor atoms (N_t) displaced from the lattice sites. One of these terms corresponds to the electron-related stopping, whereas the other corresponds to nuclear stopping [16]; i.e., we have

$$N_t = [p(E_0 - E_C) + bE_C]/E_d. \quad (3)$$

Here, p is a probabilistic factor (equal to 10^{-3}), E_d is the displacement energy for a target atom (~15 eV in GaAs [16]); $b = 1/2$ for $E_b > E_C$, and $b = 1/4$ for $E_b < E_C$, where

$$E_b = \gamma E_C^2/(4E_d), \quad \gamma = 4M_1M_2/(M_1 + M_2)^2. \quad (4)$$

It follows from formulas (3) and (4) that, for GaAs and $E_0 = 300$ keV, we have $E_C = 3$ keV, $\gamma = 0.05$, $E_b = 8$ keV, and $N_t = 50$. Thus, each proton with an energy of 300 keV produces ~50 displacements in gallium arsenide [16]. Taking into account that the proton range for $E_0 = 300$ keV is equal to ~3 μm, the average concentration of displaced atoms in the irradiated layer amounts to 1.5×10^5 cm^{-3} per proton. For typical proton beam intensities of 6×10^9–6×10^{12} cm^{-2} s^{-1} used in practice, the average defect-generation rate is ~10^{15}–10^{18} cm^{-3} s^{-1} [17, 18]. In Table 2, we list the data on the ranges of the monatomic, diatomic, and triatomic single-charged hydrogen ions with an energy of 300 keV in III–V compounds. The concept of an "average" generation rate for radiation defects in an irradiated layer of a semiconductor is quite arbitrary when applied to ion irradiation, since, as was mentioned above, the distribution of stopping losses over depth in a crystal is highly nonuniform and has a maximum at the end of the ion path.

3. DOPING OF GALLIUM ARSENIDE AND OTHER III–V SEMICONDUCTOR COMPOUNDS USING RADIATION DEFECTS

For the last 20 years, radiation defects in III–V compounds (especially, in GaAs) have been studied quite intensively; however, one obstacle to studying the radiation defects in detail in these compounds is the fact that the latter contain a much higher concentration of impurities compared to Ge and Si [1]. Several reviews have so far been published concerned with these studies [19–22]. All these reviews have been mainly devoted to basic issues in the production of radiation defects in III–V compounds irradiated with neutrons, electrons, and gamma-ray quanta. In contrast, we are primarily interested in studies devoted to purposeful changes in semiconductor properties, especially by doping III–V compounds with radiation defects. This section is based on the published results of studying the doping of III–V compounds by irradiation with light charged particles.

As is well-known, the primary radiation defects are first of all intrinsic point lattice defects [23]. In III–V compounds, there are eight types of simple different point defects; i.e., we have two types of vacancies (one type in the each sublattice), at least four types of interstitial defects (there are two types of interstices that can be occupied either by atoms of Group III or by atoms of Group V), and two types of antisite defects (when a Group III atom resides at the site in the sublattice of atoms belonging to Group V and vice versa). In addition, intrinsic defects can form complexes with each other and with impurities.

3.1. Production of Radiation Defects in Gallium Arsenide

In spite of numerous studies, the origin of the main types of radiation defects (even in gallium arsenide, the most extensively studied III–V compound) remains debatable; at present, there is no reliable way to identify introduced radiation defects. Because of this circumstance, when analyzing the origin of radiation defects, we have to rely to a large extent on the results of "indirect" methods (optical absorption, luminescence, deep-level transient spectroscopy (DLTS), the Hall effect, etc.).

Studies using electron spin resonance (a method for the direct identification of radiation defects) do not yield the required results because of an appreciable overlap of hyperfine-structure lines.

Table 2. Projected range of 300-keV hydrogen ions in III–V compounds

Material	H_1^+	H_2^+	H_3^+
GaAs	2.58	1.20	0.84
GaP	2.5	1.12	0.78
InP	2.25	1.10	0.75
InAs	2.1	1.00	0.71
InSb	1.8	0.90	0.65
$GaP_{0.4}As_{0.6}$	2.34	1.05	0.71

Note: The values of projected ranges are given in micrometers.

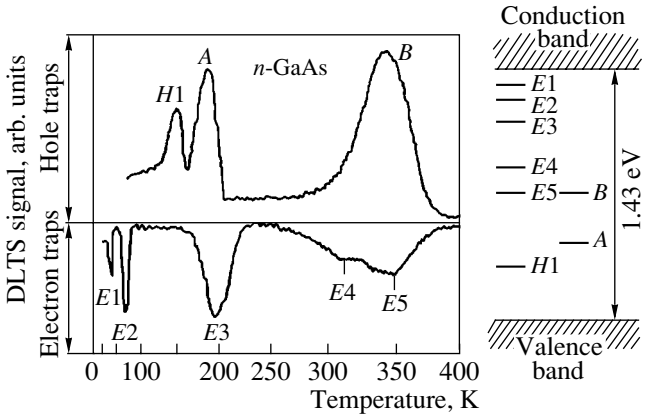

Fig. 1. DLTS spectrum of *n*-GaAs irradiated with 1-MeV electrons at room temperature [14] (on the left) and the energy spectrum of traps (on the right). Hole traps *A* and *B* are present in unirradiated *n*-GaAs. We note that the scale for *E*1 and *E*2 is reduced (×0.25) and the scale for *E*4 and *E*5 is expanded (×2.5).

As an example, we mention the publication [19] where the results of studying the radiation defects by DLTS were reported. The DLTS spectrum for *n*-GaAs irradiated at room temperature with 1-MeV electrons is shown in Fig. 1 (on the left). As can be seen from Fig. 1, five types of electron traps (*E*1–*E*5) and one type of hole trap (*H*1) are observed in the spectrum. The concentrations of these traps increase linearly with irradiation dose (in the range from 5×10^{13} to 5×10^{15} cm^{-2}), with the introduction rate of traps *E*1 and *E*2 being the highest.

In Table 3, we list the introduction rates for defects; these rates are equal to the ratio between the concentration of defects produced in the crystal and the irradiation dose. The positions of deep levels appearing in the band gap of gallium arsenide subjected to irradiation with 1-MeV electrons at room temperature are also listed [the energy positions of the electron (hole) traps are measured relative to the valence-band top (the conduction-band bottom)] [19]. The positions of the energy levels were determined from the activation energy for thermal emission on the basis of DLTS data, from the activation energy in the temperature dependence of the charge-carrier concentration, and from the photoconductivity threshold. All the deep-level introduction rates in Table 3 are given for the electron-current density of $J = 0.1$ μA cm^{-2}.

Experimentally, the dependences of introduction rates for the main electron traps (*E*1–*E*5) either on the method of material growth (liquid-phase or vapor-phase epitaxy or the Czochralski method) or on the type and concentration of the dominant dopant were not observed. An analysis of available results shows that, in GaAs irradiated with 1-MeV electrons at a temperature of $T_{irr} = 300$ K, the total introduction rate for traps *E*1–*E*5 is close to the calculated production rate for primary displaced atoms (~5 cm^{-1}) provided the displacement energy is equal to $E_d \approx 15$ eV [20]. Most probably, this indicates that annihilation of primary radiation defects at room temperature in GaAs is much less important than in Si and Ge [23, 24].

The spectrum of introduced electron traps broadens when the irradiation temperature is lowered. Thus, irradiation with 1-MeV electrons at $T_{irr} = 4$ K results in the introduction of electron traps *E*7 and *E*9 (in addition to traps *E*1–*E*5); these new traps were found to be unstable at room temperature. Ten years after the review [19] had been published, the parameters of radiation defects introduced into GaAs were refined [20, 21]. The data obtained in more recent studies of electron and hole traps are listed in Tables 4 and 5.

As the mass of incident particles increases, the spectrum of introduced radiation defects changes. Figure 2 shows the DLTS spectra of four *n*-GaAs samples irradiated at room temperature with electrons, protons, and helium and oxygen ions. We should note a general tendency towards the broadening of the spectrum with increasing mass of incident particles. It follows from Fig. 2 that radiation damage produced by low-dose protons is similar to that produced by 1-MeV electrons; however, for proton irradiation, a larger fraction of damage is accounted for by defects with levels at E_c – 0.76 eV and E_c – 0.96 eV. A broad peak corresponding

Table 3. Energy levels and the rates of their introduction into *n*-GaAs irradiated with 1-MeV electrons [19]

The method of measurements	The energy levels, eV						
	Hole traps					Electron traps	
	*E*1	*E*2	*E*3	*E*4	*E*5	*H*0	*H*1
DLTS	0.08	0.19	0.45	0.76	0.96	0.09	0.32
The Hall coefficient (corrected)	0.12	0.20	0.38			0.10	
	0.13	0.20	0.31			0.10	
The photoconductivity threshold			0.38	0.52	0.72		
Introduction rate, cm^{-1}	1.8	2.8	0.7	0.08	0.1		

Note: The energies of traps for electrons (holes) are measured from the valence-band top (conduction-band bottom).

to the level at E_c – 0.76 eV is dominant in the spectrum after irradiation with helium ions.

Radiation defects produced in any solid become mobile at sufficiently high temperatures; as a result, these defects are modified and are eventually annealed out. From the standpoint of radiation-based technology, defects with an annealing temperature T_{ann} higher than 400 K are of interest. This trend is caused by the necessity of ensuring the stability of the characteristics of semiconductor devices produced using irradiation processes.

For *n*-GaAs irradiated at T_{irr} = 4 K, thermal recovery sets in at a temperature of 220 K and occurs in several stages. Using the DLTS measurements, it has been shown that traps *E*7 and *E*9 are annealed out at T_{ann} = 230 K, whereas traps *E*1–*E*5 are annealed out at $T_{ann} \approx$ 500 K. Studies have shown that annealing of the dominant types (*E*1–*E*5) of radiation defects in *n*-GaAs can be described by a first-order differential equation and has the activation energy E_{ann} = 1.5–1.6 eV [20].

The anneal of traps in *p*-GaAs was analyzed in detail by Stievenard *et al.* [25]. It was shown that the traps *H*1 and *H*5 should be separated into two groups. The *H*1 traps should be assigned to the first group; the anneal of these traps is governed by the sum of two first-order kinetic processes with E_{ann} = 1.3 eV. The anneal of defects *H*1 is related to the recombination of the Frenkel (vacancy–interstitial) pairs in the As sublattice. The second group includes the *H*3–*H*5 traps whose anneal can be described by a first-order differential equation with $E_{ann} \approx 0.5$ eV and $\nu_0 = 10^2$ s^{-1}. The anneal of the *H*3–*H*5 defects is typically related to the migration of As interstitial atoms As_i; this migration is characterized by an activation energy of E_m = 0.5 eV. Three main stages of electrical property recovery as a result of annealing *n*- and *p*-GaAs irradiated with fast electrons were reported by Lang [19]; the corresponding annealing temperatures are $T_{ann} \approx$ 400, 500, and 750 K.

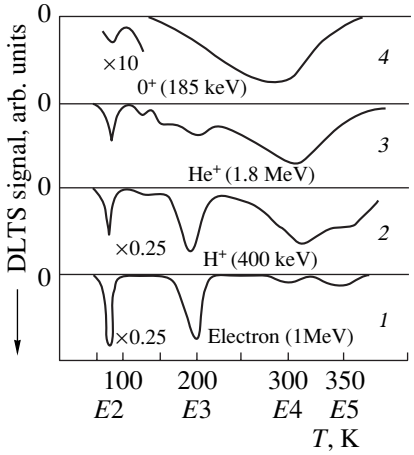

Fig. 2. DLTS spectra of *n*-GaAs samples irradiated at room temperature with (*1*) 1-MeV electrons, (*2*) 400-keV protons, (*3*) 1.8-MeV alpha particles, and (*4*) 185-keV oxygen ions [14].

Based on the available data, Pons and Bourgoin [20] advanced the following ideas about the origin of radiation defects in GaAs (Table 6). All electron traps introduced at T_{irr} = 300 K (*E*1–*E*5) are associated with the Frenkel pairs [V_{As}–As_i]. Only the traps *E*7 and *E*9 formed at T_{irr} = 4 K are related to a more complex defect [V_{As}–Ga_{As}]. In the Ga sublattice, the Frenkel pairs recombine immediately after their formation even at T_{irr} = 4 K; this is due to the charge state and, as a consequence, to the Coulomb interaction of the members of the Frenkel pairs. When the interstitial As atoms As_i are mobile (T_{irr} > 500 K), complexes of As_i with the B, P, and C impurities and also the complexes of intrinsic defects (*EL*2, *EL*5, etc.) can be formed [26, 27].

A similar opinion about the origin of radiation defects in GaAs is shared by Bourgoin *et al.* [21]. The *E*1 and *E*2 traps were assigned to different charge states of isolated V_{As} vacancies, whereas the *E*3 and *E*5 traps

Table 4. Parameters of radiation-related electron traps in *n*-GaAs irradiated with 1 MeV electrons [20]

Trap (T_{irr})	Activation energy for emission E_a, eV	Capture cross section σ_n, cm^2	Introduction rate, cm^{-1}	Annealing temperature T_{ann}, K	Activation energy for annealing E_{ann}, eV	Frequency factor ν_0, s^{-1}
*E*1 (300 K)	0.045	2×10^{-15}	1.5	500	1.6	10^{13}
*E*2 (300 K)	0.14	1×10^{-13}	1.5	500	1.6	10^{13}
*E*3 (300 K)	0.3	6×10^{-15}	0.4	500	1.55	3×10^{12}
*E*4 (300 K)	0.76	3×10^{-14}	0.08	500	1.5	10^{13}
*E*5 (300 K)	0.96	2×10^{-12}	0.1	500	1.55	3×10^{13}
*E*7 (4 K)	–		5×10^{-4}	240	0.7	10^{12}
*E*9 (4 K)	0.23		2×10^{-3}	240	0.7	10^{12}

Note: The temperature dependence of the rate of the thermal-emission of electrons (holes) from the defect level is described by the formula $g(T) = \nu_0 \exp(-E_a/kT)$, where ν_0 is the frequency factor, E_a is the activation energy for emission, k is the Boltzmann constant, and T is the absolute temperature.

Table 5. Parameters of radiation-related hole traps in *p*-GaAs irradiated with 1-MeV electrons [20]

Trap	Activation energy for emission E_a, eV	Capture cross section σ_p, cm^2	Introduction rate, cm^{-1}	Annealing temperature T_{ann}, K	Activation energy for annealing E_{ann}, eV	Frequency factor ν_0, s^{-1}
*H*0	0.06	2×10^{-16}	0.8	–	–	–
*H*1	0.25	1×10^{-15}	0.1–0.7	500	1.1–1.3	5×10^8
*H*2	0.42	–	0.04	500	–	–
*H*3	0.54	7×10^{-16}	0.17	500	0.51	155
*H*4	0.79	7×10^{-14}	0.06	500	0.52	3×10^2
*H*5	0.85	9×10^{-15}	0.21	–	–	–

Table 6. Identification of defects in GaAs by various methods [20]

Defect	Optical measurements	DLTS	Annealing
Vacancy V_{As}	–	$E1 = E_c - 0.045$ eV (–2/–) $E2 = E_c - 0.14$ eV (–/0)	–
Frenkel pair V_{As}–As_i	–	$E3 = E_c - 0.30$ eV $E5 = E_c - 0.96$ eV $H0 = E_v + 0.06$ eV $H1 = E_v + 0.25$ eV	$T_{ann} \approx 220$°C $E_{ann} \approx 1.5$ eV
Antisite defect Ga_{As}	Luminescence (1.44 eV) IR absorption (70.9, 72.9, and 74.5 meV)	$E_v + 0.077$ eV (0/–) $E_v + 0.23$ eV (–/2–)	
Complex As_{Ga}–V_{As}	–	$E4 = E_c - 0.76$ eV (+/2+) $< E_c - 0.35$ eV (0/+)	–
Complex containing As_i	–	–	$T_{ann} \approx 220$°C $E_{ann} \approx 0.5$ eV
Complex V_{As}–Ga_{As}	–	$E7$ $E9 = E_c - 0.23$ eV	–

were assumed to be related to the closely spaced components of Frenkel pairs in the As sublattice. The *H*0 and *H*1 traps were tentatively assigned [21] to two other levels of the same defect. The *E*4 trap was related to the [As_{Ga} + V_{As}] complex, and the *H*2–*H*5 traps were assigned to the As_i-containing complexes. Because of the low mobility of primary radiation defects in III–V compounds (especially, in *n*-GaAs), we have here a rather unusual situation where the consequences of irradiation at T_{irr} = 300 K are governed by intrinsic lattice defects, the contribution of secondary processes to the defect formation is insignificant, and the results of irradiation are not radically diverse. An increase in the role of secondary processes can be basically achieved by varying the irradiation conditions (by increasing the temperature and intensity of irradiation) and increasing the level of doping of the starting material with various impurities. We have performed a series of studies aimed at gaining insight into the effect of irradiation parameters (type, energy, and flux density of the particles, and the dose and temperature of irradiation) and the semiconductor's doping level on the energy spectra of radiation defects in *n*-GaAs and *n*-InP [28–35].

Using the DLTS measurements of *n*-GaAs layers, which had the initial electron concentration $n_0 = 3 \times 10^{14}$–2×10^{17} cm^{-3} and were irradiated with 900-keV electrons at T_{irr} = 20°C, we observed the levels of the known *E*1–*E*5 and *E*8 electron traps [31]. It was ascer-

tained that the introduction efficiencies of these traps depended on the concentration of donor impurities in the epilayers. For the samples with $n_0 = (1–3) \times 10^{15}$ cm^{-3}, the effect of the irradiation temperature T_{irr} on the defect-formation processes in GaAs was analyzed. It is shown [31] that, for $T_{irr} > 100$°C, the predominant defects, the Frenkel pairs (vacancy–interstitial) in the arsenic sublattice, cease to be bound; as a result, they dissociate and their components can either migrate to sinks or annihilate [33, 36]. As a result, the introduction efficiency of the electron E traps decreases drastically, and new X traps are formed; it is the latter traps that contribute largely to changes in the material properties. Figure 3 illustrates variations in the introduction rates $dN_T/d\Phi$ for the E and X traps (N_T is the concentration of traps and Φ is the irradiation dose) in relation to T_{irr} for n-GaAs with $n_0 = 10^{15}$ cm^{-3}. It can be seen that, for $T_{irr} > 150$°C, the introduction rate for the E traps decreases with T_{irr}. As T_{irr} is further increased up to 550°C, the spectrum of introduced electron traps remains virtually unchanged and includes two types of dominant centers $X1$ and $X2$ with levels at $E_c - 0.38$ eV and $E_c - 0.76$ eV, respectively.

Kinetics of the buildup of these centers at $T_{irr} = 400$°C was analyzed, and their basic parameters were determined. It was established that the introduction rate of the $X2$ traps was virtually independent of T_{irr} in the range of $T_{irr} = 150–550$°C, whereas the introduction rate of $X1$ traps depended heavily on T_{irr}. It is assumed that an increase in the introduction rate of $X1$ traps in undoped GaAs layers is caused by changes in the charge state of $X1$ defects, whereas a decrease in the introduction rate of these traps at higher T_{irr} is caused by the annihilation of the corresponding centers. An analysis of the position of the Fermi level E_F in relation to the irradiation temperature T_{irr} shows that, in the range of $T_{irr} = 350–380$°C for undoped epilayers, the level E_F is located in the vicinity of the energy level of traps $X1$; i.e., the charge state of the primary defect involved in the above center possibly changes at these temperatures. In heavily doped materials, E_F is located much higher than the aforementioned level, so that recharging of the defects is not observed in the entire range of T_{irr}. Thus, Kozlovski *et al.* [33] inferred that an increase in the introduction efficiency for traps $X1$ is possibly caused by a change in the charge state of primary defects involved in the $X1$ centers.

The absence of any appreciable change in the charge-carrier concentration for the annealing-temperature range of $T_{ann} \approx 150–200$°C in combination with the observed decrease in the removal rate of charge carriers as a result of irradiation with electrons in the given temperature range [33] indicates that high-temperature irradiation at $T_{irr} = 150–200$°C is inequivalent to irradiation at room temperature with subsequent annealing at $T_{ann} = 150–200$°C. The most probable cause of the phenomena observed is the ionization of the crystal during

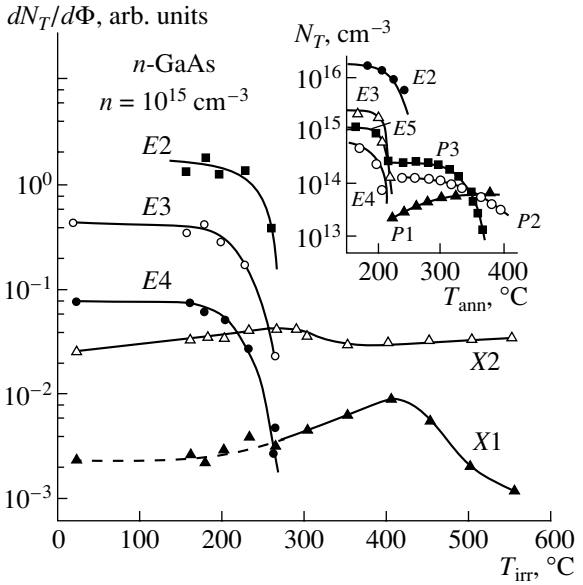

Fig. 3. Introduction efficiencies for traps E and X in n-GaAs with $n_0 = 10^{15}$ cm^{-3} in relation to the irradiation temperature [33]. The isochronous-annealing curves for electron traps in n-GaAs irradiated with electrons at a temperature of $T_{irr} = 20$°C are shown in the inset [37].

electron irradiation and, as a consequence, either an injection-related annealing of radiation defects or the separation of the Frenkel pair components enhanced by nonradiative recombination of nonequilibrium electrons and holes (the Bourgoin–Corbett mechanism [38]). The results of experiments with high-temperature irradiation of GaAs [33, 34] suggest the following:

(a) The processes of radiation-defect formation in gallium arsenide depend heavily on the irradiation temperature; for $T_{irr} > 80–100$°C, the dominant defects (Frenkel pairs of the same origin in the arsenic sublattice) dissociate and, due to an increase in mobility, can migrate to sinks and annihilate there.

(b) The lower boundary of the "transitional" temperature range of radiation-defect formation in GaAs (80–100°C) is related to the dissociation temperature of the close-origin Frenkel pairs in the arsenic sublattice, whereas the upper boundary is related to the temperature of the first of three stages of annealing of these radiation defects (250°C); in the transitional temperature range, the concentration of introduced E traps decreases, and new traps (X traps with levels at $E_c - 0.38$ eV and $E_c - 0.76$ eV) are formed.

3.2. Radiation-Defect Formation in Indium Phosphide

According to the generally accepted concept (see, for example, [39]), the majority of deep-level centers in n-InP irradiated with high-energy particles are formed owing to secondary processes; i.e., they are formed as

a result of the interaction of primary radiation defects (vacancies and interstitial atoms), which migrate in the crystal bulk, with each other and with impurities.

It was ascertained [39] that, as a result of irradiating InP with high-energy particles (gamma-ray quanta, electrons, and alpha particles) at room temperature, the same electron traps $E1$–$E6$ are mainly introduced; these traps have energy levels at 0.20, 0.19, 0.32, 0.4, 0.60, and 0.7 eV below the conduction-band bottom, respectively. Only the ratio between the introduction rates of separate types of centers depends on the incident-particle type. The fact that there is a wide variety of spectra reported for radiation defects in *n*-InP is due to the complex structure of these defects. Thus, for example, [39], it was shown that the levels $E1$, $E3$, and $E4$ correspond to transitions between different charge states of a configurationally bistable defect in InP, which is referred to as the M center. This multiple-charge center can have two different configurations, each of which has a specific spectrum of deep levels; reversible transitions between configurations can be initiated by electron-beam, thermal, or optical excitation.

For the irradiation of *n*-InP with 1-MeV electrons at room temperature, the total introduction rate of deep levels in the upper half of the band gap (determined from the DLTS measurements) is in the range of 1×10^{-3}–2×10^{-1} cm^{-1}, which is smaller than the calculated value by a factor of 100. In this situation, the carrier-removal rate defined as the ratio between the concentration of electrons removed (captured by traps) and the irradiation dose is also low and is no higher than 0.1 cm^{-1} [22].

In *p*-InP irradiated with 1-MeV electrons at room temperature, $H1$–$H5$ traps were observed [40]; these traps had levels separated from the valence-band top by 0.167, 0.22, 0.32, 0.37, and 0.53 eV. The $H4$ trap had the highest introduction rate (~2 cm^{-1}). Thus, in *p*-InP, in contrast to *n*-InP, the introduction rate for the traps of the majority charge carriers is very high.

It is noteworthy that, for irradiation with electrons and gamma-ray quanta, the introduction rate for dominant traps ($E1$–$E5$) in *n*-InP is lower than in *n*-GaAs by a factor of 100; for irradiation with 5-MeV alpha particles, this factor is equal to 3 [41]. The high concentration stability of the majority charge carriers in *n*-InP under irradiation is caused by the donorlike behavior of the $E6$ center, which is introduced with the highest rate for all kinds of irradiation. At the same time, it should be taken into account that the quasi-equilibrium concentration of the $E6$ trap is controlled by the annealing rate during irradiation in view of the low thermal stability of these traps.

For indium phosphide, an increase in temperature during electron irradiation results in a decrease in the production rate of traps $E1$, $E2$, $E4$, and $E6$ and also in a decrease in the charge-carrier removal rate in *n*-InP [29, 30]. The production rate of levels $E2$ and $E6$ decreased drastically even at 50°C, whereas the production rate of levels $E1$ and $E4$ related to the M center decreased at $T_{irr} > 150$°C. At $T_{irr} > 150$°C, a new center $ET1$ ($E_a = 0.16$ eV) appeared in the spectrum; at the same time, the production rate of the $E5$ center ($E_a = 0.60$ eV) increased appreciably. A significant increase in the probability of formation of centers $ET1$ and $E5$ under the conditions of high-temperature irradiation may be basically caused by the presence of a potential barrier to their formation; this barrier is overcome at $T_{irr} > 200$°C. However, the latter factor cannot be entirely responsible for the comparatively high and almost irradiation-temperature independent (in the range of 50–200°C) efficiency of the $E5$-center production. The second probable cause of the phenomena observed may be a change in the charge states of reacting defects as a result of a shift of the Fermi level with temperature [29, 30]. In fact, it has been previously established on the basis of studying the buildup and annealing of radiation defects in the space-charge region of the Schottky barrier that the probability of forming the $E5$ center depends on the charge state of one of the components of this complex [36]. As shown by Kozlovski *et al.* [29], this component is a high-mobility defect D(P) in the phosphorus sublattice and has an energy level of $E_c - 0.3$ eV. The transition of the D(P) defect from the zero- to positive-charged states results in an increase in the probability of producing the $E5$ state at least by a factor of 100. For high-temperature irradiation, a rapid increase in the efficiency of the $E5$-center formation sets in at $T_{irr} = 200$–250°C. At these temperatures, the Fermi level is located at 0.3 eV below the conduction-band bottom in the InP samples with $n_0 = 7 \times 10^{14}$ cm^{-3}. Thus, in the case of high-temperature irradiation (as was reported previously [29]), the efficiency of the $E5$-center formation changes when the quasi-Fermi level intersects the $E_c - 0.3$ eV level, which, according to [29], may correspond to the transition of an interstitial phosphorus atom from the zero- to positive-charged state. Kozlovski *et al.* [29] substantiated the relation between the $E5$ donor center and the antisite defect (phosphorus in the arsenic sublattice), which may be formed with the participation of interstitial phosphorus atoms according to the Watkins reaction. Thus, the most significant changes in the behavior of the defect formation in *n*-InP at elevated temperatures of irradiation are caused by a change in the charge state of one of the primary defects in the InP lattice (apparently, the interstitial phosphorus atoms) and by annealing of defects, which occurs simultaneously with irradiation.

In a practical context, the following results are of interest. As follows from the data obtained, an increase in the operation temperature of the InP-based devices to 50°C makes it possible to reduce the total introduction rate of electron traps by no less than fourfold; simultaneously, the charge-carrier removal rate decreases as well. It has been shown that irradiation at an elevated temperature is inequivalent to irradiation at a lower

temperature with subsequent annealing. High-temperature irradiation makes it possible to control the defect spectrum [30]. In particular, by choosing T_{irr}, we can extensively change the relation between the centers responsible for variation in the electrical parameters of a semiconductor (for example, the charge-carrier concentration).

As was shown experimentally [30], irradiation of *n*-InP with protons mainly gives rise to the same electron traps (*E*1–*E*5) as does electron irradiation; however, the ratio between the introduction rates of these traps changes appreciably.

3.3. Effect of Proton Irradiation on the Electrical Properties of III–V Compounds

It is known that in certain semiconductors (for example, in *n*-GaAs) the electrical conductivity decreases drastically as a result of irradiation, so that they become high-resistivity or even semi-insulating materials [1]. This behavior is related to the emergence of deep acceptor levels in the semiconductor's band gap [1]. At the same time, similar irradiation of other semiconductors (for example, *n*-InSb) results in the conversion of the conductivity type. It has been hypothesized [42] that a significant correlation exists between changes in the electrical conductivity of semiconductors and the band gap. According to this hypothesis, in a quasi-equilibrium state, the concentrations of certain types of radiation defects are highest, if the formation of these defects yields the lowest free energy of a crystal–defect system for the given total number of free and bound vacancies and interstitial atoms. In semiconductors with fairly deep levels of radiation defects, the difference in changes in the crystal's entropy upon the formation of specific kinds of complexes is unimportant; the minimum free energy is mainly attained by reducing the system's energy when the charge carriers are captured by the corresponding deep levels of the defects. It is this circumstance that causes the compensation of electrical conductivity by radiation defects. In contrast, if the binding energy of an electron (hole) to a defect is low, then the dominant role is played by a change in the entropy of the system when defects are introduced, whereas the bonding energy of a defect in a complex is mainly controlled by distortion of the lattice by the given center, rather than by its charge state. This circumstance results in the tendency towards compensation of the electrical conductivity of a semiconductor by radiation defects not being very pronounced. Thus, according to Vinetskiĭ and Smirnov [42], the compensation of conductivity by radiation defects may be expected in semiconductors with deep energy levels of these defects when the binding energy of an electron at the defect is larger than the change in the crystal's energy caused by introduction of this defect; in general, this situation relates to semiconductors with a wide band gap. Wide-gap semiconductors tend to have intrinsic conductivity as a result of irradiation. The tendency towards compensation should manifest itself starting with silicon [42]. The above physical treatment served as a basis for the formation of local semi-insulating regions using various types of radiation applied to a wide range of semiconductor devices.

However, the above treatment has been found to be applicable only if the formation energy of the radiation defect is comparable to the energy gain when the charge carrier becomes bound to the center. By the end of the 1970s, conversion of conductivity from *n*-type to *p*-type in initially lightly doped GaAs had already been accomplished using electron irradiation [43]. In connection with this, the concept of the "ultimate" position of the Fermi level in a semiconductor, widely used in the 1960s to explain experimental data [44], has been modified. The "ultimate" position of the Fermi level should now account for a quasi-equilibrium state of a system consisting of a set of defects and charge carriers; this state should ensure the minimization of the free energy. As the spectrum of introduced defects changes, which is accomplished by the experimental conditions and initial doping of the semiconductor sample, the ultimate position of the Fermi level changes as well [42, 45].

Typically, a change in the concentration of free charge carriers (for example, electrons) in a semiconductor exposed to irradiation with dose Φ is described by the formula [1]

$$n = n_0 \pm \Phi K\{1 + \lambda \exp[(E - E_F)/kT]\}^{-1}, \qquad (5)$$

where n_0 and n are the electron concentrations before and after irradiation, respectively; K is the introduction rate for radiation defects; E_F is the Fermi level position; E is the energy-level position for a radiation defect; λ is the degeneracy factor; k is the Boltzmann constant; and T is the absolute temperature.

For low irradiation doses, in which case a Fermi level shift may be ignored, the dependence of $\Delta n = n_0 - n$ on the irradiation dose becomes linear, and the coefficient K referred to in this case as the coefficient of degradation of the charge-carrier concentration is equal simply to the removal rate of charge carriers.

Matsumura and Stephens [46] studied in detail the dependence of the concentration of removed charge carriers in *n*-GaAs on the distance from the surface in a semiconductor. In Fig. 4, we show such a dependence for *n*-GaAs irradiated with 150–500-keV protons. Figure 5 illustrates the effect of the irradiation dose on the concentration of removed charge carriers [46]. The effective removal of charge carriers in gallium arsenide irradiated with protons results in an abrupt increase in the semiconductor's resistivity, which is observed both in *p*-GaAs and in *n*-GaAs. It has been shown previously [16] that the dependence of resistivity in *p*-GaAs on the dose of proton irradiation is radically different from this dependence in *n*-GaAs; this difference is affected both by the proton energy and by the concentration of

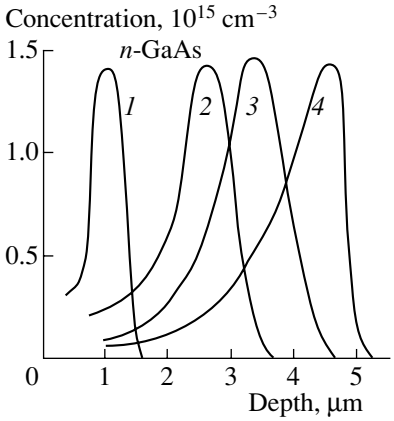

Fig. 4. Concentration profiles for removed charge carriers in *n*-GaAs after irradiation with protons with energies of (*1*) 150, (*2*) 300, (*3*) 400, and (*4*) 500 keV [46].

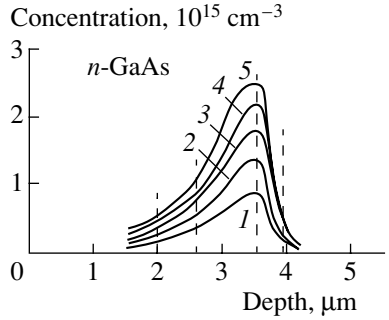

Fig. 5. Concentration profiles for removed charge carriers in *n*-GaAs after irradiation with 400-keV protons in relation to the dose of proton irradiation Φ = (*1*) 1×10^{10}, (*2*) 2×10^{10}, (*3*) 3×10^{10}, (*4*) 4×10^{10}, and (*5*) 5×10^{10} cm^{-2}.

charge carriers in the initial materials. General features of these dependences include the following: (i) the carrier-removal rate in *n*-GaAs ($dn/d\Phi$) is higher than in *p*-GaAs ($dp/d\Phi$); and (ii) the highest resistivity of GaAs is attained for a certain irradiation dose Φ_{opt}: as the dose increases beyond Φ_{opt}, a decrease in the resistivity ρ of semiconductor is observed.

Recently [35], the profiles of charge-carrier concentration and the energy spectra of radiation defects in the GaAs samples irradiated with 100-keV protons were measured simultaneously. It was established that proton irradiation induces conductivity compensation in a fairly thin layer of the material (with a thickness of $d \approx$ 0.5–0.7 μm), whereas the spectrum of introduced radiation defects (Table 7) coincides qualitatively with the spectrum of defects observed in similar samples after electron irradiation.

Table 7. Introduction rates for electron traps in *n*-GaAs irradiated with 100-keV protons [35]

n_0, cm^{-3}	Introduction rate, cm^{-1}			
	*E*2	*E*3	*E*4	*E*5
2×10^{17}	4×10^{3}	8.5×10^{3}	3×10^{3}	1.2×10^{4}
1.5×10^{17}	4×10^{4}	6×10^{3}	6×10^{3}	5.7×10^{3}
3×10^{16}	1.1×10^{4}	5×10^{3}	3×10^{3}	2×10^{3}

Donelly and Hurwitz [47] studied the dependences $\rho(\Phi)$ for *n*- and *p*-InP irradiated with protons (E_0 = 50–400 keV). It was shown that these dependences have a maximum for both materials. The largest value of ρ ($\rho \approx 10^3$ Ω cm) in *n*-InP was observed for irradiation doses of $\Phi \approx 10^{15}$ cm^{-2}, whereas the highest ρ in *p*-InP ($\rho \approx 10^8$ Ω cm) was observed for doses of $\Phi \approx 2 \times 10^{14}$ cm^{-2}. A model explaining the results obtained was suggested [47]. According to this model, the Fermi level is located at 0.30–0.34 eV above the semiconductor midgap for high irradiation doses. Therefore, the resistivity of *n*-InP irradiated with protons at high doses is relatively low. In contrast, the Fermi level in *p*-InP crystals passes through the midgap as ρ varies with Φ; it is due to conductivity compensation by radiation defects that the highest resistivity $\rho \sim 10^8$ Ω cm (close to the value corresponding to intrinsic conductivity) is observed. As the dose of irradiation of *p*-InP increases, a *p–n* conversion of conductivity type occurs.

The idea about pinning the Fermi level in heavily irradiated semiconductors was suggested first for InP [47] and then for GaAs [48]. It was shown [48] that the irradiation of gallium arsenide with protons resulted in an increase in the resistivity to ultimately high values of $\sim 6 \times 10^8$ Ω cm (at 300 K). The *n–p* conversion of conductivity and pinning of the Fermi level in the vicinity of E_v + 0.6 eV [49] were observed (as previously, see [43]). In the ascending portion of the dose dependences of electrical conductivity, these dependences can be adequately described on the basis of the numerical solution of the electroneutrality equation [49]. For the doses higher than optimal (from the standpoint of obtaining high-resistivity material), an anomalous dependence, i.e., a decrease in resistivity with dose, is observed (see also earlier results, [16]). This phenomenon is observed for irradiation doses higher than 5×10^{17} cm^{-2} for electron irradiation (E_0 = 2 MeV) and for doses higher than 10^{15} cm^{-2} in the case of proton irradiation (E_0 = 5 MeV). It is assumed that the charge-carrier transport in "overirradiated" samples occurs via hopping conduction over deep states of radiation defects [50].

Experiments with both electron and proton irradiation indicate that the irradiation-induced carrier-removal rate $dn/d\Phi$ decreases drastically with increasing T_{irr} [28, 32]. Such a decrease cannot be explained by the conditions of primary radiation-defect formation (the Frenkel pair formation) since the temperature dependence of the threshold energy for the displacement of regular atoms is fairly weak in the temperature range under consideration. In our opinion, the results

obtained can be explained only by changes in the conditions of the secondary radiation-defect formation; these changes are related to the dissociation of the bound Frenkel pairs responsible for the compensation of electrical conductivity in *n*-GaAs. As T_{irr} increases, the concentration of the bound Frenkel pairs (N_F) determined from the equation

$$dN_F/d\Phi = G - N_F/\tau, \quad (6)$$

where G and τ are the generation rate and lifetime of the bound Frenkel pairs, decreases drastically owing to a decrease in τ.

Experiments with GaAs doped with rare-earth elements [34, 51] further validate the model that accounts for the dissociation of the bound Frenkel pairs and for the migration of mobile intrinsic defects to sinks. These experiments showed that irradiation at $T_{irr} < 100$°C brings about almost the same charge-carrier removal rate (0.5 cm^{-1}) in the GaAs samples irrespective of whether or not they were doped with Yb or Er.

In Fig. 6, experimental results are represented as the ratio

$$\xi = \frac{(dn/d\Phi)_{Yb}}{dn/d\Phi} \quad (7)$$

of the charge-carrier removal rate in the samples with a Yb content of $N_{Yb} \approx 0.05$ wt % (curve *1*) and $N_{Yb} = 0.003$ wt % (curve *2*) to the carrier removal rate in the samples without the Yb impurity as a function of T_{irr}. As T_{irr} increases, the run of the curves changes radically for $T_{irr} > 100$°C. The value of $(dn/d\Phi)_{Yb}$ decreases more steeply than $dn/d\Phi$ does; as a result, at $T_{irr} = 150$°C, ξ becomes equal to ~0.4 for $N_{Yb} = 0.05$ wt % and to ~0.6 for $N_{Yb} = 0.003$ wt %. As T_{irr} increases further to 200°C, ξ increases to 0.5 and 0.7, respectively; for $T_{irr} > 250$°C, the values of ξ approach 0.8–0.9. If Er impurity is used, the values of ξ are almost the same.

In order to explain the experimental results obtained, we should take into account that the mobility of primary radiation defects (vacancies and self-interstitials) is low in *n*-GaAs; as a result, a situation arises where the consequences of irradiation at temperatures close to and below room temperature are governed by intrinsic lattice defects, whereas the contribution of various impurity–defect complexes is unimportant [14, 38]. Among five main types of radiation defects $E1$–$E5$ introduced into *n*-GaAs at room temperature, four are related to the Frenkel pairs in the As sublattice [V_{As}–As_i] and the remaining defect may be attributed to the antisite defect As_{Ga} [27]. Four types of electron traps $E1$, $E2$, $E3$, and $E5$ attributed to the Frenkel pairs in the arsenic sublattice are explained by the fact that there can be two charge states of Frenkel pairs for two characteristic distances between the pair components [22]. We are reminded, as is generally accepted, that the Frenkel pairs in the gallium sublattice are generated with opposite-charged components; as a result, these

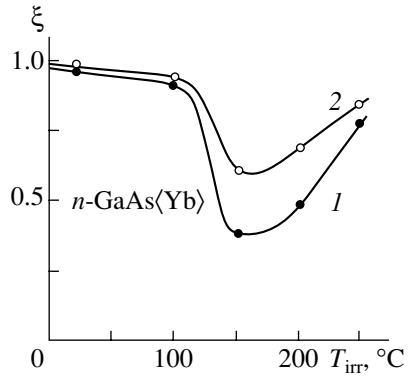

Fig. 6. Ratio of the charge-carrier removal rate in the *n*-GaAs samples with a Yb content of (*1*) 0.05 and (*2*) 0.003 wt % to the carrier-removal rate in undoped samples in relation to irradiation temperature [51].

pairs annihilate immediately after their formation even at 4 K owing to the Coulomb interaction between the pair components.

The quasi-equilibrium concentration of radiation defects, which controls the concentration of removed charge carriers, is determined from continuity Eq. (6) and is equal to the product of the defect generation rate G by the corresponding lifetime τ under the steady-state conditions. Since G remains virtually unchanged under fixed irradiation conditions when N_{Yb} varies and T_{irr} is in the range of 20–250°C, the changes in $dn/d\Phi$ are caused by variations in τ alone.

The lifetime of the Frenkel pairs is governed by two main processes; these are the dissociation of the pairs and the recombination of the pair components. The energy barriers for the above processes are such that the Frenkel pairs formed are metastable at room temperature. As T_{irr} increases, dissociation of the formed Frenkel pairs becomes more intense at $T_{irr} > 100$°C. As mentioned above, this intensification may be caused by a decrease in the height of the energy barrier for the dissociation of the Frenkel pairs, whose components change their charge owing to intense ionization of the crystal during electron irradiation. An additional mechanism may be the separation (enhanced by nonradiative recombination of nonequilibrium electrons and holes) of the Frenkel pair components (the Bourgoin–Corbett mechanism [38]). As T_{irr} increases, these point defects become more mobile; as these defects migrate, they can be trapped with a high probability by impurity atoms and form complex associations. The decrease observed in ξ at $T_{irr} > 100$°C in the samples doped with Yb (Fig. 6) supports this model. The dependence of ξ on N_{Yb} for fixed T_{irr} (in the range of 100–250°C) indicates that Yb atoms are effective as either annihilation centers for intrinsic defects or trapping centers.

At higher T_{irr} (250–350°C), differences between $dn/d\Phi$ for doped and undoped samples are no longer observed, and the quantity ξ tends to unity. In order to

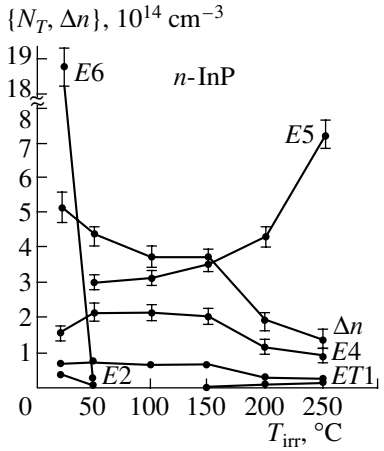

Fig. 7. Concentration N_T of deep-level centers $E1$, $ET1$, $E2$, $E4$, $E5$, and $E6$ introduced into n-InP by irradiation with 1-MeV electrons and the concentration of removed charge carriers (Δn) in relation to the irradiation temperature [30].

explain this result, it is inadequate to take into account only the Frenkel pair dissociation, which was dominant at lower T_{irr}. We should admit that annihilation is enhanced at $T_{irr} > 250$–350°C, which may be related to a decrease in the height of the energy barrier for annihilation. This decrease with increasing T_{irr} may be caused by a change in the charge states of reacting defects.

Thus, as a result of the modification of defects at intermediate irradiation temperatures, the lifetime of the point defects, their quasi-equilibrium concentration, and, consequently, the degree of compensation of conductivity in n-GaAs:Yb decrease. This inference is valid not only for electron irradiation but, according to experiments, for proton irradiation as well. It follows from our experiments that the introduction of erbium into epilayers appreciably reduces the value of $dn/d\Phi$. Thus, the introduction of Er significantly affects the radiation-defect formation in n-GaAs only at elevated temperatures of irradiation ($T_{irr} > 100$°C), which is caused by the dissociation of intrinsic Frenkel pairs in the As sublattice at these T_{irr} and by the migration of the pair components to Yb atoms; the latter act as annihilation centers for the Frenkel pair components.

It has been established [33] that, at high annealing temperatures ($T_{ann} \approx 400$°C), the charge-carrier concentration in the n-GaAs samples irradiated with electrons at $T_{irr} = 20$°C is recovered almost completely. In contrast, the rate of the charge-carrier removal in n-GaAs irradiated at $T_{irr} = 400$°C is nonzero and is equal to $\sim 2 \times 10^{-2}$ cm^{-1}, which is lower by a factor of ~25 than the removal rate at $T_{irr} = 20$°C. However, taking into account the high thermal stability of the radiation defects introduced and the fact that the main compensation of the material occurs owing to the levels lying fairly deep in the band gap, it has been concluded [34] that it is appropriate to use high-temperature irradiation to obtain high-resistivity GaAs with high thermal stability. Later [52–57], this conclusion was verified experimentally. Thus, it has been shown [53] that the resistivity of n-GaAs irradiated with protons at $T_{irr} = 300$°C exceeds by a factor of 10^3 the resistivity of n-GaAs irradiated at room temperature and then annealed at $T_{ann} = 300$°C.

Kozlovski *et al.* [30] analyzed in detail the temperature dependences of the production rate of centers $E1$–$E6$ in irradiated n-InP and of the concentration of removed charge carriers $\Delta n = n_0 - n(T_{irr})$, where $n(T_{irr})$ is the charge-carrier concentration in the films after irradiation. It can be seen from Fig. 7 that two stages can be distinguished in the dependence $n(T_{irr})$; the first stage is consistent with the disappearance of the $E2$ centers, and the second stage is related to a decrease in the concentration of traps $E1$ and $E4$ (of the multicharged M center). It is evident that the rate of charge-carrier removal in n-InP is governed by the introduction rate for traps $E1$ and $E4$ and is equal to $\sim 1 \times 10^{-2}$ cm^{-1} at $T_{irr} = 250$°C, which is smaller by a factor of ~3 than this rate at $T_{irr} = 20$°C. Comparing the data reported in [30, 34], we may state that, at room temperature, the removal rate of charge carriers in n-GaAs exceeds this rate for n-InP by more than an order of magnitude, whereas the carrier removal rates in these two materials are almost the same at elevated temperatures.

In recent years, studies using radiation defects to dope another promising material from the group of III–V compounds (gallium nitride) have started [58–60]. Thus, it has been shown [59] that irradiation of n-GaN with protons or helium ions leads to an increase in resistivity by 10 orders of magnitude.

A correlation between the thermal stability of radiation defects introduced by proton or electron irradiation into III–V compounds and changes in the electrical properties of these materials has been considered repeatedly [17, 20, 43, 61–63]. A typical dependence of the resistivity of proton-irradiated $Ga_{0.65}Al_{0.35}As$ on the annealing temperature [61] is shown in Fig. 8. The doses of proton irradiation were 10^{12}–10^{13} cm^{-2} [61]. For such irradiation doses, two main annealing stages (in the vicinity of $T_{ann} = 200$ and 400°C) are observed. As the irradiation dose increases, the features of annealing change. Thus, a stage of "negative" annealing for the samples irradiated with high doses was observed [17]. As a result of heat treatment at 300–350°C, resistivity of irradiated samples increased, whereas, for higher annealing temperatures (500°C), resistivity decreased. Similar negative annealing in n-GaAs irradiated 5-MeV protons with a dose of 2×10^{17} cm^{-2} has been observed previously [43].

The effective removal of charge carriers in III–V compounds as a result of irradiation with protons and electrons and the fairly high temperature stability of the semi-insulating semiconductor formed (up to 200°C)

make it possible to use irradiation with good results to develop new semiconductor devices.

3.4. Prospects of Using Proton Irradiation for the Development of Semiconductor Devices Based on III–V Compounds

The formation of semi-insulating gallium arsenide irradiated with protons was first observed more than 30 years ago [64]. At that time, this effect was regarded as detrimental; it had not been anticipated that after several years the implementation of the effect would start. It was shown later [65] that proton irradiation can be successfully used for the isolation of GaAs diodes in a matrix. Proton irradiation has been also employed in the fabrication of avalanche diodes [66, 67], Schottky diodes, and field-effect transistors (FETs) with a Schottky barrier [68, 69]. In all the cases, the physical basis of using proton irradiation is the possibility of effectively controlling the resistivity of *n*-GaAs by doping with radiation defects. As an example, we may analyze the publication by Pruniaux *et al.* [68], in which the results of studying the transistor structures fabricated both by mesa technology and using proton bombardment were reported. The problem of reducing the parasitic capacitance of the gate pad relative to the source in the technology of GaAs-based microwave FETs is typically solved by etching the mesa structures. A drawback of this method is that there are "thin" regions in the metallization layer; therefore, there is a high probability of ruptures in this layer. It was shown [68] that the etching of the mesa structures may be successfully replaced by proton bombardment through a photoresist mask (Fig. 9). The use of proton bombardment ensures the localization of the active region in the FET structure and the formation of a semi-insulating layer in the region under the gate electrode in order to reduce the parasitic gate–source capacitance. An unconventional attempt at improving the characteristics of the GaAs:Cr-based microstrip charged-particle detectors has been reported recently [70, 71]. It was shown that compensation of the detector's low-resistivity operating region made it possible to drastically increase the signal-to-noise ratio and increase the charge-collection efficiency to almost 100%.

The main drawback of conventional proton bombardment at T_{irr} = 20°C is the low thermal stability of the resulting semi-insulating GaAs. As was shown above, the *E* traps, which largely contribute to the high resistivity of the irradiated material, start to anneal out at 250°C. At the same time, the technological operation subsequent to proton bombardment in the course of fabrication, for example, of FETs with a Schottky barrier, and consisting in the firing-in of nonrectifying contacts is typically performed at temperatures of 400–450°C. Experiments show that radiation defects introduced by irradiation at T_{irr} = 20°C can anneal out to a large extent during firing-in of the contacts; as a result, the resistance of interelement isolation in microwave integrated circuits (ICs) is reduced drastically and returns practically to the preirradiation value. It was assumed in the 1980s that thermally stable isolation can be attained by replacing proton irradiation (irradiation isolation) by irradiation with heavier ions (of oxygen, fluorine, neon, and the like) (the so-called implantation isolation) [72, 73]. However, the use of heavier ions has its own drawbacks, which consist, in particular, in a sharp decrease in the depth of radiation treatment of the semiconductor. Difficulties related to the use of proton irradiation were overcome only in the mid-1990s, when the processes of radiation-defect formation in GaAs were studied in detail and the conditions for the formation of thermally stable *X* traps were determined (see above). An increase in the irradiation temperature and, as a consequence, in the irradiation dose (in order to compensate for the reduced removal rate for charge carriers) made it possible to form a thermally stable isolation to separate the strip microheterolasers and FETs with a Schottky barrier in ICs fabricated on the basis of GaAs and the corresponding solid solutions [35]. In the mid-1990s, it was suggested for the first time to use the irradiation-induced changes in the charge-carrier concentration not only for microwave and optoelectronic

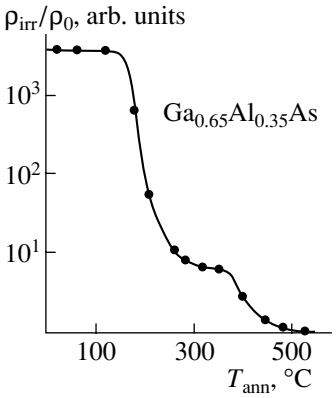

Fig. 8. Relative change in resistivity ρ_{irr}/ρ_0 of $Ga_{0.65}Al_{0.35}As$ irradiated with protons as a function of the annealing temperature [61].

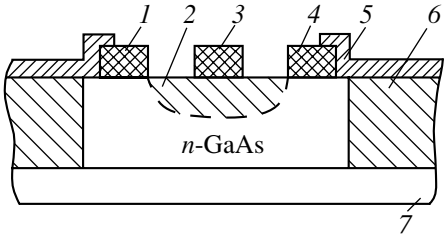

Fig. 9. The structure of a GaAs-based microwave field-effect transistor with Schottky barrier; the transistor was fabricated using proton irradiation [68] and included (*1*) the source, (*2* and *6*) semi-insulating regions formed using proton irradiation, (*3*) the gate, (*4*) the drain, (*5*) a metallization layer, and (*7*) the substrate.

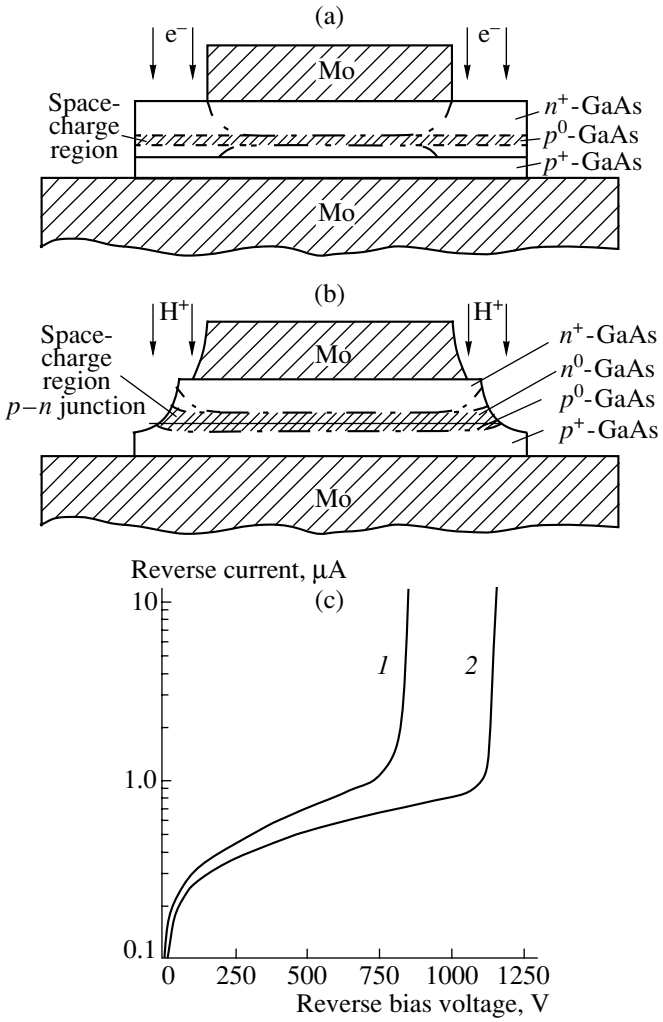

Fig. 10. A GaAs-based high-voltage *p–n* structure: (a) a schematic representation of irradiation of a p^+–p^0–n^+ structure of a high-voltage diode without formation of an edge contour before irradiation [74]; (b) a schematic representation of irradiation of a p^+–p^0–n^0–n^+ structure of a high-voltage fast-recovery drift GaAs diode with mesalike edge contour; and (c) the current–voltage characteristics of the GaAs diode (*1*) before and (*2*) after proton irradiation.

devices but also for high-voltage power devices based on gallium arsenide [74]. Kozlovski *et al.* [74] investigated the possibility of eliminating the surface breakdown of GaAs-based high-voltage diodes and thyristors (this breakdown narrows the operating-voltage range and reduces the reliability of the devices) by forming a semi-insulating GaAs layer in the peripheral region of high-voltage *p–n* structures (Fig. 10a). This GaAs layer was formed by irradiation with 5-MeV protons or 1-MeV electrons. Specific irradiation conditions were not reported [74]; however, it was stated that this type of radiation doping made it possible to almost completely eliminate the surface breakdown and increase the operating voltage from 800–900 to 1200–1300 V in the *p–n* structures. It has been noted that electron irradiation is preferable for achieving the above objectives, since, if protons with energies of about 3 MeV are used, then nuclear reactions occur in gallium arsenide; as a result, it is necessary to "age" the samples for quite a long time in order to eliminate the induced radioactivity. The study of the configuration of the electric field in the space-charge region (SCR) using the electrooptical effect in infrared light in the transmission mode made it possible to detect a bending of the SCR boundary and a sharp increase in the SCR thickness in the peripheral region of the crystal. Thus, the elimination of the surface breakdown was attributed [74] to the formation of semi-insulating zones in the peripheral region of the sample under optimized irradiation conditions and to an appreciable decrease in the electric-field strength at the structure surface.

Results similar to those reported in [74] were obtained for proton-irradiated GaAs-based power pulse diodes and dinistors whose edge contour had a mesa-like shape (Fig. 10b). Irradiation of the edge contours of such devices with 3-MeV protons with doses of 10^{12}–10^{13} cm^{-2} made it possible to eliminate the surface breakdown of the high-voltage *p–n* junction in GaAs structures and to increase the avalanche-breakdown voltage from about 600–800 V to values higher than 1000 V. An optical-beam induced current (OBIC) study at a wavelength of 0.63 μm of the spots of localization of the first microplasma channels over the surface area of *p–n* structures before and after proton irradiation showed that the "low-voltage" breakdown in unirradiated structures occurred in the vicinity of the edge mesa contour of the *p–n* junction. Data obtained by scanning laser microscopy have shown that, if the edge contour in devices is irradiated with protons using a special molybdenum mask (to shield the central part of the structure from radiation), then the electric field at the edge-contour surface is reduced and the localization area of the first microplasma channels shifts from a peripheral region of the devices to their central unirradiated part. The reverse portions of current–voltage characteristics of such GaAs-based fast-recovery drift diodes prior to and after proton irradiation are shown in Fig. 10c. Similar data on the elimination of the surface breakdown in high-voltage *p–n* junctions have been obtained in experiments with proton irradiation of ultrafast photon-injection thyristors and dinistors based on GaAs/AlGaAs heterostructures.

The prospects of using proton irradiation for other optoelectronic devices have been considered previously [3, 75–79]. The following trends should be mentioned:

(i) confinement of the recombination region in the fast light-emitting diodes;

(ii) formation of strip configuration in semiconductor lasers;

(iii) formation of guard rings in photodiodes;

(iv) formation of optical waveguides by changing the refractive index of materials by proton irradiation;

(v) fabrication of light-emitting diodes having enhanced the intensity and power of radiation and operating in the direct- and alternating-current mode under various supply voltages;

(vi) fabrication of multielement monolithic optical devices for outputting the information (linear and two-dimensional arrays of light-emitting diodes).

4. DOPING SILICON WITH RADIATION DEFECTS

4.1. Radiation Defects in Silicon Irradiated with Protons and Alpha Particles

The irradiation of silicon with protons and alpha particles gives rise to primary point radiation defects, i.e., vacancies V and the interstitial silicon atoms Si_i (the Frenkel pairs) related to them; these defects are generated along the ion track as a result of the development of collision cascades that involve the ions and the crystal-lattice atoms. The Frenkel pairs formed as a result of irradiation are metastable and can be typically observed only at low temperatures [80]. If the irradiation temperature is higher than 295 K, most of the Frenkel pairs formed [$Si_i - V$] disappear as a result of mutual annihilation; the remaining separated components of the pairs migrate and interact with each other and the impurity atoms in the crystal, thus forming more complex and stable secondary radiation defects [1, 23]. It is the secondary radiation defects that ultimately govern various properties of irradiated silicon crystals. Radiation defects are thermally unstable and anneal out at elevated temperatures. Nevertheless, many types of secondary radiation defects are stable in the temperature range corresponding to the operation of silicon devices and can be used to appropriately control the properties of Si and the parameters of Si-based devices. We will consider thermally stable secondary radiation defects in this section.

4.1.1. Levels of radiation defects in silicon irradiated with protons and alpha particles. It is well known that radiation defects are electrically active and introduce energy levels in the band gap of the semiconductor.

In silicon, which is an indirect-gap semiconductor, radiation defects control the kinetics of the generation–recombination processes. Because of this circumstance, in the majority of applications, irradiation with protons and alpha particles is used for the local (concerning the area and depth) control of the charge-carrier lifetime in the semiconductor device structures. The knowledge of the main parameters of the radiation defects and of their distribution in the bulk of a crystal is an important prerequisite to choosing irradiation conditions to obtain the required device characteristics. Therefore, radiation defects in silicon irradiated with light ions are the subject of numerous studies.

The vacancy-containing defects are found to be most important in changing the properties of silicon irradiated with protons and alpha particles. These radiation defects include first of all a complex consisting of interstitial oxygen $O_i\rangle$ and a vacancy V (the A center), a divacancy (V–V), and a complex composed of phosphorus at the lattice site P_s and a vacancy V (the E center) [1, 23, 81–87]. The A center is the most dominant (in concentration) radiation defect in silicon grown by the Czochralski method and irradiated with light ions with doses of up to 10^{13} cm^{-2}. An acceptor level $E1$ located in the upper half of the band gap and separated by ~0.17 eV from the conduction-band bottom is related to the above radiation defect. The A center has large capture cross sections for electrons and holes and thus controls the lifetime of nonequilibrium charge carriers in n-Si under a high injection level [82, 87–89]. This defect is stable in the temperature range characteristic of the operation of silicon devices and anneals out at a temperature of ~350°C.

The second radiation defect in concentration in silicon irradiated with light ions with irradiation doses of up to 10^{13} cm^{-2} is divacancy. For higher irradiation doses, in which case the buildup of A centers is limited by the concentration of dissolved oxygen, divacancy becomes the radiation defect with the highest concentration [90]. Three energy levels in the silicon band gap correspond to a divacancy. Two acceptor levels $E2$ and $E3$ are located in the upper half of the band gap; their positions are $E_c - 0.23$ eV and $E_c - 0.42$ eV below the conduction-band bottom. The donor divacancy level $H1$ is located at $E_v + 0.19$ eV in the lower half of the band gap. Divacancy is an effective recombination center in silicon and is responsible for the value of the hole lifetime in n-Si at a low level of injection [82, 87]. In addition, this radiation defect is the major trap for free charge carriers, and its buildup in the crystal leads to an increase in the resistivity of irradiated silicon [90, 91]. The temperature of annealing out divacancies is somewhat lower than that of the A centers and is in the range of 220–270°C (depending on the ratio between the C and O concentrations in silicon and on the conditions of irradiation and annealing).

In addition to the A centers and divacancies, which are the dominant radiation defects, other types of radiation defect may significantly affect the properties of irradiated silicon in a number of cases. Thus, in the n-Si grown by the floating-zone method doped with P and irradiated with protons and alpha particles, free vacancies are effectively trapped by P atoms and form the E centers. It is important that the cross section of capture of a vacancy by a P atom in n-Si is about 20 times larger than the cross section of capturing the vacancy by an electrically inactive interstitial oxygen atom due to Coulomb attraction [92]. Because of this circumstance, the formation rate of E centers typically exceeds that of A centers in silicon crystals in which the phosphorus concentration is higher than 5% of the initial oxygen concentration. The acceptor level $E4$ located at $E_c - 0.44$ eV in the upper half of the band gap corresponds

to the *E* center. In silicon crystals which are doped heavily with phosphorus and have a low oxygen content, this radiation defect and also more complex phosphorus-containing agglomerates can be dominant and control the dynamics of generation–recombination processes [88, 92]. Since the *E* centers feature a comparatively low thermal stability in the temperature range corresponding to the operation conditions of silicon devices, these centers are eliminated from irradiated device structures by thermal annealing. The annealing temperature of these centers is ~150°C.

The so-called *K* center is more thermally stable compared to the *E* center in irradiated silicon with high concentrations of oxygen and carbon. The *K* center is a point radiation defect and is a complex consisting of an interstitial oxygen atom and an interstitial carbon atom [O_i–C_i] [80, 92]. There is an opinion that the *K* defect includes a vacancy in addition to carbon and oxygen [1, 82, 83]; however, this assumption is not substantiated by any conclusive reasoning. A donor level *H*2 (E_v + 0.36 eV) lying in the lower half of the band gap and having a comparatively large cross section for charge-carrier capture corresponds to the *K* center [89, 91, 93]. The *K* centers may control the lifetime of nonequilibrium charge carriers in *p*-Si [13] and can also profoundly affect the dynamic breakdown voltage of diodes that were irradiated with protons or alpha particles and operate in actual electrical circuits at the frequencies of $\gtrsim$100 kHz [93].

There is a radiation-defect level lying close to that of the *K* center in the silicon band gap; this level belongs to a complex composed of interstitial carbon atom C_i and substitution carbon atom C_s [1, 80, 83, 91, 94, 95]. This radiation defect is typically observed in crystals with a comparatively low concentration of dissolved oxygen and a high concentration of the defects C_s, in which case the carbon atoms C_s become the main traps for the atoms C_i. The defect [C_s–Si_i–C_s] observed in proton-irradiated silicon [96, 97] has parameters close to those of the [C_i–C_s] center. A common feature of radiation defects [C_i–C_s] and [C_s–Si_i–C_s], which contain interstitial silicon atoms and carbon atoms at the lattice sites, is their low thermal stability [94, 95]. In actual Si-based devices, these defects are annealed out in order to stabilize the characteristics of irradiated devices.

The aforementioned radiation defects in silicon irradiated with light ions may be treated as "native" point radiation defects because they do not contain hydrogen or helium ions. These radiation defects are formed in silicon under other types of irradiation as well, i.e., under irradiation with electrons or gamma-ray quanta. In the case of the proton irradiation of silicon, the defects containing the implanted hydrogen atoms can be formed in addition to native radiation defects. Hydrogen is a chemically active element and interacts with defects and impurities in the crystal. This interaction may manifest itself both in the passivation of electrically active defects and impurities in silicon [85] and in the formation of new electrically active centers [8, 81–85, 87].

Radiation defects containing hydrogen in proton-irradiated silicon have been studied by DLTS. In the band gap of silicon irradiated with 300-keV protons at room temperature, six types of levels belonging to hydrogen-containing radiation defects were observed [83]; these levels are located at E_c – 0.1 eV (*EH*1), E_c – 0.13 eV (*EH*2), E_c – 0.31 eV (*EH*3), E_c – 0.41 eV (*EH*4), and E_c – 0.45 eV (*EH*5) in the upper half of the band gap and at E_v + 0.28 eV (*HH*1) in the lower half of the band gap. The results of the isochronous annealing of these radiation defects have shown that the acceptor level *EH*3 and the donor level *HH*1 belong to the same defect, whose concentration is higher than those of other hydrogen-containing defects. This hydrogen-containing radiation defect and also the trap levels *EH*4 and *EH*5 of other hydrogen-containing defects have been repeatedly observed in proton-irradiated silicon [81, 82, 84, 87]. It is noteworthy that the structure of hydrogen-containing defects in silicon remains unclarified. As for the most important defect with the levels *EH*3 and *HH*1, it has been assumed that it either contains two hydrogen atoms [83] or is a complex of a vacancy with a hydrogen atom [81]. According to recent results [82], the hydrogen-containing radiation defects affect to a much lesser extent the recombination of nonequilibrium charge carriers in proton-irradiated silicon compared to native defects such as the *A* center and divacancy. The hydrogen-containing defects are annealed out in a temperature range of 100–300°C, with a defect with the levels *EH*3 and *HH*1 having the highest thermal stability.

In addition to deep-level hydrogen-containing radiation defects, shallow-level hydrogen-containing donors are observed in silicon irradiated with protons and subjected to postimplantation annealing in a temperature range of $T_{ann} \approx$ 300–550°C [8, 80]. A supersaturated solution of hydrogen decomposes and hydrogen interacts with radiation defects and impurity atoms in the crystal during this postimplantation heat treatment of silicon. This interaction gives rise to new electrically active defects, which have the properties of shallow-level donor centers. The structure and parameters of these centers depend on the hydrogen concentration, the dose of irradiation with protons, the annealing temperature, and the initial properties of the crystal (the oxygen and carbon concentrations). Thus, depending on the experimental conditions, the formation of several families of hydrogen-containing donor centers with the following levels has been observed: E_c – 0.026 eV [8, 86, 98], E_c – 0.035 eV [80, 99], E_c – 0.043 eV [80, 100], and E_c – 0.06 eV and E_c – 0.1 eV [9, 101]. For low annealing temperatures and low hydrogen concentrations, donors with deeper levels are typically formed, whereas annealing at higher temperatures and high hydrogen concentrations are conducive to the formation of shallow-level hydrogen-containing donors [80].

The concentration of the formed hydrogen-containing donor centers is typically on the order of 0.3% of the total concentration of implanted hydrogen and is no higher than ~10^{17} cm^{-3}. The formation of shallow-level hydrogen-containing donors can appreciably enhance the electrical conductivity of *n*-Si or reduce the conductivity of *p*-Si to the point of conversion of the conductivity type [86, 90]. In this context, the effect of formation of the hydrogen-containing donor centers should be taken into account when fabricating the devices subjected to proton irradiation with subsequent thermal annealing at $T_{ann} > 300$°C. The hydrogen-containing quenched-in donors may be used intentionally to form *n*-Si layers in *p*-Si [102]; however, in our opinion, such structures with *p*–*n* junctions have excessively high generation currents and the stability of their characteristics should be investigated further.

Summing up the consideration of the radiation-defect levels in silicon irradiated with protons and alpha particles, we may state that these types of radiation treatment give rise to the levels of native point radiation defects in the silicon band gap, which are also observed after the irradiation of silicon with electrons or gamma-ray quanta. The levels belonging to hydrogen-containing radiation defects are also observed in the band gap of silicon irradiated with protons in addition to those belonging to native radiation defects. The energy positions of the levels belonging to the most important radiation defects and their parameters in silicon irradiated with light ions are given in Fig. 11 and Table 8. The most reliable (in our opinion) values of cross sections for the capture of charge carriers by the radiation-defect levels are given in brackets in Table 8.

4.1.2. The production rates and concentration profiles of radiation defects in silicon irradiated with protons and alpha particles. One of the main distinctive features of doping silicon with radiation defects by irradiating it with light ions (compared to electron or gamma-ray irradiation) is the fact that radiation treatment is highly localized both over the area and depth in the irradiated crystal. Localization of doping with radiation defects over the area of the semiconductor structure is accomplished by using the relevant masking coatings that absorb the incident ions or transmit them through windows for irradiation. Localization of the radiation treatment over the depth is ensured by choosing the energy of the implanted ions; the shape of the concentration profile of radiation defects is governed by the features of the energy losses of the ion when it interacts with the crystal lattice. For high energies of light ions (higher than 1 keV per nucleon), the prevalent mechanism of energy loss of an ion in a crystal is electron stopping, in which case the energy lost by the ion is spent mainly on the excitation of electron shells of atoms. If this mechanism is operative, the production rate of the primary radiation defects (the Frenkel pairs) is low. If an ion loses enough energy, so that it falls to ~1 keV per nucleon, the probability for an ion to interact elastically with the nuclei of atoms in a crystal increases drastically, and nuclear stopping becomes the prevalent mechanism of energy losses. When this stopping becomes effective, the production rate of primary radiation defects increases sharply. The distribution of secondary defects is close to that of primary defects and is nonuniform over the depth in an irradiated crystal. Near the surface, the concentration of radiation defects is comparatively low and increases with distance from the irradiated surface, so that there is a sharp concentration peak in the vicinity of complete ion stopping, i.e., at a depth which is slightly less than the projected ion range R_p.

Figure 12 shows the dependences of the projected ranges of protons and alpha particles in silicon on the ion energy in the range from 10 keV to 10 MeV. It can

Table 8. Main parameters of radiation-defect levels in silicon irradiated with protons and alpha particles

Designation of defect	Energy position of level	Cross section of electron capture σ_n, 10^{-16} cm^2	Cross section of hole capture σ_p, 10^{-13} cm^2	Annealing temperature T_{ann}, °C	Identification
*E*1	$E_c - (0.17 \pm 0.005)$ eV	100–400 (~130)	1.5–10 (~1)	350 ± 10	$(O–V)^{0/-}$, *A* center
*E*2	$E_c - (0.23 \pm 0.01)$ eV	10–36 (~2)	0.35–6 (~0.5)	290 ± 10	$(V–V)^{=/-}$, divacancy
*E*3	$E_c - (0.42 \pm 0.02)$ eV	6–90 (~10)	0.03–0.5 (~0.08)	290 ± 15	$(V–V)^{-/0}$, divacancy
*E*4	$E_c - (0.44 \pm 0.01)$ eV	10–50 (~30)	~3	150 ± 10	$(P–V)^{-/0}$, *E* center
*EH*1	$E_c - (0.10 \pm 0.01)$ eV	~20	–	–	Hydrogen-containing center
*EH*2	$E_c - (0.13 \pm 0.01)$ eV	~10	–	140 ± 20	Hydrogen-containing center
*EH*3	$E_c - (0.31 \pm 0.01)$ eV	4–30	0.07–0.3	330 ± 20	Hydrogen-containing center
*EH*4	$E_c - (0.41 \pm 0.02)$ eV	0.02–0.1	–	–	Hydrogen-containing center
*EH*5	$E_c - (0.45 \pm 0.01)$ eV	0.04–0.2	~0.0004	–	Hydrogen-containing center
*H*1	$E_v + (0.19 \pm 0.02)$ eV	~400	0.002–0.02 (~0.01)	290 ± 10	$(V–V)^{0/+}$, divacancy
*H*2	$E_v + (0.36 \pm 0.01)$ eV	0.02–0.5 (~0.1)	0.004–0.03 (~0.01)	340 ± 15	$(O–C)^{0/+}$, *K* center
*HH*1	$E_v + (0.28 \pm 0.01)$ eV	0.2–4	0.004–0.03	330 ± 10	Hydrogen-containing center

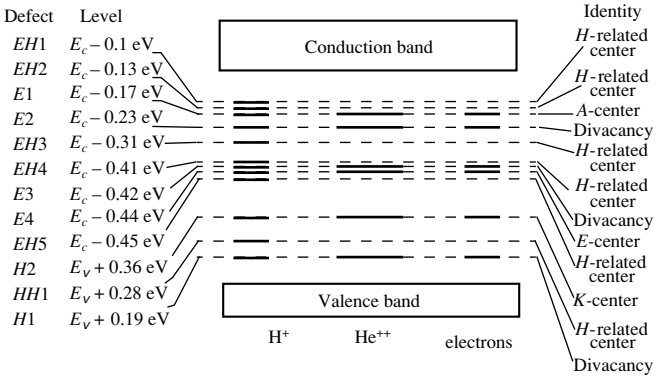

Fig. 11. Energy levels of radiation defects in the band gap of silicon irradiated with protons H^+, alpha particles He^{++}, and electrons.

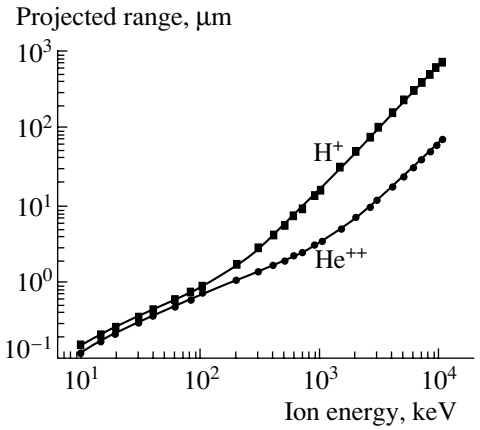

Fig. 12. Projected range of protons H^+ and alpha particles He^{++} in silicon in relation to the ion energy.

be seen from Fig. 12 that the irradiation of silicon with protons with energies in the above range ensures the possibility of local radiation-defect doping of silicon layers with a thickness from 0.15 to 700 μm. Thus, irradiation with protons with energies of up to 10 MeV covers in fact the entire range of thicknesses of modern Si-based semiconductor devices. Typical concentration profiles of some types of radiation defects over the entire path lengths of protons in *n*-Si irradiated with protons with energies of 320 keV and 3.2 MeV are shown in Fig. 13. Defects with the level *E*1 (the *A* centers) have the highest concentration over the entire path length of protons in silicon; the peak concentration of these defects observed at a depth of $\sim R_p$ exceeds by a factor of 5–10 the concentration near the surface. Similar concentration profiles have other intrinsic radiation defects as well [81, 82, 86, 87]. Hydrogen-containing defects (for example, those with levels *EH*3 and *HH*1) are observed only in a comparatively thin layer at a depth of R_p and do not feature a long concentration "tail", which extends to the surface. The concentration peak for hydrogen-containing radiation defects is located somewhat deeper than that for native defects [81]. Thus, the highest production rate of native radiation defects in Si irradiated with light ions is observed in the region of the highest generation rate of the Frenkel pairs. In contrast, the formation rate of hydrogen-containing defects is highest at a depth corresponding to the peak concentration of implanted H^+ ions or in the region where the product of concentrations of accumulated hydrogen and the generated Frenkel pairs is largest.

Studies of the kinetics of the radiation-defect buildup in silicon irradiated with light ions have shown that the concentration of native defects increases linearly with irradiation dose Φ for $\Phi < 10^{12}$ cm^{-2} [81–83, 85]. The production rate of radiation defects depends on the ion energy and decreases as the energy and range R_p of ions increase. Thus, for a proton energy of 320 keV, $R_p \approx 3$ μm and the highest formation rate of the *A* centers is $\sim 1.5 \times 10^4$ cm^{-1} [81], whereas the corresponding values are ~100 μm and ~460 cm^{-1} for a proton energy of 3.2 MeV [82]. The production rate of divacancies during proton irradiation is lower than that of the *A* centers by a factor of 3–5 [81, 82, 85, 87]. The typically observed concentrations of divacancies *E*2 are lower than those of the levels *E*3 and *H*1 for irradiation doses exceeding 10^{10} cm^{-2}. It is believed [82] that the divacancy state related to the level *E*2 disappears owing to the effect of the elastic-stress fields in the silicon lattice; these fields arise as a result of high-dose irradiation with light ions. Because of this circumstance, the concentration of *E*2 levels increases sublinearly, rather than linearly, as the irradiation dose increases.

The irradiation of silicon with deuterons or alpha particles is accompanied by more severe damage of the crystal compared to proton irradiation, all factors being equal; this is caused by the fact that the D^+ or He^{++} ions are heavier than H^+. According to [81, 87], an alpha particle produces about ten times more defects compared to protons of the same energy; the relative fraction of divacancies compared to that of the *A* centers produced by irradiation with alpha particles is larger by a factor of 1.5 than in the case of proton irradiation [87]. A feature common to the irradiation of silicon with any light ions is that the number of introduced radiation defects amounts to about 4–6% of the total number of the Frenkel pairs generated by radiation. This indicates that there is a high probability (~95%) of annihilation of the Frenkel pairs in silicon at temperatures higher than 295 K.

The kinetics of the buildup of hydrogen-containing radiation defects under proton irradiation of silicon is more complex than that of the introduction of native radiation defects and has been studied inadequately. The formation rate of hydrogen-containing radiation defects depends intricately on the irradiation conditions and the properties of silicon. For the most important of these defects (those with the levels *EH*3 and *HH*1), it has been found [81, 83] that their concentration

increases quadratically with dose for low doses of H^+ ion implantation; the dose dependence becomes linear for higher doses of irradiation. The change in the dose dependence of the buildup of these defects occurs when the implanted-hydrogen concentration becomes about twofold higher than the phosphorus concentration [81]. This change and also the inverse-linear dependence of the concentration of defects of this type on the phosphorus concentration make it possible to assume [81] that the phosphorus–vacancy complex (i.e., the *E* center) is directly involved in the formation of a hydrogen-containing defect with the levels *EH*3 and *HH*1.

An interesting feature of radiation-defect formation in silicon irradiated with light ions is the broadening of the peak and a decrease in the highest concentration of the vacancy-related radiation defects at a depth of $\sim R_p$ (Fig. 14) as the doping level of *n*-Si decreases. It has been shown [81] that the peak concentration of vacancy-related radiation defects decreases linearly with the lowering of the Fermi level caused by variation in the dopant concentration. At the same time, broadening of the concentration peak of radiation defects is not observed if the region of Frenkel pair generation during irradiation is located within the SCR of the reverse-biased Schottky diode. Distinctions between the concentration profiles of vacancy-related defects have been explained in terms of a model that accounts for the charge state of primary vacancies and their drift in an electric field, which arises under irradiation owing to the highly nonuniform distribution of charged vacancies in the region of their most intense generation [81, 103]. According to this model, immediately after the formation of vacancies due to the displacement of atoms from the lattice sites in *n*-Si, the vacancies capture electrons from the conduction band and become negatively charged. Therefore, the free-electron concentration in the region that corresponds to the most intense generation of vacancies by irradiation and is located at a distance of $\sim R_p$ from the surface may be much lower than the average donor concentration. As a consequence, a local electric field arises during irradiation in the region with a highly nonuniform distribution of vacancies; this field pulls the negatively charged vacancies toward the region where their concentration is lower. As a result of this field effect, the peak in the concentration profile of vacancy-related defects broadens. This broadening is especially pronounced in the lightly doped *n*-Si crystals for a high generation rate of vacancies. If vacancies are generated by radiation in the layer where there are no free electrons (for example, in the SCR of a Schottky diode), the primary radiation defects remain neutral and do not produce a pulling electric field, which is responsible for the broadening of the peak in the concentration profile for vacancy-related defects. Taking this model into account, we may assume that the influence of field effects on the concentration profiles of vacancy-related radiation defects will become less pronounced with decreasing intensity of the light-ion beam and with increasing ion energy; however, this assumption needs experimental verification.

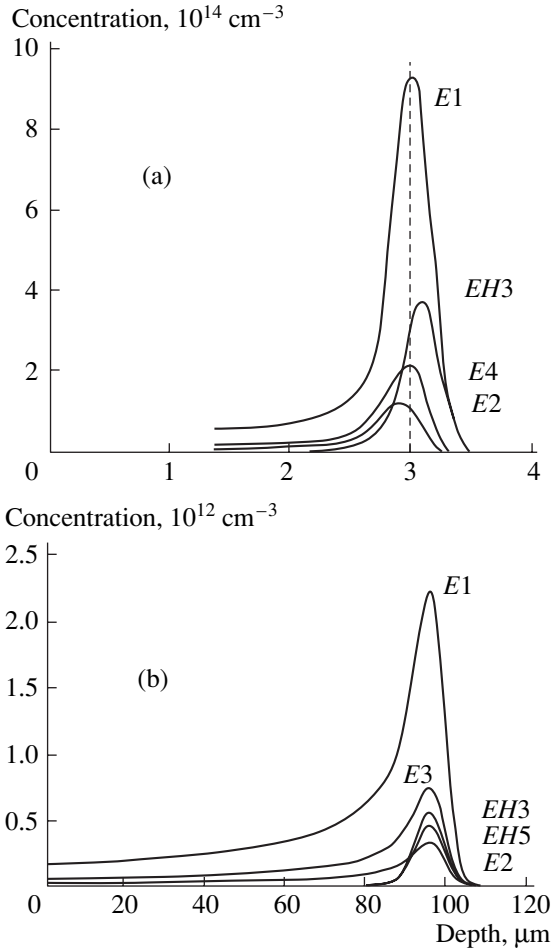

Fig. 13. Concentration profiles for radiation defects in *n*-Si irradiated with (a) 320-keV protons with a dose of 1×10^{11} cm^{-2} [81] and (b) 3.2-MeV protons with a dose of 5×10^9 cm^{-2} [82].

Summing up the consideration of the special features of radiation-defect formation in silicon irradiated with protons and alpha particles, we may conclude that irradiation with these ions makes it possible to locally dope silicon with radiation defects in layers with a thickness from several to hundreds of micrometers below the surface. If silicon is irradiated with light ions at room temperature, the main radiation defects, which govern the properties of silicon, are vacancy-containing point defects. The concentration of these defects and also that of the hydrogen-containing defects produced by proton irradiation have a well-defined peak at a distance of $\sim R_p$ below the surface. Radiation defects affect the lifetime of nonequilibrium charge carriers and the resistivity of the crystal; therefore, doping with radiation defects may be used to vary locally and purposefully the properties of Si and the characteristics of Si-based devices.

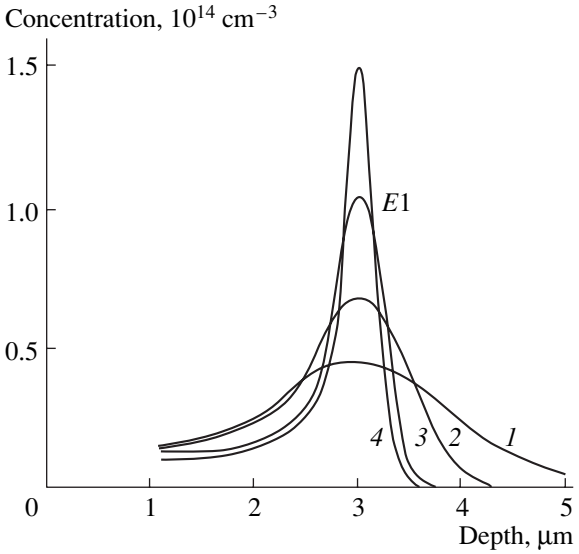

Fig. 14. Concentration profiles for *A* centers in *n*-Si with various initial electron concentrations *n* after irradiation with 320-keV protons with a dose of 1×10^{10} cm^{-2} [81]: n = 1.2×10^{14}, (*2*) 2.6×10^{14}, (*3*) 4.2×10^{14}, and (*4*) 2×10^{15} cm^{-3}.

4.2. The Implementation of Irradiation with Protons and Alpha Particles in the Technology of Fabrication of Si-Based Devices

The main practical application of doping silicon crystals with radiation defects as a result of irradiation with light ions is related to the reduction of the lifetime of nonequilibrium charge carriers in the structures of switching semiconductor devices (diodes, transistors, and thyristors). It is well-known that the maximum operating frequency of such devices is limited primarily by the comparatively slow process of switching the device from the conducting state to the blocking state and by energy losses during this switching process. In order to promote the turnoff process (i.e., to reduce the discharge time of electron–hole plasma in the course of switching the device structure to the blocking state) and to improve the speed characteristics of the devices, one typically attempts to reduce the lifetime of charge carriers in the lightly doped base layers of the semiconductor device structures. To this end, irradiation of devices with electrons or gamma-ray quanta is widely used at present. Such radiation technology for lifetime reduction is distinguished by high precision, reproducibility, and output and by low cost. However, in the devices irradiated with electrons or gamma-ray quanta, radiation defects are formed quasi-uniformly in the bulk of the base regions of semiconductor structures. For the high irradiation doses used in the production of high-frequency devices, a high concentration of radiation defects in the entire volume of base layers in a semiconductor structure leads to a severe decrease in the modulation depth for the structure's conductance and to a sharp increase of energy losses in the conducting state of the device.

In contrast to the electron and gamma-ray irradiation, irradiation with protons or alpha particles retains all the merits of radiation technologies and makes it possible to reduce the lifetime of charge carriers in the local volume of the semiconductor structure in the device. The local character of radiation treatment makes it possible to improve the totality of static and high-frequency device characteristics, which depend inversely on the lifetime of the nonequilibrium charge carriers. In fact, to effectively reduce the turnoff time in the power devices, the lifetime of charge carriers can be reduced only in part of the base-layer volume, where this reduction affects most markedly the process of switching from the conducting state to the blocking state, rather than in the entire volume of the base layers. In this situation, for the same parameters of the turnoff process, the devices with a nonuniform lifetime profile of nonequilibrium charge carriers have lower voltage drops across the structure in the conducting state. We now consider briefly the main results of studies aimed at optimizing the speed characteristics of various devices irradiated with protons or alpha particles in order to form local regions with a heightened recombination rate in the base layers of the structures.

For power semiconductor diodes, the main process limiting the maximum operating frequency of the device is the recovery of blocking properties of the high-voltage p^+–n junction during switching from the conducting state. Typically, this process is characterized by the time t_{rr} and charge Q_{rr} of reverse recovery (Fig. 15). For most practical applications, it is also necessary that the stage of the high reverse conductance of the diode t_s lasts for only a fraction of the total duration of reverse recovery ($t_s/t_{rr} < 0.5$); i.e., the recovery process should be "soft" (Fig. 15). Studies of various modes of irradiating power diodes with light ions [87, 89, 104–106] have shown that the optimal relation between the turnoff parameters and losses in the conducting state is ensured under the radiation conditions for which the concentration peak of radiation defects is located in the diode's *n*-base in the vicinity of the anode p–n junction. Compared to electron irradiation, local doping of the near-anode region in the *n*-base of diodes with proton-induced radiation defects made it possible to appreciably improve the speed characteristics of devices, with power losses in the conducting state increasing insignificantly. Thus, a transition from the conducting state to the blocking state for the identical level of power losses in the conducting state ~300 W/cm^2 occurred in a time of t_{rr} = 1.4 μs for the diodes irradiated with protons and in a time of t_{rr} = 4 μs for the devices irradiated with 1-MeV electrons [105]. Further reduction of t_{rr} by increasing the electron-irradiation dose results in a sharp increase in the static power losses in the conducting state, so that, even for $t_{rr} \approx$ 2.5 μs, these losses exceed the level of 600 W,

whereas, for proton irradiation, they remain at a level of ~300 W. Figure 15a illustrates typical relations between the forward-voltage drop across the diode structures in the conducting state (for the current density of 200 A/cm^2) and the reverse-recovery time for the proton and electron irradiations. The formation of a region with high-rate recombination in the diode's *n*-base near the high-voltage *p*–*n* junction using proton irradiation also leads to a "softer" recovery of the blocking properties of the *p*–*n* junction and to a decrease in the ratio t_s/t_{rr}. Such a change in the diode characteristics as a result of the formation of a region with high-rate recombination in the *n*-base in the vicinity of a *p*–*n* junction in the diode is quite understandable; indeed, it is the charge of nonequilibrium carriers in this region of the structure that affects most profoundly not only the quantities t_{rr} and Q_{rr} but also the duration of the stage of high reverse conductance t_s [105, 106]. Local doping of the diode's *n*-base with radiation defects in the vicinity of the n^+-emitter affects the values of Q_{rr} and t_s only slightly (especially if the light ions are implanted from the n^+-layer side); however, this doping leads to a more abrupt cutoff of the reverse current during the recovery of the blocking properties of the *p*–*n* junction [105, 106]. Therefore, light ions may be successfully implanted into the near-cathode region of the *n*-base to optimize the characteristics of another class of high-voltage diodes, i.e., fast-recovery diodes [106, 107] and diodes with reverse order of recovery [108]; for these diodes, it is necessary to ensure that the values of Q_{rr} and t_s are large, with the ratio t_s/t_{rr} being close to unity.

Static and dynamic characteristics of silicon power thyristors irradiated with protons have been studied repeatedly [106, 109–113]. For devices of this type, the optimal location of the layer with high-rate recombination is the part of the *n*-base that adjoins the high-voltage cathode *p*–*n* junction, which blocks the forward-polarity voltage. Furthermore, it is expedient to irradiate the thyristor structures from the side of the anode p^+-emitter. In doing so, radiation damage of the thyristor-structure *p*-base is eliminated; this damage typically results in a comparatively rapid increase in the control current and static power losses both in the conducting and blocking states of the device. At the same time, the formation of radiation defects throughout the entire thickness of the *n*-base with the peak of their concentration in the vicinity of the cathode *p*–*n* junction ensures an effective reduction in the time of removal of the nonequilibrium-carrier charge in this layer; it is the duration of the charge-removal process in the *n*-base that makes the largest contribution to the thyristor's turnoff time t_q. This mode of proton irradiation made it possible [112, 113] to obtain a unique combination of static and high-frequency characteristics of thyristors; i.e., after irradiation, the devices with a semiconductor-structure operating area of 20 cm^2 and blocking voltage of ~2 kV for the cathode-junction leakage current of <10 mA (at T = 125°C) had of residual voltage drop in the conducting state $U_f \approx 4$ V for a current amplitude of $I_f = 25 \times 10^3$ A and turned off in a time of $t_q \approx$ 7–8 μs under the conditions of $dI_f/dt = -3$ kA/μs.

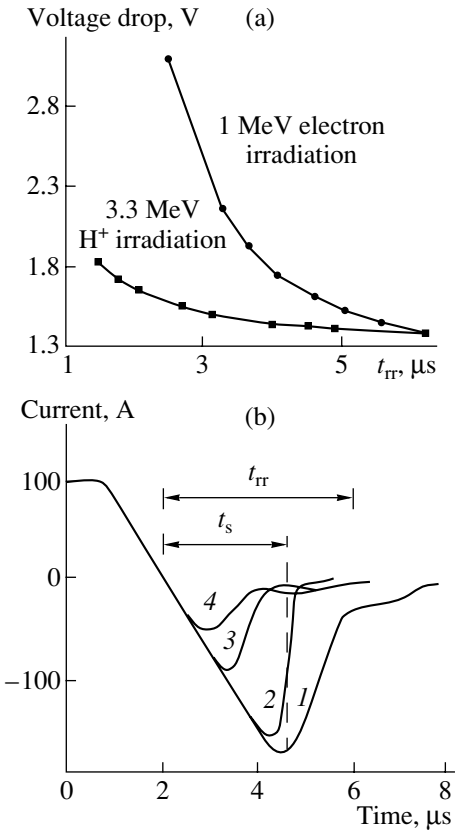

Fig. 15. (a) Correlation between the voltage drop in conducting state V_f and the reverse-recovery time t_{rr} for p^+–n–n^+ diode structures irradiated with 1-MeV electrons (the case of uniform distribution of radiation-defect concentration in the diode's *n*-base) and protons (the case of formation of a zone of enhanced recombination in the *n*-base of the diode near the p^+–n junction). The p^+–n–n^+ structure had the following parameters: the total thickness was 645 μm, the depth of the p^+–n junction was 80 μm, the depth of the n^+–n junction was 10 μm, and the donor-impurity concentration in the *n*-base was ~2.5×10^{13} cm^{-3} (according to the data reported by Hazdra and Vobecky [104]). (b) Temporal dependences of current through the p^+–n–n^+ diode structure (Fig. 15a) during the reverse recovery of the blocking property of the p^+–n junction: (*1*) for the unirradiated initial p^+–n–n^+ structure; (*2*) for the structure irradiated with 3.3-MeV protons from the n^+-layer side; (*3*) for the structure irradiated with 1-MeV electrons; and (*4*) for the structure irradiated with 3.3-MeV protons from the p^+-layer side.

The doping of base layers in the diode and thyristor structures with radiation defects using irradiation with protons or alpha particles results in a significant increase in thermal-generation current of high-voltage *p*–*n* junctions in the blocking state [87, 110]. This increase is caused by the irradiation-introduced diva-

cancies, whose acceptor level $E3$ is located near the midgap and is dominant in the process of thermal generation of charge carriers via the radiation-defect levels [87]. In order to eliminate the effect of radiation treatment on the characteristics of reverse-biased high-voltage *p–n* junctions, Bartko and Sun [109] suggested that thyristor structures should be irradiated so that the radiation defects introduced are outside the SCR of these *p–n* junctions in the blocking state, with the peak of the radiation-defect concentration being located in the base *p*-layer. However, in doing so, the layer with high-rate recombination affects to the much lesser extent the turnoff time of the device [110]. Because of this circumstance, Volle *et al*. [110, 111] suggested that a postimplantation thermal annealing at a temperature of ~300°C should be performed after the *n*-base of the structures was locally doped with radiation defects. This annealing ensures the elimination of comparatively unstable divacancies, with the *A* centers being retained; this is important because the *A* centers are the main recombination centers in the devices irradiated with protons or alpha particles. The elimination of divacancies makes it possible to significantly reduce the thermal-generation current in the blocking state, with the speed characteristics being preserved at the level attained immediately after irradiation.

Turnoff thyristors and power bipolar transistors of the switching type are devices in which the process of switching off differs from that considered above. Here, the discharge of electron–hole plasma in the structure's *n*-base in the vicinity of the cathode *p–n* junction during turnoff of these devices and the subsequent recovery of the junction's blocking capability are accomplished by the removal (extraction) of electrons to the external circuit through the control electrode, rather than by recombination of nonequilibrium charge carriers. Because of this circumstance, the limiting frequency characteristics of turnoff thyristors and power bipolar transistors are governed, as a rule, by commutation energy losses during turnoff, rather than by the turnoff time of these devices; this time can be fairly short under the relevant control. The main fraction of the above energy losses during turnoff of the devices is due to the current leakage of nonequilibrium charge carriers that were accumulated in the conducting state of the device in the *n*-base region away from the high-voltage cathode *p–n* junction. Therefore, in order to improve the speed characteristics of the devices under consideration, the above region of the base *n*-layer should be locally doped with radiation defects. Various aspects of optimizing the characteristics of turnoff thyristors and bipolar transistors using proton irradiation have been discussed in detail previously [114–117]. It should be noted that, by analogy with bipolar transistors, local doping by radiation defects may be also used with good results to improve the speed characteristics of comparatively new power devices, i.e., insulated-gate bipolar transistors and the magnetically controlled and field-controlled thyristors.

Thus, the beams of light ions H^+ and He^{++} are used in semiconductor-device technology primarily for the local control of the lifetime of nonequilibrium charge carriers and are rarely used to purposefully change the semiconductor's resistivity. When addressing the possibility of forming defect-enriched buried "insulating" layers in silicon by implantation of high doses of light ions to form structures of the "silicon on insulating defect-enriched layer" type [118], we should note that this technology is based to a large extent on the formation of buried defect-enriched layers, which contain nanoclusters of defects, including two- and three-dimensional agglomerates. In this context, this technology should not be considered as a method for doping semiconductors with point radiation defects. Rather, it may be considered as belonging to another class of method for the modification of semiconductors (see [12]); these methods are aimed at the formation of buried nanoporous defect-enriched layers in semiconductor crystals by implanting high doses of protons and alpha particles.

It is also noteworthy that the sensitivity of resistivity of silicon to irradiation with light ions limits the radiation resistance and stability of Si-based radiation detectors. At present, detectors based on ultrapure silicon crystals are widely used in the sensor systems of colliders in experimental nuclear physics. Therefore, the changes in resistivity of Si under irradiation and the problem of enhancing the radiation resistance of Si are also studied intensively [91, 94, 95]. Changes in resistivity of silicon should be also taken into account when adjusting the speed characteristics of power devices irradiated with light ions. These changes may profoundly affect the static current–voltage characteristics of power high-voltage devices made of lightly doped ultrapure *n*-Si with a dopant concentration lower than $<5 \times 10^{13}$ cm^{-3} and irradiated with H^+ ions with doses higher than 10^{11} cm^{-2}.

5. CONCLUSION

An analysis of the main current lines in the modification of semiconductors by irradiation with light ions (Table 1) (see above and [11, 12]) shows that doping semiconductors with radiation defects opens up fresh opportunities for controlling the properties of semiconducting materials and the characteristics of devices based on these semiconductors, compared to traditional doping methods (by diffusion, epitaxy, and ion implantation). A special feature common to all the methods of radiation-doping analyzed is the fact that they are local. The depth of localization of the modified layer is governed by the energy and stopping losses of protons and can actually be varied in the range from tens of nanometers to hundreds of micrometers. In addition to a high degree of localization, the modification of semiconductors by irradiation with protons and alpha particles also has the following merits typical of all radiation-based technologies:

(I) versatility of implementation with respect to various materials;

(II) simplicity and comparatively low cost of radiation treatments in combination with high precision, throughput, and reproducibility;

(III) compatibility with other technological processes in the production of semiconducting materials and devices.

Radiation-defect doping is one of the lines in the irradiation-based modification of semiconductors and is accomplished by the controlled introduction of impurity defects and intrinsic structural defects. Doping with radiation defects is one of the most important new methods of irradiation-based doping, because it is more widely used at present in the technology of semiconducting materials and devices compared to ion-implantation or nuclear-transmutation doping.

An analysis of available publications devoted to the implementation of the doping of silicon with radiation defects using irradiation with protons or alpha particles shows that the main field of actual practical application of this radiation-based technology is the local reduction of the lifetime of nonequilibrium charge carriers in the structures of power silicon switching devices with the aim to optimize their high-frequency and static characteristics. The use of this technology for optimizing the transient characteristics of devices with delayed impact ionization (such as Si-based avalanche diodes, transistors, and dinistor sharpeners [107]) may become a new and very promising field of the practical implementation of the doping of silicon with radiation defects. Thus, the phenomenon of avalanche breakdown via the levels of radiation defects may be used to trigger the mechanism of reversible wave impact-ionization breakdown in the above devices.

The control of silicon resistivity by doping with radiation defects is rarely used at present in the production of silicon devices. This is apparently because of the unsuitability of this technology for the formation of semi-insulating layers and of reliable interelement isolation in the structures based on silicon compensated with radiation defects.

The possibility of effectively controlling the charge-carrier concentration (resistivity) in the material by doping with radiation defects represents the physical motivation for implementing proton irradiation in the technology of devices based on gallium arsenide (the problem of reducing the lifetime of nonequilibrium charge carriers for a direct-gap semiconductor, such as gallium arsenide, is not as topical as for silicon). The recently developed methods for the introduction of radiation defects with a high annealing temperature into gallium arsenide made it possible to greatly expand the class of devices designed for microwave and power high-voltage electronics produced using proton irradiation. Doping with radiation defects has considerable promise for optoelectronics as well. The development of optical fiber links with an enhanced throughput also suggests that III–V compounds have good prospects in this field. In this context, the use of proton irradiation for locally (on the submicrometer scale) controlling the properties of a semiconductor crystal has a bright future.

The use of radiation-based methods for doping wide-gap semiconductors (first of all, silicon carbide) is of great interest. The data obtained recently [119–121] indicate that a complex spectrum of radiation defects is formed in *n*-Si. The irradiation of *n*-SiC with protons results not only in the formation of acceptors, which is typical of *n*-type materials, but also in the introduction of deep-level donors, whose ionization at the device operating temperatures of 500–700 K leads to a sharp increase in the electrical conductivity of the material.

The use of proton beams is not restricted to the field of microelectronics; they can be used with good results in nanoelectronics for fabricating quantum-well semiconductor structures [122, 123]. The “Smart Cut” and “Improve” technologies used for the formation of silicon-on-insulator structures with nanometer-size active silicon layers should be primarily assigned to this field of proton-beam applications [124–128].

Concerning the classification of the lines in the modification of semiconductors using beams of light ions (of hydrogen and helium, see Table 1), we think it pertinent to make the following point in concluding this review.

The doping of semiconductors with defects that contain atoms of implanted hydrogen may be conceptually assigned both to doping with radiation defects and to ion-implantation doping. Electrically active hydrogen atoms can affect the electrical properties of semiconductor crystals owing to the formation of new defects with either shallow or deep levels [8–10, 80–86, 99–101], due to changes in the ionization energy, the cross section for capturing charge carriers, and the kinetic parameters of the deep-level defects already present in the crystal [8, 9, 129–131], and also due to the passivation of electrically active defects [8, 9, 132–136].

Compared to the thermal, chemical, or plasma-chemical methods of semiconductor doping with atomic hydrogen [8, 9, 134–138], the implantation of hydrogen makes it additionally possible to introduce it comparatively easily to a depth in the range from fractions of a micrometer to a millimeter into the semiconductor crystal. This circumstance may be successfully used to passivate the electrically active defects in deeply lying layers in the semiconductor structure of devices. At present, studies in this line of modifying the semiconductors with beams of hydrogen, deuterium, or tritium ions are hardly conducted at all. Nevertheless, in our opinion, this line of research has good prospects for practical implementation, for example, for the depth-localized passivation of defects at deeply lying boundaries of multilayered semiconductor structures or for the formation of buried layers in the crystals, with

these layers differing in properties from the initial matrix to the point of changing the conductivity type and forming buried *p–n* junctions.

ACKNOWLEDGMENTS

This study was supported in part by the Civil Research & Development Foundation (grant no. PR 1-2258), the Russian Foundation for Basic Research (project no. 98-02-18217), and the Commission of the Russian Academy of Sciences devoted to young scientists (grant no. 98-03-25).

We are indebted to V.V. Emtsev for his long-standing collaboration and for his help with writing this review.

REFERENCES

1. *Problems in Radiation Technology of Semiconductors*, Ed. by L. S. Smirnov (Nauka, Novosibirsk, 1980).
2. V. S. Vavilov, B. M. Gorin, N. S. Danilin, A. E. Kiv, Yu. L. Nurov, and V. I. Shakhovtsov, *Radiation Methods in Solid-State Electronics* (Nauka, Moscow, 1990).
3. I. V. Vasil'eva, G. A. Efremov, V. V. Kozlovski, V. N. Lomasov, and V. S. Ivanov, *Radiation Processes in Technology of Materials and Electronic Products*, Ed. by V. S. Ivanov and V. V. Kozlovski (Énergoatomizdat, Moscow, 1997).
4. L. F. Zakharenkov and V. V. Kozlovski, in *Semiconductor Technology: Processing and Novel Fabrication Techniques*, Ed. by M. Levinshtein and M. Shur (Wiley, New York, 1997), Chap 2, p. 17.
5. N. B. Pleshivtsev and A. I. Bazhin, *Physics of Interaction of Ion Beams on Materials* (Vuzovskaya Kniga, Moscow, 1998).
6. *Surface Modification and Alloying by Laser, Ion, and Electron Beams*, Ed. by J. M. Poate, G. Foti, and D. C. Jacobson (Plenum, New York, 1983; Mashinostroenie, Moscow, 1987).
7. *Interaction of Charged Particles with Solids and Surfaces*, Ed. by A. Gras-Marti, H. M. Urbassek, N. R. Arista, and F. Flores (Plenum, New York, 1991; Vysshaya Shkola, Moscow, 1994).
8. S. J. Pearton, J. W. Corbett, and M. Stavola, *Hydrogen in Crystalline Semiconductors* (Springer-Verlag, Heidelberg, 1992).
9. *Hydrogen in Semiconductors*, Ed. by J. J. Pankove and N. M. Johnson (Academic, Boston, 1991).
10. *Hydrogen in Compound Semiconductors*, Ed. by S. J. Pearton (Trans. Tech., Aedermannsdorf, 1994).
11. V. V. Kozlovski, L. F. Zakharenkov, and B. A. Shustrov, Fiz. Tekh. Poluprovodn. (St. Petersburg) **26**, 3 (1992) [Sov. Phys. Semicond. **26**, 1 (1992)].
12. V. V. Kozlovski, V. A. Kozlov, and V. N. Lomasov, Fiz. Tekh. Poluprovodn. (St. Petersburg) **34**, 129 (2000) [Semiconductors **34**, 123 (2000)].
13. V. V. Kozlovski and L. F. Zakharenkov, Radiat. Eff. Defects Solids **138**, 75 (1996).
14. J. Lindhard, M. Scharff, and H. Schiøtt, K. Dan. Vidensk. Selsk., Mat. Fys. Medd. **33**, 3 (1963).
15. E. W. Maby, J. Appl. Phys. **47**, 830 (1976).
16. B. Schwartz, L. A. Koszi, P. J. Anthony, and R. L. Hartman, J. Electrochem. Soc. **131**, 1703 (1984).
17. I. P. Donelly and F. I. Leonberger, Solid-State Electron. **20**, 183 (1977).
18. H. A. Jenkinson, M. O'Tooni, J. M. Zavada, *et al.*, in *Ion Implantation and Ion Beam Proceeding of Materials: Symposium, Boston, 1983*, Ed. by G. K. Hubler *et al.* (North-Holland, New York, 1984), p. 377.
19. D. V. Lang, in *Radiation Effects in Semiconductors* (Inst. of Physics, Bristol, 1977; Mir, Moscow, 1979); Inst. Phys. Conf. Ser. **31**, 70 (1977).
20. D. Pons and J. C. Bourgoin, J. Phys. C **18**, 3839 (1985).
21. J. C. Bourgoin, H. J. Bardeleben, and D. Stievenard, J. Appl. Phys. **64**, R65 (1988).
22. J. C. Bourgoin, H. J. Bardeleben, and D. Stievenard, Phys. Status Solidi A **102**, 499 (1987).
23. V. V. Emtsev and T. V. Mashovets, *Impurities and Point Defects in Semiconductors* (Radio i Svyaz', Moscow, 1981).
24. H. Zillgen and P. Ehrhart, Mater. Sci. Forum **258-263**, 503 (1997).
25. D. Stievenard, X. Boddaert, and J. C. Bourgoin, Phys. Rev. B **34**, 4048 (1986).
26. G. Guillot, A. Nouailhat, G. Vincent, *et al.*, Rev. Phys. Appl. **15**, 679 (1980).
27. P. N. Brunkov, V. S. Kalinovsky, V. G. Nikitin, and M. M. Sobolev, Semicond. Sci. Technol. **7**, 1237 (1992).
28. E. V. Vavilov, L. F. Zakharenkov, V. V. Kozlovski, *et al.*, Izv. Vyssh. Uchebn. Zaved., Fiz. **32**, 110 (1989).
29. V. V. Kozlovski, T. I. Kol'chenko, V. M. Lomako, and S. E. Moroz, Fiz. Tekh. Poluprovodn. (Leningrad) **24**, 1123 (1990) [Sov. Phys. Semicond. **24**, 710 (1990)].
30. V. V. Kozlovski, T. I. Kol'chenko, V. M. Lomako, and S. E. Moroz, Fiz. Tekh. Poluprovodn. (Leningrad) **25**, 267 (1991) [Sov. Phys. Semicond. **25**, 161 (1991)].
31. V. V. Kozlovski, T. I. Kol'chenko, and V. M. Lomako, Fiz. Tekh. Poluprovodn. (Leningrad) **25**, 545 (1991) [Sov. Phys. Semicond. **25**, 328 (1991)].
32. L. F. Zakharenkov, V. V. Kozlovski, and Ya. Ya. Pil'kevich, Izv. Akad. Nauk SSSR, Neogr. Mater. **26**, 1145 (1990).
33. V. V. Kozlovski, T. I. Kol'chenko, and V. M. Lomako, Fiz. Tekh. Poluprovodn. (Leningrad) **25**, 1169 (1991) [Sov. Phys. Semicond. **25**, 707 (1991)].
34. V. V. Kozlovski, T. I. Kolchenko, V. M. Lomako, and L. F. Zakharenkov, Radiat. Eff. Defects Solids **138**, 63 (1996).
35. V. V. Kozlovski, T. I. Kol'chenko, and A. É. Vasil'ev, Poverkhnost, Nos. 5–6, 65 (1999).

36. V. V. Peshev and S. V. Smorodinov, Fiz. Tekh. Poluprovodn. (St. Petersburg) **31**, 1234 (1997) [Semiconductors **31**, 1060 (1997)].
37. D. Pons, A. Mircea, and J. Bourgoin, J. Appl. Phys. **51**, 4150 (1980).
38. J. Bourgoin and M. Lannoo, in *Point Defects in Semiconductors*, Vol. II: *Experimental Aspects*, Ed. by M. Cardona (Springer, New York, 1983; Mir, Moscow, 1985).
39. T. I. Kol'chenko, V. M. Lomako, and S. E. Moroz, Fiz. Tekh. Poluprovodn. (Leningrad) **22**, 740 (1988) [Sov. Phys. Semicond. **22**, 461 (1988)].
40. A. Sibille and J. C. Bourgoin, Appl. Phys. Lett. **41**, 956 (1982).
41. A. P. Mamontov and V. V. Peshev, Fiz. Tekh. Poluprovodn. (Leningrad) **17**, 1771 (1983) [Sov. Phys. Semicond. **17**, 1131 (1983)].
42. V. L. Vinetskiĭ and L. S. Smirnov, Fiz. Tekh. Poluprovodn. (Leningrad) **5**, 176 (1971) [Sov. Phys. Semicond. **5**, 153 (1971)].
43. J. C. Farmer and D. C. Look, J. Appl. Phys. **50**, 2970 (1979).
44. H. James and K. Lark-Horowitz, Z. Phys. Chem. (Leipzig) **198**, 107 (1951).
45. D. C. Look and J. P. Sizelove, J. Appl. Phys. **62**, 3660 (1987).
46. H. Matsumura and K. G. Stephens, J. Appl. Phys. **48**, 2779 (1977).
47. I. P. Donelly and C. E. Hurwitz, Solid-State Electron. **22**, 727 (1977).
48. V. N. Brudnyi, M. A. Krivov, and A. I. Potapov, Solid State Commun. **34**, 117 (1980).
49. V. N. Brudnyi, S. N. Grynaev, and V. E. Stepanov, Physica B (Amsterdam) **212**, 429 (1995).
50. A. I. Potapov, Author's Abstract of Candidate's Dissertation (Tomsk State Univ., Tomsk, 1999).
51. V. V. Kozlovski and L. F. Zakharenkov, Fiz. Tekh. Poluprovodn. (St. Petersburg) **27**, 349 (1993) [Semiconductors **27**, 190 (1993)].
52. J. P. de Souza, I. Danilov, and H. Boudinov, J. Appl. Phys. **81**, 650 (1997).
53. J. P. de Souza, I. Danilov, and H. Boudinov, J. Appl. Phys. **84**, 4757 (1998).
54. J. P. de Souza, I. Danilov, and H. Boudinov, Radiat. Eff. Defects Solids **147**, 109 (1998).
55. I. Danilov, J. P. de Souza, H. Boudinov, *et al.*, Appl. Phys. Lett. **75**, 1917 (1999).
56. J. P. de Souza, I. Danilov, and H. Boudinov, Appl. Phys. Lett. **68**, 535 (1996).
57. J. P. de Souza, I. Danilov, and H. Boudinov, Nucl. Instrum. Methods Phys. Res. B **122**, 51 (1997).
58. V. V. Emtsev, V. Yu. Davydov, V. V. Kozlovski, *et al.*, Semicond. Sci. Technol. **15**, 73 (2000).
59. C. Uzan-Saguy, J. Salzman, R. Kalish, *et al.*, Appl. Phys. Lett. **74**, 2441 (1999).
60. S. C. Binari, H. B. Dietrich, G. Kelner, *et al.*, J. Appl. Phys. **78**, 3008 (1995).
61. P. N. Favennec and D. Diguet, Appl. Phys. Lett. **23**, 546 (1973).
62. K. Steeples, G. Dearnaley, and A. M. Stoneham, Appl. Phys. Lett. **36**, 981 (1980).
63. H. H. Tan, J. S. Williams, and C. Jagadish, J. Appl. Phys. **78**, 1481 (1995).
64. K. Wohlleben and W. Beck, Z. Naturforsch. A **21**, 1057 (1966).
65. A. G. Foyt, W. T. Kindley, C. M. Wolfe, and J. P. Donelly, Solid-State Electron. **12**, 209 (1969).
66. R. A. Murphy, W. T. Lindley, and D. F. Peterson, in *Proceedings of the Symposium on Gallium Arsenide and Related Compounds, 1972* (Inst. of Physics, Bristol, 1973), p. 224.
67. J. D. Speight, P. Leigh, N. McIntyre, *et al.*, Electron. Lett. **10**, 98 (1974).
68. B. R. Lruniaux, J. C. North, and A. V. Payer, IEEE Trans. Electron. Devices **ED-19**, 672 (1972).
69. V. V. Kozlovski, I. A. Kozlovskaya, Yu. A. Lifshits, and V. M. Marakhonov, Pis'ma Zh. Tekh. Fiz. **20** (2), 5 (1994) [Tech. Phys. Lett. **20**, 48 (1994)].
70. V. B. Chmill, A. V. Chuntonov, S. S. Khludkov, *et al.*, J. Phys. D **28**, 559 (1995).
71. S. S. Khludkov, L. S. Okaevitch, A. I. Potapov, and O. P. Tolbanov, Nucl. Instrum. Methods Phys. Res. A **395**, 132 (1997).
72. S. J. Pearton, Mater. Sci. Rep. **4**, 313 (1990).
73. K. T. Short and S. J. Pearton, J. Electrochem. Soc. **135**, 2835 (1988).
74. V. V. Kozlovski, S. I. Ponomarev, and I. A. Kozlovskaya, Pis'ma Zh. Tekh. Fiz. **20** (2), 1 (1994) [Tech. Phys. Lett. **20**, 46 (1994)].
75. R. J. Fu, C. J. Hwang, and C. S. Wange, Appl. Phys. Lett. **45**, 716 (1984).
76. J. C. Dyment, L. A. D'Asaro, J. C. North, *et al.*, Proc. IEEE **60**, 726 (1972).
77. J. J. Hsieh, J. A. Rossi, and J. P. Donnelly, Appl. Phys. Lett. **28**, 709 (1976).
78. V. O. Naidenov, in *Proceedings of the International School of Physics "Enrico Fermi"*, Ed. by E. Bussoletti and G. Strazzula (North-Holland, Amsterdam, 1991), p. 371.
79. B. Zhang, M. Yi, J. Song, *et al.*, Jpn. J. Appl. Phys., Part 1 **38**, 6729 (1999).
80. B. N. Mukashev, Kh. A. Abdullin, and Yu. V. Gorelkinskiĭ, Usp. Fiz. Nauk **170**, 143 (2000).
81. L. Palmetshofer and J. Reisinger, J. Appl. Phys. **72**, 2167 (1992).
82. A. Hallen, N. Keskitalo, F. Masszi, and V. Nagl, J. Appl. Phys. **79**, 3906 (1996).
83. K. Irmscher, H. Klose, and L. Maass, J. Phys. C **17**, 6317 (1984).

84. A. Hallen, B. U. R. Sundgvist, Z. Paska, *et al.*, J. Appl. Phys. **67**, 1266 (1990).

85. W. Wondrak, K. Bethge, and D. Silber, J. Appl. Phys. **62**, 3464 (1987).

86. W. Wondrak and D. Silber, Physica B & C (Amsterdam) **129**, 322 (1985).

87. P. Hazdra and J. Vobecky, Solid State Phenom. **69–70**, 545 (1999).

88. P. V. Kuchinskii and V. M. Lomako, Solid-State Electron. **29**, 1041 (1986).

89. A. M. Ivanov, N. B. Strokan, and V. B. Shuman, Fiz. Tekh. Poluprovodn. (St. Petersburg) **32**, 359 (1998) [Semiconductors **32**, 325 (1998)].

90. H. Kauppinen, C. Corbel, K. Skog, *et al.*, Phys. Rev. B **55**, 9598 (1997).

91. V. Eremin, A. Ivanov, E. Verbitskaya, *et al.*, Nucl. Instrum. Methods Phys. Res. A **426**, 120 (1999).

92. A. S. Zubrilov and S. V. Koveshnikov, Preprint No. 1342, Fiz.-Tekh. Inst. im. A. F. Ioffe Ross. Akad. Nauk (Ioffe Physicotechnical Institute, Russian Academy of Sciences, Leningrad, 1989).

93. J. Lutz, W. Sudkamp, and W. Gerlach, Solid-State Electron. **42**, 931 (1998).

94. E. M. Verbitskaya, V. K. Eremin, A. M. Ivanov, *et al.*, Fiz. Tekh. Poluprovodn. (St. Petersburg) **31**, 299 (1997) [Semiconductors **31**, 189 (1997)].

95. E. M. Verbitskaya, V. K. Eremin, A. M. Ivanov, *et al.*, Fiz. Tekh. Poluprovodn. (St. Petersburg) **27**, 1136 (1993) [Semiconductors **27**, 1207 (1993)].

96. A. O. Evwaraye and B. J. Baliga, J. Electrochem. Soc. **124**, 913 (1977).

97. R. Laiho, L. S. Vlasenko, M. P. Vlasenko, *et al.*, Appl. Phys. Lett. **74**, 3948 (1999).

98. Y. Ohmura, Y. Zohta, and M. Kanazawa, Solid State Commun. **11**, 263 (1972).

99. Yu. V. Gorelkinskii and N. N. Nevinnyi, Physica B (Amsterdam) **170**, 155 (1991).

100. V. P. Markevich, Mater. Sci. Forum **196–201**, 945 (1995).

101. B. N. Mukashev, M. F. Tamendarov, S. Zhtakmoldin, and V. V. Frolov, Phys. Status Solidi A **91**, 509 (1985).

102. R. Job, J. A. Weima, G. Grabosch, *et al.*, Solid State Phenom. **69–70**, 551 (1999).

103. J. Reisinger and L. Palmetshofer, Appl. Phys. Lett. **59**, 3583 (1991).

104. P. Hazdra and J. Vobecky, Solid-State Electron. **37**, 127 (1994).

105. J. Vobecky, P. Hazdra, J. Voves, *et al.*, in *Proceedings of the International Symposium on Power Semiconductor Devices, ISPSD-94, Davos, 1994*, p. 265.

106. V. A. Kozlov and I. V. Grekhov, in *Proceedings of the VI International Conference "Radiation Physics of the Solid State", Sevastopol, 1996*, p. 140.

107. A. F. Kardo-Sysoev, V. I. Brylevsky, Y. S. Lelikov, *et al.*, in *Abstracts of the Ultra Wide Band (UWB'99) Conference, Washington, DC, 1999*, p. 4.

108. I. V. Grekhov, V. A. Kozlov, and S. V. Shendereĭ, RF Inventor's Certificate No. 95109009/20 (1997).

109. J. Bartko and K. N. Sun, US Patent 4 056 408 (1977).

110. V. M. Volle, V. B. Voronkov, I. V. Grekhov, *et al.*, Zh. Tekh. Fiz. **57**, 1925 (1987) [Sov. Phys. Tech. Phys. **32**, 1158 (1987)].

111. V. M. Volle, V. B. Voronkov, I. V. Grekhov, *et al.*, USSR Inventor's Certificate No. 1533569 (1988).

112. I. V. Grekhov, V. A. Kozlov, S. V. Korotkov, *et al.*, in *Abstracts of the 12th International Conference "Beams'98", Haifa, 1998*, p. 443.

113. I. V. Grekhov, V. A. Kozlov, S. V. Korotkov, *et al.*, Izv. Akad. Nauk, Énerg., No. 4, 106 (1996).

114. B. Thomas, D. Silber, H.Berg, and M. Tscharn, in *Proceedings of the IEEE Industry Applications Society Annual Meeting, IEEE-IAS-1985, 1985*, p. 882.

115. A. Hallen and M. Bakowski, Solid-State Electron. **32**, 1033 (1989).

116. V. M. Volle, V. B. Voronkov, I. V. Grekhov, *et al.*, Élektrotekhnika, No. 6, 58 (1991).

117. V. A. Kozlov, I. V. Grekhov, I. V. Eremin, and S. V. Shenderey, in *Abstracts of the 12th International Conference "Beams'98", Haifa, 1998*, p. 398.

118. J. Li, K. W. Jones, J. H. Coleman, *et al.*, Mater. Res. Soc. Symp. Proc. **396**, 745 (1996).

119. A. M. Strelchuk, A. A. Lebedev, V. V. Kozlovski, *et al.*, Nucl. Instrum. Methods Phys. Res. B **147**, 74 (1999).

120. A. A. Lebedev, A. I. Veinger, D. V. Davydov, *et al.*, J. Appl. Phys. **88**, 6265 (2000).

121. N. B. Strokan, A. M. Ivanov, A. A. Lebedev, *et al.*, Fiz. Tekh. Poluprovodn. (St. Petersburg) **34**, 1443 (2000) [Semiconductors **34**, 1386 (2000)].

122. K. A. Valiev, in *Proceedings of the All-Russia Scientific and Technical Conference "Micro- and Nanoelectronics-98", Zvenigorod, 1998*, Vol. 1, p. L1-1.

123. K. A. Valiev and A. A. Orlikovskiĭ, Élektron. Nauka, Tekhnol., Biznes, Nos. 5–6, 3 (1996); No. 1, 3 (1997).

124. V. V. Kozlovski and V. A. Kozlov, in *Proceedings of the All-Russia Scientific and Technical Conference "Micro- and Nanoelectronics-98", Zvenigorod, 1998*, Vol. 1, p. 01-4.

125. K. D. Hobart, F. J. Kub, G. G. Jernigan, *et al.*, Electron. Lett. **34**, 1265 (1998).

126. V. V. Kozlovski and V. A. Kozlov, in *Abstracts of the Conference on Perspectives, Science and Technologies for Novel Silicon on Insulator Devices, Kiev, 1998*, Ed. by P. L. F. Hemment, V. S. Lysenko, and A. N. Nazarov (Kluwer, Doedrecht, 2000), NATO Sci. Ser., Ser. 3: High Technol. **73**, 94 (2000).

127. V. K. Smirnov and A. B. Danilin, in *Perspectives, Science and Technologies for Novel Silicon on Insulator Devices, Kiev, 1998*, Ed. by P. L. F. Hemment, V. S. Lysenko, and A. N. Nazarov (Kluwer, Dordrecht,

2000), NATO Sci. Ser., Ser. 3: High Technol. **73**, 315 (1998).

128. Y. Omura, in *Perspectives, Science and Technologies for Novel Silicon on Insulator Devices, Kiev, 1998*, Ed. by P. L. F. Hemment, V. S. Lysenko, and A. N. Nazarov (Kluwer, Doedrecht, 2000), NATO Sci. Ser., Ser. 3: High Technol. **73**, 257 (1998).
129. J. Weber, in *Proceedings of the 24 International Conference "The Physics of Semiconductors", Jerusalem, 1998*, p. 209.
130. T. Sadoh, K. Tsukamoto, A. Baba, *et al.*, J. Appl. Phys. **82**, 3828 (1997).
131. Y. Kamiura, M. Hayashi, Y. Nishiyama, *et al.*, Jpn. J. Appl. Phys. **36**, 6579 (1997).
132. I. P. Ipatova, O. P. Chikalova-Luzina, and K. Hess, J. Appl. Phys. **83**, 814 (1998).
133. I. P. Ipatova, O. P. Chikalova-Luzina, and K. Hess, Superlattices Microstruct. **27**, 437 (2000).
134. N. Achtziger, J. Crillenberger, W. Witthuhn, *et al.*, Appl. Phys. Lett. **73**, 945 (1998).
135. P. A. Ivanov, O. I. Kon'kov, V. N. Panteleev, and T. P. Samsonova, Fiz. Tekh. Poluprovodn. (St. Petersburg) **31**, 1404 (1997) [Semiconductors **31**, 1212 (1997)].
136. P. Gluche, A. Aleksov, A. Vescan, *et al.*, IEEE Electron. Device Lett. **18**, 547 (1997).
137. V. A. Kagadei and D. I. Proskurovsky, J. Vac. Sci. Technol. A **16**, 2556 (1998).
138. V. G. Bozhkov, V. A. Kagadeĭ, and N. A. Torkhov, in *Proceedings of the All-Russia Scientific and Technical Conference "Micro- and Nanoelectronics-98", Zvenigorod, 1998*, Vol. 1, p. R1-49.

Translated by A. Spitsyn

Semiconductors, Vol. 35, No. 7, 2001, pp. 762–765. Translated from Fizika i Tekhnika Poluprovodnikov, Vol. 35, No. 7, 2001, pp. 796–800.

ATOMIC STRUCTURE AND NONELECTRONIC PROPERTIES OF SEMICONDUCTORS

The Microstructure and Physical Properties of Thin SnO_2 Films

S. I. Rembeza*, T. V. Svistova*, E. S. Rembeza, and O. I. Borsyakova***

** Voronezh State Technical University, Moskovskiĭ pr. 14, Voronezh, 394026 Russia*

*** Voronezh State University, Universitetskaya pl. 1, Voronezh, 394693 Russia*

Submitted February 16, 1999; accepted for publication February 26, 2001

Abstract—Thin polycrystalline SnO_2 films were deposited on glass substrates by magnetron sputtering. Electrical, optical, and gas-sensing properties, as well as the structure and phase composition of the films, were studied. The electrical resistance of the films and the concentration and mobility of free charge carriers were determined by the four-point-probe and van der Pauw methods. The band gap and the type of optical transitions in the films were derived from optical absorption spectra. The sensitivity to toxic and explosive gases was measured. The composition, morphology, and crystal structure of the films annealed at 600°C were examined by X-ray diffraction and electron microscopy. The films were found to contain only a tetragonal SnO_2 phase and have good crystallinity. The average grain size in the annealed films is 11–19 nm. A model of the electrical conduction in the polycrystalline SnO_2 films is discussed. © *2001 MAIK "Nauka/Interperiodica".*

INTRODUCTION

Thin SnO_2 semiconductor films are used as sensitive layers in integral gas sensors for environmental monitoring and measuring concentrations of toxic and explosive gases in air [1–3]. When the SnO_2 films interact with gases, their electrical conductance changes in proportion to the gas concentration in air. The gas sensitivity of the films is governed mainly by their electrical resistance and microstructure, a mechanism for the charge-carrier transport, and the presence and concentration of dopants.

The limiting operating temperature of the gas sensors may be as high as 400°C, whereas the SnO_2 films are prepared at lower temperatures. Therefore, the electrical parameters and the structure of the films are stabilized by annealing at high temperatures. This study is devoted to the effect of isothermal annealing of the SnO_2 films on their electrical and optical properties, microstructure, and gas sensitivity as well as to a mechanism for electrical conduction in thin SnO_2 films prepared by magnetron sputtering.

EXPERIMENTAL

Polycrystalline SnO_2 films were deposited on glass substrates by magnetron sputtering of an Sn(99.98) target doped with Sb (3 vol %) in an Ar (25%) and O_2 (75%) atmosphere in a VUP-4 unit. The substrates were not heated prior to the deposition. The target-to-substrate spacing was varied from 15 to 20 mm, the cathode voltage was 440 V, and the current was 0.25 mA. The film thickness was measured with an MII-4 interference microscope and ranged from 1 to 5 μm depending on the deposition time and the target-to-substrate distance.

Sheet resistance of the films was measured by the four-point-probe technique with a TsIUS-1 device, and the concentration and mobility of free carriers were determined by the van der Pauw method in a magnetic field of 0.63 T in the temperature range from 20 to 400°C. The optical absorption coefficients and absorption spectra were derived from transmission spectra measured with an SF-16 spectrophotometer in the wavelength range from 300 to 1200 nm at room temperature. The samples were isothermally annealed at 600°C for 4 h in air in a specially designed furnace.

The composition of the SnO_2 films was analyzed by X-ray diffraction with a Philips diffractometer (CuK_α radiation). The grain size was estimated by the Scherrer formula: $D = k\lambda/[(B - b)\cos\theta]$. Here, $k = 0.89$ is the constant, D is the particle diameter, λ is the wavelength of radiation, B is the angular full-width at half-maximum (FWHM) of the highest of the peaks under consideration (110 reflection at $2\theta = 26.8°$), and b is the FWHM of 111 reflection of a Si standard (at $2\theta = 28.44°$). With this method, the average grain size can be calculated [4]. The shape of grains and their size distribution were studied by transmission electron microscopy (TEM). TEM micrographs and selected-area electron-diffraction patterns were obtained with a CM-20 Philips electron microscope operating at an accelerating voltage of 200 kV. A quantitative microanalysis was performed with the same microscope and a LINK energy-dispersive analyzer. To prepare samples for TEM investigations, we separated the SnO_2 films from the glass substrates in a vapor of 45% HF, placed the films on a Cu mesh, and thinned them by Ar-ion milling at 3 keV for 1 h.

1063-7826/01/3507-0762$21.00 © 2001 MAIK "Nauka/Interperiodica"

RESULTS AND DISCUSSION

Like the films studied by Voshchilova *et al.* [5], the films prepared in the atmosphere containing 75% oxygen are transparent and have a yellowish color and mirror surfaces.

As can be seen from the optical absorption spectra (Fig. 1), the absorption coefficient α of the SnO_2 film varies from 10^3 to 10^4 cm^{-1}, and α of the glass substrate ranges from 2 to 20 cm^{-1} in the spectral region used. The fundamental-absorption edge is 2.8–3.3 eV. To estimate the band gap to greater accuracy and assess, where possible, the type of optical transitions, we plotted α^2 vs. $h\nu$ (direct transitions) and $\alpha^{1/2}$ vs. $h\nu$ (indirect transitions) [6]. We found that the plot of $\alpha^{1/2}$ against $h\nu$ provides a better linearization of the spectra, and the band gap ΔE is close to 3 eV. This is noticeably smaller than that of single-crystal SnO_2 (ΔE = 3.54 eV [7]), which is attributable to the deviation from perfect stoichiometry as well as to the presence of band tails appearing due to a high concentration of defects in the films.

The sheet resistance R_s of the as-deposited films varies from 10^2 to 10^3 Ω/sq. However, R_s changes upon heating of the films to the highest operating temperature of the gas sensors (400°C) followed by cooling to room temperature. Isothermal annealing at T = 600°C in air stabilizes the electrical resistance of the films. Therefore, all SnO_2 films under study were annealed at T = 600°C for 4 h. The resistance of the annealed SnO_2 films remains unchanged upon temperature cycling in the range of the operating temperatures of the gas sensors (20 to 400°C).

Figure 2 shows temperature dependences of the concentration and mobility of free charge carriers in the films annealed at 600°C for 4 h. The dependences were measured in the temperature range from 20 to 400°C in air. One can see from Fig. 2 that the electron concentration decreases from ~2×10^{18} to 3×10^{17} cm^{-3} with increasing temperature in this range (curve *1*), whereas the carrier mobility increases from 70 to 150 cm^2 V^{-1} s^{-1} as temperature increases from 20 to 130°C and remains virtually unchanged as the temperature rises further to 400°C (curve *2*).

The temperature dependences of the carrier concentration and mobility may be governed by the interaction of oxygen vacancies in the SnO_2 film with oxygen molecules in air [8], which results in a decrease in the electron concentration.

Figure 3 shows the X-ray diffraction pattern from the annealed SnO_2 film. One can see that the pattern contains only reflections of tetragonal SnO_2 (a = 0.4760 nm and c = 0.3178 nm) that has a rutile structure [4]. No Sb-containing phase is found, which may be indicative of the formation of a substitutional solid solution or the incorporation of Sb in the SnO_2 lattice. The average grain size estimated by the Scherrer formula is 11.0–19.4 nm.

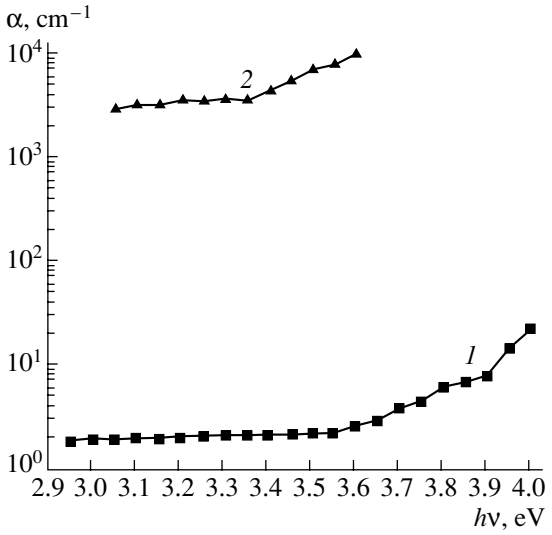

Fig. 1. Representative absorption spectra of (*1*) the glass substrate and (*2*) the SnO_2 film.

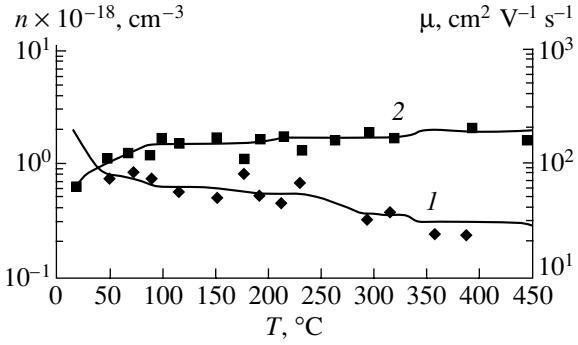

Fig. 2. Temperature dependences of (*1*) concentration and (*2*) mobility of free carriers in the annealed SnO_2 films.

The microstructure of the SnO_2 films was studied by the TEM (Fig. 4). The results are consistent with the X-ray diffraction data. One can see that the grains are very irregular in size and shape. Grain agglomerates are also observed. Figure 4a shows a dark-field micrograph of the film. Crystallites whose orientations are favorable to the Bragg diffraction are bright. Interplane distances determined from diameters of the first seven diffraction rings (Fig. 4b) correspond to the rutile structure, which is consistent with the X-ray diffraction data. Using the dark-field image, we determined major and minor axes of ellipsoids for more than 100 crystallites. The average grain size was found to range from 11.0 to 19.4 nm. Unfortunately, it was difficult to take into account very fine grains (<3 nm).

The quantitative microanalysis showed that the average content of Sb in the films is about 3 at. %. SnO_2 films doped with Sb to this concentration show a high electrical conductance, stability, and gas sensitivity [9]. The Sb content at the central part of the film is about 1.5 times higher than that at the periphery, possibly

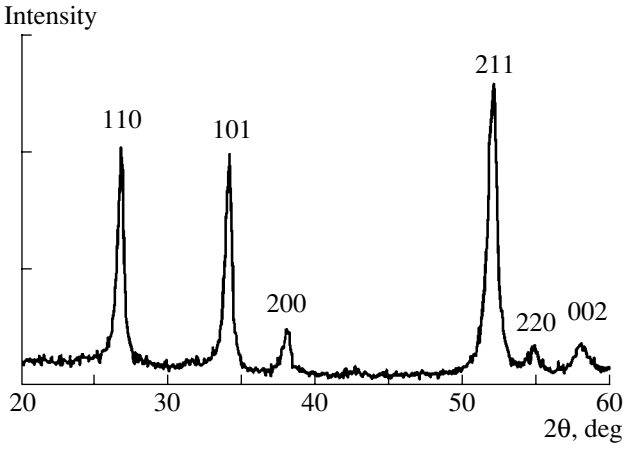

Fig. 3. X-ray diffraction pattern for the annealed SnO_2 film.

because the sample holder was not rotated during the film deposition.

The gas sensitivity of the SnO_2 films was defined routinely [10] as the ratio of the electrical conductance of the film in the presence of a gas in air (G_r) to that in the absence of a gas (G_0): $S = G_r/G_0$. The electrical conductance of the SnO_2 films was determined using the four-point-probe method in a wide range of substrate temperatures (100 to 400°C). We measured the steady-state gas sensitivity of the annealed films to ethanol and acetone vapors.

Temperature dependences of the gas sensitivity were measured at a gas concentration in air of 1000 ppm (~0.1%). The SnO_2 films under study were found to exhibit the maximum gas sensitivity to ethanol and acetone at T = 330 and 360°C, respectively. In Fig. 5, the sensitivity of the SnO_2 film to ethanol and acetone is plotted against the logarithm of the gas concentration in the range from 100 to 10000 ppm. One can see from Fig. 5 that these dependences are linear, which is characteristic of thin SnO_2 films [10].

From the measured electrical parameters of the SnO_2 films and the experimental data on the average grain size, we can assess the validity of the current models describing the electrical conduction in the films under consideration. As can be seen from the TEM micrograph, grain agglomerates are rather abundant in the polycrystalline film. In such a situation, charge carriers can move through a conducting chain without overcoming potential barriers between grains. However, for the current to flow through isolated grains or contacting chains, the charge carriers should overcome the potential barriers, whose heights depend on the band bending near the grain surfaces. In any case, the region where the carriers move freely is affected by the Debye shielding length (L). The smaller the value of L in comparison to the radius (or diameter D) of grains, the less profound this effect. At $D/2L \geq 1$, the electrical conduction in a film containing agglomerated particles

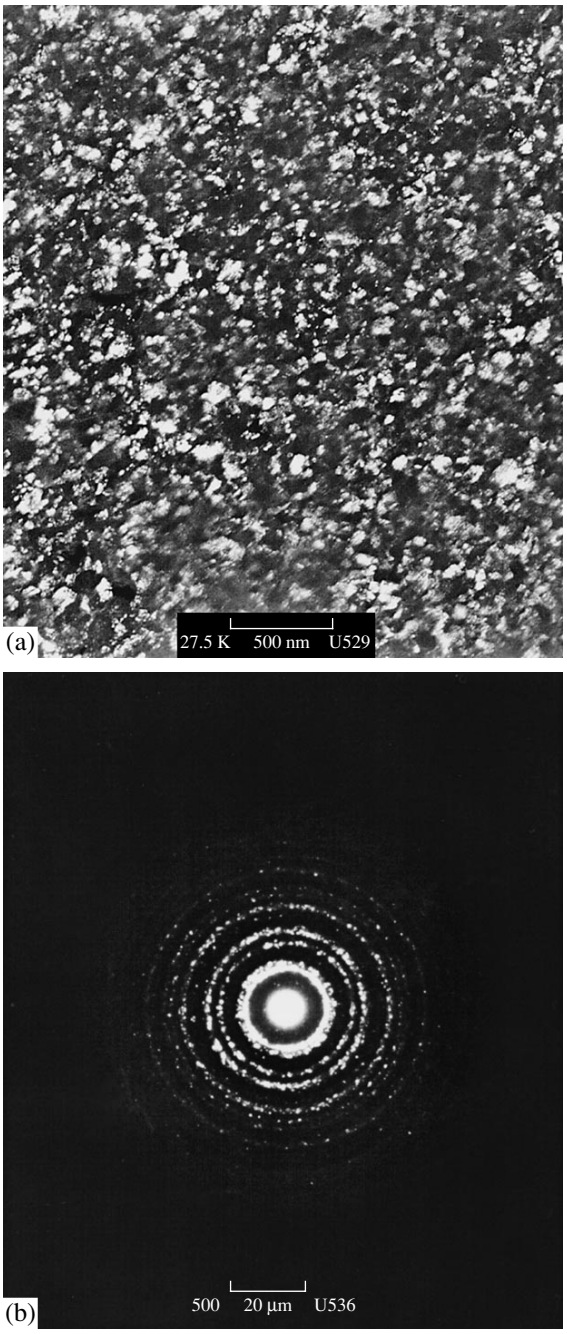

Fig. 4. (a) Dark-field TEM micrograph and (b) selected-area electron-diffraction pattern for the annealed SnO_2 film.

is described by the bottleneck model [11], and, in the case of a system of individual grains, the barrier heights are modulated. If the space-charge regions in the grains overlap because of their small sizes ($D/2L < 1$), the ultrafine-particle model is valid.

To estimate the Debye length $L = (\varepsilon\varepsilon_o kT/e^2 n)^{1/2}$, we used the value ε = 13.5 for SnO_2 [12] and the temperature dependence of the charge-carrier concentration obtained in this study. Even the smallest grain size (D =

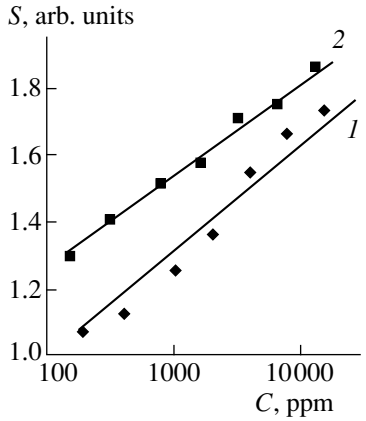

Fig. 5. Gas sensitivity of the SnO_2 film versus the concentration of (*1*) ethanol vapor (T = 330°C) and (*2*) acetone vapor (T = 360°C) in air.

11 nm) was found to satisfy the bottleneck condition ($D/(2L) \geq 1$) in the range from room temperature (L = 3.35 nm) to 100°C ($L \approx 7$ nm). At higher temperatures, including the temperatures of the highest sensitivity of the films (330 and 360°C), the ultrafine-particle condition ($D/2L < 1$) is fulfilled. Thus, we may conclude that the bottleneck and ultrafine-particle models adequately describe electrical conduction in the SnO_2 films studied. This provides a rather high gas sensitivity of the polycrystalline SnO_2 layers.

CONCLUSION

Conditions for the fabrication of magnetron-sputtered Sb-doped SnO_2 films with reproducible properties were determined. The electrical parameters of the films were stabilized by annealing at T = 600°C for 4 h. The structure and the electrical and optical properties of the films were investigated. The results obtained lead us to the conclusion that electrical conduction in the films is adequately described by the bottleneck and ultrafine-particle models. The gas sensitivity of the films is sufficiently high so that they can be used as active elements of solid-state gas sensors.

ACKNOWLEDGMENTS

We are grateful to A.M. Abakumov for the X-ray diffraction measurements and G.V. Gorlova for her assistance with this study. E.S. Rembeza thanks the Belgian Ministry of Science, Technology, and Culture for a research grant and Professor D. van Landuit for his participation and discussions of the results of microstructure investigations.

This study was supported in part by the Russian Ministry for General and Special Education (grant no. 005505-98) in the field of automatics and teleautomatics, computer engineering, cybernetics, and metrology as well as by the Science and Information Center for Problems in Intellectual Property of Institutes of Higher Education.

REFERENCES

1. W. Gopel, Sens. Actuators B **16**, 167 (1989).
2. J. Watson, K. Ihokura, and G. S. V. Coles, Mater. Sci. Technol. **4**, 711 (1993).
3. T. Hirayashi, Sens. Technol. **6**, 78 (1986).
4. G. McCarthy and J. Welton, Powder Diffr. **4**, 156 (1989).
5. R. M. Voshchilova, D. P. Dimitrov, N. I. Dolotov, *et al.*, Fiz. Tekh. Poluprovodn. (St. Petersburg) **29** (11), 1987 (1995) [Semiconductors **29**, 1036 (1995)].
6. J. I. Pankove, *Optical Processes in Semiconductors* (Prentice-Hall, Englewood Cliffs, 1971).
7. E. E. Kohnke, J. Phys. Chem. Solids **23**, 1557 (1962).
8. N. Barsan, Sens. Actuators B **17**, 241 (1997).
9. M. Rekas and Z. Szklarski, Bull. Pol. Acad. Sci., Chem. **44**, 155 (1996).
10. J. Watson, K. Ihokura, and G. S. V. Colest, Meas. Sci. Technol. **4**, 717 (1993).
11. C. Xu, J. Tamaki, N. Miura, and N. Yamazoe, Sens. Actuators B **3**, 147 (1991).
12. R. Summitt, J. Appl. Phys. **39**, 3762 (1968).

Translated by N. Izyumskaya

Semiconductors, Vol. 35, No. 7, 2001, pp. 766–772. Translated from Fizika i Tekhnika Poluprovodnikov, Vol. 35, No. 7, 2001, pp. 801–807.

ELECTRONIC AND OPTICAL PROPERTIES OF SEMICONDUCTORS

The Accuracy of Reconstructing the Semiconductor Doping Profile from Capacitance–Voltage Characteristics Measured during Electrochemical Etching

I. R. Karetnikova*, I. M. Nefedov, and V. I. Shashkin

Institute for Physics of Microstructures, Russian Academy of Sciences, ul. Ul'yanova 46, Nizhniĭ Novgorod, 603950 Russia

**e-mail: kart@ipm.sci-nnov.ru*

Submitted November 23, 2000; accepted for publication November 25, 2000

Abstract—The accuracy of a number of techniques for the reconstruction of doping profiles on the basis of the capacitance–voltage measurements in an electrochemical cell are numerically analyzed. The two previous simple methods proposed by us are shown not only to allow the direct determination of the doping profile at the surface but also to be potentially more accurate than the conventionally used procedure. However, our calculation techniques require experimental data of a higher accuracy. In particular, the relative error of measurements should be within 5×10^{-4}, which is an order of magnitude smaller than the commonly available values. © *2001 MAIK "Nauka/Interperiodica".*

1. INTRODUCTION

Knowledge of the depth distribution of an impurity (doping profile) is important for the production and application of semiconductor structures. One of the simplest methods for the profile determination is offered by capacitance–voltage (C–V) measurements at the Schottky metal–semiconductor contact at a reverse bias. An approximate solution to this problem (the so-called apparent profile) was obtained more than 50 years ago [1] and has been successfully employed. The drawbacks of this technique were repeatedly discussed elsewhere (see, e.g., [1, 2]) and are well known: the failure to determine the profile at the contact region, the resolution being limited by several Debye shielding lengths, and the finite depth of profiling. The latter problem was overcome in the mid-1970s when the use of an electrolyte–semiconductor contact instead of the metal–semiconductor one [3, 4] made it possible to combine C–V measurements with a successive electrochemical etch removal of the material, thus gaining access to the deeper semiconductor layers. Recent methods provide for a higher resolution in reconstructing the doping profile in the near-contact region [5–8]. These calculating techniques are relatively cumbersome and require *a priori* data on the doping profile. Simpler numerical schemes that yield the impurity concentration from the measurements in electrochemical cell and are free from the above-mentioned disadvantages of conventional methods were suggested by Shashkin *et al.* [9, 10].

Despite the wide application of the current techniques for the doping profile reconstruction and efforts to develop new ones, the accuracy of the doping profile derived from actual C–V measurements does not exceed that of an apparent profile (except for [7], where the class of piecewise constant profiles was considered). To improve the situation, more attention should be given to the accuracy of the proposed schemes and to their sensitivity to the experimental errors. This has been partially done, for example, in [11], where the numerical simulation of an apparent profile for the unit step function was performed, and in [2], where the accuracy of an apparent profile for a uniform distribution of impurities was quantitatively estimated. In the majority of the other studies, the accuracy and the influence of experimental errors are not mentioned at all or are considered only qualitatively [5–8].

The aim of this study was to investigate the accuracy of the apparent profile reconstruction by the techniques proposed in [9] as well as to analyze the consequences of the experimental errors. We report the results of the numerical simulations performed for the basic distributions of impurity: uniform, linear, and that described by a unit step function.

The new methods are shown to be more accurate than the conventional ones. At the same time, they are more sensitive to experimental errors; therefore, to be implemented, they require an increase in the conventional experimental accuracy by approximately an order of magnitude, which corresponds to the relative error of 5×10^{-4}.

2. BASIC EXPRESSIONS AND CALCULATING TECHNIQUES

Let us assume a one-dimensional distribution of the doping impurity $N(x)$ (x axis is normal to the surface and points into the studied structure, and the zero point

$x = 0$ is taken at the initial position of the surface). The volumes of the material etched off at each of the I steps are denoted by $y_1, y_2, \ldots, y_I$. Therefore, the coordinates of the etch points are $x_0 = 0$, $x_i = x_{i-1} + y_i/S$, $i = 1, 2, \ldots, I$, where S is the area of the etch crater bottom. The profiling procedure includes the measurements of the capacitance C_{ij} as a function of the applied voltage V_{ij}, $j = 1, 2, \ldots, J$ at each etch step x_i. The table $C_{ij} = C(x_i, V_{ij})$ as well as the values of V_{ij}, y_i, and S, represent the input data for the reconstruction of the doping profile $N(x)$. Henceforth, dimensionless variables are used. We chose the normalizing voltage as $V_0 = kT/e$ (k is the Boltzmann constant, e is the elementary charge, and T is temperature), the normalizing concentration as that in the bulk with a uniform distribution of dopant N_∞, the normalizing length as the Debye length $\lambda_D = \sqrt{kT\varepsilon/e^2N_\infty}$ (ε is the permittivity), and the normalizing specific capacitance as $C_0 = \varepsilon/\lambda_D$.

In what follows, we analyze three techniques for the reconstruction of the doping profile $N(x)$. The first of them is well known (see, for example, [2]); let it be referred to as the A formula:

$$N_A(x_{d_i}) = \left\{\frac{\partial[1/C^2(x_i, V)]}{\partial V}\right\}^{-1}, \quad x_{d_i} = x_i + \frac{1}{C(x_i, V)}, \quad i = 1, 2, \ldots, I. \tag{1}$$

Expression (1) is based on the assumption of a complete depletion, which implies an abrupt interface between the depleted contact region and the rest of the sample bulk. Then, the apparent profile can be derived at the depletion region edge x_d, where the applied approximation proves to be roughest.

The next technique (referred to as the Q formula) was proposed in [9]:

$$N_Q(x_i) = Q(x_i, V)C(x_i, V) - \left.\frac{\partial Q(x, V)}{\partial x}\right|_{x = x_i}, \quad Q(x, V) = \frac{1 + \dfrac{\partial}{\partial x}[1/C(x, V)]}{\dfrac{\partial}{\partial V}[1/C(x, V)]}. \tag{2}$$

The Q formula is also obtained within the complete-depletion approximation. However, in contrast to the A formula, it yields the dopant concentration at the electrolyte–semiconductor interface where the above approximation is quite valid. Thus, the Q formula yields a result more accurate than that of the apparent profile (see [9] and Section 3 of this paper).

Finally, the third technique (V formula), also described in [9], is based on the expression

$$N_V(x_i) = \left.\frac{\partial^2\psi(x, V)}{\partial x^2}\right|_{x = x_i}, \tag{3}$$

where $\psi(x, V)$ is the electrostatic potential of the semiconductor. Expression (3) directly follows from the Poisson equation, which will be discussed below. The accuracy offered by the V formula is defined by the degree of depletion at the interface with the electrolyte and is therefore quite high.

To calculate the doping profile, the following procedure is suggested. For a few selected model functions $N(x)$, the dependences $C(x, V)$ are calculated and in turn are used to derive the doping profile. The obtained profiles will be compared with the input $N(x)$.

We will now describe how the initial data are obtained. Let us specify a doping profile $N(x)$. We next assume that the minority carrier's contribution can be disregarded and the concentration of majority carriers is not too high (for GaAs, of $\leq 5 \times 10^{17}$ cm^{-3} at room temperature) so that their distribution can be described by the Boltzmann statistics. With these assumptions, the electrostatic potential $\psi_i(x, V)$ at each etch step obeys the Poisson equation, which can be written in dimensionless variables as

$$\frac{\partial^2\psi_i}{\partial x^2} = N(x) - \exp(-\psi_i), \quad x \geq x_i, \tag{4}$$

$$\psi_i(x_i, V) = V, \quad \psi_i(\infty, V) = 0, \quad i = 0, 1, 2, \ldots, I, \tag{5}$$

where V stands for the sum of the external and the built-in voltage at the contact. Then, the specific capacitance of the sample is defined as

$$C(x_i, V) = \frac{\partial}{\partial V}\left[\frac{\partial\psi_i(x, V)}{\partial x}\right]\Bigg|_{x = x_i}. \tag{6}$$

We also assume that the studied structure is homogeneous in the bulk; i.e., there is an x^* such that, for $x \geq x^*$, the dopant concentration is constant and equals N_∞. In order to avoid numerical differentiation with respect to V in Eq. (6), as is common practice (see, e.g., [11, 12]), we introduce the additional functions $\phi_i = \partial\psi_i/\partial V$ in order to determine the capacitance $C_{ij} = C(x_i, V_{ij})$. Differentiating Eqs. (4) and (5) with respect to V and assuming that $N(x)$ is independent of V, we readily obtain the equation and the boundary conditions for $\phi_i(x, V)$:

$$\frac{\partial^2\phi_i}{\partial x^2} = \phi_i\exp(-\psi_i), \quad x \geq x_i, \tag{7}$$

$$\phi_i(x_i, V) = 1, \quad \phi_i(\infty, V) = 0, \quad i = 0, 1, 2, \ldots, I. \tag{8}$$

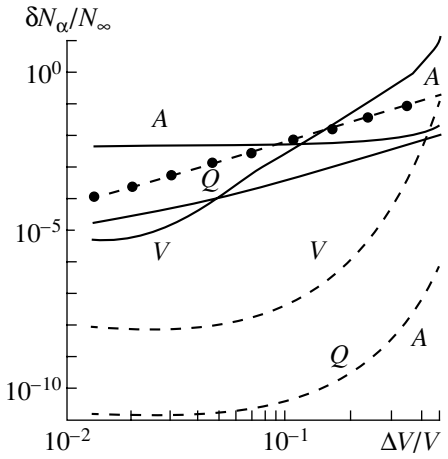

Fig. 1. Error of the reconstruction of uniform (dashed curves) and linear (solid curves) doping profiles according to the *A*, *Q*, and *V* formulas; the dotted curve shows the error of profile calculated according to expression (A.1); $\Delta x/\lambda_D = 0.165$.

Finally, the capacitance is derived from the expression

$$C(x_i, V) = \left.\frac{\partial \phi_i(x, V)}{\partial x}\right|_{x = x_i}.$$

The system of equations (4) and (7) was numerically solved at each etch step x_i and for every voltage V_{ij}, $j = 1, 2, \ldots, J$. Integration by the fourth-order Runge–Kutta method with an automatic step selection was performed in the range from $x = x^*$ to $x = x_i$, similar to the procedure described in [13]. The addition of Eq. (7) increases negligibly the calculation time significantly but enhances the accuracy by several orders of magnitude.

As was already mentioned above, the input data for the doping profile determination are the discrete values of the capacitance C_{ij}, the voltage V_{ij}, the volumes y_i, and the area S. To apply the reconstruction formulas (1)–(3), they should be replaced by their discrete analogues $\hat{N}_\alpha$, $\alpha = A, Q, V$. Note that the additional error introduced by this procedure is defined by the applied specific discretization method. The numerical expressions used for the profile reconstruction are given in the Appendix. The reconstructed profile accuracy δN_α was taken as the maximum deviation from the true profile:

$$\begin{aligned} \delta N_A &= \max_i \left|\hat{N}_A(x_{d_i}) - N(x_{d_i})\right|, \\ \delta N_\alpha &= \max_i \left|\hat{N}_\alpha(x_i) - N(x_i)\right|, \quad \alpha = Q, V. \end{aligned} \tag{9}$$

3. THE RESULTS OF NUMERICAL SIMULATIONS

The methods presented above were compared by applying them to the following model profiles: uniform, linear, and that given by a unit step function. The numerical values of the parameters were taken close to the actual experimental values for GaAs:

$$N_\infty = 5 \times 10^{17}\ \text{cm}^{-3}, \quad \lambda_D = 6.1\ \text{nm}, \quad V_0 = 0.026\ \text{V},$$
$$C_0 = 0.019\ \text{F/m}^2, \quad S = 2.1 \times 10^{-5}\ \text{m}^2,$$
$$x^* = 2.5 \times 10^4\ \text{nm}.$$

Most of the calculations implied a constant etch step $\Delta x \geq 1$ nm, with the voltage at the electrolyte–semiconductor interface $V_{ij} = V_j$ ($j = 1, 2, \ldots, 5$) being constant for every etch step:

$$V_1 = V - 2\Delta V, \quad V_2 = V - \Delta V, \quad V_3 = V,$$
$$V_4 = V + \Delta V, \quad V_5 = V + 2\Delta V, \quad V = 0.75\ \text{V},$$

and the ΔV varied in the range from $0.01V$ up to $0.05V$.

3.1. Accuracy of Reconstruction Formulas

First of all, let us consider the accuracy of the formulas for reconstructing the doping profile, with input data (the capacitance, the voltage, the etch step, and the area of the etch crater bottom) being assumed precise. Under this condition, the errors δN_α in (9) can be represented as the sum of the discretization errors δ_α^d and the formula-introduced errors δ_α^f:

$$\delta N_\alpha = \delta_\alpha^f + \delta_\alpha^d, \quad \alpha = A, Q, V. \tag{10}$$

The formula errors δN_α^f evidently depend neither on the voltage increment ΔV nor on the etch step Δx, whereas the quantity δ_α^d varies with ΔV and Δx and tends to zero when $\Delta V \longrightarrow 0$ and $\Delta x \longrightarrow 0$. Therefore, knowing the dependences of δN_α on ΔV and Δx, we can estimate the contribution from every term in the right-hand side of (10).

For a uniform profile, the distribution of the normalized concentration of the dopant is given by $N(x) = 1$, and the system of equations (4) and (5) can be solved analytically. The C–V characteristic then becomes

$$C(V) = \frac{1 - e^{-V}}{\sqrt{2(V + e^{-V} - 1)}}. \tag{11}$$

The substitution of Eq. (11) into (1) yields an apparent doping profile, which is independent of x:

$$N_A^0 = \frac{(1 - e^{-V})^3}{1 - 2Ve^{-V} - e^{-2V}}.$$

With the voltage V specified above, the accuracy of the A formula δ_A^f turns out to be within 4×10^{-11}. Due to the x-independent capacitance (11), expressions (1) and

(2) coincide and the accuracy of the Q formula δ_Q^f is equal to δ_A^f. The dependences of δN_α errors on ΔV are shown by dashed lines in Fig. 1. It can be seen that, at small ΔV, the discretization errors δ_A^d and δ_Q^d are negligible, since $1/C^2$ is a nearly linear function of V. We note that calculation of the apparent profile according to expression (A.1) (where the $C(V)$ function is numerically differentiated) instead of Eq. (1) considerably increases the discretization error, which is indicated by the dotted curve in Fig. 1. The accuracy of the V formula for uniform profile proves to be poorer than those of the A and Q formulas because of the larger discretization error. On the whole, at small ΔV, the uniform doping profile is adequately reconstructed by any of the three formulas.

As is evident from comparing the dashed and solid curves of Fig. 1, the error in the reconstruction of a linear profile considerably exceeds that of a uniform distribution. It is also seen that for small ΔV, the Q and V formulas provide better accuracy than the A formula. The distinctive shape of the dependences of δN_Q and δN_V on ΔV suggests that the contribution of the finite-difference approximation of the derivatives is prevalent; i.e., the key role in the right-hand side of Eq. (10) is played by δ_α^d term, $\alpha = Q, V$. It can be shown that, for a constant etch step Δx, the discrete analogues of expressions (2) and (3) have a different approximation order, in particular, $\delta_Q^d = 0(\Delta V^2)$ and $\delta_V^d = 0(\Delta V^3)$. This accounts for the fact that δN_V increases more rapidly than δN_Q with increasing ΔV. The δN_A error is practically independent of ΔV. Therefore, the apparent profile is reconstructed with the error inherent in the method itself (δ_A^f).

A similar situation is observed for the profile given by a unit step function (Fig. 2). As in the previous case, the Q and V formulas ensure better accuracy than the A formula, though the errors are considerably larger than those for linear or uniform profiles. As can be seen from Fig. 2, the value of δN_Q is independent of ΔV and coincides with δN_V for small ΔV. As mentioned above, an increase in δN_V for large ΔV is due to the fact that the order of approximation with respect to ΔV is higher for δN_V than for δN_Q. Calculations performed with large etch steps demonstrate that, for small ΔV, the δN_Q and δN_V errors are defined by the difference approximation of the second spatial derivative and depend primarily on Δx. We note that the integrated measure of deviation (9) of the calculated profile from the true one does not completely reflect the reconstruction quality. This is demonstrated by the inset in Fig. 2 depicting the doping profiles reconstructed for fixed Δx and ΔV. The Q and V formulas evidently provide a better resolution of an abrupt change in the dopant concentration, whereas an apparent profile is known to smooth out this jump.

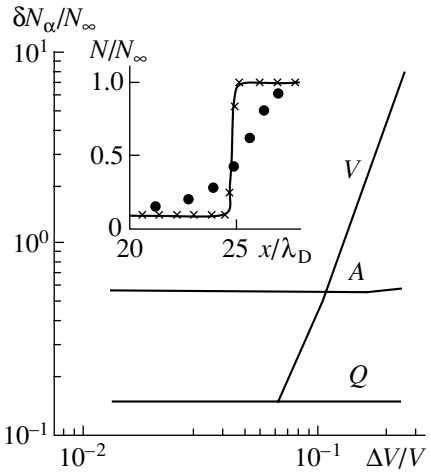

Fig. 2. Error of the unit step function reconstructed with the A, Q, and V formulas. Inset: the input profile (solid curve), an apparent profile (dots), and the profile reconstructed according to the Q formula (crosses); $\Delta V/V = 0.0133$ and $\Delta x/\lambda_D = 0.165$.

Summing up the aforesaid, under the assumption of precise initial data, the proposed Q and V formulas yield a better precision for all of the considered profile shapes. A similar inference follows from the results of reconstruction of a profile with multiple discontinuities [9, 10]. This assertion also seems valid for a wider range of actual experimental profiles.

3.2. Influence of Measurement Errors

The extent to which the accuracy of the doping profile is affected by the measurement errors is important for the practical applicability of one or another reconstruction formula. If the measurement errors are random, the total error of the reconstructed profile can be represented as a sum of three terms:

$$\delta N_\alpha = \delta_\alpha^f + \delta_\alpha^d + \delta_\alpha^C, \quad \alpha = A, Q, V, \tag{12}$$

where δ_α^f and δ_α^d are the same as in Eq. (10) and δ_α^C denotes an error associated with imprecise measurement of the capacitance C. Actually, δC includes contributions from both the error of the direct measurement of capacitance δ_0^C and the errors originating from the measurements of voltage δV, the amount of the etched material δy, and the area of the etch crater bottom δS:

$$\delta C = \delta_0^C + M_1\delta V + M_2\delta y + M_3\delta S,$$

where the constants M_i are defined by the capacitance $C(x, V)$ and its derivatives $\partial C/\partial x$ and $\partial C/\partial V$. In our numerical simulation, the influence of the total error ∂C on exactness of the reconstructed profile is analyzed.

In order to construct a model for the measurement error, we added a Gaussian random variable ξ_{ij} with

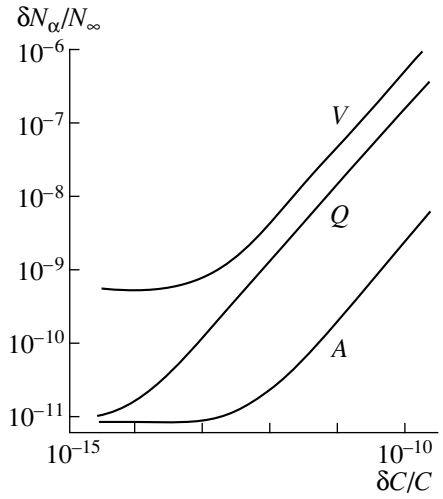

Fig. 3. Error of reconstructing a uniform profile (*A*, *Q*, and *V* formulas) versus the capacitance measurement error; $\Delta V/V = 0.0133$ and $\Delta x/\lambda_D = 0.165$.

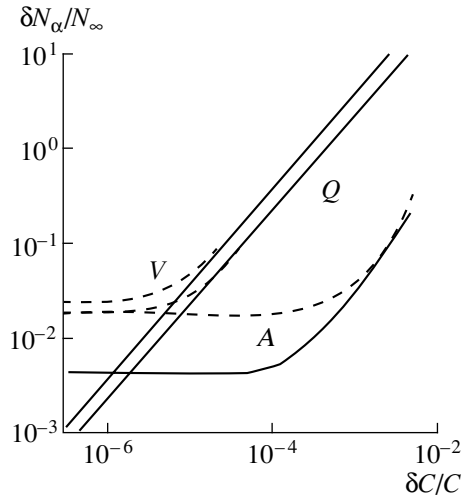

Fig. 4. Error of reconstructing a linear profile (*A*, *Q*, and *V* formulas) versus the capacitance measurement error for $\delta S = 0$ (solid curves) and $\delta S = 0.03$ (dashed curves); $\Delta V/V = 0.0133$ and $\Delta x/\lambda_D = 0.165$.

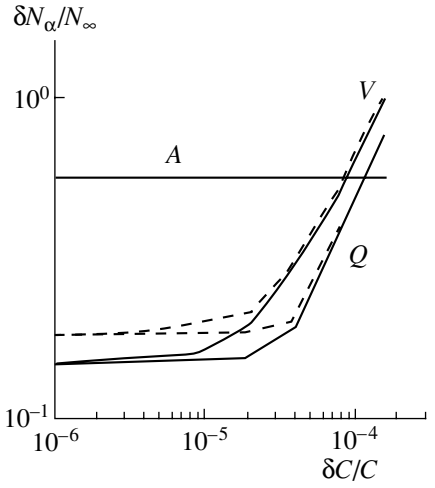

Fig. 5. Error of reconstructing a profile described by a unit-step function (*A*, *Q*, and *V* formulas) versus the capacitance measurement error for $\delta S = 0$ (solid curves) and $\delta S = 0.09$ (dashed curves); $\Delta V/V = 0.0133$ and $\Delta x/\lambda_D = 0.165$.

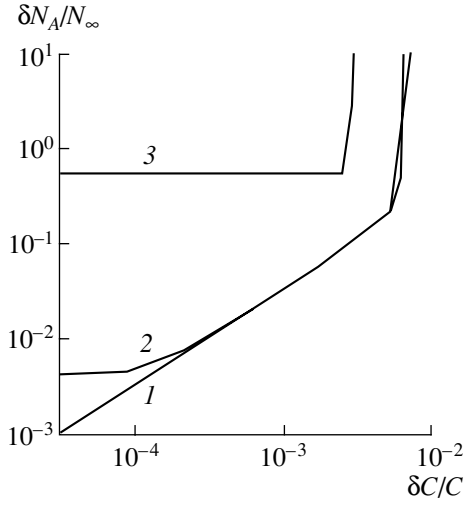

Fig. 6. Error of reconstructing an apparent (*1*) uniform, (*2*) linear, and (*3*) unit-step profile versus the capacitance measurement error; $\Delta V/V = 0.0133$ and $\Delta x/\lambda_D = 0.165$.

zero average value and σ_C/C_{ij} variance to every of the capacitance values C_{ij} ($i = 1, 2, \ldots, I$ and $j = 1, 2, \ldots, J$) obtained by solving the Poisson equation (4). In other words, for reconstructing the doping profile, the following table of values was used:

$$\tilde{C}_{ij} = C_{ij}(1 + \xi_{ij}).$$

As a relative error δC, the quantity $3\sigma_C$ was used. The contribution of δS—the error connected with measuring the area of the etch crater bottom—to the total error was additionally analyzed. To do this, a Gaussian variable η with zero mean value and σ_S/S variance was added to S. Then, the area to be used in the calculations takes the form

$$\tilde{S} = S(1 + \eta),$$

with the relative error being given by $\delta S = 3\sigma_S$.

As an error of the reconstructed profile, we consider the maximum standard deviation from the true profile function:

$$\delta N_A = \max_i \sqrt{\langle [\hat{N}_A(x_{d_i}) - N(x_{d_i})]^2 \rangle},$$

$$\delta N_\alpha = \max_i \sqrt{\langle [\hat{N}_\alpha(x_i) - N(x_i)]^2 \rangle}, \quad \alpha = Q, V,$$

where the brackets signify averaging over the random values ξ_{ij} and η.

The errors δN_α of a uniform profile reconstructed with the *A*, *Q*, and *V* formulas versus the capacitance measurement error δC are shown in Fig. 3, the area of the crater bottom *S* being specified exactly. We can see that the errors of *Q* and *V* formulas are significantly larger than that of the *A* formula, even for very small δC values.

The influence of the measurement errors on the accuracy of the reconstructed linear profile and unit step function is demonstrated in Figs. 4 and 5, where the solid lines represent the errors of reconstruction for $\delta S = 0$ and dashed lines, for $\delta S = 0.03$ and 0.09 for Figs. 4 and 5, respectively. As δC increases, the errors δN_Q and δN_V increase more rapidly than δN_A. The errors of the *Q* and the *V* formulas exceed that of the *A* formula even for small δC (Fig. 4) and become unacceptably large for $\delta C/C \approx 3 \times 10^{-4}$. A several-percent measurement error in *S* contributes noticeably to the total reconstruction error only for small $\delta C/C \le 10^{-5}$.

The error of an apparent profile reconstructed with the *A* formula δN_A starts to depend on the measurement error δC for a considerably higher δC than δN_Q or δN_V errors. An acceptable δN_A is maintained up to the $\delta C \approx (2\text{–}5) \times 10^{-3}$ (Fig. 6). Owing to this, the *A* formula can be applied to the processing of data obtained in actual experiments, where the conventionally ensured accuracy is $\delta C/C \approx 10^{-3}$ [14]. It is of interest to note that the numerical calculations suggest that there is a critical value δC above which the reconstruction of the profile becomes impossible (Fig. 6).

The results of numerical simulation demonstrate that the *Q* and the *V* formulas are more sensitive to the measurement errors that the *A* formula. In particular, the relative error $\delta C/C$ for which the errors of *Q* and *V* formulas are within the error of an apparent profile turns out to be smaller than $\sim 7 \times 10^{-5}$. This sensitivity to errors contained in the initial data is understandable, since the *Q* and the *V* formulas contain the second spatial derivative of capacitance, and the numerical differentiation of inaccurate tabulated data is known to introduce large errors.

4. CONCLUSION

We numerically analyzed the three methods for the reconstruction of a doping profile in semiconductor structures using *C*–*V* measurements in an electrochemical cell. The *Q* and *V* formulas suggested by Shashkin *et al.* [9, 10] not only make it possible to obtain the doping profile directly at the electrolyte–semiconductor contact but also yield a more exact result than the traditionally used apparent profile [1]. It is important for the practical application of these formulas that their accuracy depends much more on the capacitance measurement error than that of an apparent profile. Our calculations indicate that the *Q* and the *V* formulas yield an acceptable result if the relative error of the capacitance measurement is within $\sim 5 \times 10^{-4}$.

In general, the problem of high sensitivity of the result to errors in the input data is the main obstacle to the application of recently proposed new methods for the doping profile reconstruction [5, 6, 8]. These difficulties stem from the fact that the doping profile reconstruction constitutes an inverse problem that is ill-posed. Therefore, the design of the effective procedures for reconstruction requires a detailed investigation of approximations and so on.

APPENDIX

DISCRETIZATION OF THE RECONSTRUCTION FORMULAS

The voltage and coordinate derivatives appearing in the *A* and *Q* formulas were taken in the form of central differences

$$\hat{N}_A(x_{d_i}) = \left(\frac{1/C_{ij+1}^2 - 1/C_{ij-1}^2}{V_{ij+1} - V_{ij-1}}\right)^{-1},$$

$$x_{d_i} = x_i + \frac{1}{C_{ij}}, \quad j = 2, \ldots, J-1.$$

We note that expression (1) is sometimes written in the equivalent form of

$$N_A(x_{d_i}) = -C^3(x, V)/\frac{\partial C(x_i, V)}{\partial V} \qquad \text{(A.1)}$$

and the corresponding discrete analogue is used. However, expression (1) is preferable, since it gives a more accurate reconstruction of a uniform profile. This is due to the fact that $1/C^2(x, V)$ is nearly linear with respect to *V*; therefore, the discretization error is very small (see Section 3).

The discrete analogue of the *Q* formula has the form

$$\hat{N}_Q(x_i) = Q_{ij}C_{ij} - (Q_{i+1,j} - Q_{i-1,j})/(x_{i+1,j} - x_{i-1,j}),$$

$$Q_{ij} = \left(1 + \frac{1/C_{i+1,j} - 1/C_{i-1,j}}{x_{i+1,j} - x_{i-1,j}}\right)/\left(\frac{1/C_{i,j+1} - 1/C_{i,j-1}}{V_{i,j+1} - V_{i,j-1}}\right),$$

$$i = 2, 3, \ldots, I-1, \quad j = 2, 3, \ldots, J-1.$$

The main difficulty encountered in discretization of the *V* formula is associated with the estimation of $\partial^2\psi_i/\partial x^2$. To do this, one should know the electrostatic potential $\psi_i(x, V)$ at three consecutive etch steps, $\psi_i(x_{i-1}, V)$, $\psi_i(x_i, V)$, and $\psi_i(x_{i+1}, V)$, whereas only one value at *i* step is known: $\psi_i(x_i, V) = V$. In order to find the $\psi_i(x_{i-1}, V)$ and $\psi_i(x_{i+1}, V)$ values, we used the following procedure. Considering the etched off layer as a series-connected plane capacitor, we can determine

the capacitance $\tilde{C}_{i-1,j}$ at the $(i-1)$ etch step from the formula

$$1/\tilde{C}_{i-1,j} = (x_i - x_{i-1}) + 1/C_{ij}.$$

Using the inverse interpolation and the table $C_{i-1,j} = C(x_{i-1}, V_{i-1,j})$ $(j = 1, 2, \ldots, J)$, we can find the voltage $\tilde{V}_{i-1,j}$ corresponding to the capacitance $\tilde{C}_{i-1,j}$. An interpolating polynomial $P_{J-2}(C)$ of the $(J-2)$ degree is constructed by the method of least squares on the basis of $V_{i-1,1}$, $V_{i-1,2}$, …, $V_{i-1,J}$; then, the quantity $\tilde{V}_{i-1,j} = P_{J-2}(\tilde{C}_{i-1,j})$ is determined. A similar procedure is used to find $\tilde{V}_{i+1,j}$ at the $(i+1)$th etch step. Finally, the doping profile is derived from

$$\hat{N}_V(x_i) = \frac{\tilde{V}_{i-1,j} - 2V_{i,j} + \tilde{V}_{i+1,j}}{(x_{i+1} - x_i)(x_i - x_{i-1})},$$

$$i = 2, 3, \ldots, I-1; \quad j = 1, 2, \ldots, J.$$

This is the simplest method of finite-difference approximation of the second derivative $\partial^2\psi_i/\partial x^2$. Another approach was described in [10].

ACKNOWLEDGMENTS

We thank I. A. Sereshevskiĭ and A. V. Murel for their fruitful participation in numerous discussions.

This study was supported in part by the Russian Foundation for Basic Research, project no. 01-02-16451, and the "Physics of Solid-State Nanostructures" MNTP program.

REFERENCES

1. V. V. Batavin, Yu. A. Kontsevoĭ, and Yu. F. Fedorovich, *Measurement of Parameters of Semiconductor Materials and Structures* (Radio i Svyaz', Moscow, 1985).
2. P. Blood, Semicond. Sci. Technol. **1**, 7 (1986).
3. M. M. Faktor, T. Ambridge, and E. G. Bremmer, UK Patent Specification No. 1482929 (1975).
4. M. M. Faktor, T. Ambridge, C. R. Elliott, and J. C. Regnault, Curr. Top. Mater. Sci. **6**, 1 (1980).
5. G. J. L. Quwerling, Solid-State Electron. **33**, 757 (1990).
6. K. Iniewski and C. A. T. Salama, Solid-State Electron. **34**, 309 (1991).
7. M. F. Kokorev, N. A. Maleev, V. M. Ustinov, *et al.*, in *Abstracts of the International Symposium "Nanostructures: Physics, and Technology", St. Petersburg, 1996*, p. 161.
8. Y. K. Yeo, G. H. Gainer, Jr., Jong Hyun Kin, and R. L. Hengehold, Appl. Phys. Lett. **56**, 75 (1990).
9. V. I. Shashkin, I. R. Karetnikova, A. V. Murel', *et al.*, Fiz. Tekh. Poluprovodn. (St. Petersburg) **31** (8), 926 (1997) [Semiconductors **31**, 789 (1997)].
10. V. Shashkin, I. Karetnikova, A. Murel, *et al.*, IEEE Trans. Electron. Devices **ED-6**, 47 (2000).
11. W. C. Johnson and P. T. Panousis, IEEE Trans. Electron. Devices **ED-18**, 965 (1971).
12. B. Jogal and C. E. Stutz, J. Appl. Phys. **78**, 2531 (1995).
13. L. H. Hollway, IEEE Trans. Electron. Devices **ED-37**, 1104 (1990).
14. I. V. Irin and A. V. Murel', Prib. Tekh. Éksp., No. 6, 150 (1993).

Translated by A. Sidorova-Biryukova

Semiconductors, Vol. 35, No. 7, 2001, pp. 773–776. Translated from Fizika i Tekhnika Poluprovodnikov, Vol. 35, No. 7, 2001, pp. 808–811.

ELECTRONIC AND OPTICAL PROPERTIES OF SEMICONDUCTORS

Optical Properties of $Cd_{1-x}Zn_xTe$ ($0 < x < 0.1$) Single Crystals in the Infrared Spectral Region

A. I. Belogorokhov*,[1], V. M. Lakeenkov†*, and L. I. Belogorokhova**

** Federal State Unitary Enterprise, Research Center Giredmet, Moscow, 109017 Russia*

[1] e-mail: belog@mig.phys.msu.su

*** Moscow State University, Vorob'evy gory, Moscow, 119899 Russia*

Submitted November 15, 2000; accepted for publication November 27, 2000

Abstract—Frequency dependences of the transmittance $T(\omega)$ of $Cd_{1-x}Zn_xTe$ ($0 < x < 0.1$) single crystals grown by a modified Bridgman method were studied using long-wavelength optical spectroscopy in the temperature range of 5–300 K. A sharp increase in absorption for energies smaller than the band gap was observed for unannealed samples of *p*-type conductivity. Moreover, with the temperature variation of the sample from 5 to 300 K, the dependences $T(\omega)$ intersect almost at the same wavelength. The theoretical frequency dependences $T(\omega)$ with allowance for substantial contribution of the intersubband transition of charge carriers in the valence band were calculated. The Fermi level position was evaluated for the samples at $T = 77.3$ and 295 K. A nonmonotonic dependence of the Fermi level position on the composition was observed for $x = 0.040$–0.047. The possible influence of tellurium precipitates on the transmittance decrease in $Cd_{1-x}Zn_xTe$ in the wave number range of 3000–400 cm^{-1} is discussed. © *2001 MAIK "Nauka/Interperiodica".*

1. INTRODUCTION

Semiconductor $Cd_{1-x}Zn_xTe$ solid solutions are promising materials for the production of various optoelectronic and thermal-imaging devices [1]. They are widely used as the materials for substrates in growing the $Cd_xHg_{1-x}Te$ epitaxial structures, which form the basis for arrays of infrared photodetectors operating in the spectral regions of 3–5 and 8–14 μm [2]. Solid solutions $Cd_{1-x}Zn_xTe$ show considerable potential for the production of high-efficiency large-area gamma-ray detectors based on them [3], which is caused by a wide band gap and large zinc atomic number, as well as by a possibility of obtaining the material with resistivity $\rho \approx 10^{10}$ Ω cm. The trends envisaged in the fabrication of infrared-photodetector arrays and γ-detectors with a large area dictate strict requirements on the control of the $Cd_{1-x}Zn_xTe$ solid-solution properties and on the local homogeneity of the material. Variation of optical properties of the material with the composition and concentration of charge carriers in the spectral region of interband transitions has been considered previously [4, 5]. In particular, it was found [5] that the absorption coefficient behavior in the above range of wavelengths obeys the exponential law (the Urbach rule). The transmittance spectra of $Cd_{1-x}Zn_xTe$ beyond the fundamental absorption edge were reported in [6]. The variation of the weight ratio of the solid solution components with temperature (thermograms) was studied, which made it possible to associate the absorption increase in the range of wave numbers 700–4000 cm^{-1} with the presence of tellurium precipitates in the material bulk. The results obtained are of a significant interest as many researchers are eager to learn the causes of the changes in the $Cd_{1-x}Zn_xTe$ optical properties in this spectral region [7]. This is, in turn, caused by the fact, as was noted above, that a solid solution under consideration is often used as a substrate in growing the epitaxial $Cd_xHg_{1-x}Te$ structures and development of the corresponding devices for the aforementioned infrared (IR) spectral range. The reason indicated above motivated a series of studies directed at gaining insight into the effect of $Cd_{1-x}Zn_xTe$ doping on its optical properties [8]. Despite a number of publications, the issue regarding the cause of a decrease in the absorption in the range of wave numbers of 3000–400 cm^{-1} has not been resolved unambiguously.

2. EXPERIMENTAL RESULTS AND DISCUSSION

Single-crystal $Cd_{1-x}Zn_xTe$ samples ($0 < x < 0.18$) were *p*-type and were grown by the Bridgman method; they have a resistivity at room temperature ($T = 300$ K) from 0.5 to 2.5×10^2 Ω cm and hole mobility of 40–100 $cm^2\ V^{-1}\ s^{-1}$. The charge-carrier concentration was 10^{15}–10^{18} cm^{-3} at $T = 300$ K. Single-crystal wafers oriented in the crystallographic plane (111) were cut from the crystals. The composition of the samples was

† Deceased.

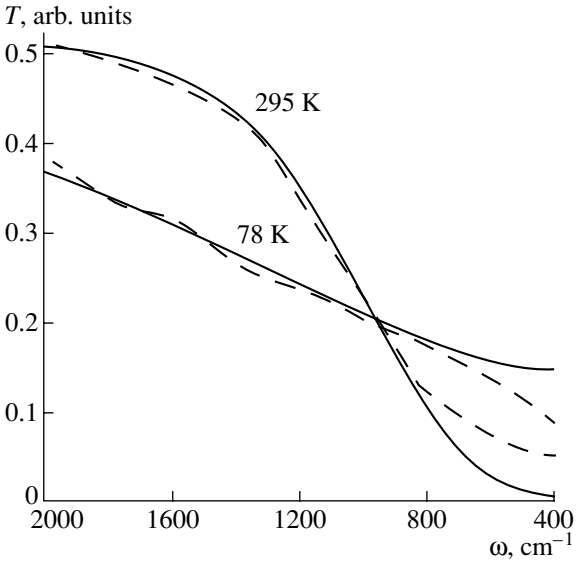

Fig. 1. Experimental (dashed curves) and calculated (solid curves) transmittance spectra for $Cd_{0.948}Zn_{0.052}Te$ sample.

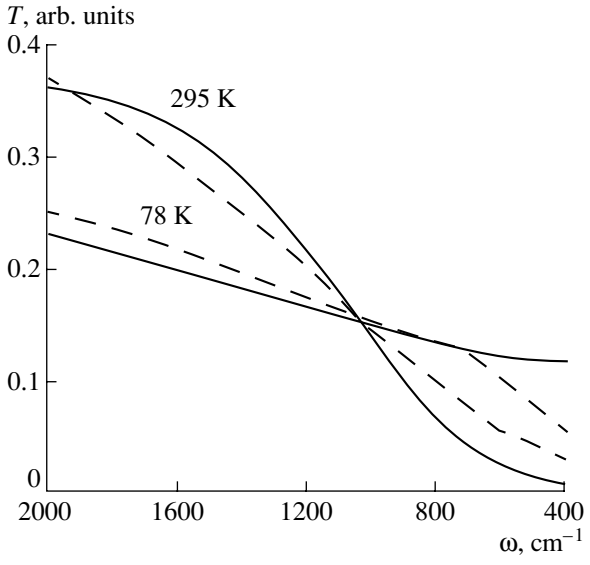

Fig. 2. Experimental (dashed curves) and calculated (solid curves) transmittance spectra for $Cd_{0.956}Zn_{0.044}Te$ sample.

determined from the X-ray energy-dispersive analysis, laser mass-spectroscopy, and the interband absorption edge. The crystal lattice parameters were measured using X-ray high-resolution diffractometry. The surface of the samples was subjected to chemical–mechanical polishing prior to the measurement with subsequent etching in a Br_2/CH_3OH solution.

Transmittance optical spectra $T(\omega)$ were recorded at temperatures T = 5–300 K using an IFS-113v (Bruker, Germany) Fourier spectrometer in the range of wave numbers 10–5000 cm^{-1} with a spectral resolution no worse than 1 cm^{-1}. Spectral dependences of transmittance $T(\omega)$ of the samples studied in the IR wavelength range varied from sample to sample (Figs. 1, 2). Thus, the samples with a low concentration of carriers had a transmittance of 60–63% in the wavelength range studied up to the frequencies at which the multiphonon effects of light absorption set in. However, the samples with a higher concentration of charge carriers, especially if the situation is close to the hole-gas degeneracy, have strong absorption in the frequency range ω = 3000–400 cm^{-1}. The modification of the dependences $T(\omega)$ with the temperature decrease attracts attention: they have an intersection point with the plot at higher temperature, the intersection point being shifted to the right and to the left on the energy scale depending on the degree of hole-gas degeneracy. Similar dependences of the absorption coefficient on the wavelength $\alpha(\omega)$ in a wide temperature range were observed in CdTe crystals [9], and this can be explained by the resonance behavior of the dielectric constant $\varepsilon(\omega)$ behavior caused by the carrier transitions between the branches of light and heavy holes. For this purpose, we use the relation [9] for the absorption coefficient related to the transitions between the branches of light and heavy holes, which has the following form disregarding the effect of the valence-band top corrugation:

$$\alpha_{12}(\omega) = \frac{e^2\omega^{1/2}}{nc\hbar^{3/2}\left(\frac{1}{2m_2}-\frac{1}{2m_1}\right)} \times\left\{\left[\exp\left(\frac{\hbar\omega\rho}{kT(1-\rho)}-\frac{E_F}{kT}\right)+1\right]^{-1} - \left[\exp\left(\frac{\hbar\omega}{kT(1-\rho)}-\frac{E_F}{kT}\right)+1\right]^{-1}\right\}. \quad (1)$$

Here, k is the Boltzmann constant; $\rho = m_2/m_1$; m_1 and m_2 are the light and heavy hole masses, respectively; n is the refractive index; c is the speed of light; and E_F is the energy position of Fermi level, whose variation with the temperature decrease is approximated as

$$E_F(T) = E_F(0)\left[1-\frac{\pi^2}{12}\left(\frac{kT}{E_F(0)}\right)^2\right]. \quad (2)$$

Consideration of the valence band corrugation results in a substantial change in the frequency dependence shape $\mathrm{Im}\varepsilon(\omega)$, in particular in a strong spreading of the high-frequency absorption edge, but, as is shown in [9], only at low temperatures ($4 < T < 15$K). In the case under study, consideration of this correction was meaningless.

The optical spectra, both experimental and theoretically calculated according the approach presented above, are shown in Figs. 1 and 2 for two $Cd_{1-x}Zn_xTe$

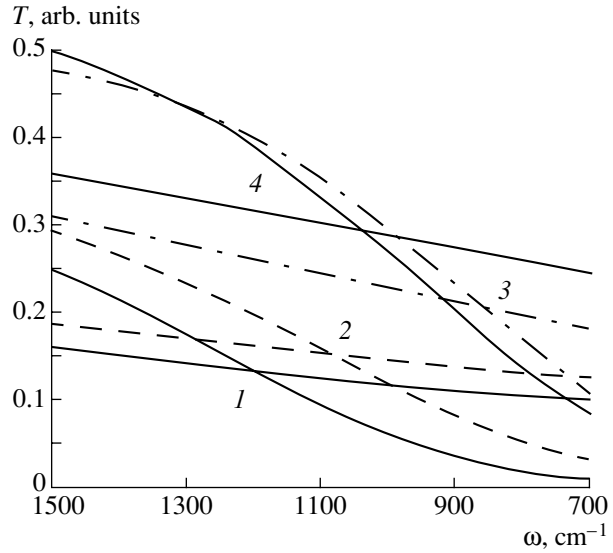

Fig. 3. Experimental transmittance spectra for $Cd_{1-x}Zn_xTe$ sample of various composition at $T = 78$ and 295 K. Values of x: (*1*) 0.041, (*2*) 0.044, (*3*) 0.046, and (*4*) 0.031.

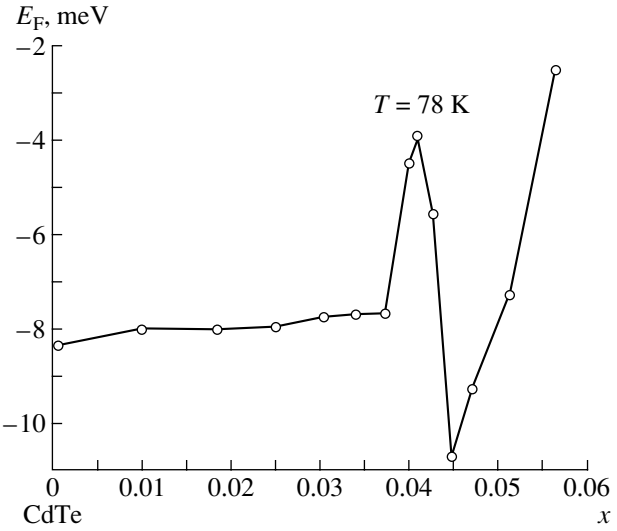

Fig. 4. Fermi-level dependence on the $Cd_{1-x}Zn_xTe$ solid solution composition calculated for $T = 78$ K.

samples of various compositions. It can seen that we succeeded in obtaining a satisfactory agreement between experimental and theoretical data, which, in turn, allowed us to assess the applicability of the model used. A certain discrepancy observed at lower energies is explained by the manifestation of the multiphonon absorption, which was not taken into account in simulating the $T(\omega)$ spectra. A characteristic intersection point of spectral dependences is specific for each sample, which can be readily seen in Fig. 3. This is natural because the samples differ in the concentration and carrier mobility values. Knowing the position of this point in the spectra, we can determine the Fermi level position in the CdZnTe material under study. The results of calculation carried out for the series of samples with the composition $x = 0$–0.06 at room and liquid-nitrogen temperatures are shown in Figs. 4 and 5. As can be seen, a monotonic dependence of the Fermi level position E_F on the composition is observed in $Cd_{1-x}Zn_xTe$ samples up to a value of $x = 0.04$. Furthermore, the composition range $x \approx 0.04$–0.05 is prominent; here, strong deviations from the monotonic behavior of the dependences indicated above are observed, with their manifestation being similar to each other for the two different temperatures. It was previously reported [10] that the frequencies of optical phonons in $Cd_{1-x}Zn_xTe$ samples for the same composition range differed from those theoretically calculated within the context of the uniform cell-displacement model. On the basis of results reported here and in [10], we may assume that the modification of crystal-lattice local dynamics takes place in the composition region of $x \approx 0.04$–0.05; these modifications significantly affect the charge carrier system, specifically in this case, holes. Similar effects should manifest themselves in the immediate vicinity of the cadmium vacancy, in which case the nearest tellurium atoms turn out to be displaced from their central positions. In this case, to balance the change of the lattice polarizability in this crystal region, a hole should be localized at this site. As a result, a Te–p^+–Te-type complex is formed. Local self-organization of Te–p^+–Te-type centers into 2D- or 3D-dimensional formations can occur in unannealed crystals; the sizes of these formations range from tens of nanometers to fractions of a nanometer. We cannot estimate correctly the sizes of such formations within the framework of this study. Selective etching of CdZnTe wafers consisting of the twinned crystals has shown that characteristic etching

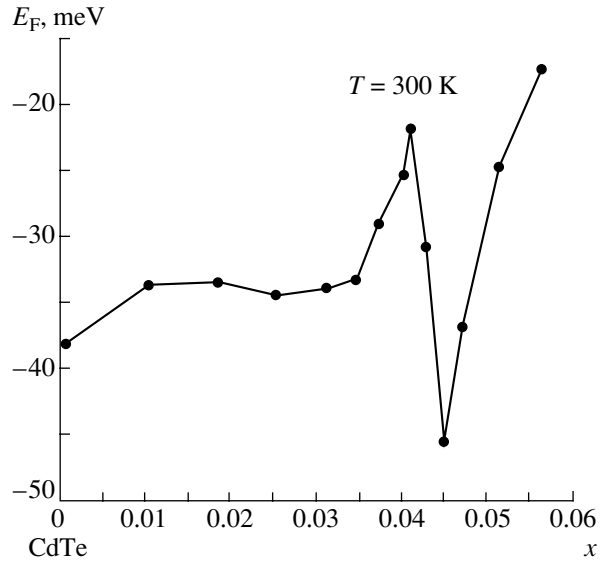

Fig. 5. The same as in Fig. 4 but for $T = 300$ K.

pits appear in the part of the sample for which a decrease in the absorption coefficient in the range of wave numbers 3000–400 cm^{-1} is observed. Zhu *et al.* [6] have studied the effect of tellurium inclusions in CdZnTe on light transmission in the IR wavelength region. It was noticed that, in CdZnTe samples with the content of tellurium precipitates as high as 0.6 wt %, the light transmittance level in the IR wavelength range did not exceed 55%, and the spectral dependences $T(\omega)$ were similar to those shown in Figs. 1 and 2. In our case, in CdZnTe crystals after additional annealing in cadmium vapor at temperatures $T > 480°C$, the light transmittance in the 3000–400 cm^{-1} range increased. In the submillimeter wavelength range, beyond the crystal lattice vibration absorption ($\omega < 80$ cm^{-1}), the value of $T(\omega)$ increased again by ~40–50% in the samples under study. This is evidence of the absence of the optical absorption by shallow impurity levels in the band gap of the CdZnTe crystals under consideration.

CONCLUSION

On the basis of the above results we may conclude that tellurium inclusions appreciably affect the increase in the optical absorption at energies lower than the CdZnTe band gap. Nonmonotonic dependence $E_F(x)$ for $x = 0.04$–0.05 is associated most probably with deviations from stoichiometry in growing the material of the composition indicated.

ACKNOWLEDGMENTS

This study was supported by the Russian Foundation for Basic Research, project no. 00-02-17104.

REFERENCES

1. E. A. Paten, M. H. Kalisher, G. R. Chapman, *et al.*, J. Vac. Sci. Technol. B **9**, 1746 (1991).
2. S. M. Johnson, M. H. Kalisher, W. L. Ahlgren, *et al.*, Appl. Phys. Lett. **56**, 946 (1990).
3. P. Fougeres, M. Hage-Ali, J. M. Koebel, *et al.*, J. Cryst. Growth **184/185**, 1313 (1998).
4. D. Ohimann, M. Mazilu, R. Levy, and B. Honerlage, J. Appl. Phys. **82**, 1355 (1997).
5. A. J. Syllaios, P.-K. Liao, B. J. Greene, *et al.*, J. Electron. Mater. **26**, 567 (1997).
6. J. Zhu, X. Zhang, B. Li, and J. Chu, Infrared Phys. Technol. **40**, 411 (1999).
7. A. R. Gareeva, V. I. Petrov, N. A. Smirnova, *et al.*, in *Proceedings of the VIII All-Union Symposium on Narow-Gap Semiconductors and Semimetals, Lvov, 1991*, Vol. 2, p. 148.
8. N. V. Agrinskaya and V. V. Shashkova, Fiz. Tekh. Poluprovodn. (Leningrad) **24**, 697 (1990) [Sov. Phys. Semicond. **24**, 437 (1990)].
9. A. I. Belogorokhov, Fiz. Tverd. Tela (Leningrad) **34**, 1045 (1992) [Sov. Phys. Solid State **34**, 558 (1992)].
10. A. I. Belogorokhov, L. I. Belogorokhova, A. G. Belov, *et al.*, J. Cryst. Growth **159**, 186 (1996).

Translated by T. Galkina

Semiconductors, Vol. 35, No. 7, 2001, pp. 777–783. Translated from Fizika i Tekhnika Poluprovodnikov, Vol. 35, No. 7, 2001, pp. 812–818.

ELECTRONIC AND OPTICAL PROPERTIES OF SEMICONDUCTORS

Metallic Conductivity over an Acceptor Band of Lightly Compensated Copper-Doped *p*-$Hg_{0.78}Cd_{0.22}Te$ Crystals

V. V. Bogoboyashchiĭ

Kremenchuk State Polytechnical University, Kremenchuk, 39614 Ukraine

Submitted September 20, 2000; accepted for publication December 19, 2000

Abstract—The conductivity and Hall effect of heavily doped *p*-$Hg_{0.78}Cd_{0.22}Te$:Cu crystals were studied in the temperature range of 4.2–125 K. The conductivity over the impurity band is of a metallic type for the acceptor concentration $N_A > 3.8 \times 10^{17}$ cm^{-3}. The conductivity and the Hall coefficient governed by the delocalized charge carriers in the impurity band are independent of temperature. The sign of the Hall effect is positive in the metallic conductivity range. Near the metal–insulator transition point, the Hall mobility increases linearly with the acceptor concentration and is independent of the acceptor concentration at $N_A > 1.6 \times 10^{18}$ cm^{-3}. The metallic conductivity is proportional to N_A in the concentration range under study at $N_A < 3.1 \times 10^{18}$ cm^{-3}. The Anderson transition occurs at the Cu concentration $N_A = 1.4 \times 10^{17}$ cm^{-3} in the A^+ impurity band, which is formed by positively charged acceptors. Minimum metallic conductivity corresponding to this transition equals 5.1 Ω^{-1} cm^{-1}. It is shown that ε_2 conductivity in the subthreshold region is defined by delocalized carriers in the upper Hubbard band only for fairly heavy doping ($N_A > 1.4 \times 10^{17}$ cm^{-3}). For $N_A < 1.4 \times 10^{17}$ cm^{-3}, the hopping conductivity is observed. © *2001 MAIK "Nauka/Interperiodica".*

INTRODUCTION

Studies of the impurity states in semiconductors using magnetotransport measurements are popular due to the relative simplicity and reliability of the experimental method. One of the most widely known directions of these studies is the investigation of the metal–insulator transition in the impurity band of doped crystals (the Mott transition). The mechanisms of this transition depend directly on the specific size of the impurity centers [1] and, thus, can give additional information about the energy state parameters. In particular, it is possible to obtain some useful information from the study of a metallic conductivity over the impurity band of a semiconductor [1].

It has been shown [2] that the Cu-doped narrow-gap crystals of the *p*-$Hg_{1-x}Cd_xTe$ solid solution are promising materials for studies of the impurity conductivity mechanism near the Mott transition. In this material, Cu forms fairly large simple acceptor centers. This circumstance makes it possible to successfully apply the effective mass approximation for their description and, thereby, to simplify significantly the theoretical model. On the other hand, the Cu solubility and its diffusion coefficient in the narrow-gap $Hg_{1-x}Cd_xTe$ crystals are large [3], but the concentration of the uncontrolled impurities is very low. Due to this fact, it is quite easy to grow lightly compensated *p*-type crystals with any desirable concentration of the major acceptors. In addition, the conductivity over the impurity states in *p*-$Hg_{1-x}Cd_xTe$ is observed at fairly high temperatures [2, 4]. This fact also appreciably simplifies the experimental procedure.

In [2], the experimental data of the conductivity study in the *p*-$Hg_{1-x}Cd_xTe$:Cu crystals in the subthreshold concentration region when the conductivity has an activation character are presented. In particular, it was shown that at $x = 0.22$ the Mott transition is observed in the impurity band of this material at the acceptor concentration $N_A = 3.8 \times 10^{17}$ cm^{-3}. In this paper, we continue these investigations. The conductivity, the Hall effect, and the Hall mobility of charge carriers were studied in the impurity band of the heavily doped *p*-$Hg_{0.78}Cd_{0.22}Te$:Cu crystals (especially at $N_A > 3.8 \times 10^{17}$ cm^{-3} when conductivity of the crystals becomes metallic at low temperature).

EXPERIMENTAL

We selected for the experiments compositionally homogeneous *p*-$Hg_{0.78}Cd_{0.22}Te$ wafers submitted by OAO Pure Metals (Svetlovodsk, Ukraine). The concentration of uncompensated donors in the selected crystals was lower than 3×10^{14} cm^{-3}; the dislocation density did not exceed 3×10^5 cm^{-2}. These were no dislocation rosettes and inclusions of the second phase.

The wafers were cut into samples $1.2 \times 0.3 \times 0.1$ cm in size. Copper was then evaporated on the samples in amounts varying from 10^{16} to 3×10^{17} cm^{-2}. Copper

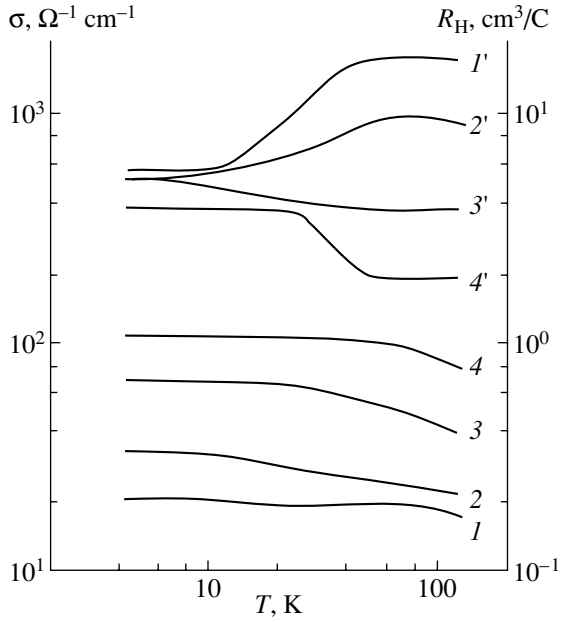

Fig. 1. The temperature dependences of (*1*–*4*) the conductivity and (*1*'–*4*') the Hall coefficient of the *p*-$Hg_{0.78}Cd_{0.22}Te$:Cu crystals for the acceptor concentration N_A = (*1*, *1*') 4.2×10^{17}, (*2*, *2*') 8.2×10^{17}, (*3*, *3*') 1.7×10^{18}, and (*4*, *4*') 3.1×10^{18} cm^{-3}.

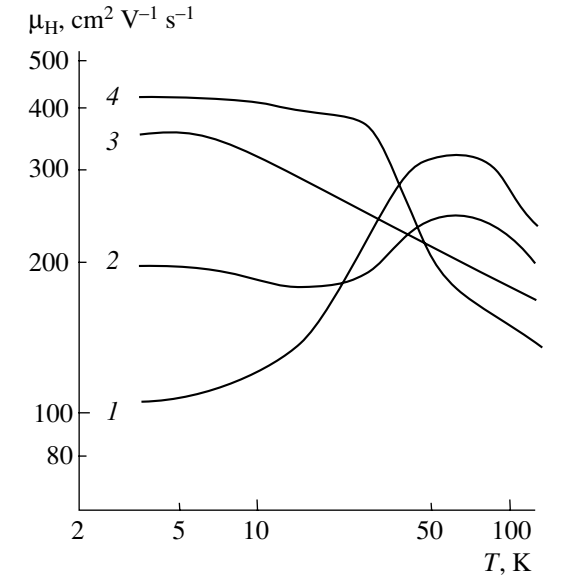

Fig. 2. The temperature dependence of the charge-carrier Hall mobility in the *p*-$Hg_{0.78}Cd_{0.22}Te$:Cu crystals. N_A = (*1*) 4.2×10^{17}, (*2*) 8.2×10^{17}, (*3*) 1.7×10^{18}, and (*4*) 3.1×10^{18} cm^{-3}.

was introduced into the crystals by annealing for three days in a saturated Hg vapor at temperatures no lower than 473 K. The copper distribution in these samples after such an annealing was macroscopically uniform.

The solid solution of Cu in $Hg_{0.78}Cd_{0.22}Te$ is stable at $N_A < 6 \times 10^{17}$ cm^{-3}; therefore, these crystals were annealed at T = 473 K in order to reduce the Hg vacancy concentration. If there are no Hg vacancies, such a solid solution is unstable at $N_A > 6 \times 10^{17}$ cm^{-3} and decomposes rapidly into two phases: Cu inclusions and a crystal matrix with $N_A \approx 6 \times 10^{17}$ cm^{-3}. Vacancies stabilize the solid solution, decreasing the Cu diffusion coefficient and increasing its solubility [5]. Due to this fact, the crystals with $N_A > 6 \times 10^{17}$ cm^{-3} were annealed at a higher temperature (623–673 K). The equilibrium concentration of Hg vacancies in these conditions was about 10^{16} cm^{-3}. Since this concentration is much lower than N_A and the ionization energy of the Hg vacancy exceeds the Cu ionization energy by more than 100% [6], the native defects in such crystals do not affect their electrical properties at a low temperature.

Samples were chemically etched in a solution of Br_2 in HBr and were rinsed in deionized water. Immediately after this procedure, the resistivity and the Hall coefficient in the magnetic field B = 0.03 T were measured. The measurements were performed in the temperature range of 4.2–125 K. The concentration of an active Cu in the samples was obtained from the Hall coefficient measurements in the magnetic field B = 1 T at T = 77 K. It is assumed that in these conditions the Hall factor equals 1.24 [7] and that all impurities are completely ionized [8].

RESULTS

Experimental temperature dependences of conductivity σ of the *p*-$Hg_{0.78}Cd_{0.22}Te$ crystals with various Cu concentrations ($N_A > 3.8 \times 10^{17}$ cm^{-3}) are shown in Fig. 1 (curves *1*–*4*). It can be seen that at $T < 125$ K, σ depends on temperature only slightly.

In contrast to the lightly doped samples, the Hall effect in the heavily doped *p*-$Hg_{0.78}Cd_{0.22}Te$ crystals with $N_A > 2 \times 10^{17}$ cm^{-3} can easily be measured down to T = 4.2 K even in a low magnetic field (B = 0.03 T). In this case, the Hall coefficient (R_H) sign in the extrinsic conductivity region is positive. Experimental curves $R_H(T)$ are also shown in Fig. 1 (curves *1*'– *4*').

The temperature dependences of the charge-carrier Hall mobility ($\mu_H = R_H\sigma$) in the same samples are shown in Fig. 2.

Analysis shows that it is possible to separate each experimental curve shown in Figs. 1 and 2 into three portions.

In the low-temperature region (below 8–20 K, depending on N_A), all three quantities (σ, R_H, and μ_H) are independent of temperature. The Hall coefficient depends only slightly on N_A, while σ and μ_H increase distinctly with N_A. These features indicate that, in this temperature region and at these acceptor concentrations, we observe metallic conductivity.

At comparatively high temperatures T (higher than 40–80 K), the Hall effect is independent of temperature and σ and μ_H decrease as temperature increases. As the copper concentration increases, R_H and μ_H decrease. Therefore, in this case the charge is transported mostly by the valence-band holes.

In the intermediate temperature region, the shape of $R_H(T)$ and $\mu_H(T)$ is defined by N_A. There is no doubt that in this temperature range a change of the dominant conduction mechanism occurs with variation in T.

The conductivity, the Hall effect, and the Hall mobility of carriers in the acceptor band at $T = 4.2$ K in the metallic conductivity region as a function of the acceptor concentration N_A are shown in Figs. 3–5.

Experimental dependence of the metallic conductivity on N_A at $N_A > N_{AM}$ is extremely simple (Fig. 3) and can be described by the relation

$$\sigma_{met} = \sigma_M \frac{N_A}{N_{AM}}, \quad (1)$$

where $N_{AM} = 3.8 \times 10^{17}$ cm^{-3} is the acceptor concentration at the Mott transition point [2] and $\sigma_M \approx 14$ Ω^{-1} cm^{-1} is the metallic conductivity at the same point. The following experimental fact should be noted. According to [2], in the Cu-doped p-$Hg_{0.8}Cd_{0.2}Te$ crystals, the ε_2 conductivity of the activation type is observed at low temperatures below the Mott transition point:

$$\sigma_2 = \sigma_{02} \exp\left(\frac{\varepsilon_2}{k_B T}\right). \quad (2)$$

It can easily be seen (Fig. 3) that at $N_A > 1.5 \times 10^{17}$ cm^{-3} the preexponential factor σ_{02} satisfies relation (1) with a smooth transition to σ_{met} at $N_A = N_{AM}$.

The law of variation in the Hall mobility of delocalized holes in the acceptor band with N_A is more complicated. At $N_A < 1.6 \times 10^{18}$ cm^{-3}, the experimental data may be approximated with good accuracy by the linear dependence

$$\mu_{Hmet} = \mu_{H0} \frac{N_A - N_{AA}}{N_{AA}}, \quad (3)$$

which includes the subthreshold concentration region $N_{AA} < N_A < N_{AM}$ (Fig. 4). Here, $\mu_{H0} \approx 35$ cm^2 V^{-1} s^{-1} and $N_{AA} \approx 1.4 \times 10^{17}$ cm^{-3} are experimental constants. For higher Cu concentrations (in the range of 1.6×10^{18} cm^{-3} $< N_A < 3 \times 10^{18}$ cm^{-3}), the mobility virtually does not vary as N_A increases and is equal to 350–400 cm^2 V^{-1} s^{-1}.

The Hall coefficient R_{Hmet} controlled by the delocalized charge carriers of the acceptor band depends on N_A only slightly in the concentration range under study (Fig. 5). In the N_A range from 4×10^{17} to 1.6×10^{18} cm^{-3}, R_{Hmet} increases insignificantly with N_A (approximately from 4.5 to 6 cm^3/C), and, for $N_A > 1.6 \times 10^{18}$ cm^{-3}, R_{Hmet} decreases approximately in accordance with the conventional formula

$$R_H = \frac{r_H}{ep}, \quad (4)$$

under the assumption that $p = N_A$ and $r_H \approx 1.9$.

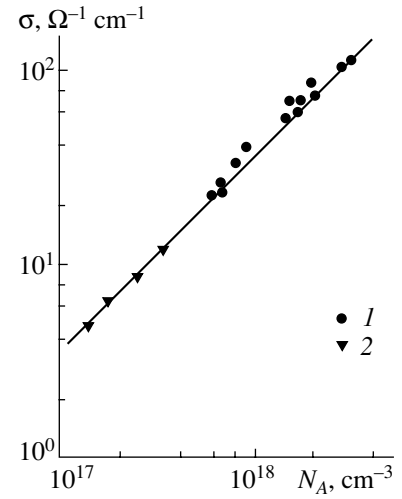

Fig. 3. (*1*) The conductivity and (*2*) σ_{02} factor (parameter in the Arrhenius law (2) for ε_2 conductivity) dependence on the acceptor concentration in the p-$Hg_{0.78}Cd_{0.22}Te$:Cu crystals at $T = 4.2$ K.

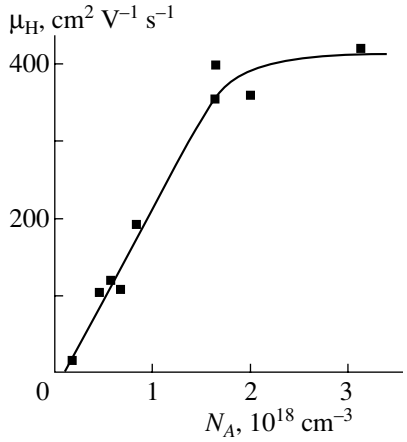

Fig. 4. The Hall mobility dependence on the acceptor concentration N_A in the p-$Hg_{0.78}Cd_{0.22}Te$:Cu crystals at $T = 4.2$ K.

DISCUSSION

A. Critical Points

Studies of the concentration dependences of the metallic conductivity parameters and ε_2 conductivity of the p-$Hg_{0.78}Cd_{0.22}Te$:Cu crystals show that there are

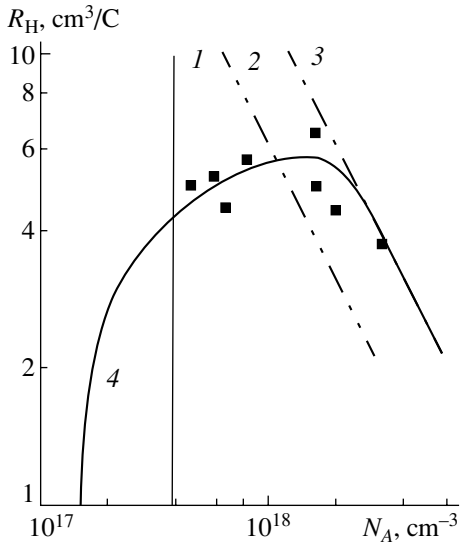

Fig. 5. The Hall coefficient dependence on the acceptor concentration N_A in the p-$Hg_{0.78}Cd_{0.22}Te$:Cu crystals at T = 4.2 K. The dots represent experimental data. Line (*1*) corresponds to $N_A = N_{AM}$; (*2*) the results of R_H calculation with formula (4) for $r_H = 1$; (*3*) the results of R_H calculation with formula (4) for $r_H = 1.9$; (*4*) $R_H(N_A)$ experimental dependence calculated from the data presented in Figs. 3 and 4.

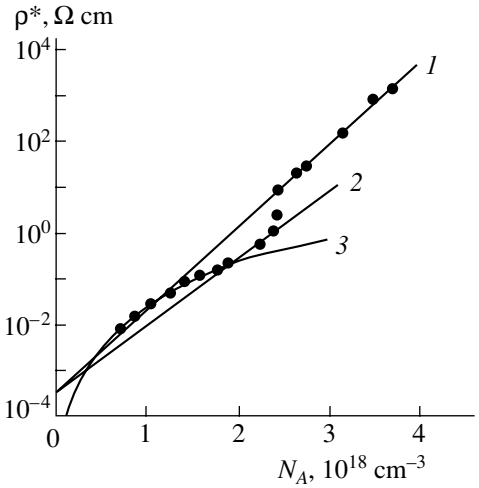

Fig. 6. The concentration dependence of the ρ* factor in relation (5) for resistivity of the p-$Hg_{0.78}Cd_{0.22}Te$:Cu crystals. The dots represent the experimental data, the lines correspond to the empiric interpolated dependences. (*1*) ε_3 hopping conductivity region, (*2*) the region of ε_2 hopping conductivity over the states in the A^+ band, and (*3*) the region ε_2 conductivity over the states at the mobility edge in the A^+ band.

three specific acceptor concentrations: $N_{AA} \approx 1.4 \times 10^{17}$ cm^{-3}, $N_{AM} \approx 3.8 \times 10^{17}$ cm^{-3}, and $N_{AB} \approx 1.6 \times 10^{18}$ cm^{-3}. These concentrations separate regions where the σ, R_H, and μ_H coefficients have a radically different behavior.

The point $N_A = N_{AM}$ is unambiguously associated with the Mott transition in the acceptor band of the crystal. This was convincingly proven in the previous paper [2], in which the concentration dependence of the activation energy of the low-temperature ε_2 conductivity was measured in the same material. For $N_A < N_{AM}$, the energy $\varepsilon_2 > 0$ and, therefore, the Fermi level lies at $T = 0$ in the band of localized acceptor states. For $N_A > N_{AM}$, the ε_2 conductivity does not have an activation character, so that the Fermi level lies in the band of the extended states.

As is well known [1], in the lightly compensated doped semiconductors, the Mott transition occurs as a result of the overlap of two impurity bands. In the case of p-type conductivity crystals, one of these bands (similar to the lower Hubbard band) is formed by the neutral acceptor states. At the Mott transition point, these states are considered to be localized (at least in the vicinity of the Fermi level). The other band (similar to the upper Hubbard band) is formed by the A^+-acceptor states with an attached excess hole. Because the binding energy of an excess hole is small in comparison with the acceptor ionization energy, it is assumed that the A^+-state radius is large and that these states are extended [1, 9].

In fact, as it was shown recently [2], due to the identity of bound holes, the size of the A^+ state of the isolated simple acceptor slightly exceeds its radius a_h in the neutral state: $a_{A^+} = 4a_h/3$. For this reason, the question concerning the localization of states in the A^+ band is appropriate. It was suggested [2] that delocalization can occur either as a result of the Anderson transition or due to overlap with the valence band. According to [2], the second mechanism is more preferable because the Anderson transition occurs at heavier doping. This conclusion is based on the experimental dependence of the ρ* factor on concentration, which has a discontinuity in the Arrhenius law

$$\rho = \rho^* \exp\left(\frac{\varepsilon^*}{k_B T}\right), \qquad (5)$$

which is observed at the Cu concentration $N_A \approx 6 \times 10^{16}$ cm^{-3} (Fig. 6), i.e., approximately at the moment when A^+ band comes into contact with the valence band.

Our studies of the Hall charge-carrier mobility in the impurity band of the heavily Cu-doped p-$Hg_{0.78}Cd_{0.22}Te$ crystals contradict this assumption and at the same time confirm the Anderson–Lifshits mechanism of the state localization in the A^+ band.

If the Cu ionization energy in $Hg_{0.78}Cd_{0.22}Te$ E_A = 7.6 meV [6] is a reliable estimate, then, using the theory [2, 10] and data [11] for the other constants of this material, we obtain the following values for the isolated

acceptor radii: a_h = 3.6 nm and a_{A^+} = 4.8 nm. We then use the Anderson localization criterion

$$(N_{AA})^{1/3} a_{A^+} \approx 0.25 \quad (6)$$

to find that, in the Cu-doped $Hg_{0.78}Cd_{0.22}Te$, the critical concentration $N_{AA} \approx 1.4 \times 10^{17}$ cm^{-3}. However, according to Fig. 4, $\mu_H \longrightarrow 0$ at $N_A \longrightarrow 1.4 \times 10^{17}$ cm^{-3} + 0, i.e., exactly at $N_A \longrightarrow N_{AA}$ + 0. Therefore, for $N_A < N_{AA}$, the charge transport by carriers excited into the A^+ band is most likely characterized by the hopping mechanism because the absence of the Hall effect [1] is typical of the hopping conductivity.

This conclusion is also confirmed by other facts. The concentration dependence of the ρ* factor of the Arrhenius law (5) is shown in Fig. 6. For $N_A > N_{AA}$, it consists of two portions separated by a narrow region in which the ρ* variation has a jumplike variation. In each of these portions, the $\rho^*(N_A)$ dependence has a form typical of the hopping conductivity

$$\rho^* = \rho_0^* \exp\left(\frac{\alpha}{a^* N_A^{1/3}}\right) \quad (7)$$

(here α = 1.73 [9]). For $N_A < 6 \times 10^{16}$ cm^{-3}, in which case ε_3 conductivity is dominant at low temperatures [2], the approximation of the experimental data by dependence (7) yields a^* = 3.7 nm and $\rho_0^* \approx 6 \times 10^{-5}$ Ω cm. In the concentration range of $1.4 \times 10^{16} < N_A < 6 \times 10^{16}$ cm^{-3}, where ε_2 conductivity is dominant [2], we obtain a^* = 4.9 nm and $\rho_0^* \approx 2.5 \times 10^{-4}$ Ω cm. It can be seen that, in the ε_3 conductivity region, the value of a^* approximately equals the neutral acceptor radius a_h, but in the ε_2 conductivity region, $a^* \approx a_{A^+}$. It should be noted that, in both cases, ρ_0^* obtained experimentally is in agreement with the results of calculation with the formulas given in [9]. In particular, it follows from the calculation that $\rho_{03} \sim 10^{-5}$ Ω cm for the ε_3 conductivity and $\rho_{02} \sim 10^{-4}$ Ω cm for the ε_2 conductivity.

For heavier doping (in the region $N_A > N_{AA}$), the Hall mobility exceeds 10 cm^2 V^{-1} s^{-1}. This is quite a large value and suggests that the charge transport is realized by the delocalized carriers activated into the A^+ band.

Thus, the point $N_A = 1.4 \times 10^{17}$ cm^{-3} is really the Anderson transition point in the A^+ band of p-$Hg_{0.78}Cd_{0.22}Te$. A rapid change in ρ*, which is observed at $N_A \approx 6 \times 10^{16}$ cm^{-3}, is related only to the transition from ε_3 conductivity to ε_2 conductivity.

An important circumstance should be noted. The data shown in Fig. 6 indicate that the effective localization radius of the A^+ state, which defines the hop probability, remains constant up to the moment when the first extended states appear in the band center. At first glance, this inference is inconsistent with the well-known opinion according to which the impurity-state radius increases up to the size of the crystal when the critical point is approached [1, 9]. The cause of this phenomenon probably consists in the fact that the hop probability is defined by the overlap only of the nearest-neighbor wave functions. In the first approximation, the wave function of the localized state is the linear combination of the wave functions belonging to separate potential wells. The overlap integral of the nearest neighbors decreases as the distance between the potential wells increases and obeys the same law as for isolated centers.

The third specific concentration $N_{AB} \approx 1.6 \times 10^{18}$ cm^{-3} corresponds to the point which lies deep in the metallic conductivity region and which separates the regions with different behavior of the concentration dependences $R_{Hmet}(N_A)$ and $\mu_{Hmet}(N_A)$ (Figs. 4, 5). For $N_A < N_{AB}$, the Hall coefficient is almost independent of N_A and is appreciably smaller than the value predicted by classical formula (4). For $N_A > N_{AB}$, the $R_{Hmet}(N_A)$ dependence, on the contrary, approaches relation (4). We believe that the point $N_A = N_{AB}$ is the lower boundary of the weak scattering region, where the Ioffe–Regel criterion ($\lambda k_F > 1$) is satisfied and the Born approximation is valid. Here, λ is the mean free path and k_F is the hole quasi-momentum at the Fermi level.

In fact, for $N_A > N_{AB}$, the Hall mobility of holes is fairly high: $\mu_{Hmet} \approx 400$ cm^2 V^{-1} s^{-1} (Fig. 4). If in these conditions the Fermi level lies deep enough in the A^+ band so that it is possible to assume that $k_F \approx \pi/a$ ($a \approx N_A^{1/3}$ is the average distance between the acceptors), then the mean free path $\lambda = \mu\hbar k_F/e \approx 10$ nm. It is easy to evaluate that in this case $\lambda k_F \approx 3 > 1$; i.e., the Ioffe–Regel criterion is satisfied.

If this assumption is true, the conductivity at $T = 0$ at the point $N_A = N_{AB}$ should be equal to $0.2e^2\hbar^{-1}N_{AB}^{1/3}$ [1]. Substituting $N_{AB} \approx 1.6 \times 10^{18}$ cm^{-3} into this expression, we obtain $\sigma = 56\ \Omega^{-1}$ cm^{-1}. The experimental σ_{met} value at this point approximately equals 60 Ω^{-1} cm^{-1}; i.e., it practically coincides with the result of the calculation.

B. The Hall Effect and the Hall Mobility

The Hall effect characteristics controlled by the carriers in the impurity band of the Cu-doped $Hg_{0.78}Cd_{0.22}Te$ crystals at low ($N_A < N_{AA}$) and high ($N_A > N_{AB}$) Cu concentrations do not contradict the conventional views on this phenomenon.

For $N_A < N_{AA}$, the hopping conductivity is dominant in the low-temperature region. In this case, the Hall effect cannot be measured. Our experiment confirms this result.

The condition $N_A = N_{AB}$ is equivalent to the condition for close packing of balls with radii of a_{A^+}: $(4\pi/3)N_{AB}a_{A^+}^3 \approx 0.74$. Thus, for $N_A > N_{AB}$ (with regard to random distribution of impurity atoms and a free overlap of their hole shells), the acceptors form a single whole cluster with metallic conductivity that contains individual inclusions of the semiconductor phase. It is evident that in these conditions the influence of inhomogeneity of the medium on conductivity becomes quite weak; as a result, the mean free path can be large and satisfy the Ioffe–Regel inequality. In such structures, the classical law (4) is obeyed with the Hall factor r_H equal to unity (due to degeneracy of holes) [1]. In fact, the experimental dependence $R_{Hmet}(N_A)$ is similar to relation (4); however, R_{Hmet} is twice as large as the expected value. Obviously, this can be explained by a decrease in the density of states in the impurity band due to disorder, which should cause an increase in R_{Hmet} [1].

The behavior of R_{Hmet} and μ_{Hmet} in the intermediate Cu concentration region $N_{AA} < N_A < N_{AB}$ is less clear. In this case, the mobility increases linearly from 0 for $N_A = N_{AA}$ to 350–400 cm^2 V^{-1} s^{-1} for $N_A \approx N_{AB}$.

Usually, the Friedman model [12] developed for materials with the diagonal type of disorder is used to describe the Hall effect in heavily disordered systems. According to the Friedman model, the Hall coefficient must be invariably negative if the three-site approximation is true (for example, for a crystal structure with close packing). In the case of a four-site approximation (for example, in a simple cubic lattice), the Hall effect coefficient for holes must be positive. As is shown in [1], the three-site approximation is appropriate for the random structures. In particular, this approximation satisfactorily describes the Hall effect in liquid metals and in amorphous semiconductors.

It is easy to show that, in our case, the Friedman model is not quite appropriate for describing the experimental data. First, the Hall coefficient is positive. This, contrary to expectations, is more consistent with a four-site approximation. Second, the Friedman model predicts that the Hall mobility at the Anderson transition point ($N_A = N_{AA}$) is approximately equal to $ea^2/(7\hbar)$, i.e., about 800 cm^2 V^{-1} s^{-1}. The actual value of μ_{Hmet} at this point is at least two orders of magnitude smaller (Fig. 4).

Apparently, it is necessary to use the percolation theory to describe the Hall effect controlled by holes of the impurity band in Cu-doped p-$Hg_{0.78}Cd_{0.22}Te$ crystals. According to this theory, for $N_A = N_{AA}$, an infinite metallic-conductivity cluster is formed in the impurity system. However, such a cluster has a complicated topology; due to this fact, the corresponding Hall effect is small. As N_A increases, the metallic cluster incorporates more and more acceptors, its topology is simplified, and the Hall coefficient and the Hall mobility increase in magnitude. For $N_A = N_{AA}$ (when the metallic cluster fills the entire crystal), the mobility approaches the value predicted by the Friedman model.

Indirectly, such a mechanism controlling μ_{Hmet} is confirmed by the conclusion (well known in the percolation theory) that, in the lattice models, the percolation mobility near the Anderson transition is proportional to the difference $N_A - N_{AA}$ [13].

C. Minimum Metallic Conductivity

An important feature in the transport theory of disordered systems is the minimum metallic conductivity σ_{min}, which is the conductivity of a metallic cluster at the Anderson transition point. The σ_{min} was calculated by Mott using the Kubo–Greenwood formula [1]:

$$\sigma_{min} = \frac{\pi}{4z}\left(\frac{B}{V_0}\right)^2\frac{e^2}{\hbar a}, \qquad (8)$$

where z is the nearest neighbor number, B is the band width in the ordered system, and V_0 is the ultimate energy of disordering in the Anderson model. Assuming that $z = 6$, $V_0/B = 2$ [1], and $a = N_{AA}^{-1/3}$, we obtain $\sigma_{min} \approx 4.1\ \Omega^{-1}\ cm^{-1}$.

On the other hand, it is easy to show that at $T \approx 4$ K the conductivity governed by the charge carriers excited at the mobility threshold is equal with a precision of small terms on the order of k_BT/B to

$$\sigma_2 = \sigma_{E_C}\exp\left(-\frac{|E_C - F|}{k_BT}\right), \qquad (9)$$

where E_C is the mobility threshold energy, σ_{E_C} is the conductivity of the crystal at $T = 0$, and $F = E_C$. Comparing relation (9) with the Arrhenius law (2) for the ε_2 conductivity, we obtain $\sigma_{02} = \sigma_{E_C}$. This circumstance explains the fact that the dependence $\sigma_{02}(N_A)$ coincides with the concentration dependence of σ_{met} extended to the range of $N_{AA} < N_A < N_{AM}$ (Fig. 3).

Therefore, σ_{min} should be experimentally determined as the value of the σ_{02} factor at the point $N_A = N_{AA}$. Then, using formula (5), we find that $\sigma_{min} \approx 5.1\ \Omega^{-1}\ cm^{-1}$. As can be seen, both σ_{min} values (calculated and experimental) are in agreement.

The experimental σ_{min} is often identified with the conductivity of doped semiconductor at the Mott transition point [1]. On the basis of the aforesaid, it becomes clear that this is the wrong idea. It is precisely this fallacy which underlies the assumption that, in doped semiconductors, σ_{min} is twice as high as in amorphous semiconductors and in liquid metals [1].

It should be noted that conductivity at the extreme points of the $N_{AA} < N_A < N_{AB}$ interval is in good agreement with the values predicted by Mott [1]. At the same

time, within this interval, according to Mott, the conductivity should be inversely proportional to the average distance between the impurities [1], while, in practice, $\sigma_{met} \propto N_A \approx a^{-3}$.

CONCLUSION

(1) In the impurity band of the Cu-doped lightly compensated p-$Hg_{0.78}Cd_{0.22}Te$ crystals, metallic conductivity is observed for $N_A > N_{AM} \approx 3.8 \times 10^{17}$ cm^{-3}. The conductivity and the Hall coefficient are independent of temperature in the metallic conductivity region.

(2) Prior to the transition to the metallic state in the Cu-doped lightly compensated p-$Hg_{0.78}Cd_{0.22}Te$ crystals, ε_2 conductivity is observed. This conductivity is controlled by holes excited to the A^+ band. In this band, the Anderson transition occurs at $N_A = N_{AA} \approx 1.4 \times 10^{17}$ cm^{-3}. As a result, in the ε_2 conductivity region, the charge is transported at $N_A < N_{AA}$ by bound carriers (the hopping conductivity) and by delocalized carriers excited to the mobility threshold at $N_A > N_{AA}$.

(3) The radius of the state in the A^+ band which defines the hop probability at $N_A < N_{AA}$ is 33% larger than the radius of an isolated neutral-acceptor state and is approximately equal to 4.8 nm. The radius is virtually independent of the Cu concentration up to the Anderson transition point in this band.

(4) The Hall effect in the Cu-doped p-$Hg_{0.78}Cd_{0.22}Te$ crystals, which is governed by the charge carriers in the impurity band, can be measured only if there are extended states in the A^+ band (at $N_A > N_{AA}$). The Hall coefficient sign defined by the contribution of these carriers is positive. This corresponds to the four-site approximation in the Friedman model. It is necessary to use the percolation theory methods for a quantitative description of the Hall effect in the metallic conductivity region at a relatively low acceptor concentration (at $N_A < N_{AB} \approx 1.6 \times 10^{18}$ cm^{-3}). For $N_A > N_{AB}$, the Born approximation of weak scattering is realized.

REFERENCES

1. N. F. Mott and E. A. Davis, *Electronic Processes in Non-Crystalline Materials* (Clarendon, Oxford, 1979; Mir, Moscow, 1982), Vol. 1.
2. V. V. Bogoboyashchiĭ, G. A. Shepel'skiĭ, and S. G. Gasanzade, Fiz. Tekh. Poluprovodn. (St. Petersburg) **34** (4), 411 (2000) [Semiconductors **34**, 398 (2000)].
3. V. V. Bogoboyashchiĭ, A. I. Elizarov, V. A. Petryakov, *et al.*, Fiz. Tekh. Poluprovodn. (Leningrad) **21** (8), 1469 (1987) [Sov. Phys. Semicond. **21**, 893 (1987)].
4. A. I. Elizarov and V. I. Ivanov-Omskiĭ, Fiz. Tekh. Poluprovodn. (Leningrad) **15** (5), 927 (1981) [Sov. Phys. Semicond. **15**, 531 (1981)].
5. N. N. Berchenko, V. V. Bogoboyashchiĭ, A. I. Elizarov, *et al.*, in *Proceedings of the All-Union Workshop on the Problems in the Physics and Chemistry of Semiconductors, Pavlodar, 1987*, p. 129.
6. V. V. Bogoboyashchiĭ, Fiz. Tekh. Poluprovodn. (St. Petersburg) **34** (8), 955 (2000) [Semiconductors **34**, 916 (2000)].
7. V. V. Bogoboyashchiy, Proc. SPIE **3486**, 325 (1997).
8. V. A. Bazakutsa, V. I. Belozertseva, V. V. Bogoboyashchiĭ, *et al.*, in *Proceedings of the All-Union Workshop on the Problems in the Physics and Chemistry of Semiconductors, Pavlodar, 1987*, p. 148.
9. B. I. Shklovskiĭ and A. L. Éfros, *Electronic Properties of Doped Semiconductors* (Nauka, Moscow, 1979; Springer-Verlag, New York, 1984).
10. B. L. Gel'mont and M. S. D'yakonov, Fiz. Tekh. Poluprovodn. (Leningrad) **5** (11), 2191 (1971) [Sov. Phys. Semicond. **5**, 1905 (1971)].
11. A. V. Lyubchenko, E. A. Sal'kov, and F. F. Sizov, in *Physical Basics of Semiconductor Quantum Photoelectronics* (Naukova Dumka, Kiev, 1984), p. 126.
12. L. Friedman, J. Non-Cryst. Solids **6**, 329 (1971).
13. J. M. Ziman, *Models of Disorder: the Theoretical Physics of Homogeneously Disordered Systems* (Cambridge Univ. Press, Cambridge, 1979; Mir, Moscow, 1982).

Translated by I. Kucherenko

Semiconductors, Vol. 35, No. 7, 2001, pp. 784–787. Translated from Fizika i Tekhnika Poluprovodnikov, Vol. 35, No. 7, 2001, pp. 819–822.

ELECTRONIC AND OPTICAL PROPERTIES OF SEMICONDUCTORS

Fermi Level Pinning and Electrical Properties of Irradiated $Cd_xHg_{1-x}Te$ Alloys

V. N. Brudnyĭ* and S. N. Grinyaev

Kuznetsov Physicotechnical Institute, Tomsk, 634050 Russia

** e-mail: brudnyi@ic.tsu.ru*

Submitted December 5, 2000; accepted for publication December 27, 2000

Abstract—The composition dependence of the local neutrality level E_{lnl} in $Cd_xHg_{1-x}Te$ alloys has been studied theoretically. It is shown that for compositions with $x < 0.47$ the E_{lnl} level lies within the conduction band, and at $x > 0.47$ it lies in the upper half of the band gap. The identification of the calculated E_{lnl} values with the limiting position of the Fermi level (F_{lim}) in $Cd_xHg_{1-x}Te$ irradiated with high-energy particles suggests that irradiation is responsible for the n^+- or n-type conduction in the material. © *2001 MAIK "Nauka/Interperiodica".*

INTRODUCTION

Solid solutions of $Cd_xHg_{1-x}Te$ allow wide variation of the energy gap (from 0 to 1.6 eV) by changing the composition X at a virtually unchanged lattice constant. It is this property that has made these compounds the focus of intensive experimental and theoretical studies, especially in optoelectronics.

According to modern data, the electrical, optical, and recombination characteristics of $Cd_xHg_{1-x}Te$ mainly depend on whether or not structural defects—growth dislocations, low-angle boundaries, and clusters of intrinsic defects and point defects (vacancies, antisite defects)—are present in the lattice. Nominally undoped crystals generally show p-type conduction, which is commonly attributed to the acceptor states related to Hg vacancies. Therefore, one of the problems of physics and technology is to gain control over the ensemble and concentration of intrinsic defects in $Cd_xHg_{1-x}Te$. This is commonly done by various methods: growth of the material under controlled partial pressures of components of the gas phase, homogenizing annealing of the material in Hg vapor, chemical doping of the melt, etc., and also by various high-energy treatments (electron or ion bombardment, laser irradiation, plastic deformation, ultrasonic processing, hydrostatic compression, etc.). This allows a certain extent of control over the ensemble of structural imperfections to obtain a material with prescribed properties.

In this study, a vast body of experimental data concerning the effect of irradiation with high-energy particles (electrons and ions) on the electrical properties of $Cd_xHg_{1-x}Te$ alloys is analyzed on the basis of theoretical investigations.

RESULTS AND DISCUSSION

Despite numerous experimental studies, from the very first investigations to the most recent ones, it remains unclear why high-energy irradiation (bombardment with electrons or ions at varied temperature) leads to the formation of regions with n-type conduction (n^+ at low Cd concentrations and n-type otherwise) in $Cd_xHg_{1-x}Te$ (see, e.g., [1–4]). This behavior of the material upon exposure to high-energy radiation is used to change its electrical properties, obtain n-type conduction, and create p–n junctions by means of ion bombardment.

Commonly, such behavior of $Cd_xHg_{1-x}Te$ under high-energy irradiation is attributed to the specificity of formation and accumulation of defects in the given material and, in particular, to the preferential formation of intrinsic lattice defects of donor type. As shown below, the n-type of conduction of irradiated $Cd_xHg_{1-x}Te$ samples is determined by the specific electronic structure of the material and changes in this structure on varying the composition of the solid solution, rather than by the characteristic type of the introduced radiation defects.

Our previous investigations concerned with diamond-like semiconductors and III–V binary compounds have shown that the electrical properties of irradiated materials can be analyzed and described in terms of the local electroneutrality concept. This concept was intensively developed as applied to investigations of the metal–semiconductor interfaces [5], and has been used recently in analyzing the electrical properties of irradiated bulk semiconductors [6].

In accordance with experimental data, high-energy irradiation of a semiconductor always leads, irrespective of the irradiation conditions and history of the

material, to Fermi level pinning in the limiting state (steady-state) F_{lim} specific to each particular crystal [6, 7]. Since the electrical properties of a material (conduction type, free carrier concentration) are determined by the position of the Fermi level with respect to the band gap edges, this, in turn, governs the electronic properties of the irradiated material. It has also been shown that the stationary position of the Fermi level in an irradiated semiconductor coincides with the local electroneutrality level E_{lnl} of the crystal, which can be calculated theoretically. This makes it possible to evaluate the expected stationary position of the Fermi level $F_{\text{lim}}(E_{\text{lnl}})$ in the irradiated material, and, thereby, not only analyze the experimental results, but also calculate in advance the expected electrical parameters of the irradiated semiconductor.

The present study is devoted to a theoretical analysis of how the position of the local electroneutrality level E_{lnl} depends on the temperature and composition of $Cd_xHg_{1-x}Te$ alloys. E_{lnl} is calculated using the analytical expression [5]

$$\left|\sum_{c\mathbf{k}}\frac{\exp(i\mathbf{kR})}{(E_{c\mathbf{k}}-E_{\text{lnl}})}\right| = \left|\sum_{v\mathbf{k}}\frac{\exp(i\mathbf{kR})}{(E_{v\mathbf{k}}-E_{\text{lnl}})}\right|,$$

used in our previous studies in similar calculations of the E_{lnl} value for solid solutions of III–V semiconductors. Here $E_{c\mathbf{k}}(E_{v\mathbf{k}})$ are the energy eigenvalues for conduction (valence) bands, $\mathbf{k}$ is the wave vector, and $\mathbf{R}$ is the lattice radius vector.

This expression, derived as a generalization to the three-dimensional case of the relation between the E_{lnl} level and the branching point of the complex band structure of a one-dimensional crystal, gives good agreement, as regards the $F_{\text{lim}} \cong E_{\text{lnl}}$ values, with experimental data for irradiated III–V semiconductors and solid solutions on their base. The E_{lnl} value was estimated in [5] for a number of semiconductors on the basis of a band structure obtained using the augmented plane wave method yielding rather inaccurate $E_{c\mathbf{k}}(E_{v\mathbf{k}})$ values. Therefore, it was of interest to calculate the E_{lnl} for the $Cd_xHg_{1-x}Te$ solid solution by a technique describing more adequately the band structure of the crystal.

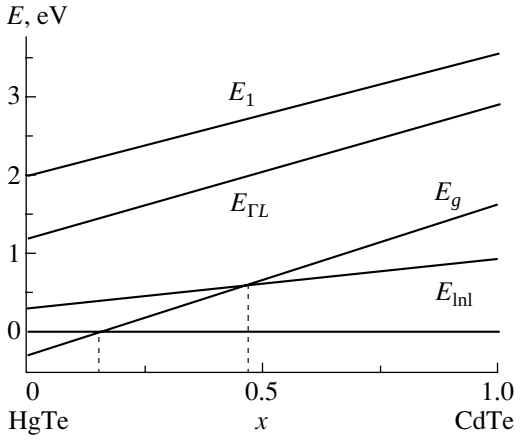

Fig. 1. Calculated composition dependence of the band gaps $\Gamma_6^c - \Gamma_8^v = E_g$, $L_c^c - L_6^v = E_{\Gamma L}$, and $L_6^c - L_{4,5}^v = E_1$ and the position of the local electroneutrality level E_{lnl} (relative to Γ_8^v level) in $Cd_xHg_{1-x}Te$ (T = 0 K).

In this study, the band structure of the $Cd_xHg_{1-x}Te$ alloy was calculated using the method of the transferable model pseudopotential which is efficient as regards the completeness and accuracy of the data obtained on the electronic structure of a crystal. The method was described in detail in [9], and we only mention here that, compared with [9], nonlocal corrections to the pseudopotential were additionally taken into account, which allowed a better agreement of the interband optical transition energies with the experimental data.

Taken together with reliable experimental data, the calculated quantitative parameters of some band gaps for boundary compositions of the $Cd_xHg_{1-x}Te$ solid solution confirm the high quality of the band structure of the materials, used in estimating E_{lnl} (see the table).

Calculated and experimental values of selected band gaps for boundary compositions of the $Cd_xHg_{1-x}Te$ alloy, used in evaluating $E_{\text{lnl}}(x)$, T = 0 K

Material	Band gaps, eV							
	Γ_6^c–Γ_8^v E_g	Γ_7^c–Γ_8^v E_0'	L_6^c–$L_{4,5}^v$ E_1	X_6^c–Γ_8^v $E_{\Gamma X}$	L_6^c–Γ_8^v $E_{\Gamma L}$	X_6^c–X_7^v E_2	Γ_8^v–Γ_7^v Δ_0	$L_{4,5}^v$–L_6^v Δ_1
HgTe Calculation	–0.29	4.08	2.01	2.47	1.23	4.51	0.94	0.64
Experiment	–0.30 [14]	4.10 [13]	2.15 [10]			4.47 [10]	1.08 [12]	0.63 [10]
CdTe Calculation	1.58	5.46	3.64	3.41	2.88	5.11	0.89	0.54
Experiment	1.60 [15]	5.20 [13]	3.29 [10]			5.07 [10]	0.90 [11]	0.58 [10]

Note: The experimental data were taken from references indicated at the figures.

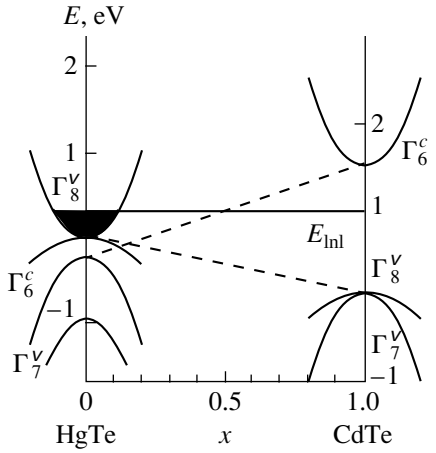

Fig. 2. Positions of the levels Γ_6^c, Γ_7^v, and Γ_8^v relative to the local electroneutrality level E_{lnl} vs. the Cd content x in the $Cd_xHg_{1-x}Te$ alloy ($T = 0$ K).

A calculated composition dependence of the first interband transitions in $Cd_xHg_{1-x}Te$ is presented in Fig. 1. It is noteworthy that the concentration dependence of the band gap in $Cd_xHg_{1-x}Te$, studied in [16] using the tight-binding technique with account of chemical disordering effects, reveals a weak nonlinearity of the band gap of $Cd_xHg_{1-x}Te$ as a function of the composition (x). This nonlinearity is associated with disorder in the substitution of atoms in the cation sublattice, which is due to the closeness of Cd and Te potentials. These investigations are confirmed by experimental data concerning the dependence of the gap ($\Gamma_6^c - \Gamma_8^v$) on the alloy composition at $T = 2$ K [17]. This allows the application of the virtual crystal approximation to calculating the band gaps in $Cd_xHg_{1-x}Te$.

The calculated band gaps of the alloy are in good agreement with the experimental data. For example, the critical concentration of transition to a zero-gap material ($x_c \cong 0.14$) is close to the published data. The composition dependences obtained of the lowest energy direct ($\Gamma_6^c - \Gamma_8^v$), ($L_6^c - L_{4,5}^v$) and nondirect ($L_c^c - \Gamma_8^v$) transitions are practically linear (Fig. 1).

The E_{lnl} values were calculated for various solid solution compositions by the special (10) point method [18] with account of 100 spin wave functions. The following calculated values were obtained (for $T = 0$ K): E_{lnl} (HgTe) = E_v + 0.32 eV and E_{lnl} (CdTe) = E_v + 0.98 eV, with the dependence on composition, $E_{lnl}(x)$, being nearly linear. The calculated composition dependences of the energy positions of the levels Γ_8^v, Γ_6^c, and Γ_7^y with respect to the local electroneutrality level E_{lnl} are presented in Fig. 2. These dependences can be used to analyze and prognosticate the electronic properties of irradiated $Cd_xHg_{1-x}Te$. Indeed, according to the data presented, the Fermi level in irradiated $Cd_xHg_{1-x}Te$ is pinned in the conduction band at $x \le 0.47$, which corresponds to an n^+-type material, and in the upper half of the band gap at $x > 0.47$, which corresponds to an n-type material. These calculations are confirmed by numerous experimental studies of irradiated $Cd_xHg_{1-x}Te$, e.g., [1–4].

Thus, the results of numerical estimates of the position of the level $E_{lnl}(x) \cong (F_{lim}(x))$ show that the n-type conduction of $Cd_xHg_{1-x}Te$ samples irradiated with high-energy particles is determined not by the nature of introduced defects, but rather by specific features of the electronic structure of the given material and changes in this structure upon varying the composition of the solid solution. Although the type of defects introduced into the lattice may depend on the prehistory of the material and the conditions of its irradiation, the processes of defect accumulation in the crystal occur so as to ensure the evolution of the Fermi level toward E_{lnl} and its pinning in this position at a radiation defect density exceeding that of dopants or growth defects. The critical doses necessary for the Fermi level to reach its stationary position are determined by the initial doping level of the material.

In this case, the electroneutrality equation for an irradiated material in which the Fermi level is pinned at E_{lnl} can be written as

$$n_{st}(x) + \sum_j N_j^-(x) \cong p_{st}(x) + \sum_i N_i^+(x),$$

where $n_{st}(x)$ and $p_{st}(x)$ are the steady-state concentrations of free electrons and holes in the irradiated material; $\sum_j N_j^-(x)$ and $\sum_i N_i^+(x)$ are the concentrations of charged acceptors (j) and donors (i). Here we disregard the initial chemical impurities and growth defects under the conditions when the density of radiation defects in the material exceeds that of the initial dopants or growth defects. As in the case of irradiated diamond-like semiconductors and III–V compounds, the stabilization of the Fermi level in $Cd_xHg_{1-x}Te$ upon radiation treatment must be ensured by the simultaneous introduction of donor and acceptor radiation defects. This issue has been studied in detail for InAs in which irradiation leads to Fermi level pinning within the conduction band, as in the case of $Cd_xHg_{1-x}Te$ with $x < 0.47$. For the compositions with $x > 0.47$, corresponding to Fermi level pinning in the band gap, similar investigations have been carried out for GaAs [19, 20]. This means that it is the difference in concentration of charged donors and acceptors of radiation origin in an irradiated $Cd_xHg_{1-x}Te$ solid solution that determines the stationary concentration of free electrons and predetermines the n-type conduction of this material.

CONCLUSION

High-energy irradiation leads to pinning of the Fermi level at the local electroneutrality level of the $Cd_xHg_{1-x}Te$ solid solution, which corresponds to its position within the conduction band for compositions with $x < 0.47$ and in the upper half of the band gap for other compositions and predetermines, respectively, an n^+- or n-type of the irradiated material. The effect of the radiation treatment is manifested in the compensation of the initial conductivity of the material. The electronic properties of irradiated $Cd_xHg_{1-x}Te$ are governed by the minimum energy gap between $E_{lnl}(x) \cong (F_{lim}(x))$ and the closest extremum in the energy spectrum of the ideal crystal and change, on varying the solution composition, from n^+-type conduction in the case of the boundary composition HgTe to high-resistivity n-type samples in the case of CdTe.

ACKNOWLEDGMENTS

This study was supported in part by the Ministry of Education of the Russian Federation, Program "Basic Research in Nuclear Technology and Physics of Ionizing Radiation Beams," (grant no. 97-12-9, 2-2).

REFERENCES

1. J. Meingailis, J. L. Ryan, and T. C. Herman, Appl. Phys. Lett. **44**, 2647 (1973).
2. V. N. Brudnyĭ, A. V. Voĭtsekhovskiĭ, Z. G. Grechukh, *et al.*, Fiz. Tekh. Poluprovodn. (Leningrad) **11**, 1540 (1977) [Sov. Phys. Semicond. **11**, 905 (1977)].
3. A. V. Voĭtsekhovskiĭ, A. G. Korotaev, and A. P. Kokhanenko, Fiz. Tekh. Poluprovodn. (St. Petersburg) **30**, 1565 (1996) [Semiconductors **30**, 821 (1996)].
4. A. V. Voĭtsekhovskiĭ and A. P. Kokhanenko, Izv. Tomsk. Politekh. Univ. **3** (2), 104 (2000).
5. J. Tersoff, Surf. Sci. **168**, 275 (1986).
6. V. N. Brudnyi, S. N. Grinyaev, and V. E. Stepanov, Physica B (Amsterdam) **212**, 429 (1995).
7. V. N. Brudnyĭ, Izv. Vyssh. Uchebn. Zaved., Fiz. **29** (8), 84 (1986).
8. V. N. Brudnyĭ and S. N. Grinyaev, Fiz. Tekh. Poluprovodn. (St. Petersburg) **32**, 315 (1998) [Semiconductors **32**, 284 (1998)].
9. S. N. Grinyaev and S. G. Kataev, Physica B (Amsterdam) **191**, 317 (1993).
10. L. Vina, C. Umbach, M. Cardona, *et al.*, Phys. Rev. B **29**, 6752 (1984).
11. D. T. Marple and H. Ehrenreich, Phys. Rev. Lett. **8**, 87 (1962).
12. P. M. Amirtharaj, F. H. Pollak, and J. K. Furduna, Solid State Commun. **39**, 35 (1981).
13. Shin-ichi Katsuki and Manoto Kunimune, J. Phys. Soc. Jpn. **31**, 337 (1971).
14. J. Guldner, C. Rigaux, M. Gnynberg, and A. Mycielski, Phys. Rev. B **8**, 3875 (1973).
15. M. Nawrocki and A. Twardowski, Phys. Status Solidi B **97**, K61 (1980).
16. K. C. Hass, H. Ehrenreich, and B. Velerhy, Phys. Rev. B **27**, 1088 (1983).
17. J. Camassel, J. P. Laurenti, A. Bouhemadou, *et al.*, Phys. Rev. B **38**, 3948 (1988).
18. D. J. Chadi and M. L. Cohen, Phys. Rev. **8**, 5747 (1973).
19. N. G. Kolin, V. B. Osvenskiĭ, N. S. Rytova, and U. S. Yurova, Fiz. Tekh. Poluprovodn. (Leningrad) **21**, 521 (1987) [Sov. Phys. Semicond. **21**, 320 (1987)].
20. V. N. Brudnyi and V. M. Diamond, Solid State Commun. **54**, 355 (1985).

Translated by M. Tagirdzhanov

Semiconductors, Vol. 35, No. 7, 2001, pp. 788–795. Translated from Fizika i Tekhnika Poluprovodnikov, Vol. 35, No. 7, 2001, pp. 823–830.

SEMICONDUCTOR STRUCTURES, INTERFACES, AND SURFACES

Effect of Ballistic Electron Transport in Metal–*n*-GaAs–*n*$^+$-GaAs Schottky-Barrier Structures

N. A. Torkhov

Research Institute of Semiconductors, Tomsk, 634045 Russia

e-mail: tna@ic.tsu.ru

Submitted December 29, 2000; accepted for publication January 10, 2001

Abstract—The interaction of an electron with the potential formed at the Schottky-barrier metal–semiconductor contact was investigated under the assumption that the motion is ballistic. Three cases of interaction of the electron with the barrier potential were considered; i.e., strong and weak interactions and above-barrier transport. It is demonstrated that the interaction of the electron with the above-barrier region substantially affects the scattering process for all three cases, which manifests itself in the behavior of steady-state current–voltage characteristics. Based on the model suggested, it is predicted that reverse currents increase as the width of the diode's thin (~0.35 μm) base increases. This prediction is verified and confirmed experimentally. It is found that an increase in reverse current is related to the increasing influence of a strong electric field on the moving carriers as the width of the thin base increases. © *2001 MAIK "Nauka/Interperiodica".*

INTRODUCTION

When calculating the forward and reverse steady-state current–voltage (*I–V*) characteristics of Schottky-barrier (SB) diodes, the theory of thermal electron emission and carrier tunneling (the theory of thermal–field emission) is currently used [1–11]. The theory of thermal–field emission was later extended to SBs with nonuniform impurity distribution in the semiconductor [12–14]. In this case, the parameters of tunneling through the barrier (probability $T(E)$ and transit time $t(E)$) were calculated disregarding the mechanisms of interaction of a charged particle with the potential, particularly with the above-barrier region [9]. As was pointed out [15, 16], this leads to an inaccurate description of scattering and to errors in the calculation of the parameters of tunneling through the barrier. This is especially noticeable when calculating the reverse-bias regions of steady-state *I–V* characteristics of SB diodes. Therefore, it is interesting to investigate the interaction of the electron with the potential formed at the SB metal–semiconductor (MS) contact while simultaneously considering tunneling and above-barrier transit.

The interaction of an electron with the potential formed at the SB MS contact was investigated by studying the behavior of the electron wave function in the potential region, and the reverse *I–V* characteristics were calculated for the case of uniform impurity distribution in the semiconductor. It was demonstrated that the effect of the above-barrier region leads to an increase in reverse currents (a decrease in reverse voltages) as the width of the diode base increases. The results of calculations are in reasonably good agreement with the experimental data.

CALCULATION PROCEDURE

In order to investigate the interaction of an electron with the potential according to the model suggested recently [15], we assume that the electron, which passes through a thin *n*-diode base with thickness *W*, does not interact with any defects in the base region. In this case, scattering occurs only at the potential formed by the SB MS contact; i.e., the following condition is satisfied:

$$l^* \geq W. \quad (1)$$

Here, l^* is the free path length for precisely such (hot) electrons.

In order to carry out the calculations, the barrier potential $\varphi(x)$, where $x \in [0; W]$, which is shown in Fig. 1, was divided into N rectangular potential barriers (RPBs). Electron wave functions $\Psi(x, E)$ were calculated for each RPB [17] and were plotted as the functions $\Psi_1(x)$, $\Psi_2(x)$, and $\Psi_3(x)$ for electron energy E = 0.5, 0.79, and 0.95 eV, respectively. In order to obtain the parameters for transit through the system of RPBs, an exact calculation in the context of the transfer-matrix method was used [17–19]. In contrast to [9], where the transport-matrix method was used to describe tunneling for subbarrier transit only, the transfer-matrix method used in this study is absolutely convergent. The absolute convergence is achieved by the choice of the transfer matrix characterizing the electron transit through a single RPB rather than through adjoining regions, as in [9]. As was demonstrated previously [17, 18], the form of this matrix is independent of the procedure of specifying the potential, which makes this technique convenient to implement using a computer. It was demonstrated [17–19] that in order to find the

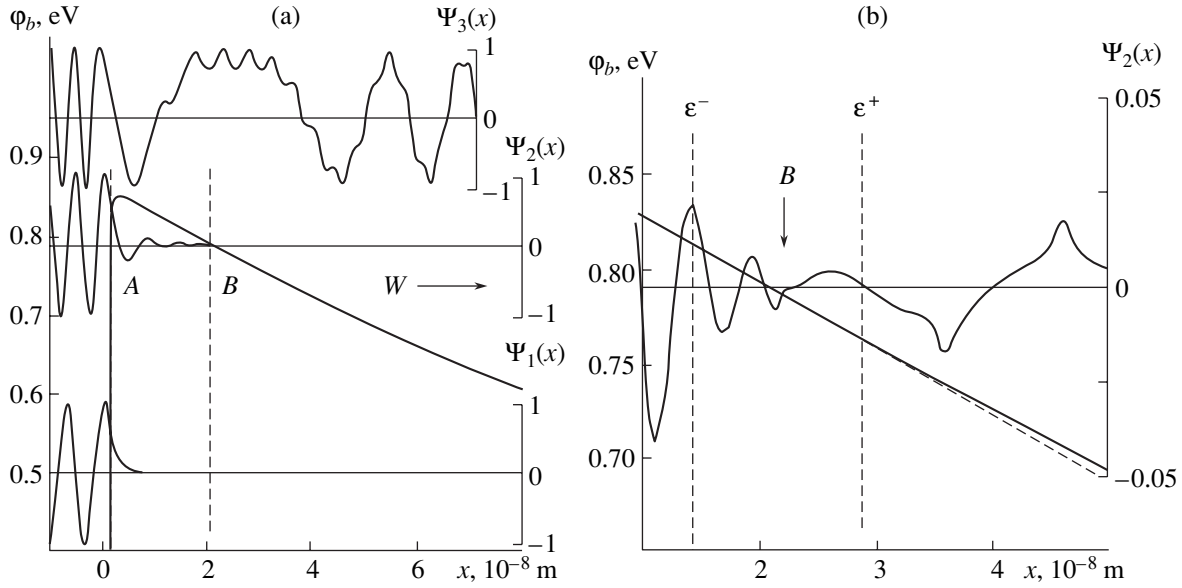

Fig. 1. (a) Potential $\varphi_b(x)$ formed by the Schottky-barrier metal–semiconductor contact with regard to image forces in the absence of the external electric field ($U = 0$), and the electron wave functions in the potential region, with the electron function propagating from the left to the right (⟶): $\Psi_1(x, E)$ for electron energy $E = 0.5$ eV, $\Psi_2(x, E)$ for $E = 0.79$ eV, and $\Psi_3(x, E)$ for $E = 0.95$ eV. The potential and electron wave functions are shown in the spatial range from $x = -10^{-8}$ m to $x = 8 \times 10^{-8}$ m. (b) Detailed representation of $\varphi_b(x)$ and wave function $\Psi_2(x, E)$ for $E = 0.79$ eV in the vicinity ε of point *B*; the dashed curve is the tangent to point *B*.

parameters of transit through the system of RPBs, it is possible to use recursive relations. These relations allow the calculation of tunneling parameters with any required degree of accuracy, which is determined by the number of partitions of the potential $\varphi(x)$.

The potential $\varphi(x)$ was found from the numerical solution of the Poisson equation with regard to image forces. The energy origin was the Fermi level in metal for $U_r < 0$, and in semiconductors for $U_f > 0$, where U_f and U_r are the forward and reverse bias applied to the SB, respectively.

In order to calculate the steady-state *I–V* characteristics of SB diodes, the analytical expression [4] was used; i.e.,

$$J(E) = \frac{4\pi q m^* kT}{\hbar^3} \times \int_0^\infty T(E) \ln\left[\frac{1 + \exp[(E_F - E)/kT]}{1 + \exp[(E_F - E - qU)/kT]}\right] dE, \quad (2)$$

where q is the elementary charge, m^* is the electron effective mass, k is the Boltzmann constant, T is the temperature, $\hbar$ is the Planck constant, $T(E)$ is the tunneling probability, E_F is the Fermi level, E is the electron energy, and U is the voltage drop.

EXPERIMENTAL

An n–n^+ semiconductor structure (sample) in a wafer form was used in the experiments. A *n*-GaAs:Sn epilayer (base) about 0.85 μm thick was grown on the n^+-GaAs:Te (100)-oriented substrate. The charge carrier concentrations in the epilayer and substrate were ~2.5×10^{16} and ~2×10^{18} cm^{-3}, respectively. On the substrate side, a nonrectifying contact was formed by the electrochemical deposition of GeNi + Au with subsequent annealing in a N_2 atmosphere at 450°C for 5 min. Regions with $W = 0.85$, 0.62, and 0.35 μm were subsequently formed on the epilayer side. Thus, three regions having a different base thickness W were formed on a single chip. The epilayer surface was then treated with an ammonia solution $NH_3OH : H_2O = 1 : 5$ to remove the native oxide. As was shown previously [20], the surface of the *n*-GaAs epilayer treated in an ammonia solution acquires the periodic structure 4×2, which is indicative of a good surface quality. Ellipsometric investigations were carried out immediately after sample treatment in an ammonia solution. It was demonstrated that the thickness of the surface layer with the dielectric constant ε, which was different from the ε value in the bulk, was no greater than 7–10 Å. It is possible that this layer is related to the surface reconstruction.

Barrier contacts 325 μm in diameter were formed by electrochemical deposition of a Au film 0.3 μm thick on the *n*-epilayer surface using conventional technology. Deposition was carried out through the photoresist windows with the subsequent removal of the photoresist. The mesas were then formed by etching off the material along the periphery of a contact to a depth of 1 μm. This

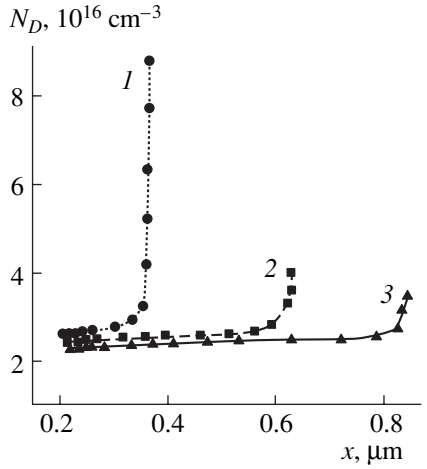

Fig. 2. Concentration profiles of the ionized shallow-donor impurity $N_D(x)$ for the Au–n–n^+-GaAs structures with the thickness W = (*1*) 0.35, (*2*) 0.62, and (*3*) 0.85 μm.

was done in order to weaken the influence of the periphery on the electrical characteristics of diodes.

The SB height was determined from the capacitance–voltage (C–V) characteristics at a frequency of 1 MHz and, for comparison, from the saturation current of the I–V characteristics. The C–V and I–V characteristics of SBs were measured at 295°C directly on the wafers. The SB heights obtained by the two independent techniques are practically identical.

The concentration profiles of the ionized shallow-donor impurity $N_D(x)$ along the base thickness for three regions having different W values were obtained from the C–V characteristics (Fig. 2). The effective base width and impurity concentration N_D were estimated from the concentration profiles. Based on the experimental data obtained, the dopant concentration in the n-layer N_D for the calculation of steady-state I–V characteristics of the SB diodes was assumed to be equal to 2.5×10^{16} cm^{-3}. The thickness of n epilayers W was taken equal to 0.85, 0.62, or 0.35 μm. The potential barrier height φ_{b0} at 295°C with regard to image forces was taken equal to 0.841 eV.

The parameters of transit through the barrier were calculated in an energy range from 0 to 1 eV. The number of potential partitions N was equal to 650 points along the spatial coordinate and to 600 according to energy. The correctness of the program execution was verified by calculating the tunneling probability $T(E)$ and transit time $t(E)$ for superlattices [21, 22].

RESULTS AND DISCUSSION

Let us consider an electron with energy E = 0.79 eV, which moves from left to right and impinges on the potential $\varphi(x)$ from the left (Fig. 1). Let B be the escape point for an electron with energy E = 0.79 eV from the subbarrier region AB (Fig. 1, $\Psi_2(x)$). Consider the ε-vicinity of point B—$]\varepsilon^-; \varepsilon^+[$ (Fig. 1b). We refer to the region $]\varepsilon^-; B[$ as the left-sided neighborhood of point B, and $]B; \varepsilon^+[$, as the right-sided neighborhood. It can be seen from Fig. 1b that the slope of $\varphi(x)$ in the vicinity of point B varies only slightly. Hence, it follows that the electric field strengths to the right and left of the point under consideration are practically identical and are determined by the tangent (dashed line) to this point:

$$\lim_{x \to B} \frac{\partial \varphi(x)}{\partial x} = \text{const}. \qquad (3)$$

Let us consider the behavior of the electron wave function in the vicinity of point B. Directly at point B, the electron wave function should be continuous; i.e., the joining conditions for wave functions should be satisfied [17–19]. We consider three cases of interaction of the electron with the potential formed by the SB MS contact by monitoring the behavior of its wave function.

The first case is related to the strong interaction of the electron with the potential. This case is characteristic of low electron energies, for which the SB width (range AB) exceeds the electron wavelength. As can be seen from Fig. 1a, the electron wave function $\Psi_1(x)$ undergoes strong variations. While penetrating into the subbarrier region, it transforms from the harmonic function to the exponentially decaying function of the coordinate. It can be seen that even at a distance of about 10^{-8} m, the amplitude of $\Psi_1(x)$ decays practically to zero. According to calculations, the tunneling probability T is very low in this case. It is clear that such electrons make a negligibly small contribution to the current flow through the device.

The second case is related to the weak interaction of the electron with the potential. This case is characteristic of electrons with energies that are below or equal to the potential barrier height φ_{b0}. No violations of the oscillatory behavior are observed for wave functions $\Psi_2(x)$ characteristic of the electrons of this type within the subbarrier region. This is indicative of a weaker interaction of the electron with the potential for such energies. In this case, the decrease in the amplitude of $\Psi_2(x)$ is small, whereas the $T(E)$ quantity tends to unity. It is evident that these electrons contribute significantly to the current flow through the device. In this case, two portions with substantially different behavior may be recognized in the $\Psi_2(x)$ dependence (Fig. 1b). These portions are the exponentially decaying harmonic portion lying in the subbarrier region AB and the anharmonic oscillatory portion lying in the above-barrier region BW. As can be seen from Fig. 1b, the electron wave function in the above-barrier region is a complicated function of the coordinate, and this function may be unsuitable for the description of the wave process. The interaction between the electron and above-barrier region depends on the $\varphi(x)$ slope, i.e., on the electric field magnitude in the above-barrier region. Where the

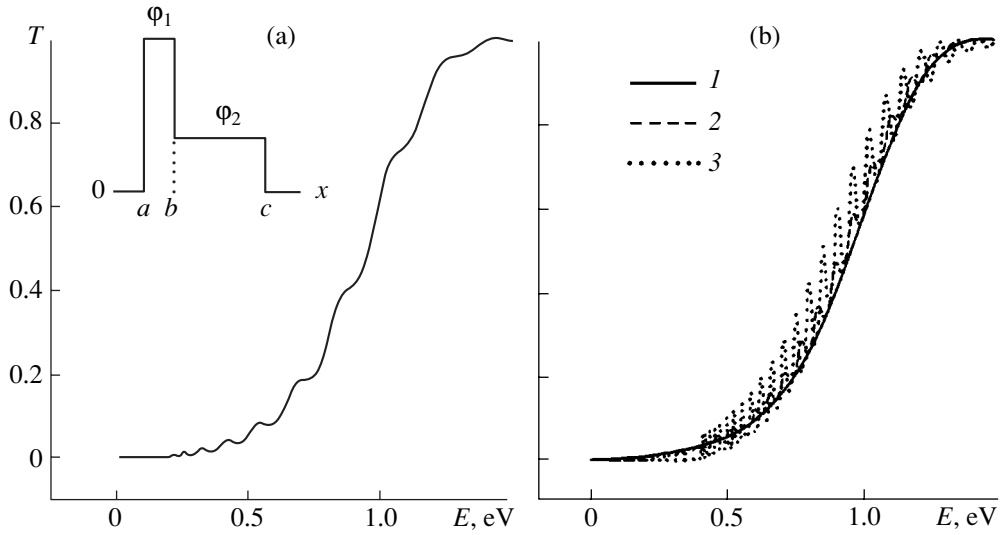

Fig. 3. Tunneling probability $T(E)$ for the model barrier (see inset). Calculation parameters: $\varphi_1 = 0.8$ eV, the extent of the *ab* region is equal to 3 nm; for $T(E)$ dependence in Fig. 3a: *bc* region amounts to 20 nm, $\varphi_2 = 0.2$ eV; for curves (*1*–*3*) in Fig. 3b: *bc* region extent is 60 nm, $\varphi_2 =$ (*1*) 0, (*2*) 0.2, and (*3*) 0.6 eV.

field is strong, for example, in the space-charge region (SCR), the harmonicity of $\Psi(x)$ oscillations is disturbed strongly, and the oscillations are randomized. $\Psi(x)$ oscillations become harmonic again only with escape from the SCR, when the electric field effect decreases considerably.

The third case is related to the above-barrier transit, when the electron energy exceeds the potential barrier height φ_{b0}. In this case, the electron does not penetrate into the subbarrier region at all, but passes strictly through the thin *n*-base above the potential barrier. This case is also related to the specific features in the electron motion. Since the amplitude of $\Psi_3(x)$ varies weakly over the entire *n*-base length, one may assume that the electron undergoes weak interaction with the potential when it passes through the space-charge region (SCR). On the other hand, as can be seen from Fig. 1a, the behavior of $\Psi_3(x)$ varies substantially in the SCR, specifically, oscillations of $\Psi_3(x)$ are randomized. Similarly to the second case, $\Psi_3(x)$ oscillations become harmonic again only with escape from the SCR. Because of their low concentration, the contribution of these electrons to the current flow through the device is small.

The influence of interaction of an electron with the above-barrier region on scattering by the potential formed at the SB MS contact may be conveniently illustrated for the model barrier. Let us model the potential $\varphi(x)$ by two SB RPBs of height $\varphi_1 = 0.8$ eV and $\varphi_2 = 0.2$ eV with a zero distance between them, as is shown in the inset to Fig. 3a. Let us assume that the widths of the first and second RPBs are equal to 30 and 200 Å, respectively. The shape of the $T(E)$ dependence for this case is shown in Fig. 3a. The appearance of oscillations of $T(E)$, as it is easy to verify, is related to the occurrence of the above-barrier region with electron transit through the *ac* region. It can be seen that, for the energy range from 0 to 0.2 eV, when the electron moves in the subbarrier region only, the $T(E)$ dependence is monotonic. As the energy of the incident wave increases above 0.2 eV, any electron that passes through the *ac* region encounters the *bc* region along its path. In this region, the electron moves above the potential barrier. In this case, oscillations appear in the $T(E)$ curve.

An increase in the extent of the *bc* region (Fig. 3b), in which the electron passes above the barrier φ_2, leads to an increase in the number of oscillations in the $T(E)$ curve. The oscillation amplitude does not vary in this case. A simulation demonstrated that the oscillation amplitude depends on the value of φ_2. A decrease in φ_2 leads to a decrease in the oscillation amplitude. For $\varphi_2 = 0$, the $T(E)$ dependence becomes monotonic (Fig. 3b). For the actual SB, subsequent to tunneling through the potential barrier, the electron begins to move in the above-barrier region. The width of this region should be rather large (thousands of angstroms), which should lead to the appearance of a large number of oscillations in the $T(E)$ dependence.

The $T(E)$ dependences of the diode structure with $W = 0.35$ μm for a zero bias and $U_f = 0.5$ V for a forward bias, which were calculated with and without regard to the effect of the above-barrier region, are shown in Fig. 4a. It can be seen that the allowance made for the interaction of charge carriers with the above-barrier region leads not only to the appearance of oscillations in the $T(E)$ curve, but also to a decrease in the tunneling probability. A similar situation also arises in the case of the reverse bias (Fig. 4b), with the only dif-

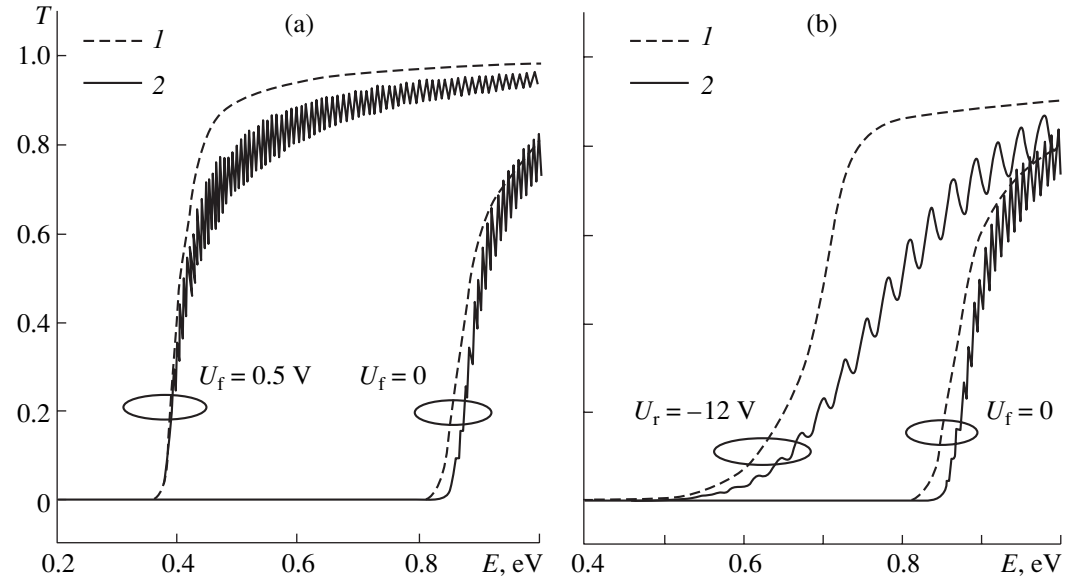

Fig. 4. Effect of the above-barrier region on the tunneling probability $T(E)$ for the Au–n–n^+-GaAs region with W = 0.35 μm: (a) for a forward bias voltage U_f = 0.5 V, (b) for a reverse bias voltage U_r = –12 V; $T(E)$ dependence: (*1*) with no regard to the effect of the above-barrier region and (*2*) with regard to its effect.

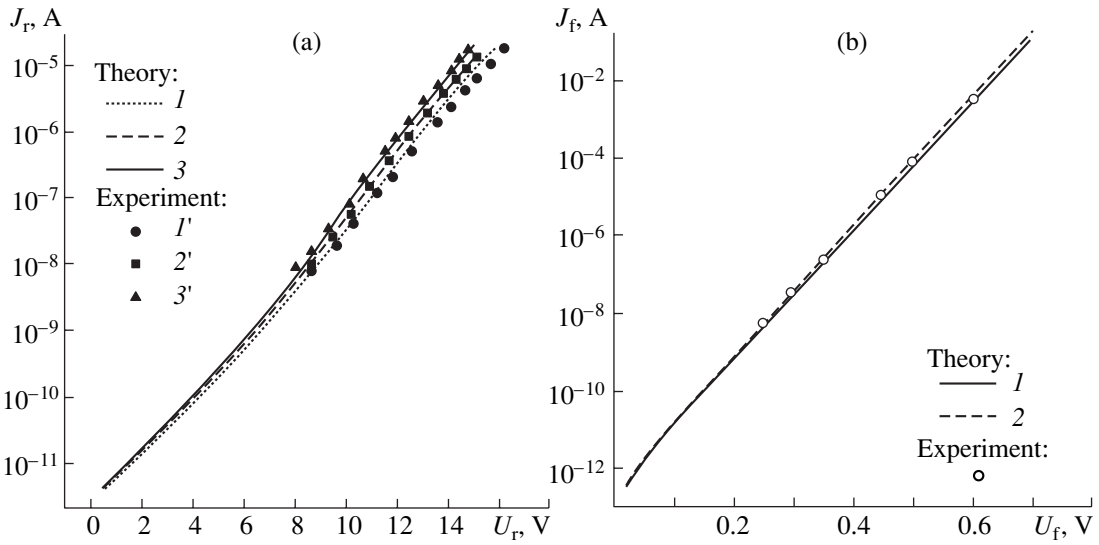

Fig. 5. Current–voltage characteristics: (a) reverse and (b) forward. (a) Base thickness W = (*1*, *1*') 0.35, (*2*, *2*') 0.62, and (*3*, *3*') 0.85 μm. (b) W = 0.35 μm, calculation: (*1*) with regard to the effect of the above-barrier region, and (*2*) with no regard to its effect.

ference being that the oscillation frequency in the $T(E)$ curve is lower.

As was demonstrated above, the allowance made for the effect of the above-barrier region leads to a considerable variation in transit parameters. It was reported [15] that the effect of the above-barrier region was taken into account when calculating the steady-state reverse *I–V* characteristics of the SB diodes by the transport-matrix method. In this case, the rate of increase in the reverse currents for voltages close to the breakdown voltage increases. The calculation of steady-state *I–V* characteristics for different values of the base thickness *W*, which was based on the model suggested recently [15] and was carried out in this paper by the transport-matrix method, demonstrates a considerable decrease in reverse currents with decreasing *W*. In this case, the experimental data agree reasonably well with the calculations (Fig. 5). The statistical analysis of the *I–V* characteristics of diodes, which were fabricated on a single chip, also confirmed the effect observed from calculations. The dependence of the number of diodes N on U_r (see Fig. 6) is described

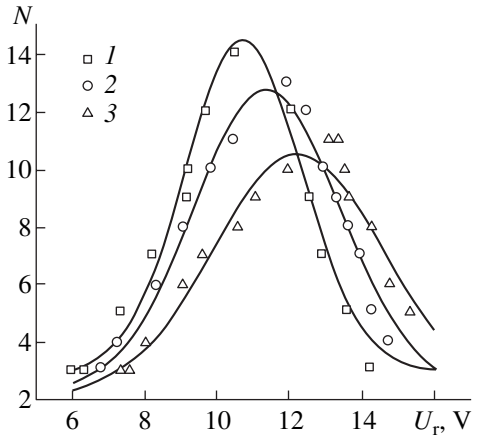

Fig. 6. Steady-state distribution of the magnitude N (the number of the Au–n–n^+-GaAs diodes arranged on a single substrate) as a function of the reverse voltage U_r measured for the current of 10 μA and the thickness W = (*1*) 0.85, (*2*) 0.62, and (*3*) 0.35 μm. Points are the experimental data, and curves are approximations by Gaussian functions. For statistics, 110 diode structures were selected in every case.

adequately by Gaussian functions. In this case, the peaks in the $N(U_r)$ curves shift to larger U_r with decreasing W.

The behavior observed for I–V characteristics with a decrease in W can be explained by analyzing the transit parameters for each individual case.

The phenomena observed for reverse I–V characteristics could not be explained by classical notions of the electron. Thus, according to the results obtained, an increase in W from 0.35 to 0.85 μm leads to an increase in transit time. From the classical concept, this should lead to an increase in the reverse currents, which is in contradiction with the experiment (Fig. 5). In contrast with this, according to the quantum-mechanical concept, a decrease in transit time is accompanied by an increase in the average tunneling probability (Figs. 7a, 7b). Superficially (according to the behavior of the I–V characteristics, Fig. 5), this manifests itself in an increase in reverse currents. An increase in transit time, as the investigations demonstrated, is related to the broadening of the region of a strong electric field, in which the electron passes above the potential barrier. This enhances the effect of the above-barrier region on the electron motion.

As can be seen from Fig. 7b, the $t(E)$ dependences are not monotonic. It should be noted that the peak (valley) values in the $t(E)$ curve correspond to the peak (valley) values in $T(E)$ curves; i.e., an increase (decrease) in T is accompanied by an increase (decrease) in the duration of electron transit through the region of $\varphi(x)$. This is in agreement with the known notions of the behavior of the phase-transit time [17]. As a result, we can conclude that the nonmonotonic behavior of both the $t(E)$ and $T(E)$ curves is determined by the presence of the above-barrier region.

For forward biases, the phenomena observed are consistent with conventional notions. A decrease in W leads to a decrease in transit time and an increase in tunneling probability (Fig. 8). For large forward biases, the region of the above-barrier electron transit increases considerably due to a decrease in the extent of the subbarrier region, which practically disappears. This

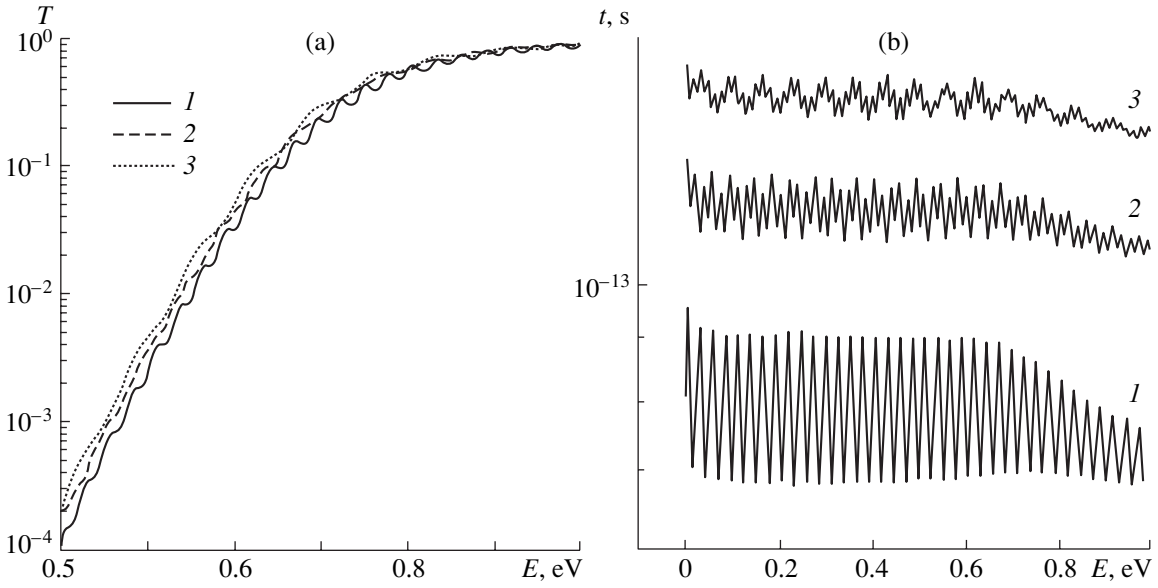

Fig. 7. (a) Tunneling probability $T(E)$ and (b) transit time $t(E)$ for a reverse bias U_r = –12 V across the structures with the base thickness W = (*1*) 0.35, (*2*) 0.62, and (*3*) 0.85 μm.

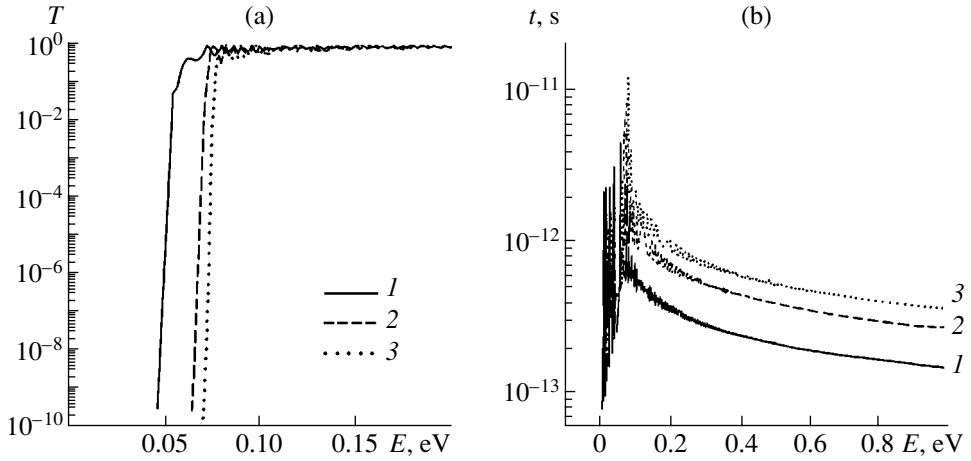

Fig. 8. (a) Tunneling probability $T(E)$ and (b) transition time $t(E)$ with the reverse bias $U_r = 0.5$ V for the structures with the base thickness W = (*1*) 0.35, (*2*) 0.62, and (*3*) 0.85 μm.

affects the $T(E)$ and $t(E)$ curves, specifically, the oscillation frequency increases considerably.

A sharp distinction in the behavior of the forward and reverse *I–V* characteristics in relation to the base thickness (especially in the region of large currents) is associated with broadening of the above-barrier region, in which the electric field is strong (the SCR). Thus, for reverse *I–V* characteristics, the electron moves in a very strong electric field. In addition, it should tunnel through the potential barrier, which cannot be described in the context of classical notions. For a forward bias, the situation is reversed; i.e., the electron moves in a weak field region, predominantly above the barrier. In this case, the electron motion can be described in the context of classical notions. We observe this behavior in both experimental and theoretical results.

The results of investigations in the transit time $t(E)$ in relation to the value of W are shown in Figs. 7b and 8b. It is known [23] that the energy relaxation time for intrinsic electrons in GaAs is about 10^{-12} s. According to calculations (Fig. 8b), the transit time of hot electrons for a forward bias $U_f = 0.5$ V in the energy range from 0.8 to 0.9 eV was no larger than 4×10^{-13} s. For a negative bias $U_r = -12$ V (Fig. 7b), it is no larger than 1.5×10^{-13} s. Thus, this confirms the assumption (inequality (1)) that the mean free path for hot electrons l (under a bias voltage) equals or exceeds the width $W \approx 0.82$ μm of the diode's thin base. This is because the electrons passing through the *n*-base have no time to lose their energy.

CONCLUSION

On the basis of the aforesaid, we may conclude that the charge transport through the region of the MS contact and diode thin base (*n*-GaAs layer $W < 1$ μm thick) can be described adequately in terms of quantum-mechanical tunneling. It is demonstrated in this paper that the model of charge transport in the SB MS contacts suggested recently [15] does not contradict existing notions. It allows the forward and reverse steady-state *I–V* characteristics to be described from a unified viewpoint for a wider bias range.

Using the behavior of the electron wave functions in the potential region as an example, the interaction of the electron with the potential formed by the SB MS contact was investigated for the first time. It was demonstrated that the interaction of the electron with the above-barrier region of the potential substantially affects the scattering process, which manifests itself in the behavior of steady-state current–voltage characteristics. Three cases of interaction of the electron with the barrier potential are considered; specifically, strong and weak interactions and above-barrier transit.

Based on the model suggested, it was predicted that reverse currents increase with increasing width of the diode's thin base, and this prediction was confirmed experimentally. It was demonstrated in this paper that an increase in the reverse current is related to an increase in the effect of the strong electric field on moving carriers with an increase in the extent of the above-barrier region.

REFERENCES

1. F. A. Padovani and R. Stratton, Solid-State Electron. **9**, 695 (1966).
2. K. Shenai and R. W. Dutton, IEEE Trans. Electron. Devices **35** (4), 468 (1988).
3. *Modern Semiconductor Device Physics*, Ed. by S. M. Sze (Wiley, New York, 1997).
4. M. I. Veksler, Fiz. Tekh. Poluprovodn. (St. Petersburg) **30** (9), 1718 (1996) [Semiconductors **30**, 899 (1996)].
5. V. N. Dobrovol'skiĭ, G. K. Nitsidze, and V. N. Petrusenko, Fiz. Tekh. Poluprovodn. (St. Petersburg) **28** (4), 651 (1994) [Semiconductors **28**, 390 (1994)].

6. J. Martinez, E. Calleja, and J. Piqueras, Phys. Status Solidi A **60**, 277 (1980).
7. J. Crofton and S. Sriram, IEEE Trans. Electron Devices **43** (12), 2305 (1996).
8. H. C. Card and E. H. Rhoderick, J. Phys. D **4**, 1589 (1971).
9. D. Mui, S. Strite, and H. Morkoc, Solid-State Electron. **34** (10), 1077 (1991).
10. V. L. Rideout and C. R. Crowell, Solid-State Electron. **13**, 993 (1970).
11. J. M. Andrews, J. Vac. Sci. Technol. **11**, 972 (1974).
12. M. É. Raĭkh and I. M. Ruzin, Fiz. Tekh. Poluprovodn. (Leningrad) **21**, 456 (1987) [Sov. Phys. Semicond. **21**, 283 (1987)].
13. T. A. Polyanskaya and Kh. G. Nazhmudinov, Fiz. Tekh. Poluprovodn. (Leningrad) **21**, 1737 (1987) [Sov. Phys. Semicond. **21**, 1053 (1987)].
14. M. É. Raĭkh and I. M. Ruzin, Zh. Éksp. Teor. Fiz. **92**, 2257 (1987) [Sov. Phys. JETP **65**, 1273 (1987)].
15. N. A. Torkhov and S. V. Eremeev, Fiz. Tekh. Poluprovodn. (St. Petersburg) **34** (1), 106 (2000) [Semiconductors **34**, 108 (2000)].
16. N. A. Torkhov, in *Proceedings of the 4th International Conference on Actual Problems of Electronic Instrument Engineering "APEIE-98", Novosibirsk, 1998*, Vol. 2, p. 217.
17. N. L. Chuprikov, Available from VINITI, No. 492-V91 (1991).
18. N. L. Chuprikov, Fiz. Tekh. Poluprovodn. (St. Petersburg) **30** (3), 443 (1996) [Semiconductors **30**, 246 (1996)].
19. N. L. Chuprikov, Fiz. Tekh. Poluprovodn. (St. Petersburg) **26** (12), 2040 (1992) [Sov. Phys. Semicond. **26**, 1147 (1992)].
20. N. A. Torkhov and V. G. Bozhkov, Available from VINITI, No. 313-V99 (1999).
21. L. Esaki, IEEE J. Quantum Electron. **22** (9), 1611 (1986).
22. S. D. Collins, D. Lowet, and J. R. Barker, J. Phys. C **20**, 6213 (1987).
23. V. L. Bonch-Bruevich and S. G. Kalashnikov, *Physics of Semiconductors* (Nauka, Moscow, 1990).

Translated by N. Korovin

Semiconductors, Vol. 35, No. 7, 2001, pp. 796–799. Translated from Fizika i Tekhnika Poluprovodnikov, Vol. 35, No. 7, 2001, pp. 831–834.

SEMICONDUCTOR STRUCTURES, INTERFACES, AND SURFACES

Calculation of the Variation in the Work Function Caused by Adsorption of Metal Atoms on Semiconductors

S. Yu. Davydov and A. V. Pavlyk

St. Petersburg State Electrotechnical University, St. Petersburg, 197376 Russia

Submitted October 26, 2000; accepted for publication November 22, 2000

Abstract—A simple model is suggested for calculating the variation of the work function $\Delta\phi$, which is caused by the adsorption of metal atoms on semiconductor surfaces. The model accounts for both the dipole–dipole repulsion of adatoms and metallization of the adsorbed layer for large coverages. The results of calculating $\Delta\phi$ for the adsorption of alkali metals on the Si(001) surface are in good agreement with the experimental data. *© 2001 MAIK "Nauka/Interperiodica".*

The work function is one of the most important characteristics of the adsorption system [1, 2]. Theoretically, the calculation of the variation in the work function $\Delta\phi$ with an increase in the surface coverage $\Theta = N_a/N_{ML}$, where N_a is the concentration of adsorbed atoms and N_{ML} is the concentration of adatoms in the monolayer (ML), is of great interest. This calculation allows the character of atomic interaction for the adsorbed layer to be established [3, 4].

In contrast with the adsorption of metals on metals [2, 5], systematic investigations of adsorption of metal on semiconductor crystals are relatively recent. Only the adsorption of alkali metals by the Si(001) surface has so far been studied adequately (see, for example, [6] and references therein). Investigations [7–15] demonstrated that the structure of submonolayer ($0 \le \Theta \le 1$) alkali metal films is rather complex and varies with an increase in Θ. Furthermore, the metal–insulator transitions along with the structural phase transitions occur in a system consisting of alkali metal and Si(001) [14]. However, in spite of this, the $\Delta\phi(\Theta)$ dependence is similar to that for the adsorption of alkali metals on refractory substrates (compare, for example, results [7, 8, 10, 12, 13] with the experimental data [2, 5]). For this reason, it is logical to use the approach that was developed for the adsorption of metals on metals [16–18] for semiconductor substrates as well [19, 20].

In this paper, a simple model suitable for calculating the $\Delta\phi(\Theta)$ dependence for a system consisting of alkali metal and Si(001) is suggested. The model ignores the details of the geometric parameters of the adsorbed layer and accounts for the variation in the surface concentration of adatoms only, i.e., the adsorbed layer density. We will simultaneously take into account that the adatom quasi-level Θ starts to broaden into a band due to both indirect [21] and direct [22] interaction between adatoms. This broadening can be taken into account by introducing the half-width of the quasi-level Γ, which depends on the coverage Θ:

$$\Gamma(\Theta) = \Gamma_0(1 + \gamma\Theta), \tag{1}$$

where γ is a dimensionless coefficient. We have already used this approach in order to take into account spreading of the quasi-level into the band [23, 24].[1]

Let us consider an atom, whose outer *s* shell is occupied by a single electron. As a result of adsorption, due to the possibility of electron transfer from the adatom to the substrate (or from the substrate to the adatom), the occupation number *n* becomes different from unity, and the adatom acquires the charge $Z = 1 - n$. The dependence of Z on the coverage Θ may be calculated from the formula [16–18, 20]

$$Z(\Theta) = \frac{2}{\pi}\arctan\frac{\Omega - \xi\Theta^{3/2}Z(\Theta)}{\Gamma(\Theta)}, \qquad \xi = 2e^2\lambda^2 N_{ML}^{3/2} A. \tag{2}$$

Here, Ω is the energy of the adatom quasi-level in reference to the Fermi level of the substrate, ξ is the constant of the dipole–dipole repulsion of adatoms, 2λ is the bond length of the surface dipole formed by the adsorbed adatom and its image in the substrate (we ignored the dielectric correction $(\varepsilon_0 - 1)/(\varepsilon_0 + 1)$, where ε_0 is the static dielectric constant), and $A \approx 10$ is a dimensionless coefficient dependent only slightly on the configuration of the lattice of adatoms.

[1] In adopting the structureless model of the adsorbed layer, we consider the adatom position as a random quantity. For this reason, we assume that the quasi-level broadens proportionally to a first power of coverage (see [23] for details).

1063-7826/01/3507-0796$21.00 © 2001 MAIK "Nauka/Interperiodica"

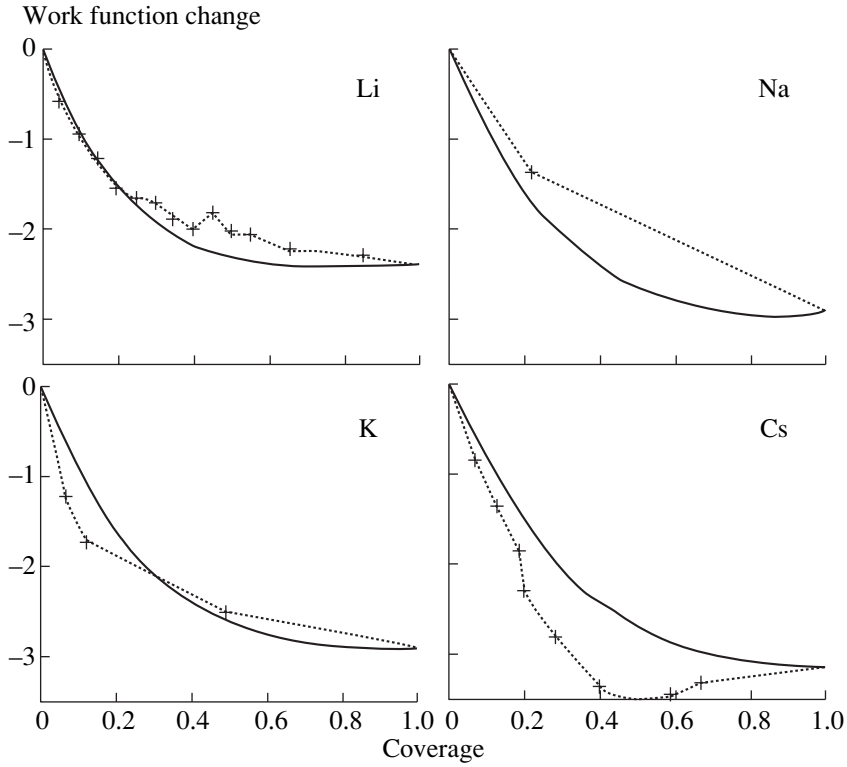

Variation of the work function against the coverage. Solid and dashed lines with crosses represent the results of calculations and experimental data, respectively.

The variation of the work function $\Delta\phi$ is defined by [2, 16, 17]

$$\Delta\phi(\Theta) = -\Phi\Theta Z, \quad \Phi = 4\pi e^2 N_{ML}\lambda. \tag{3}$$

The question of the determination of model parameters arises. For this purpose, we will use the experimental data and start with Li [10]. Let us take the half-sum of the ionic r_i and atomic r_a radii as the λ quantity: $\lambda = (r_i + r_a)/2$, which accounts for the fact that the charge of alkali metal adatoms is fractional. We assume that the coefficient A is equal to 10. We will consider that the coverage formed by a single monolayer amounts to 1 ML = 6.78×10^{14} cm^{-2} and is attained in an exposure time t_{ML} = 10 min (see Fig. 1 from [10]). Let us also assume that the coverage Θ is directly proportional to the exposure time t. Then, using the value $\Delta\phi(\Theta = 0.1) \approx$ 1 eV (for t = 1 min) from [10], we find from expression (3) $Z\lambda \approx 0.815$ and, since $\lambda = 1.125$ Å (data on r_i and r_a are taken from [25]), we obtain $Z_0 \equiv Z(\Theta = 0) \approx 0.72$. We furthermore assume that

$$\Omega = \Omega_0 + \Delta, \quad \Omega_0 = \phi - I, \quad \Delta = e^2/4\lambda. \tag{4}$$

Here, I is the ionization energy for the alkali metal atom, ϕ = 4.85 eV is the work function for the Si(001) surface [25], and Δ is the Coulomb shift of the adatom quasi-level. In this case, the quasi-level half-width for a zero coverage Γ_0 can be determined from the relation

$$\Gamma_0 = \frac{\Omega}{\tan\left(\frac{\pi}{2}Z_0\right)}. \tag{5}$$

For Li, Γ_0 = 0.96 eV.

In order to determine coefficients γ, we obtain $Z_{ML} \equiv Z(\Theta = 1)$ using the experimental value $\Delta\phi_{ML} \approx$ –2.35 eV. The calculation yields $Z_{ML} \approx 0.17$. Now, using relation

$$\gamma = \frac{\Omega - \xi Z_{ML}}{\Gamma_0 \tan\left(\frac{\pi}{2}Z_{ML}\right)} - 1, \tag{6}$$

we obtain γ = 3.20. Thus, we determined all the parameters necessary for the case of Li.

The parameters for Na, K, and Cs can be found similarly (see table). The experimental data on Na, K, and Cs adsorption were taken from [9], [26, 27], and [19], respectively. The results of calculations in comparison with the experimental data are shown in the figure. It can be seen that agreement is good for Li and K. However, our computed values for Na are substantially smaller than the results in [9], whereas for Cs, on the

contrary, they are larger than the data in [19]. In general, taking into account that we used an extremely simplified model, the agreement between the theory and experiment should be considered satisfactory.

Let us analyze the variation of parameters in the series Li ⟶ Cs. An increase in the parameter Ω_0 can be attributed to a decrease in the ionization energy I in this series. A decrease in Δ and an increase in ξ and Φ are related to an increase in r_i and r_a (and consequently, λ) when passing from Li to Cs. A decrease in the charge Z_0 can be explained by both an increase in energy of the quasi-level Ω and a decrease in its half-width Γ_0. Note that the charge Z_0 decreases by a factor of 2 when passing from Li to Cs, whereas the charge Z_{ML} only varies by 25%. This is related to the fact that in contrast to Γ_0, which increases in the series Li ⟶ Cs by a factor of 4, the parameter $\Gamma_{ML} = \Gamma_0(1 + \gamma)$, which is equal to 4.05, 3.05, 5.95, and 5.81 eV for Li, Na, K, and Cs, respectively, increases by a factor of less than 1.5. Being combined with an increase in Ω, this levels off the variations in Z_{ML}.

In order to gain insight into the pattern of the variation in the parameter γ, whose values are related to each other as 7.62 : 1.69 : 2.33 : 1 in the series Li–Na–K–Cs, let us refer again to paper [23], in which it was demonstrated that the band spreading can be described by the parameter

$$\eta = \frac{T_{ML}^2 \Gamma_0 \Omega}{(\Omega^2 + \Gamma_0^2)^2}, \quad (7)$$

where T_{ML} is the two-center integral of the interaction between s orbitals of the nearest alkali metal atoms in the adsorbed monolayer. We assume that this integral is proportional to d^{-2}, where d is the distance between the nearest neighbors [28]. The calculation of the parameter η yields the following ratio for the Li–Na–K–Cs series: 8.33 : 6.12 : 2.30 : 1. Thus, except for Na, we obtain reasonable qualitative and quantitative consistency with the experiment. The reasons of such a large discrepancy for Na are not clear.

Parameters of the model (values of Ω_0, Δ, ξ, Φ, and Γ_0 are given in electronvolts)

Parameters	Li	Na	K	Cs
Ω_0	−0.49	−0.24	0.56	1.01
Δ	2.57	2.35	1.95	1.61
ξ	5.72	7.07	9.38	11.39
Φ	13.80	17.05	22.64	27.48
Γ_0	0.96	1.79	3.02	4.07
Z_0	0.72	0.59	0.44	0.36
Z_{ML}	0.17	0.18	0.13	0.13
γ	3.02	0.71	1.10	0.43

We note that, in the context of the standard adsorption model, which is based on the use of Anderson's Hamiltonian [29, 30], the quasi-level half-width for the isolated adatom $\Gamma_0 \propto V^2\rho_S$. Here, in our case, the quantity V should be a matrix element of interaction between the s orbital of the adatom and the sp^3 orbital of the substrate atom, and ρ_S is the density of states. It is clear that such a simple interpretation of the parameter Γ_0 is not valid here. One possible reason is that, in contrast with the density of states for metal substrates, the conventional approximation ρ_S = const seems to be excessively simplified for a semiconductor substrate, since the band gap, surface-state bands, etc., are ignored in this case. Later, we intend to use the model suggested here to describe other metal/semiconductor adsorption systems and, as new information on the parameter Γ_0 becomes available, to offer corresponding interpretation of this parameter.

It should also be noted that both for zero and for multilayer coverage, the position of the adatom quasi-level or the center of the band formed by adatoms overlaps with the conduction band of Si. Actually, the electron affinity for Si is equal to 3.99 eV [31], whereas the level energy measured from the Fermi level in the series Li–Na–K–Cs is Ω = 2.08, 2.11, 2.51, and 2.62 eV; and $\Omega_{ML} \equiv \Omega - \xi Z_{ML}$ = 1.11, 0.84, 1.29, and 1.14 eV, respectively. Because of such overlapping, the problem of alkali metal adsorption on the Si(001) surface is basically no different from the problem of adsorption on a metal surface, in which the adatom quasi-level (band) also overlaps with the conduction band of the substrate.

Thus, a simple model suggested in this paper makes it possible to describe quite satisfactorily the variation in the work function for the system, which is caused by the adsorption of alkali metal atoms on the Si surface.

ACKNOWLEDGMENTS

This study was supported by the Federal Program "Surface Atomic Structures," grant no. 4.5.99.

REFERENCES

1. É. Ya. Zandberg and N. I. Ionov, *Surface Ionization* (Nauka, Moscow, 1969).
2. L. A. Bol'shov, A. P. Napartovich, A. G. Naumovets, and A. G. Fedorus, Usp. Fiz. Nauk **122** (1), 125 (1977) [Sov. Phys. Usp. **20**, 432 (1977)].
3. O. M. Braun, Ukr. Fiz. Zh. **23** (8), 1234 (1978).
4. O. M. Braun and V. K. Medvedev, Usp. Fiz. Nauk **157** (4), 631 (1989) [Sov. Phys. Usp. **32**, 328 (1989)].
5. *Physics and Chemistry of Alkali Metal Adsorption*, Ed. by H. P. Bonzel, A. M. Bradshow, and G. Ertl (Elsevier, Amsterdam, 1989).
6. S. Yu. Davydov, Fiz. Tverd. Tela (St. Petersburg) **42** (6), 1129 (2000) [Phys. Solid State **42**, 1164 (2000)].
7. M. Tikhov, G. Boishin, and L. Surnev, Surf. Sci. **241** (1), 103 (1991).

8. L. S. Johansson and B. Reihl, Phys. Rev. B **47** (3), 1401 (1993).
9. Y.-J. Ko, K. J. Chang, and J.-Y. Yi, Phys. Rev. B **51** (7), 4329 (1995).
10. C. Y. Kim, K. S. Shin, K. D. Lee, and J. W. Chung, Surf. Sci. **324** (1), 8 (1995).
11. K. D. Lee, C. Y. Kim, and J. W. Chung, Surf. Sci. **366** (3), L709 (1996).
12. Y.-C. Chao, L. S. Johansson, and R. I. G. Uhrberg, Phys. Rev. B **54** (8), 5901 (1996).
13. Y.-C. Chao, L. S. O. Johansson, and R. I. G. Uhrberg, Phys. Rev. B **55** (11), 7198 (1997).
14. K. D. Lee and J. Chung, Phys. Rev. B **55** (19), 12906 (1997).
15. H. Hamamatsu, H. W. Yeom, T. Yokoyama, *et al.*, Phys. Rev. B **57** (19), 11883 (1998).
16. J. P. Muscat and D. M. Newns, J. Phys. C **7** (15), 2630 (1974).
17. S. Yu. Davydov, Fiz. Tverd. Tela (Leningrad) **19** (11), 3376 (1977) [Sov. Phys. Solid State **19**, 1971 (1977)].
18. S. Yu. Davydov, Fiz. Tverd. Tela (St. Petersburg) **41** (9), 1543 (1999) [Phys. Solid State **41**, 1413 (1999)].
19. T. Kato, K. Ohtomi, and M. Nakayama, Surf. Sci. **209** (1), 131 (1989).
20. S. Yu. Davydov, Appl. Surf. Sci. **140** (1), 58 (1999).
21. S. Yu. Davydov, Fiz. Met. Metalloved. **47** (3), 481 (1979).
22. S. Yu. Davydov, Fiz. Tverd. Tela (Leningrad) **20** (6), 1752 (1978).
23. S. Yu. Davydov, Surf. Sci. **407** (1–3), L652 (1998).
24. S. Yu. Davydov, Surf. Sci. **411** (1–3), L878 (1998).
25. *Physical Quantities. Handbook*, Ed. by I. S. Grigor'ev and E. Z. Meĭlikhov (Énergoizdat, Moscow, 1991).
26. H. Ishida and K. Terakura, Phys. Rev. B **40** (17), 11519 (1989).
27. K. Kobayashi, Y. Morikawa, K. Terakura, and S. Blügel, Phys. Rev. B **45** (7), 3469 (1992).
28. W. A. Harrison, *Electronic Structure and the Properties of Solids: The Physics of the Chemical Bond* (Freeman, San Francisco, 1980; Mir, Moscow, 1983), Vol. 1.
29. C. Kittel, *Quantum Theory of Solids* (Wiley, New York, 1963; Nauka, Moscow, 1967).
30. *Theory of Chemisorption*, Ed. by J. R. Smith (Springer-Verlag, Berlin, 1980; Mir, Moscow, 1983).
31. T. Bechshtedt and R. Enderlein, *Semiconductor Surfaces and Interfaces. Their Atomic and Electronic Structures* (Akademie-Verlag, Berlin, 1988; Mir, Moscow, 1990).

Translated by N. Korovin

Semiconductors, Vol. 35, No. 7, 2001, pp. 800–806. Translated from Fizika i Tekhnika Poluprovodnikov, Vol. 35, No. 7, 2001, pp. 835–840.

SEMICONDUCTOR STRUCTURES, INTERFACES, AND SURFACES

Charge Transport in HgCdTe-based n^+–p Photodiodes

J. V. Gumenjuk-Sichevskaja*,[1], F. F. Sizov*,[1], V. N. Ovsyuk, V. V. Vasil'ev**, and D. G. Esaev****

** Institute of Semiconductor Physics, National Academy of Sciences of Ukraine, Kiev, 01028 Ukraine*

[1] e-mail: kolezhuk@joanna.ru.kiev.ua; sizov@dep38.semicond.kiev.ua

*** Institute of Semiconductor Physics, Siberian Division, Russian Academy of Sciences, pr. Akademika Lavrent'eva 13, Novosibirsk, 630090 Russia*

Submitted November 3, 2000; accepted for publication December 7, 2000

Abstract—It is shown that dark currents measured at 77 K in $Hg_{1-x}Cd_xTe$ ($x \simeq 0.21$) homojunctions can be adequately described by the balance equations with allowance made for the two main charge-transport mechanisms, i.e., tunneling assisted by traps in the band gap and recombination via these traps; the above homojunction may find application in microphotoelectronics in the infrared spectral range of 8–12 μm. Other charge-transport mechanisms are included in the consideration as additive terms. A comparison between the experimental current–voltage characteristics and dynamic resistance of HgCdTe diodes with the results of calculations was carried out. A good agreement was obtained between experimental data and the results of calculations, in which the donor and acceptor concentrations in the *n* and *p* regions of diodes, the concentration of traps and the position of their levels in the band gap, and the lifetimes of charge carriers for recombination via these traps were used as adjustable parameters. © *2001 MAIK "Nauka/Interperiodica".*

1. INTRODUCTION

At present, high-sensitivity infrared (IR) imaging systems with the best characteristics and a high resolution include multielement arrays of photodiode structures cooled to low temperatures and made of narrow-gap semiconductors and a silicon signal processor located in the focal plane connected to the photodiode array via, for example, In microbumps. This hybrid technology is widely used because it makes it possible to separately optimize the parameters of the detectors and the silicon readout device connected to the photodetector array [1]. Photovoltaic optical-radiation detectors based on mercury-cadmium telluride (MCT) compounds [1–3] and silicon integrated circuits for readout of the charge from the detectors and for its subsequent multiplexing are mainly used in the hybrid technology. At present, the use of multielement linear and two-dimensional arrays of MCT-based detectors for applications in the middle-IR (3–5 μm) and far-IR (8–12 μm) wavelength ranges is well substantiated. The medium- and long-wavelength IR HgCdTe photodiodes and arrays have parameters that are optimized to a greater extent as compared to other semiconductor photodiodes for IR photoelectronics [4–6]. Since the front-end transistors of readout devices should be reverse-biased for the effective operation of focal hybrid IR arrays [1, 7], a reverse bias should also be applied to the photodiodes. In this situation, the dynamic resistance of IR photodiodes depends heavily on the bias voltage and to a large extent governs the efficiency of the hybrid-structure operation. Therefore, in order to optimize the control over the arrays, it is important to determine the IR-photodiode reverse-bias range in which the parameters of hybrid structures are optimal for transmission of IR signals.

Deep levels observed in the band gap of MCT compounds are apparently related to native defects, which arise during the growth of crystals or epilayers, and to uncontrolled impurities. However, additional deep levels can also be caused by a difference in the thermal-expansion coefficients between the silicon readout cells and the photodiode arrays based on narrow-gap MCT compounds, which can lead to the generation of extra noise currents. Impurities used in fabricating narrow-gap photodiodes and the damage appearing in such semiconductors in the course of hybridization may give rise to defect-levels of another type in the band gap; these levels can impair the array parameters. Compared to the detectors based on binary compounds (such as InSb-based photovoltaic detectors), HgCdTe-based detectors can be compositionally adjusted to optimize the spectral response. Furthermore, HgCdTe-based detectors, by virtue of their positive temperature coefficient for the band-gap variation, can be used in the wavelength range of 3–5 μm in a wider temperature range (up to $T > 180$ K, see, e.g., [8]) as compared to InSb-based detectors, which is important from the standpoint of cooling conditions.

In this study, we compare the experimental "dark" current–voltage (I–V) characteristics and the dependences of dynamic resistance on the bias voltage for MCT diodes at $T = 77$ K with the results of model calculations for several plausible mechanisms of charge-carrier recombination.

We used the carrier-balance equations, which accounted for the two main transport mechanisms, spe-

cifically, trap-assisted tunneling (TAT) and the Shockley–Read–Hall (SRH) recombination via the trap levels. For adjustable parameters, we used the concentrations of donors and acceptors in the *p–n* junction, the concentrations of traps and position of the trap levels in the band gap, and the lifetimes of charge carriers recombining at the traps. We obtained good agreement with the experimental results.

2. THE APPROXIMATION OF BALANCE EQUATIONS

In order to describe the tunneling processes and dark currents in the $Hg_{1-x}Cd_xTe$ photodiodes, we employed the so-called approximation of balance equations [9]. We consider the two main processes in the *p–n* junction: TAT and the SRH thermal recombination with the traps involved. We assume that the charge carriers of both types can be captured by a free trap or be emitted from an occupied trap to the free site in the band by two mechanisms, i.e., by TAT or SRH. The calculation procedure has been described in detail previously [10]. Below, we outline briefly the scheme of the calculations. We used the three following assumptions introduced first in [11] and then used in [9]:

(i) the field in the barrier is constant;

(ii) the quasi-Fermi levels in the *p–n* junction are fixed (this is valid for the forward and low reverse bias voltages); and

(iii) the Boltzmann statistics may be used for charge carriers.

For the concentration of charge carriers within the junction ($0 \le x \le W$), we then have

$$p(x) = N_a \exp[-q(V_0 + V)(W - x)/kTW],$$

$$n(x) = N_d \exp[-q(V_0 + V)x/kTW],$$

where V_0 and V are the built-in and applied voltages, respectively, and N_a and N_d are the acceptor and donor concentrations. The rate of tunneling of electron from the trap, whose level is located by E_t above the valence-band top, is given by [12]

$$\omega_{c,v} N_{c,v} = \frac{\pi^2 q F m_{eff}}{h^3 (E_g - E_t)} |W_c|^2 \exp(-2\theta_{c,v}), \qquad (1)$$

where F is the electric-field strength in the junction,

$$E_g = -0.302 + 1.93x - 0.81x^2 + 0.832x^3$$
$$+ 5.32 \times 10^{-4}(1 - 2x)(-1882 + T^3)/(255.2 + T^2)$$

is the band gap of MCT [13], and $N_{c,v}$ is the effective density of states in the conduction or valence bands. We use the two-band *k–p* model and thus assume that the effective densities of the states of electrons in the conduction band and light holes in the valence band are expressed as

$$N_c \simeq N_{vlh} = 2(3E_g kT/8\pi P^2)^{3/2},$$

where $P = 0.83$ eV nm is the interband-transition matrix element and the effective density of states of holes in the valence band is approximately equal to the effective density of states of heavy holes; thus, for a parabolic dispersion relation, we have

$$N_v \simeq N_{vhh} = (2\pi m_{hh} kT)^{3/2}/4(\pi\hbar)^3.$$

In expression (1), $|W_c|^2$ is the squared matrix element for trap ionization. In calculations, we used the experimental value of $|W_c|^2$ for an Au impurity in Si [9, 12]: $|W_c|^2 = 3 \times 10^{-67}$ J^2 m^3. This quantity affects the TAT to a much lesser extent than does the exponential factor. The exponent θ in expression (1) is defined as the following integral:

$$\theta = \int_{x_1(E)}^{x_2(E)} \mathrm{Im}[k_x(E)]dx. \qquad (2)$$

Here, k_x is the momentum vector along the *p–n*-junction axis and is defined by the dispersion relation in the Kane two-band model and x_1 and x_2 are the turning points in tunneling.

In relation to the trap coordinate along the *p–n*-junction axis (x) and to the trap-level position (E_t), we consider which of the processes of the charge-carrier arrival at the trap are possible; these processes may be vertical (in energy) or horizontal (a charge carrier arrives at the point $x + x_t$ in the valence band or at the point $x - x_t$ in the conduction band). The rates of the charge-carrier capture by the trap and of the corresponding emission from the trap are equated; thus, the number of occupied traps is found. Hereafter, the capture and emission rates are expressed in terms of the known parameters. Taking into account that in the depletion region

$$p_{lh}(x + x_t) = p_{lh}(x)\exp(E_t/kT),$$
$$n(x - x_t) = n(x)\exp[(E_g - E_t)/kT], \qquad (3)$$

the recombination rate for nonequilibrium charge carriers in the situation where both the SRH recombination and tunneling from the trap to the conduction band ($E_g \le E \le q(V_0 + V) + E_t$) are possible is given by

$$U_a = \frac{N_t \gamma_v n_i^2 [\gamma_c + \omega_c e^{(E_g - E_t)/kT}](e^{-qV/kT} - 1)}{R},$$
$$R = [p(x) + p_1]\gamma_v + [n(x) + n_1]\gamma_c \qquad (4)$$
$$+ [n(x)e^{(E_g - E_t)/kT} + N_c]\omega_c,$$

where N_t is the trap concentration;

$$n_i^2 = N_c N_v \exp[-E_g/kT]$$

is the squared intrinsic concentration of charge carriers, the temperature dependence of the thermal-emission rate is controlled by the parameters

$$n_1 = N_c \exp[(E_g - E_t)/kT]$$

and

$$p_1 = N_v \exp[-E_t/kT];$$

$\omega_{c(v)}$ is the tunneling-capture cross section defined by expression (1); and $\gamma_{c(v)} = 1/(N_t\tau_{e(p)})$ is the cross section of thermal capture at the traps, with $\tau_{e(p)}$ standing for the electron (or hole) lifetime.

If tunneling via traps is impossible and only the generation–recombination processes of the SRH type occur [$q(V_0 + V) \le E \le E_g$], the recombination rate is given by

$$U_b = \frac{N_t\gamma_c\gamma_v n_i^2(e^{-qV/kT} - 1)}{[p(x) + p_1]\gamma_v + [n(x) + n_1]\gamma_c}. \quad (5)$$

If tunneling from the valence band to the trap level is possible [$E_t \le E \le q(V_0 + V)$], the recombination rate is expressed as

$$U_c = \frac{N_t\gamma_c n_i^2(\gamma_v + \omega_v e^{E_t/kT})(e^{-qV/kT} - 1)}{R_1},$$
$$R_1 = [p(x) + p_1]\gamma_v + [n(x) + n_1]\gamma_c + [p_{lh}(x)e^{E_t/kT} + N_{vlh}]\omega_v. \quad (6)$$

Finally, if TAT can occur from the valence band to the trap level with ther subsequent transition of the charge carrier to the conduction band [$E_g \le E + E_t \le q(V_0 + V)$], we obtain the following expression for the recombination rate:

$$U_d = \frac{R_2}{R_3},$$

Here,

$$R_2 = N_t n_i^2(e^{-qV/kT} - 1) \times [\omega_v\omega_c e^{E_g/kT} + \omega_c\gamma_v e^{(E_g - E_t)/kT} + \omega_v\gamma_c e^{E_t/kT} + \gamma_c\gamma_v], \quad (7)$$
$$R_3 = [p(x) + p_1]\gamma_v + [n(x) + n_1]\gamma_c + [n(x)e^{(E_g - E_t)/kT} + N_c]\omega_c + [p_{lh}(x)e^{E_t/kT} + N_{vlh}]\omega_v.$$

The density of the generation–recombination current is obtained by integrating the recombination rate along the *p–n*-junction axis as

$$J = q\left(\int_0^{x_1} dx U_c + \int_{x_1}^{x_2} dx U_d + \int_{x_2}^{W} dx U_a\right), \quad \text{if } q(V_0 + V) > E_g,$$
$$J = q\left(\int_0^{x_1} dx U_c + \int_{x_1}^{x_2} dx U_b + \int_{x_2}^{W} dx U_a\right), \quad \text{if } q(V_0 + V) \ge E_t, \quad E_g - E_t,$$
$$J = q\left(\int_0^{x_2} dx U_c + \int_{x_2}^{W} dx U_b\right), \quad \text{if } E_t \le q(V_0 + V) < E_g - E_t, \quad (8)$$
$$J = q\left(\int_0^{x_1} dx U_b + \int_{x_1}^{W} dx U_a\right), \quad \text{if } E_g - E_t \le q(V_0 + V) < E_t,$$

where

$$x_1 = W(E_g - E_t)/q(V_0 + V),$$
$$x_2 = W[1 - E_t/q(V_0 + V)].$$

The remaining currents (such as the diffusion current, the current of the band-to-band tunneling, the current of thermal recombination via traps in quasi-neutral *n* and *p* regions of the diode, and the current related to the Auger recombination) are considered as additive terms. The largest contributions to the dark current of the diode are made by the diffusion component, the SRH component for holes in the quasi-neutral region of the *p–n* junction, and band-to-band tunneling. For band-to-band (BTB) tunneling and a constant field in the junction, we used the following expression derived previously [13, 14] in the Wentzel–Kramers–Brillouin (WKB) approximation for the two-band dispersion relation with allowance made for nonparabolicity of the band spectrum:

$$I_{BTB} = -A\frac{(q\varphi - E_g/2)q^2F}{\sqrt{2}\pi^3\hbar^2}\left(\frac{m_y^* m_z^*}{E_g m_x^*}\right)^{1/2} \times \left\{E_4\left[\left(\frac{q\varphi}{q\varphi - E_g/2}\right)^{1/2}K\right] - \left(\frac{E_g}{2q\varphi} - E_g\right)^{3/2}E_4[(2q\varphi/E_g)^{1/2}K]\right\}. \quad (9)$$

Here,

$$E_4(C) \equiv \int_1^\infty e^{-Cx} x^{-4} dx$$

is an exponential integral,

$$K = \pi/2qF\hbar(m_x E_g^3)^{1/2},$$

F is the electric-field strength in the junction, A is the diode area, and φ is the junction potential. Expression (9) yields values for the BTB-tunneling currents that are smaller by several orders of magnitude than those of the conventional expression for a quadratic dispersion relation; the latter is typically used for analysis of BTB-tunneling currents in the HgCdTe photodiodes [15, 16] and yields inadequate results.

3. EXPERIMENT AND DISCUSSION OF THE RESULTS

We compared the experimental dark current–voltage characteristics and the differential resistance of a $Hg_{1-x}Cd_xTe$-based photodiode with the results of a simulation according to the above model. The HgCdTe layers were grown by molecular-beam epitaxy on the GaAs single-crystal substrates using a CdZnTe interfacial buffer layer [17]. In order to alleviate the effect of surface recombination, we grew the $Hg_{1-x}Cd_xTe$ layers with increased x at both surfaces [18] (see Fig. 1). In the graded-gap layer with a thickness of about 0.5 μm, the index x varied from 0.212 in the bulk to 0.55 at the surfaces. The total thickness of the HgCdTe layer was 12 μm. The as-grown layers had the n-type conductivity and, as a result of annealing in Hg vapors, were converted to the p type; the n^+–p junctions with areas of $A = 50 \times 50$ μm^2 were formed by implanting B ions with an energy of 150 keV and a dose of 3×10^{13} cm^{-2}. The Cd content x was determined from the cutoff wavelength of photoresponse (12.2 μm) and was found to be $x = 0.212$, which corresponded to a band gap of $E_g = 0.1016$ eV. Figures 2a and 2b show the experimental data and the results of a simulation for a temperature of 77 K. Curves *1* and *2* in Figs. 2a and 2b correspond to high-quality diodes that satisfy the condition for the high impedance required for matching the diodes to the input circuits of the readout devices, whereas curve *3* corresponds to low-quality diodes for which the above condition is not satisfied.

For the adjustable parameters, we used the following quantities: the donor and acceptor concentrations N_d and N_a, the position of the trap level E_t, the trap concentration in the region of depletion layer N_t and its concentration outside the depletion layer N_{tv}, and the lifetimes of the charge carriers at the traps within the p–n junction (τ_n and τ_p) and those outside the junction (τ_{nv} and τ_{pv}). The effect of the above parameters on the photodiode currents may be generalized in the following way: the TAT and SRH rates are highest when the E_t position coincides with the midgap; N_a and N_d appreciably affect the depletion-layer thickness and, consequently, the probability of the TAT and SRH processes; and the SRH recombination rate depends on the values of N_t, τ_n, and τ_p.

Graded gap HgCdTe layer x from 0.21 to 0.55 d = 0.5 μm
Homogeneous HgCdTe layer x = 0.21 d = 12 μm
Graded gap HgCdTe layer x from 0.21 to 0.55 d = 0.5 μm
Buffer layer of CdZnTe d = 3–4 μm
GaAs substrate d = 300–400 μm

Fig. 1. Schematic representation of photodiode structure.

An important comment is necessary. When forcing the results of calculations to fit the experimental data, it is worthwhile to fix some of the adjustable parameters using other experimental data; otherwise, the results of fitting may be ambiguous. In other words, there is a certain family of groups of adjustable parameters that yield almost the same dependences $R(V)$; therefore, in order to obtain correct results, we have to fix certain parameters in this family. At present, there are no reliable data on the origin of traps in the materials under consideration, their energy levels, and the lifetimes of the charge carriers at the traps; however, there are numerous publications in which it is shown that deep levels in the band gap of MCT are located at $(0.6–0.7)E_g$ above the valence-band top (see, for example, [19]). For both high- and low-quality diodes, the dark-current curves in Fig. 2a for bias voltages lower than 0.2 V have the shape characteristic of a diffusion current with an allowance made for nontunneling components such as the currents of Shockley–Read recombination outside the depletion layer in the p and n regions and the Auger and radiative recombination currents; these currents are not involved in the charge-carrier balance within the depletion layer. By varying the donor and acceptor concentrations and charge-carrier lifetimes outside the depletion layer, we obtain the following values of the parameters that make it possible to adequately approximate the current curves for reverse-bias voltages lower than 0.2 V: $N_d = 10^{15}$ cm^{-3}, $N_a = 3 \times 10^{16}$ cm^{-3}, and $\tau_v = (6–8) \times 10^{-6}$ s. It is noteworthy that, for these values of the parameters, the diffusion current and the Shockley–Read recombination in the p region of the diode are most important. Fixing these parameters, we managed to fit the other adjustable parameters as well, so that the calculated curves for currents and resistances closely matched the experimental curves. The obtained charge-carrier lifetimes within and outside the p–n junction are in excellent agreement with the data [17] for HgCdTe photoresistors. The low-qual-

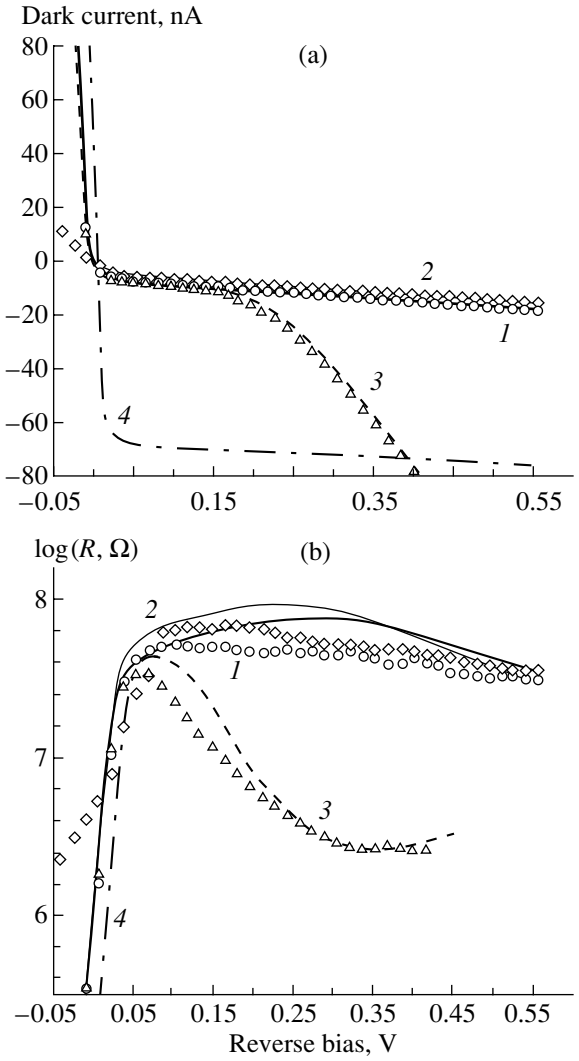

Fig. 2. Experimental (a) current–voltage characteristics and (b) dependences of differential resistance on the reverse-bias voltage for $Hg_{1-x}Cd_xTe$ photodiodes with $x = 0.212$ and $R_0A = 6\ \Omega\ cm^2$ for $\lambda_{c0} = 12.2\ \mu m$ and $T = 77$ K in comparison with the results of calculations. Curves *1*: circles represent experimental data, and the thick solid line corresponds to the results of calculations for the values of adjustable parameters equal to $E_t = 0.6E_g$, $N_d = 10^{15}\ cm^{-3}$, $N_a = 3 \times 10^{16}\ cm^{-3}$, $N_t = 2 \times 10^{13}\ cm^{-3}$, $N_{tv} = 2 \times 10^{13}\ cm^{-3}$, $\tau_{n,p} = 3 \times 10^{-7}$ s, and $\tau_{nv,pv} = 6 \times 10^{-6}$ s. It was determined that $E_g = 0.1016$ eV and $R_0A = 1.0\ \Omega\ cm^2$. Curves *2*: diamonds represent experimental data and thin solid line corresponds to the results of calculations. The optimal values of adjustable parameters were $N_t = 3 \times 10^{13}\ cm^{-3}$ and $\tau_{n,p} = 4 \times 10^{-7}$ s. Curves *3*: triangles represent experimental data, and the dashed line corresponds to the results of calculations. The optimal values of adjustable parameters are $N_t = 6 \times 10^{15}\ cm^{-3}$, $N_{tv} = 6 \times 10^{14}\ cm^{-3}$, $\tau_{n,p} = 3 \times 10^{-7}$ s, and $\tau_{nv,pv} = 8 \times 10^{-6}$ s. The dash-and-dot line *3* represents the results of calculation for an inverted structure with $N_a = 10^{15}\ cm^{-3}$ and $N_d = 3 \times 10^{16}\ cm^{-3}$. The remaining parameters for calculated curves *2–4* are the same as for curve *1*.

ity photodiodes differ from the high-quality ones only in the trap concentration. A larger number of trap levels in the band gap leads to a higher rate of recombination at these traps.

In Fig. 3, we show the photodiode currents calculated with the same parameters as for curves *1* and *3* in Fig. 2. The diffusion current (in combination with other additive components of the current) is prevalent for reverse-bias voltages no higher than 0.2 V. It is this current that governs the parameter R_0A, which is typically considered as a characteristic of the diode's quality. We obtained $R_0A = 1.0\ \Omega\ cm^2$ for both high- and low-quality diodes. It can be seen from Fig. 2a that, for low-quality diodes, the roll off of the current–voltage curve is observed at fairly high reverse-bias voltages in the operating region of the diode, which is caused by a rapid increase in the combined TAT and SRH currents in the junction. In the high-quality diodes, the rates of increase in the TAT and SRH currents are nearly the same; therefore, the current increases almost linearly and a nearly horizontal portion appears in the curve of differential resistance. If the current–voltage curve bends slightly, additional peaks may emerge in the resistance curve, which has been observed repeatedly in calculations (see, for example, [10]).

For both types of structures, the BTB tunneling current remains unimportant because the width of the depletion layer in the unbiased junction is comparatively large ($W = 0.37\ \mu m$). However, currents in the structures are very sensitive to variations in the junction parameters, in particular to variations in the concentration of dopants, which affects the depletion-layer thickness. For example, as the donor concentration increases twofold compared to the value used in the calculations (Fig. 2), the width of the depletion layer decreases to $W = 0.275\ \mu m$ and the current of BTB tunneling increases by several orders of magnitude and becomes dominant in the formation of the photodiode's characteristics for the reverse bias (see Fig. 3b).

In addition, from the standpoint of applications, the following numerical experiment appears to be of interest: the calculation of the parameters of an inverted structure, i.e., the p^+–n structure in which the donor concentration is equal to the acceptor concentration in the n^+–p structure under investigation, whereas the acceptor concentration in the inverted structure equals the donor concentration in the conventional structure. The value of R_0A in the inverted structure is much smaller than that in the above-considered structure owing to a higher diffusion current (the mobility of electrons differs markedly from that of heavy holes). Nevertheless, in the operating range of bias voltages in which the TAT and SRH processes are dominant, the differential resistances of p^+–n diodes (see the dash-and-dot line *4* in Fig. 2b) are virtually equal to those of the n^+–p diodes due to the almost identical probability of tunneling for electrons and heavy holes. Thus, the MCT-based n^+–p photodiodes do not offer advantages

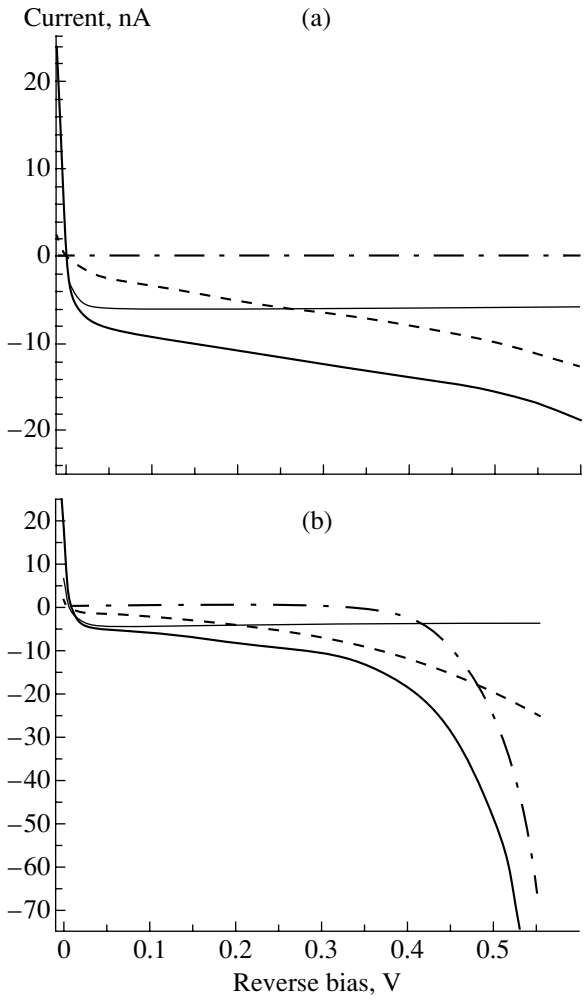

Fig. 3. Dark currents of a photodiode according to calculations (a) with the same parameters as for curves *1* in Fig. 2 and (b) with a higher donor concentration ($N_d = 2 \times 10^{15}$ cm^{-3}). The thin solid line represents the sum of the diffusion current and the generation–recombination currents outside the depletion layer, the dashed line corresponds to the currents according to the combined TAT and SRH mechanisms, the dash-and-dot line represents the current of BTB tunneling, and the thick solid line corresponds to the total current.

over the p^+–n photodiodes in the systems that include reverse-biased structures (in arrays or multielement linear arrays with readout devices) despite the fact that, for unbiased diodes, the dynamic resistance of the former may exceed that of the latter by at least an order of magnitude.

In all the above-considered cases, we used the fitting procedure and found that the trap concentration is comparable to the concentrations of doping impurities, which is caused by taking the balance of the TAT and SRH processes into consideration. If these processes are considered separately, we obviously obtain underestimated values of trap concentrations ($N_t \approx 10^{12}$ cm^{-3} according to [15, 20]) for similar carrier lifetimes.

4. CONCLUSION

We showed that the approximation based on balance equations that accounts for the two main mechanisms of charge transport in a p–n junction—the trap-assisted tunneling (TAT) and the Shockley–Read–Hall (SRH) thermal generation–recombination—makes it possible to describe adequately the experimental data on currents and differential resistance of HgCdTe (MCT) photodiodes in the temperature range of interest.

As a result of adjusting the parameters used in calculations, we found that the high-quality diodes differ from the low-quality ones only in the concentration of traps with the same energy level in the band gap. According to the experiments, the flat portion of the dependence of differential resistance on the bias voltage in high-quality diodes is related to the region in which the rates of the buildup of the TAT and SRH currents are close to each other. In the low-quality diodes, the breakdown in the current–voltage (I–V) characteristic is related to the same processes; however, in view of the tenfold higher trap concentration, the TAT current increases more rapidly than the SRH current. However, the SRH mechanism reduces the buildup rate for the TAT process because the balance of charge carriers at the traps is taken into account; consequently, the breakdown of the I–V characteristic is slower than might be expected for the trap concentration of $N_t \approx 10^{15}$ cm^{-3}. The BTB tunneling is unimportant for both types of diodes; however, the corresponding current may become prevalent if the dopant concentration is changed slightly, which will lead to an appreciable deterioration of the characteristics of photodiodes. We showed that, for the diodes based on HgCdTe with the band gap of $E_g \approx 0.1$ eV, the resistance of unbiased diodes R_0 is governed by the diffusion current and does not specify the quality of diodes in the operating region for reverse bias of input stages in the readout-integrated circuits. Using numerical experiments, we showed that, for the n^+–p and p^+–n diodes with inverted concentrations of donors and acceptors, the differential resistance of biased diodes is independent of the diode type in the region where the combination of the TAT and SRH currents is prevalent, although the value of R_0 is different in these structures under zero bias due to distinctions in mobilities for electrons and heavy holes.

REFERENCES

1. E. Fossum and B. Pain, Proc. SPIE **2020**, 262 (1994).
2. Ph. Tribolet, Ph. Hirel, A. Lussereau, and M. Vuillermet, Proc. SPIE **2552**, 369 (1996).
3. F. F. Sizov, Semicond. Phys., Quantum Electron. Optoelectron. **3**, 52 (2000).
4. A. Rogalski, Opt. Eng. **33**, 1395 (1994).
5. L. J. Kozlowski, W. V. McLevige, Sc. A. Cabelli, *et al.*, Opt. Eng. **33**, 704 (1994).
6. C. C. Wang, J. Vac. Sci. Technol. B **9**, 1740 (1991).

7. T. Tung, L. V. DeArmond, R. F. Herald, *et al.*, Proc. SPIE **1735**, 109 (1992).
8. G. N. Pultz, P. R. Norton, E. E. Krueger, and M. B. Reine, J. Vac. Sci. Technol. B **9**, 1724 (1991).
9. W. W. Anderson and H. J. Hoffman, J. Appl. Phys. **53**, 9130 (1982).
10. J. V. Gumenjuk-Sichevskaja and F. F. Sizov, Semicond. Sci. Technol. **144**, 1124 (1999).
11. C. T. Sah, R. N. Noyce, and W. Shockley, Proc. IRE **45**, 1228 (1957).
12. C. T. Sah, Phys. Rev. **123**, 1594 (1961).
13. J. P. Lowney, D. G. Siler, C. L. Litter, and I. T. Yoon, J. Appl. Phys. **71**, 1253 (1992).
14. W. W. Anderson, Infrared Phys. **17**, 147 (1977).
15. Y. Nemirowski and A. Unikowski, J. Vac. Sci. Technol. B **10** (4), 1602 (1992).
16. A. Ajisawa and N. Oda, J. Electron. Mater. **24** (9), 1105 (1995).
17. V. S. Varavin, S. A. Dvoretsky, V. I. Liberman, *et al.*, J. Cryst. Growth **159**, 1161 (1996).
18. V. V. Vasil'ev, D. G. Esaev, A. F. Kravchenko, *et al.*, Fiz. Tekh. Poluprovodn. (St. Petersburg) **34** (7), 877 (2000) [Semiconductors **34**, 844 (2000)].
19. J. Yoshino, J. Morimoto, H. Wada, *et al.*, Proc. SPIE **3436**, 120 (1998).
20. Y. Nemirowski, D. Rosenfeld, R. Adar, and A. Kornfeld, J. Vac. Sci. Technol. B **7** (2), 528 (1989).

Translated by A. Spitsyn

Semiconductors, Vol. 35, No. 7, 2001, pp. 807–815. Translated from Fizika i Tekhnika Poluprovodnikov, Vol. 35, No. 7, 2001, pp. 841–849.

LOW-DIMENSIONAL SYSTEMS

Electronic State Mixing in X_x and X_y Valleys in AlAs/GaAs (001)

G. F. Karavaev and V. N. Chernyshov*

Siberian Institute of Physics and Technology, Tomsk State University, Novosobornaya pl., Tomsk, 634050 Russia

** e-mail: vnchern@elefot.tsu.ru*

Submitted January 15, 2001; accepted for publication January 21, 2001

Abstract—The $X_x - X_y$ mixing of *X*-valley electronic states in AlAs/GaAs(001) heterostructures is analyzed. General, structure symmetry-related constraints on the parameters of a matrix matching the envelopes are derived. A model describing the $X_x - X_y$ mixing is proposed. The obtained structure of the matching matrix differs essentially from those used previously. The parameters of the model are determined on the basis of pseudopotential calculations. Both the model and pseudopotential calculations have been carried out for the level dispersion in AlAs *X* quantum wells, the electronic spectra of $(AlAs)_M(GaAs)_N(001)$ superlattices, and the *X*-electron transmission coefficient for structures with a single *X*-well and two *X*-barriers. The good agreement of the results of both sets of calculations shows the efficiency of the proposed model for envelopes with parameters determined in the study. *© 2001 MAIK "Nauka/Interperiodica".*

INTRODUCTION

Under certain conditions (high pressure or a thin GaAs layer [1–5]), the electronic properties of AlAs/GaAs(001) structures are mainly determined by electrons from the *X*-valleys of the AlAs and GaAs conduction bands. There have been a few reports concerning the problem of the *X*-electron behavior in structures of this kind. The X_x–X_y electron mixing was studied in [6] for the first time by calculating the electronic spectrum of the $(AlAs)_M(GaAs)_N$ superlattices in the (001) direction within the tight-binding approximation for a varied number of layers, *M* and *N*. The nature of the miniband spectrum was shown to depend essentially on the *M* and *N* values; in particular, it is doubly degenerate at odd *M* and *N*. A simple model for the X_x and X_y state mixing at heterointerfaces was proposed in [7] within the envelope formalism, and, in addition, the miniband dispersion in directions perpendicular to the superlattice axis (001) was considered. This simple model was used in [5] with minor corrections to analyze the experimental data on magnetotunneling in double-barrier AlAs/GaAs(001) heterostructures. The conclusion was made that the $X_x - X_y$ state mixing at the heterointerface leads to rotational displacement of the constant energy ellipsoids so that the dispersion laws along the (110) and $(1\bar{1}0)$ directions are essentially different.

As far as we know, no direct theoretical calculations substantiating the matching conditions in $X_x - X_y$ mixing have been made. We make an attempt to fill this gap, keeping in mind the great interest in this problem and the essential conclusions based on the previously proposed model.

1. PROPERTIES OF MATCHING MATRICES FOR ENVELOPES

A model with a discontinuous potential at the boundary is used in the study. Within this model, a general solution of the Schrödinger equation, Ψ^n, in a medium n ($n = 1, 2$) at fixed energies E and a wave vector component $\mathbf{k}_\parallel$ parallel to the heterointerface can be represented as (see, e.g., [8–10])

$$\Psi^n = \sum_\nu C_\nu^n \Psi_{\mathbf{k}_\nu}^n, \qquad (1)$$

where $\mathbf{k}_\nu = \mathbf{k}_\parallel + \mathbf{k}_{\perp\nu}$ are the wave vectors for the subsystem n; $\mathbf{k}_{\perp\nu}$ are vectors perpendicular to the heterointerface; and $\Psi_{\mathbf{k}_\nu}^n$ are particular solutions of the Schrödinger equation for the medium n, indexed by the wave vector $\mathbf{k}_\nu$ at fixed E and $\mathbf{k}_\parallel$ values. The coefficients C_ν^n in the general solution (1) can be found from the matching conditions at the heterointerface and conditions at infinity. The matching conditions at the interface can be written as [8–10]

$$\mathbf{C}^{(1)} = \mathbf{I}(z_0)\mathbf{C}^{(2)}, \qquad (2)$$

where $\mathbf{C}$ is a column vector with components C_ν; $\mathbf{I}(z_0)$ is the matching matrix at the $z = z_0$ heterointerface; and medium 1 is situated to the left of medium 2.

The envelope method is widely used in describing electronic processes in heterostructures. The general solution (1) can be written in terms of this method as

$$\Psi^n = \exp[i(q_x x + q_y y)] \sum_m F_m^n(z) |\mathbf{K}_{\nu 0 m}^n\rangle, \qquad (3)$$

where $\mathbf{q}_\nu = \mathbf{k}_\nu - \mathbf{k}_{\nu 0}$, the z-axis is perpendicular to the heterointerface, and $|\mathbf{K}^n_{\nu 0 m}\rangle$ is the Bloch function at the point $\mathbf{k}_{\nu 0}$. The functions $F^n_m(z)$ have the meaning of envelopes and satisfy at given E, $\mathbf{k}_\parallel$, and $\mathbf{k}_{\nu 0}$ the following system of equations:

$$\sum_m \{[E_m(\mathbf{k}_{\nu 0}) - E + \mathbf{p}^2]\delta_{ml} + 2\mathbf{p}_{lm}\mathbf{p}\} \times F_m(z)\exp[i(q_x x + q_y y)] = 0, \quad (4)$$

where $\mathbf{p}$ is the momentum operator, $\mathbf{p}_{lm} = \langle \mathbf{K}_{\nu 0 l}|\mathbf{p}|\mathbf{K}_{\nu 0 m}\rangle$ is the matrix element of the momentum operator, and $E_m(\mathbf{k}_0)$ is the energy of the $|\mathbf{K}^n_{0m}\rangle$ state. We use the atomic units for which the free electron mass is 1/2. The reference points $\mathbf{k}_{\nu 0}$ can be chosen arbitrarily, but it is more convenient to take them equal to the wave vector values at the bottom of various valleys. Thus, the entire set of $\mathbf{k}_{\perp\nu}$ can be divided into several groups, each characterized by a specific value of $\mathbf{k}_{\nu 0}$. For instance, it may be assumed, for a heterointerface lying in the (001) plane at $\mathbf{k}_\parallel = 0$, that $\mathbf{k}_{\nu 0}$ takes two values corresponding to Γ and X_z valleys. The functions $F^n_m(z)$ can be represented as

$$F^n_m(z) = \sum_\nu C^n_\nu D^n_m(\mathbf{k}_\nu)\exp(iq_{z\nu}z), \quad (5)$$

where the expansion coefficients $D^n_m(\mathbf{k}_\nu)$ can be found from the algebraic system of equations obtained by substituting into the system (4) particular solutions $\propto \exp(iq_z z)$ for a given $\mathbf{k}_{\nu 0}$. It is noteworthy that, for a rigorously formulated problem, the possible values of $k_\perp$ obtained by solving the system (4) must coincide with the $\mathbf{k}_{\perp\nu}$ values found by calculating the complex band structure, and $D_m(\mathbf{k}_\nu) = \langle \mathbf{K}_{\nu 0 m}|\Psi_{\mathbf{K}_\nu}\rangle$.

The derivatives of the envelopes with respect to z read

$$(F^n_m)' = \frac{\partial F^n_m(z)}{\partial z} = i\sum_\nu q_{z\nu} C^n_\nu D^n_m(\mathbf{k}_\nu)\exp(q_{z\nu}z). \quad (6)$$

At $z = z_0$, relations (5) and (6) can be written in the matrix form

$$\mathbf{F}^n = \Phi^n C^n, \quad (7)$$

where $\mathbf{F}$ is a $2m_{\max}$-dimensional column vector with the components F_m and F'_m; Φ is a $(2m_{\max} \times 2\nu_{\max})$-matrix with elements determined from (5) and (6). Here, $m_{\max}$ is the number of valleys taken into account in the expansion (3), and $2\nu_{\max}$ is the number of particular solutions in (1).

Obviously, unambiguous matching conditions for the envelopes can only be obtained from the matching conditions for the wave functions (2) in the case of square matrices Φ; i.e. only $\nu_{\max}$ for different F^n_m should be chosen in (7). Then it is clear that

$$\mathbf{F}^{(1)} = \mathbf{T}(z_0)\mathbf{F}^{(2)}, \quad (8)$$

where the matching matrix for the envelopes has the form

$$\mathbf{T}(z_0) = \Phi^1 \mathbf{I}(z_0)(\Phi^2)^{-1}. \quad (9)$$

Commonly, in numerical calculations, e.g., when using pseudopotential technique, $\nu_{\max} < m_{\max}$ since $m_{\max}$ depends on the number of plane waves taken into account in the wave function expansion, whereas $\nu_{\max}$ is equal to the number of different components of the wave vector projected onto the heterointerface plane. The adequacy of the matching conditions for envelopes (8) to the problem under consideration can be established by analyzing relations (1)–(3) in any particular case.

Attention is drawn to the circumstance used in our previous studies [9, 10], in particular, for verifying numerical calculations, but overlooked in [6, 7, 11, 12]. The matching conditions must have a form independent of the layer sequence order, AB or BA. To clarify the above statement, let us consider a structure with two heterointerfaces coinciding with the z_1 and z_2 planes, e.g., ABA. The matching conditions for the envelopes (8) at $z = z_1$ read

$$\mathbf{F}^{\mathrm{A}}(z_1) = \mathbf{T}^{\mathrm{AB}}(z_1)\mathbf{F}^{\mathrm{B}}(z_1), \quad (10)$$

where 1 = A, 2 = B. The matching conditions at the second heterointerface $z = z_2$ (here, 2 = A, 1 = B) can be written in the form

$$\mathbf{F}^{\mathrm{A}}(z_2) = (\mathbf{T}^{\mathrm{BA}}(z_2))^{-1}\mathbf{F}^{\mathrm{B}}(z_2) = \mathbf{T}'^{\mathrm{AB}}(z_2)\mathbf{F}^{\mathrm{B}}(z_2). \quad (11)$$

Applying the matching conditions (10) and (11) and the transfer matrix $L(z_1, z_2)$ to the layer B we obtain

$$\mathbf{F}^{\mathrm{A}}(z_1) = \mathbf{T}^{\mathrm{AB}}(z_1)L(z_1, z_2)(\mathbf{T}'^{\mathrm{AB}}(z_2))^{-1}\mathbf{F}^{\mathrm{A}}(z_2). \quad (12)$$

Let us make the B layer thickness approach zero, i.e. $z_2 \longrightarrow z_1$. Since in this case $L(z_1, z_2)$ tends to the unity matrix, we obtain that $\mathbf{T}(\mathbf{T}')^{-1} = \mathbf{E}$; i.e., $\mathbf{T} = \mathbf{T}'$ for the properly matched phases of wave functions in layers A. It was mentioned in [11] that the equality $\mathbf{T} = \mathbf{T}'$ is occasionally valid. We believe that it is always valid.

Let us consider AlAs/GaAs(001) heterostructures with interfaces lying in planes of As atoms, common to both materials, at $\mathbf{k}_\parallel = (2\pi/a)(100)$ (a is the lattice constant). This $\mathbf{k}_\parallel$ value is related to the corner of the square surface Brillouin zone. There are two X valleys at this $\mathbf{k}_\parallel$: with $\mathbf{k}_\perp = (2\pi/a)(000)$ ($\mathbf{k} = (2\pi/a)(100)$, X_x valley) and $\mathbf{k}_\perp = (2\pi/a)(001)$ ($\mathbf{k} = (2\pi/a)(101)$. This state is equivalent to the X_y valley up to the reciprocal lattice vector $\mathbf{b} = (2\pi/a)(\bar{1}1\bar{1})$. In such structures there are two

X quantum wells (QWs) (X_x and X_y) in AlAs and two X barriers in GaAs, and X_x–X_y state mixing at the heterointerfaces is possible.

Our numerical calculations (for details, see below) of the matching matrix $\mathbf{I}(z_0)$ for energies in the vicinity of X_1 states in AlAs and GaAs demonstrated that a (8×8) block can be separated out of the matching matrix with good precision, and at $\mathbf{q}_\parallel = 0$ it splits (for symmetry reasons) into two (4×4) subblocks corresponding to states related to, respectively, the X_1 and X_3 states of both valleys (X_x and X_y). Thus, for the given situation $\nu_{max} = 4$, the condition $m_{max} = 4$ should be met in constructing an envelope model adequate to the exact formulation of the problem. As shown by our calculations, it is indeed possible to restrict the consideration to only X_{1x}, X_{1y}, X_{3x}, and X_{3y}, and we have a four-valley model.

Let us analyze some symmetry-related properties of the matching matrix $\mathbf{T}$ for the envelopes in (8). We consider the structure AB with a single heterointerface and the origin of coordinates coinciding with an As atom at the heterointerface. This structure is obviously self-congruent in symmetry transformations from the D_{2d} space group, leaving the z-axis direction unchanged, and passes from the sequence order AB to BA under transformations reversing the z-axis direction. Since the $\mathbf{T}$ matrix is independent of the sequence order of the layers, it must be invariant under any transformation from the D_{2d} symmetry group. We consider here the case of $\mathbf{q}_\parallel = 0$. To obtain all the necessary relations, it will suffice to choose only generators of the group and analyze the conditions for the $\mathbf{T}$ matrix invariance under them. It is worth mentioning here that, similarly to the matching matrices $\mathbf{T}$, the envelopes and their derivatives, corresponding to the X_1 states at the heterointerface in no way mix with the envelopes and their derivatives for the X_3 states. This is due to different symmetries of the X_{1x}, X_{1y} and X_{3x}, X_{3y} functions at the heterointerface. The first two functions do not change their sign upon 180° rotation about the z-axis, whereas the other two do. Thus, the $\mathbf{T}$ matrix can be represented as a direct sum of two (4×4) matrices $\mathbf{T}(X_1)$ and $\mathbf{T}(X_3)$:

$$\mathbf{T} = \mathbf{T}(X_1) \oplus \mathbf{T}(X_3), \tag{13}$$

and the matching conditions for the envelopes of the X_1 and X_3 states, as the following two relations:

$$\begin{aligned} \mathbf{F}^{\mathrm{A}}(X_1) &= \mathbf{T}(X_1)\mathbf{F}^{\mathrm{B}}(X_1), \\ \mathbf{F}^{\mathrm{A}}(X_3) &= \mathbf{T}(X_3)\mathbf{F}^{\mathrm{B}}(X_3), \end{aligned} \tag{14}$$

where $\mathbf{F}^{\mathrm{A}}(X_1)$, $\mathbf{F}^{\mathrm{B}}(X_1)$ are column vectors with components ($F_{X_{1x}}$, $F_{X_{1y}}$, $F'_{X_{1x}}$, $F'_{X_{1y}}$) and $\mathbf{F}^{\mathrm{A}}(X_3)$, $\mathbf{F}^{\mathrm{B}}(X_3)$ are column vectors with components ($F_{X_{3x}}$, $F_{X_{3y}}$, $F'_{X_{3x}}$, $F'_{X_{3y}}$).

Let us choose the 90° rotatory reflection $S_{4z}^{(1)}$ about the z-axis as the first generator and the 180° rotatory reflection $S_{4x}^{(2)}$ about the x-axis as the second. It can be shown that the matrices $R_1(S_{4z}^{(1)})$, $R_1(S_{4x}^{(2)})$ and $R_3(S_{4z}^{(1)})$, $R_3(S_{4x}^{(2)})$, with which the matrices $\mathbf{T}(X_1)$ and $\mathbf{T}(X_2)$, commute, must respectively have the block structure:

$$R_1(S_{4z}^{(1)}) = \begin{pmatrix} \sigma_x & 0 \\ 0 & -\sigma_x \end{pmatrix}, \quad R_1(S_{4x}^{(2)}) = \begin{pmatrix} E & 0 \\ 0 & -E \end{pmatrix},$$

$$R_3(S_{4z}^{(1)}) = \begin{pmatrix} \sigma_y & 0 \\ 0 & -\sigma_y \end{pmatrix}, \quad R_3(S_{4x}^{(2)}) = \begin{pmatrix} \sigma_z & 0 \\ 0 & -\sigma_z \end{pmatrix}.$$

Here, σ_x, σ_y, and σ_z are Pauli matrices, and E is a (2×2) unity matrix.

Therefore, the matrices $\mathbf{T}(X_1)$ and $\mathbf{T}(X_3)$ also have a block structure:

$$\mathbf{T}(X_1) = \begin{pmatrix} t_1 & t_2 & 0 & 0 \\ t_2 & t_1 & 0 & 0 \\ 0 & 0 & t_3 & t_4 \\ 0 & 0 & t_4 & t_3 \end{pmatrix},$$

$$\mathbf{T}(X_3) = \begin{pmatrix} \tau_1 & 0 & 0 & \tau_2 \\ 0 & \tau_1 & \tau_2 & 0 \\ 0 & \tau_4 & \tau_3 & 0 \\ \tau_4 & 0 & 0 & \tau_3 \end{pmatrix}. \tag{15}$$

The matrix elements of $\mathbf{T}$ must also satisfy some conditions related to the periodicity properties of the $|X_x\rangle$ and $|X_y\rangle$ functions [5, 7, 10, 13, 14]. The $\mathbf{T}$ matrix elements describing the X_x–X_y state mixing (these are the parameters with even numbers t_2, t_4, τ_2, and τ_4) must change sign on passing from one heterointerface to another if the number of monoatomic layers separating the heterointerfaces is odd. Other elements of $\mathbf{T}$, describing intravalley scattering, must remain unchanged in such a shift. It is clear from our matching matrices $\mathbf{T}(X_1)$ and $\mathbf{T}(X_3)$ that for the X_1 states, the functions are matched with functions, and the derivatives with derivatives, whereas for the X_3 states, the functions are matched with derivatives, and the derivatives, with functions. This result fundamentally differs from that reported in [5, 7].

Let us now consider procedures to approximately calculate the envelopes. In compliance with formula (3), we represent the general solution of the Schrödinger equation for any of the media at fixed E and $\mathbf{k}_\parallel$ in the

vicinity of $\mathbf{k}_\parallel = (2\pi/a)(100)$ as ($\mathbf{k}_{v0}$ here assumes two values corresponding to the X_x and X_y valleys):

$$\Psi = (F_{X_{1x}}|X_{1x}\rangle + F_{X_{1y}}|X_{1y}\rangle + F_{X_{3x}}|X_{3x}\rangle + F_{X_{3y}}|X_{3y}\rangle + \chi)\exp[i(q_x x + q_y y)]. \quad (16)$$

The function χ has the form

$$\chi = F_{X_{5xz}}|X_{5xz}\rangle + F_{X_{5xy}}|X_{5xy}\rangle + F_{X_{5yz}}|X_{5yz}\rangle + F_{X_{5yz}}|X_{5yz}\rangle \quad (17)$$

and describes the contribution from the X_5 states of the valence band. The contributions from other bands will be disregarded. Numerical calculations for the energies close to the X_1 states of AlAs and GaAs confirm these assumptions. Here $X_{5\alpha\beta}$ means that, for a degenerate X_5 state in the α-valley ($\alpha = x, y$), wave functions with symmetry β are used ($\beta = z, y$ for $\alpha = x$; $\beta = z, x$ for $\alpha = y$).

For any of the valleys (X_x or X_y) Eqs. (4) are a system of four equations. Let us write equations for determining the envelopes in the vicinity of the X_x valley:

$$\begin{pmatrix} E_{X_3} - E + \mathbf{p}^2 & 2ip_1p_x & 2ip_2p_y & 2ip_2p_z \\ -2ip_1p_x & E_{X_1} - E + \mathbf{p}^2 & 2ip_3p_z & 2ip_3p_y \\ -2ip_2p_y & -2ip_3p_z & E_{X_5} - E + \mathbf{p}^2 & 0 \\ -2ip_2p_z & -2ip_3p_y & 0 & E_{X_5} - E + \mathbf{p}^2 \end{pmatrix} \times \begin{pmatrix} F_{X_{3x}} \\ F_{X_{1x}} \\ F_{X_{5xz}} \\ F_{X_{5xy}} \end{pmatrix} \exp[i(q_x x + q_y y)] = 0. \quad (18)$$

Here, the following designations are introduced for the momentum operator matrix elements:

$$ip_1 = \langle X_{3x}|p_x|X_{1x}\rangle,$$
$$ip_2 = \langle X_{3x}|p_y|X_{5xz}\rangle = \langle X_{3x}|p_z|X_{5xy}\rangle,$$
$$ip_3 = \langle X_{1x}|p_y|X_{5xz}\rangle = \langle X_{1x}|p_z|X_{5xy}\rangle.$$

With all the functions $|X_1\rangle$, $|X_3\rangle$, and $|X_5\rangle$ chosen being real, p_1, p_2, and p_3 are real, too, as are the elements of the matching matrices. The equations for the envelopes $F_{X_{1y}}$, $F_{X_{3y}}$, $F_{X_{5yz}}$, and $F_{X_{5yx}}$ are obtained from (18) by the substitution $x \longleftrightarrow y$.

Assuming the envelopes in (18) to be proportional to $\exp(iq_z z)$, we obtain a system of equations, with q_z found from the solvability condition of the system. Out of the eight roots forming pairs with opposite signs, four do not satisfy the applicability condition of the system (18) and should be disregarded. Any of the remaining four roots corresponds to a particular solution of the system of equations (18).

Let us now consider a simpler case of $\mathbf{k}_\parallel = (2\pi/a)(100)$; i.e., $q_x = q_y = 0$. Then the system of equations (18) decouples into two independent subsystems for $F_{X_{1x}}$, $F_{X_{5xz}}$ and $F_{X_{3x}}$, $F_{X_{5xy}}$. This case is discussed below. For the envelopes $F_{X_{1x}}$, $F_{X_{5xz}}$ we have:

$$F_{X_{1x}} = A_{1x}\exp(iq_1 z) + B_{1x}\exp(-iq_1 z);$$
$$F_{X_{5xz}} = 2ip_3 q_1\left[\frac{A_{1x}\exp(iq_1 z) - B_{1x}\exp(-iq_1 z)}{E_{X_5} + q_1^2 - E}\right], \quad (19)$$

where q_1 is found from the equation for q_z:

$$(E_{X_1} + q_z^2 - E)(E_{X_5} + q_z^2 - E) - 4p_3^2 q_z^2 = 0. \quad (20)$$

If we ignore in (20) q_z^2, compared with $E_{X_5} - E$, q_1 takes the form

$$q_1 \approx \sqrt{2m_{1z}(E)(E - E_{X_1})};$$
$$[m_{1z}(E)]^{-1} = 2 + \frac{8p_3^2}{E - E_{X_5}}, \quad (21)$$

where $m_{1z}(E)$ is the energy-dependent transverse effective mass in the X_1 valley.

A general solution for the envelopes $F_{X_{3x}}$, $F_{X_{5xy}}$ can be obtained from (19) by substitution $A_{1x} \longrightarrow A_{2x}$, $B_{1x} \longrightarrow B_{2x}$, $q_1 \longrightarrow q_2$, $p_3 \longrightarrow p_2$. The wave number q_2 is determined from (20) after appropriate substitutions, with the following approximation valid for the q_2:

$$q_2 \approx \sqrt{2m_{3z}(E)(E - E_{X_3})};$$
$$[m_{3z}(E)]^{-1} = 2 + \frac{8p_2^2}{E - E_{X_5}}, \quad (22)$$

where $m_{3z}(E)$ is the energy-dependent transverse effective mass in the X_3 valley.

It is noteworthy that the envelopes cannot be considered similar (or identical, as in [5]), since the wave numbers q_1 and q_2 are, respectively, real and imaginary within the energy range $E_{X_1} < E < E_{X_3}$.

Thus, we have found the envelopes in the vicinity of the X_x valley. In order to obtain the corresponding envelopes for the X_y valley it suffices, as already noted, to make a substitution $x \longleftrightarrow y$ in all the relations.

Our calculations show that the envelopes F_{X_5} make a minor contribution to the general solution and can be expressed in terms of F_{X_1}, F_{X_3}, and their derivatives. However, to determine the $q(E)$ dependences correctly, it is necessary to take into account the X_5 valley band

states. Therefore, we come to the four-valley model for envelopes considered previously.

Let us consider the problem of continuity of the probability flow density and the arising constraints on matrix elements of the matching matrices for the envelopes (13)–(15). The unit-cell-averaged z-component of the flow density for the X_1 states is approximately proportional to

$$I_z \propto \frac{i}{m_{1z}}\left(F^*_{X_{1x}}\frac{\partial}{\partial z}F_{X_{1x}} + F^*_{X_{1y}}\frac{\partial}{\partial z}F_{X_{1y}} - F_{X_{1x}}\frac{\partial}{\partial z}F^*_{X_{1x}} - F_{X_{1y}}\frac{\partial}{\partial z}F^*_{X_{1y}}\right), \quad (23)$$

with m_{1z} in (23) accounting for the contribution of the X_5 states to the flow density. The flow density must be continuous at the interface, and, hence, we assume that $I_z^{\mathrm{A}} = I_z^{\mathrm{B}}$. Using the matching conditions (15) in the last expression, we obtain that the flow continuity takes place if the following equations hold:

$$t_1t_4 + t_3t_2 = 0; \quad (m_{1z}^{\mathrm{A}})^{-1}(t_1t_3 + t_2t_4) = (m_{1z}^{\mathrm{B}})^{-1}. \quad (24)$$

Similar calculations for the X_3 flow yield:

$$(m_{3z}^{\mathrm{A}})^{-1}(\tau_1\tau_3 - \tau_2\tau_4) = (m_{3z}^{\mathrm{B}})^{-1}. \quad (25)$$

Naturally, the conditions (24) and (25) are approximate by virtue of the approximate nature of the starting expressions (23) for the flow density. The question naturally arises as to what constraints are imposed on the matching matrix elements by the condition of continuity of the electronic density at the heterointerface. We believe that it is not quite correct to use unit-cell-averaged wave functions for formulating these constraints, since, in contrast to the z-component of the flow density, averaged over the x, y plane, the plane-averaged electronic density strongly depends on z. Therefore, one has to analyze the electronic density continuity at the heterointerface, relying upon the complete expressions for the wave functions.

2. ELECTRONIC STATES IN THE AlAs X QW ACCOUNTING FOR $X_x - X_y$ MIXING

When the parameters of the matching matrix for the envelopes of the X_x and X_y valleys (13)–(15) are determined, we can proceed to studying the electronic spectrum and the distribution of the electronic density in various heterostructures. Let us first consider the single AlAs X QW (a thin AlAs layer confined on both sides by GaAs layers) and restrict ourselves to the consideration of X_x and X_y states only. As mentioned above, we should consider for this purpose states in the vicinity of $\mathbf{k}_\parallel = (2\pi/a)(100)$ ($\mathbf{q}_\parallel = 0$). Apparently, the q_x and q_y components of the wave vector are the quantum numbers of the problem. The structure under consideration is characterized by the point symmetry group D_{2d} with respect to the origin of coordinates, coinciding with an atom in the plane lying in the middle of the AlAs layer. (This is a plane of As atoms, for the even number of monolayers in AlAs, and a plane of Ga atoms, if this number is odd.) In any case, the spectrum $\varepsilon_i(\mathbf{q}_\parallel)$ must reflect the problem symmetry and satisfy the condition $\varepsilon_i(\mathbf{q}_\parallel) = \varepsilon_i(g\mathbf{q}_\parallel)$, where g is an element of the group D_{2d}. Hence, it follows that the energy bands in the X QW have a similar dispersion along the directions (110) and $(\bar{1}10)$, in contradiction to the conclusions made in [5].

Let us analyze the spectrum at $\mathbf{q}_\parallel = 0$. In this case, as seen from (18), there is no $X_1 - X_3$ interaction and the spectrum can be found independently for each pair of the valleys X_{1x}, X_{1y} and X_{3x}, X_{3y}. We consider first the spectrum related to the X_{1x} and X_{1y} valleys. Let the wave numbers q_1^{A} and q_1^{B} correspond, respectively, to AlAs and GaAs. As it follows from (20)–(21), q_1^{B} is purely imaginary for energies inside the well, and q_1^{A} is purely real. Let us introduce symmetrized ($F_{X_{1x}} + F_{X_{1y}}$) and antisymmetrized ($F_{X_{1x}} - F_{X_{1y}}$) combinations of solutions for the X_{1x} and X_{1y} valleys. Using relations (14) and (15), in which the superscript A refers to AlAs, and B, to GaAs, it can be readily shown that the spectrum can be found from the equations

$$[S_1^{(+)} \pm (-1)^M S_2^{(+)}][S_1^{(+)} \pm S_2^{(+)}]\exp(-iq_1^{\mathrm{B}}d) - [S_1^{(-)} \pm (-1)^M S_2^{(-)}][S_1^{(-)} \pm S_2^{(-)}]\exp(iq_1^{\mathrm{B}}d) = 0, \quad (26)$$

where "+" and "–" refer to symmetrized and antisymmetrized solutions, respectively;

$$S_1^{(\pm)} = t_1 \pm t_3\frac{q_1^{\mathrm{A}}}{q_1^{\mathrm{B}}}, \quad S_2^{(\pm)} = t_2 \pm t_4\frac{q_1^{\mathrm{A}}}{q_1^{\mathrm{B}}}.$$

Here, d is the AlAs layer thickness, and M is the number of monolayers in the AlAs layer. It is seen from (26) that these two equations are different for even M and coincide for the odd number of layers. Thus, at odd M, the $\varepsilon_i(0)$ levels are doubly degenerate, whereas at even M the degeneracy is lifted. This observation was made in a symmetry analysis made in [6].

If we analyze in a similar way the spectrum related to the X_{3x} and X_{3y} valleys in a thin GaAs layer confined between two AlAs layers (in our calculations the X_3 valley in GaAs lies lower than the X_3 valley in AlAs), the result obtained is opposite to that obtained for the X_1 valley. At an even number of monolayers M in the GaAs layer, the levels are doubly degenerate, whereas at odd M the degeneracy is lifted.

At $q_x \neq 0$, $q_y \neq 0$, the $X_1 - X_y$ interaction comes into play in both the semiconductors, and the analysis of the spectrum gets more complicated. In the general case of

$q_x \neq q_y$, four different particular solutions corresponding to different $q_z(q_x, q_y, E)$ should be taken into account for each X_x and X_y valley. In two directions of the wave vector $\mathbf{q}_\parallel$, corresponding to $q_x = q_y$ and $q_x = -q_y$ (along the boundaries of the surface Brillouin zone), the quantities $q_z(q_x, q_y, E)$ are the same for both valleys. Therefore, taking the matching conditions for envelopes in the form (13)–(15), we obtain two equations for determining the spectra of, respectively, symmetrized and antisymmetrized solutions. As in the case of (26), the latter will differ from the former in sign at t_2, t_4, τ_2, and τ_4. The validity of choosing the matching conditions in the form (13)–(15), independent of q_x, q_y, was demonstrated by our numerical calculations. Owing to the $X_1 - X_3$ interaction and different matching conditions for the X_1 and X_3 states, there are no degenerate levels at any M for $q_x \neq 0$, $q_y \neq 0$.

3. PSEUDOPOTENTIAL CALCULATIONS

As mentioned above, we studied the $X_x - X_y$ mixing of electronic states in AlAs/GaAs (001) structures in terms of a model with a pseudopotential discontinuous at heterointerfaces. The calculation was done using the scattering matrix technique [8–10]; the complex band structure was determined using the empirical pseudopotential method. This calculation technique was described in detail in [8–10]. We used pseudopotentials [15] with parameters determined from the condition of best fit of the calculated and experimentally found band gaps. The reciprocal lattice vectors $\mathbf{b}_l$ satisfying the condition $(\mathbf{k}_0 + \mathbf{b}_l)^2 a^2 \leq 10(2\pi)^2$ were taken into account exactly in the expansion of the wave function; in addition, about 250 plane waves were taken into consideration in terms of Löwdin's perturbation theory. Our study has shown that taking into account such a large number of plane waves is necessary for satisfying the scattering matrix unitarity conditions. Calculations were carried out in the vicinity of $\mathbf{k}_\parallel = (2\pi/a)(100)$ (100) for energies E in the range $0.21\ \text{eV} \leq E \leq 0.6\ \text{eV}$ including the energies of the AlAs and GaAs X_1 levels. The energy is reckoned from the GaAs conduction band bottom.

We first calculated the matching matrices $\mathbf{I}(z_0)$ in (2) at the AlAs/GaAs (AlAs layer on the left) heterointerface passing through the common sheet of As atoms. As mentioned above, the numerical calculations at $\mathbf{k}_\parallel = (2\pi/a)(100)$ show that two (4×4) blocks related to the X_1 and X_3 states of both the valleys (X_x and X_y) are distinguished in the matching matrix with good precision. The contribution of all other branches of the complex band structure is insignificant in this energy range. Second, we calculated the momentum matrix elements $\mathbf{p}_{lm} = \langle \mathbf{K}_{v0l} | \mathbf{p} | \mathbf{K}_{v0m} \rangle$ and the energies $E_m(\mathbf{k}_0)$ to obtain the following values:

$$p_1 = -0.11399(-0.10793),$$

$$p_2 = 0.52863(0.52922),$$

$$p_3 = 0.49235(0.49409);$$

$$E_{X_1} = 0.46877(0.20823),$$

$$E_{X_3} = 0.90684(1.18303),$$

$$E_{X_5} = -3.84209(-4.24294).$$

The energies are given in electronvolts, and the momentum matrix elements, in atomic units; the first value for each parameter corresponds to GaAs, and the second (in parentheses), to AlAs. Numerical calculations of the expansion coefficients $D_m^n(\mathbf{k}_v)$ demonstrated that it suffices to retain only the X_1, X_3, and X_5 states in the chosen energy range and that the contribution from the last kind of states is insignificant. The calculated $\mathbf{p}_{lm}$ and $E_m(\mathbf{k}_0)$ values were then used in (18) to determine, with the help of (20), the functions $q_1(E)$ and $q_2(E)$ and the envelopes (19). We established that the data obtained using the approximate formulas (18)–(20) reproduce well the results of the pseudopotential calculations. Thus, we can substantiate the previously formulated four-valley model.

In the next stage, we found the matching matrix $\mathbf{T}$ for the envelopes, using (8). A calculation for the matrix elements of $\mathbf{T}$ demonstrated their weak energy dependence, which can be ignored and, therefore, the energy-averaged values of the matrix elements can be used. This approximation was verified by calculating the matching matrices $\mathbf{I}(z_0)$ for different energies from the obtained $\mathbf{T}$ using a relation inverse with respect to (8). We obtained that the matching matrices calculated by this method virtually exactly coincide with the starting matrices $\mathbf{I}(z_0)$, which verifies the validity of the assumption made. It is noteworthy that the phases in the wave functions were chosen so that the $|X_1\rangle$, $|X_3\rangle$, and $|X_5\rangle$ functions were real and all the symmetry-related expressions for the functions were fulfilled exactly (without any phase multipliers other than unity) at $q \neq 0$. It is with this choice of phases that the matrix elements of $\mathbf{T}$ are real. We found that nonvanishing matrix elements of $\mathbf{T}$ have the following values in atomic units:

$$t_1 = 0.99318, \quad t_2 = -0.02421,$$
$$t_3 = 1.04120, \quad t_4 = 0.02430;$$

$$\tau_1 = 1.00476, \quad \tau_2 = 0.06564,$$
$$\tau_3 = 1.08057, \quad \tau_4 = 0.01660.$$

It should be noted that, unlike other parameters, τ_2 and τ_4 depend on the choice of units. These parameter values satisfy with good precision relations (24) and (25) on substituting into these relations the energy-averaged

transverse effective masses obtained in the pseudopotential calculations:

$$m_{1z}^{\mathrm{GaAs}} \approx 0.25, \quad m_{1z}^{\mathrm{AlAs}} \approx 0.26, \quad m_{3z}^{\mathrm{GaAs}} \approx 0.24,$$
$$m_{1z}^{\mathrm{AlAs}} \approx 0.26$$

(in free electron mass units). It should be emphasized that the presented values of elements of the matching matrices $T(X_1)$ and $T(X_3)$ refer to the case when the superscript A in (14) corresponds to AlAs, and B, to GaAs.

Let us now discuss the results of calculations for some AlAs/GaAs (001) heterostructures, obtained both with the use of the "exact" pseudopotential approach and in terms of the model of envelope functions. We believe that, at $q_x \neq 0$, $q_y \neq 0$, the matching conditions for the envelopes can also be written as in the case $\mathbf{q}_\parallel = 0$ in the form (13)–(15) with $\mathbf{q}_\parallel$-independent parameters. The validity of this approximation can be verified by comparing the results of exact and approximate calculations.

Let us consider the discrete spectrum $\varepsilon_i(\mathbf{q}_\parallel)$ of an AlAs X QW for $\mathbf{k}_\parallel$ in the vicinity of $\mathbf{k}_\parallel = (2\pi/a)(100)$ ($\mathbf{q}_\parallel = 0$). This dependence can be found from the relation

$$\det(S^{-1}(2)) = 0, \tag{27}$$

where $S(2)$ is the scattering matrix for a system with two heterointerfaces at fixed E and $q_\parallel$ [16]. The results of calculations of the $\mathbf{q}_\parallel$ vector for the (110) and (100) directions at two QW thicknesses (M = 10 and $M = 11$) are presented in Fig. 1. The dispersions of the lowest two energy levels are shown in this figure. It is noteworthy that the results of the pseudopotential and model calculations (in terms of the four-valley model formulated above) virtually coincide. As follows from the above analysis (see formula (26)), at $\mathbf{q}_\parallel = 0$ the $\varepsilon_i(0)$ levels are doubly degenerate for $M = 11$, whereas for $M = 10$ there is a splitting of about 0.004 eV, associated with the interaction of the X_x and X_y states at the heterointerfaces. We note that the splitting decreases with increasing M (for even M). For the (100) direction of the $\mathbf{q}_\parallel$ vector we have two curves with essentially different dispersions for both the QW thicknesses. The following qualitative explanation of this observation can be offered. At these $\mathbf{q}_\parallel$ values the X_x and X_y QWs become different, the states at the edges of the X_x QW vary along the longer axis of the constant energy ellipsoid for the X_x valley (with large longitudinal effective mass); for the X_y QW the motion occurs along the shorter axis of the ellipsoid for the X_y valley (with a much smaller transverse effective mass). Therefore, there is good reason to believe that the lower curve with small dispersion is mainly associated with the X_x valley states, and the upper one, with the X_y valley states. For the (110) direction of the wave vector $\mathbf{q}_\parallel$, the symmetry

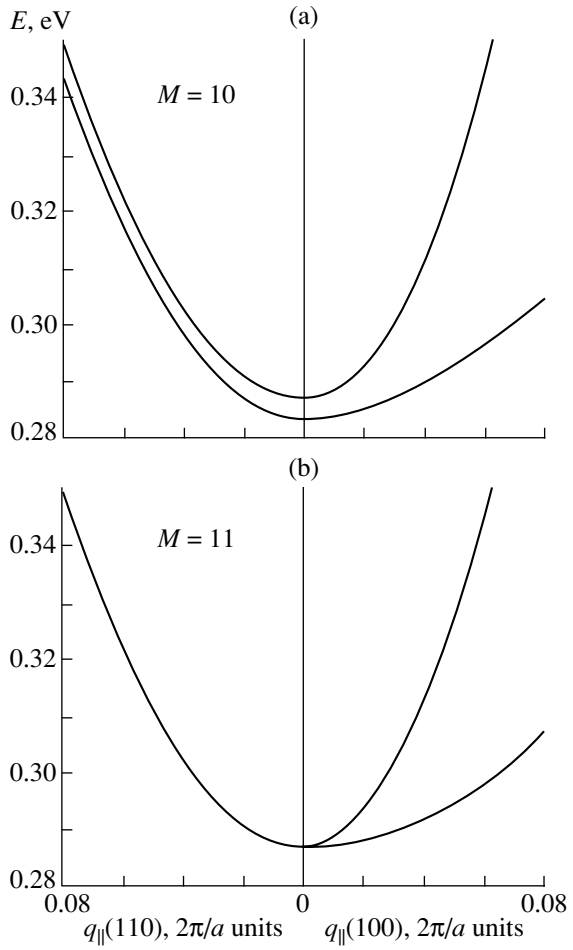

Fig. 1. Electronic energy spectrum $\varepsilon_i(\mathbf{q}_\parallel)$ in an AlAs(001) X QW for the (110) and (100) directions of the vector $\mathbf{q}_\parallel$ for different QW thicknesses: (a) $M = 10$, (b) $M = 11$.

between the valleys is preserved and the X_x and X_y QWs are identical. The dispersions for both the curves are virtually similar for each M, except for the splitting value (larger for $M = 10$ and smaller, hardly visible in Fig. 1, for $M = 11$). It is noteworthy that such a dependence takes place only for sufficiently small $q_\parallel$; with $q_\parallel$ increasing in the (110) direction, the pattern essentially changes and the concept of the $X_x - X_y$ interaction becomes incorrect; in particular, at $q_x = q_y = 0.5$ it is more appropriate to consider the LL interaction.

Let us now consider the $(\mathrm{AlAs})_M(\mathrm{GaAs})_N(001)$. We have carried out calculations for the same four superlattices as in [6] with $M = 10$, 11 and $N = 7$, 8 in various combinations. It can be shown, using the Bloch theorem for superlattices, that their electronic spectrum can be found from the equation [16]

$$\det(S^{-1}(2) - Q) = 0, \tag{28}$$

where, as in (27), $S(2)$ is the scattering matrix for a system with two heterointerfaces spaced by M AlAs layers

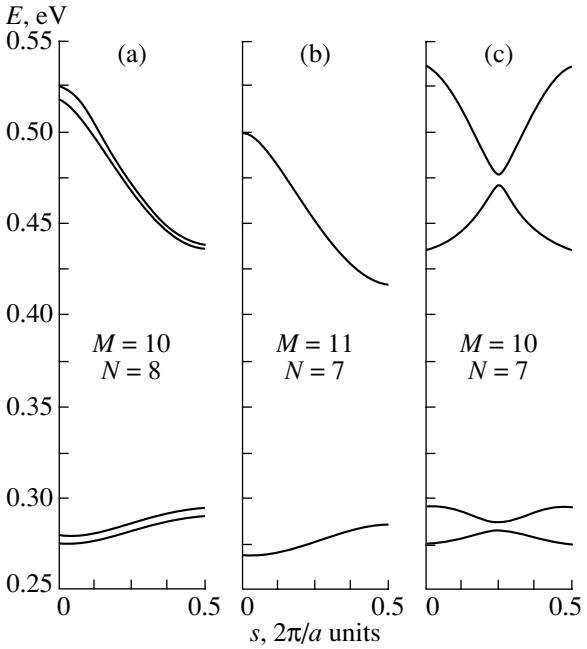

Fig. 2. Electronic energy spectra of $(AlAs)_M(GaAs)_N(001)$ superlattices; (a) $M = 10$, $N = 8$; (b) $M = 11$, $N = 7$; (c) $M = 10$, $N = 7$.

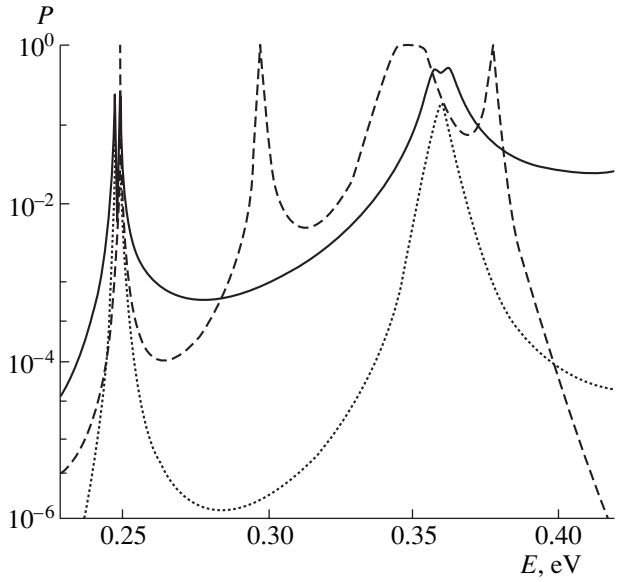

Fig. 3. Energy dependence of the transmission coefficients for the AlAs/GaAs(7)/AlAs(16)/GaAs(7)/AlAs heterostructure at $\mathbf{q}_\parallel = 0$. The solid line represents the dependence $P_{X_{1x}X_{1x}} = P_{X_{1y}X_{1y}}$; the dotted line, the dependence of $P_{X_{1x}X_{1y}} = P_{X_{1y}X_{1x}}$; and the dashed line, the transmission coefficient at $\mathbf{k}_\parallel = 0$.

at fixed E and $\mathbf{q}_\parallel$. As it was done in [6], we consider the case of $\mathbf{q}_\parallel = 0$. The Q matrix reads

$$Q = \begin{pmatrix} Q_{11} & 0 \\ 0 & Q_{22} \end{pmatrix},$$

$$(Q_{11})_{\nu\nu'} = \delta_{\nu\nu'}\exp\left[i(k_{z\nu}^{(1)} - s)\frac{a(M+N)}{2}\right],$$

$$(Q_{22})_{\mu\mu'} = \delta_{\mu\mu'}\exp\left[-i(k_{z\mu}^{(1)} - s)\frac{a(M+N)}{2}\right],$$

where s is the (001) component of the superlattice wave vector; subscripts ν and μ enumerate, respectively, the incident and reflected waves; the Bloch waves are classified into incident and reflected waves as in [8–10]; the superscript "1" corresponds to GaAs.

We carried out both exact pseudopotential calculations and approximate calculations in terms of the four-valley model for the envelopes. As before, the results are virtually the same. The calculated electronic spectra for $(AlAs)_M(GaAs)_N(001)$ superlattices, related to the conduction band X_1 states, are presented in Fig. 2. Our results are qualitatively similar to those obtained in [6]. (The results for $M = 11$, $N = 8$, not presented here, also qualitatively coincide with those in [6].) Some numerical differences are related to different choices of the bulk band structure parameters for both the materials and to different models of the heterointerface region. We use the model with a discontinuous potential at the heterointerface, whereas the average values for both substances are taken as tight-binding approximation parameters at the heterointerface in [6].

In addition, we carried out both pseudopotential and model calculations of the transmission coefficients for various AlAs/GaAs(001) structures at different $\mathbf{q}_\parallel$ values in the vicinity of the $\mathbf{q}_\parallel = 0$ point, and a good fit of the calculation results was achieved in all cases. This confirms once again the efficiency of the proposed model for the envelope functions with the parameters determined in this study. The energy dependence of the transmission coefficient for the AlAs/GaAs(7)/AlAs(16)/GaAs(7)/AlAs structure at $\mathbf{q}_\parallel = 0$ is presented as an example in Fig. 3 (the number of monolayers is shown in parentheses). Four transmission coefficients exist within the energy range mentioned

$$P_{X_{1x}X_{1x}}, \quad P_{X_{1y}X_{1y}}, \quad P_{X_{1x}X_{1y}}, \quad P_{X_{1y}X_{1x}};$$

with the first and second subscripts indicating, respectively, the type of incident and transmitted waves. The first two coefficients describing the intravalley scattering are equal at $\mathbf{q}_\parallel = 0$ because of the symmetry of the system. The energy dependence of these transmission coefficients is represented in Fig. 3 by the solid line. The dotted line in this figure shows the energy dependence of $P_{X_{1x}X_{1y}} = P_{X_{1y}X_{1x}}$ corresponding to the $X_x - X_y$ intervalley scattering. It is seen from the figure that the resonances for both the curves occur at close energies. It is noteworthy that, if we take an AlAs layer compris-

ing an odd number of monomolecular layers, there is no $X_x - X_y$ transmission, naturally, in agreement with the results for a single AlAs QW presented above. At $\mathbf{q}_{\|} \neq 0$, the resonance peaks in the transmission coefficients are shifted and split similarly to the dispersion $\varepsilon_i(\mathbf{q}_{\|})$ in the AlAs *X* QW considered above.

The dashed line in Fig. 3 shows the energy dependence of the transmission coefficients for the same structure at $\mathbf{k}_{\|} = 0$, i.e., for electron incidence normal to the heterointerface. It is seen that at 0.25 and 0.35 eV there are resonances related to the AlAs *X* QWs for both $\mathbf{k}_{\|} = 0$ and $\mathbf{q}_{\|} = 0$. This fact points to the importance of taking into account not only normally incident electrons (as is commonly done), but also those incident at some angle to the normal. Thus, it is possible to construct structures that may possess interesting current–voltage characteristics determined by superposition of different resonances.

CONCLUSION

In this communication, the matching conditions for the envelope functions of X_x and X_y states in GaAs/AlAs(001) heterostructures are considered. Under certain conditions, these states make the principal contribution to the electronic properties of heterostructures and superlattices on their base. These states are invoked in discussing some experimental results. The parameters of the model are determined on the basis of structure symmetry considerations and pseudopotential calculations. The efficiency of the proposed model for the envelope functions is confirmed by the good fit of the results of model and pseudopotential calculations of level dispersion in AlAs *X* QWs, electronic spectra of $(AlAs)_M(GaAs)_N(001)$ lattices, and transmission coefficients for *X* electrons in structures with a single *X* QW and two *X* barriers. We demonstrated that the matching conditions used in some studies [5, 7] should be corrected in accordance with the relations obtained here. The conclusion of [5, 7] that rotation of the constant energy ellipsoids only occurs owing to the X_x–X_y state mixing contradicts the consequences of the system symmetry. Our direct calculations of the energy band dispersion in the (110) and $(1\bar{1}0)$ directions also did not reveal any distinction between these directions. The anisotropy observed in [5] is presumably related to the lower symmetry of the states responsible for the observed effect, compared with those considered by the authors of [5].

ACKNOWLEDGMENTS

We thank E.L. Ivchenko who drew our attention to the study [5]. This study was supported by the Ministry of Science of the Russian Federation, Program "Surface Atomic Structures" (project no. 5.12.99) and by the Russian Foundation for Basic Research (project no. 00-02-17996).

REFERENCES

1. J. M. Smith, A. C. Klipstein, R. Grey, and G. Hill, Phys. Rev. B **57**, 1746 (1998).
2. J. M. Smith, A. C. Klipstein, R. Grey, and G. Hill, Phys. Rev. B **57**, 1740 (1998).
3. J. M. Smith, A. C. Klipstein, R. Grey, and G. Hill, Phys. Rev. B **58**, 4708 (1998).
4. J. J. Finley, M. S. Skolnick, J. W. Cockburn, *et al.*, Superlattices Microstruct. **23**, 513 (1998).
5. H. Im, A. C. Klipstein, R. Grey, and G. Hill, Phys. Rev. Lett. **83**, 3693 (1999).
6. Y. Lu and L. J. Sham, Phys. Rev. B **40**, 5567 (1989).
7. Y. Fu, M. Willander, E. L. Ivchenko, and A. A. Kiselev, Phys. Rev. B **47**, 13498 (1993).
8. D. Y. Ko and J. C. Inkson, Phys. Rev. B **38**, 9945 (1988).
9. S. N. Grinyaev and V. N. Chernyshov, Fiz. Tekh. Poluprovodn. (St. Petersburg) **26**, 2057 (1992) [Sov. Phys. Semicond. **26**, 1157 (1992)].
10. G. F. Karavaev, S. N. Grinyaev, and V. N. Chernyshov, Izv. Vyssh. Uchebn. Zaved., Fiz., No. 9, 64 (1992).
11. T. Ando, S. Wakahara, and H. Akera, Phys. Rev. B **40**, 11609 (1989).
12. T. Ando and H. Akera, Phys. Rev. B **40**, 11619 (1989).
13. G. F. Karavaev, V. N. Chernyshov, and S. N. Grunyaev, in *Abstracts of Invited Lectures and Contributed Papers of the International Symposium on Nanostructures: Physics and Technology, St. Petersburg, 1994*, p. 62.
14. G. F. Karavaev, V. N. Chernyshov, and A. A. Voronkov, Izv. Vyssh. Uchebn. Zaved., Fiz., No. 1, 63 (1997).
15. V. A. Chaldyshev and S. N. Grinyaev, Izv. Vyssh. Uchebn. Zaved., Fiz., No. 3, 38 (1983).
16. G. F. Karavaev and V. N. Chernyshov, in *Abstracts of Invited Lectures and Contributed Papers of the International Symposium on Nanostructures: Physics and Technology, St. Petersburg, 1995*, p. 126.

Translated by S. Ktitorov

Semiconductors, Vol. 35, No. 7, 2001, pp. 816–820. Translated from Fizika i Tekhnika Poluprovodnikov, Vol. 35, No. 7, 2001, pp. 850–853.

AMORPHOUS, VITREOUS, AND POROUS SEMICONDUCTORS

Adsorption-based Porosimetry Using Capacitance Measurements

E. A. Tutov*, A. Yu. Andryukov, and E. N. Bormontov

Voronezh State University, Universitetskaya pl. 1, Voronezh, 394693 Russia

**e-mail: phssd126@main.vsu.ru*

Submitted September 20, 2000; accepted for publication December 4, 2000

Abstract—It is shown that the dependence of capacitance of an Al/*por*-Si/Si structure on relative humidity is represented as an isothermal curve of physical adsorption. An analysis of this dependence makes it possible to determine the total porosity, the effective fraction of the oxide phase in *por*-Si, and the ratio between the volumes of micropores (the monomolecular and polymolecular adsorption of water which results in filling of their volume) and mesopores (which are filled according to the mechanism of capillary condensation). The size distribution for mesopores was obtained. © *2001 MAIK "Nauka/Interperiodica".*

INTRODUCTION

Special features of porous systems as subjects of structure and phase studies, the current state of theoretical notions about the structure of actual porous materials, and the development of methods for preparation of such materials make it possible to set off the porosimetry as an independent field of the structure analysis. About 60 methods of studying the porous structure of solids [1] are known; these methods differ in informativeness, range of applicability, and sensitivity [2] and include pycnometry, mercury-based porosimetry, combined adsorption–structure analysis, microscopy, calorimetry, etc. All these methods are supposed to be applied to macroscopic amounts of material to be analyzed and to yield integrated data on porosity. It is noteworthy that the adsorption–structure method, for which the primary source of data is the adsorption isothermal curve, is best suited for studying materials with a pronounced porous structure and a large proportion of micropores.

Recently, studies of porous films of metal oxides (Al_2O_3 [3]) or semiconductors (for example, porous silicon (*por*-Si) [4]), which are practically and theoretically very interesting, have become topical. The specificity of these films prohibits the wide use of volumetric or weighing adsorption measurements; however, the structure of these films makes it possible to use the high sensitivity of the electrical parameters of a heterointerface between the porous anodic layer and metal or semiconductor to external factors, in particular, to adsorption of water vapor.

The choice of water vapor is caused not so much by the small values of both the kinetic diameter (d_{H_2O} = 0.264 nm [1]) and the accommodation-site area (S = 0.125 nm^2 [5]) of a water molecule as by the anomalously large dielectric constant of water (ε = 81 [6]). The latter circumstance is bound to result in appreciable changes in the electrical impedance of the porous layer as a result of the water-vapor adsorption.

In the case of porous silicon, the *c*-Si–*por*-Si heterojunction is naturally formed in the course of preparing the porous layer, and it remains only to deposit a metal contact with a known area in order to obtain a capacitor structure. At the same time, the large dipole moment of a water molecule, which increases the total energy of interaction with *por*-Si, makes it possible to ignore the adsorption of N_2, CO_2, and O_2 molecules from atmospheric air.

Measurements of capacitance (for a metal–⟨anodic oxide⟩–metal structure) complemented with measurements of high-frequency capacitance–voltage characteristics (for a semiconductor–⟨anodic oxide⟩–metal structure) for various water-vapor pressures can be used not only to determine the characteristics of a porous anodic film but also to ensure that the analysis has a high areal resolution, which is unattainable with other methods.

The fact that various properties of semiconductors depend on the composition of surrounding gas ambiance has been noted in many publications. The main objective of the studies has been to gain insight into possible variations in the inherent properties of semiconductors exposed to a gaseous medium. There is an idea, in a sense opposite to the above, that consists in the possibility of determining the composition of the gas atmosphere surrounding a semiconductor from the analysis of variations in electrical characteristics of the

1063-7826/01/3507-0816$21.00

semiconductor [7]. In this paper, we consider the third aspect of the problem, i.e., the study of the semiconductor adsorbent itself on the basis of analyzing its response to a change in the surrounding atmosphere.

DETERMINATION OF THE MAIN STRUCTURE- AND PHASE-RELATED CHARACTERISTICS OF POROUS SILICON

According to model notions about the structure formation of porous silicon [8] and experimental data on the morphology of the *por*-Si layers [9], the structure of porous layer produced under certain conditions of anodization may be represented (with insignificant simplifications) as an irregular structure of cylindrical pores that have various diameters but an identical depth and thread through the silicon matrix.

It is known that silicon, with the degrees of oxidation of Si^{2+} and Si^{4+} (i.e., the SiO and SiO_2 oxides [10, 11]), may be found in porous silicon obtained by anodization in addition to unoxidized silicon; the fraction of oxide phase decreases with increasing distance from the surface. If a metal electrode (for example, aluminum) is deposited onto the porous silicon surface, we obtain an Al/*por*-Si/*c*-Si capacitor structure (*c*-Si stands for crystalline silicon) of the metal–oxide–semiconductor (MOS) type.

For relative humidity RH = 0%, the capacitance $C^0_{\max}$ of such a MOS structure in the enhancement mode tends asymptotically to the geometric capacitance of SiO_x insulating layer and is a combination of two components, i.e., the capacitance of a nonporous framework with a dielectric constant of ε_{SiO_x} and the capacitance of pores filled with air with dielectric constant ε_{air}. Thus, the effective dielectric a constant of ε_{eff} of the insulator layer is defined by the expression

$$\varepsilon_{eff} = \varepsilon_{SiO_x}(1-P) + \varepsilon_{air}P, \quad (1)$$

where $P = S_{por}/S$ is the parameter specifying the layer's porosity, with S standing for the gate-electrode area and S_{por} standing for the area occupied by pores at the *por*-Si surface under the electrode. The geometric capacitance $C^0_{\max}$ of the structure is specified by the effective thickness d_{eff} and effective dielectric constant ε_{eff} of the gate insulator layer; i.e., we have

$$C^0_{\max} = \frac{\varepsilon_{eff}S}{d_{eff}}. \quad (2)$$

In the depletion mode, the total high-frequency (HF) capacitance of the structure decreases because the capacitance of the space-charge region (SCR) in silicon [12] becomes connected in series to the geometric capacitance of the insulating layer and, for pronounced inversion, attains a minimum $C_{\min}$ defined as

$$\frac{1}{C_{\min}} = \frac{1}{C^0_{\max}} + \frac{1}{C_{SCR\min}}, \quad (3)$$

where

$$C_{SCR\min} = \frac{\varepsilon_{Si}(1-P)S}{W_m} \quad (4)$$

is the minimum HF capacitance of the SCR in silicon and W_m is the maximum width of SCR in silicon for the given impurity concentration N and is expressed as [12]

$$W_m = 2\left(\frac{\varepsilon_{Si}kT\ln(N/n_i)}{q^2N}\right)^{1/2}. \quad (5)$$

Here, ε_{Si} is the dielectric constant of silicon, n_i is the intrinsic charge-carrier concentration in silicon, k is the Boltzmann constant, T is absolute temperature, and q is the elementary charge.

Using expressions (3)–(5) and the experimental data for $C^0_{\max}$ and $C_{\min}$ in silicon and for the impurity concentration N in silicon, we obtain the porosity parameter P. Substituting this parameter into formula (1), we obtain the effective dielectric constant ε_{eff} of the insulator layer; finally, inserting ε_{eff} into expression (2), we obtain the effective thickness d_{eff} of the insulator layer.

The total capacitance $C_{\max}$ of an Al/*por*-Si/*c*-Si structure in the enhancement mode of the surface SCR and in the presence of water vapors can be represented as the sum of three components, i.e., the capacitance of the nonporous SiO_x framework with the dielectric constant ε_{SiO_x}, the capacitance of pores filled with air having the dielectric constant ε_{air}, and the capacitance of pores filled with a condensate having the dielectric constant ε_{H_2O} (taking into account partial penetration of water vapors under the metal electrode); thus, we have

$$C_{\max} = \frac{S}{d_{eff}}\{\varepsilon_{SiO_x}(1-P) + \varepsilon_{air}[Pk(1-\eta) + P(1-k)] + \varepsilon_{H_2O}Pk\eta\}. \quad (6)$$

Here, $\eta = S_{fill}/S_{por}$ is the degree of filling of pores with the condensate, with S_{fill} standing for the area occupied by the pores at the *por*-Si surface that are filled with the condensate for a specified vapor pressure; k is the ratio between the area occupied by the pores accessible to water vapors and the total area occupied by pores (the coefficient of accessibility of pores to water vapors).

It is assumed in this model that the effective thickness of the insulating layer for air and water is equal to the oxide-layer thickness at the surface of porous silicon. We note that the definitions of the surface and bulk

porosities coincide for the assumed cylindrical shape of the pores.

As the humidity approaches 100%, the capacitance of the structure increases owing to the capillary condensation of water vapor in the micropores and mesopores along the boundary of the aluminum electrode. For RH = 100% ($\eta = 1$), expression (6) can be written as

$$C_{\max}^{100} = \frac{S}{d_{\text{eff}}}[\varepsilon_{SiO_x}(1-P) + \varepsilon_{\text{air}}P + (\varepsilon_{H_2O} - \varepsilon_{\text{air}})Pk] = \frac{S}{d_{\text{eff}}}[\varepsilon_{\text{eff}} + (\varepsilon_{H_2O} - \varepsilon_{\text{air}})Pk]. \quad (7)$$

The relation between the values of the structure's largest capacitance for RH = 0% ($C_{\max}^0$) and RH = 100% ($C_{\max}^{100}$) is given by

$$C_{\max}^{100} = C_{\max}^0\left[1 + \frac{\varepsilon_{H_2O} - \varepsilon_{\text{air}}}{\varepsilon_{\text{eff}}}Pk\right], \quad (8)$$

and makes it possible to determine the coefficient k ($0 < k < 1$), which depends on the ratio between the area of the electrode to its perimeter, on the total porosity, on the degree of connectivity of the pores, and possibly on the relative humidity. This coefficient is the upper bound of the degree of connectivity of the pores because, for a system of connected pores, the entire volume under the electrode would be filled in the course of adsorption; i.e., we would have $k = 1$ irrespective of the capacitor's configuration.

Thus, measurements of HF capacitance of an Al/*por*-Si/*c*-Si structure in the enhancement and inversion regions for the relative humidity of RH = 0 and 100% ($C_{\max}^0$, $C_{\max}^{100}$ and $C_{\min}$) makes it possible to calculate the total porosity, the degree of connectivity of pores, and the fraction of oxide phase in the porous layer. The results of the calculations for specific *por*-Si samples have been reported recently [13].

AN ANALYSIS OF THE SIZE DISTRIBUTION FOR PORES

Solid-state adsorbents may contain pores with various sizes and morphology, depending on the nature and the preparation technology of the adsorbent. In many situations, the cross-sectional size of pores is of particular interest. The classification of pores by size officially adopted by the International Union of Pure and Applied Chemistry (IUPAC) is based on the correlation between each range of pore sizes and a characteristic adsorption mechanism [14]. According to this classification, porous silicon can be separated into microporous Si (the pore diameter $D < 2$ nm), for which monomolecular and polymolecular adsorption is characteristic; mesoporous Si (2 nm $< D <$ 50 nm), for which capillary condensation is the characteristic mechanism of adsorption; and macroporous Si ($D >$ 50 nm), whose adsorption properties differ little from those of nonporous material. The current technology makes it possible to form the *por*-Si layers with various distributions of pore size; as a result, the humidity sensors sensitive in different ranges of relative humidity may be produced [15].

We now turn our attention to an analysis of distribution of pore sizes. Using the above designations, the volume of adsorbed water is given by

$$V = d_0 SPk\eta, \quad (9)$$

where d_0 is the thickness of porous layer. It follows from formula (6) that the dependence of the structure capacitance in the enhancement mode on the degree of filling of the pores (dependent on humidity) can be expressed as

$$C_{\max} = C_{\max}^0 + (C_{\max}^{100} - C_{\max}^0)\eta = C_{\max}^0 + (C_{\max}^{100} - C_{\max}^0)V/V_0, \quad (10)$$

where $V_0 = d_0 SPk$ is the total porous-layer volume accessible to adsorption. This dependence, combined with formula (6) and measured at a constant temperature, represents the isothermal curve for water vapor, and its analysis allows one to obtain all the characteristics available for the structure–adsorption methods of porosimetry, including the distribution of pore sizes.

The simulation of water-vapor adsorption in porous silicon amounts to the calculation of the parameter η in expression (6) as a function of the relative humidity.

In the range of low relative humidities, two stages are recognized: (i) the formation of a molecular monolayer and (ii) the subsequent polymolecular overgrowth. Qualitatively, this situation takes place for both continuous and porous surfaces. For mesoporous adsorbents, capillary condensation is most typical. However, in the general case, these two processes make a comparable contribution; this should be taken into account in the analysis of adsorption. It is also noteworthy that, for pores with effective sizes 2–3 times the diameters of the adsorbed molecules, the monolayer is not formed and adsorption proceeds by volume filling. An analysis of this portion of the isothermal curve for adsorption makes it possible to determine just the specific volume occupied by such micropores [16].

Under certain conditions, the formation of a porous layer may be expected if the radii r of emerging pores are within some range of values. When simulating the

distribution of pore sizes $f(r)$, the logarithmically normal distribution is most often used [14], i.e.,

$$f(r) = \frac{1}{\ln(\sigma_g\sqrt{2\pi})}\exp\left[-\frac{(\ln r - \ln r_g)^2}{2\ln^2\sigma_g}\right], \quad (11)$$

where r_g is the geometric average of r and $\ln\sigma_g$ is the standard deviation of $\ln r$ and specifies the variations from the average.

The amount of water adsorbed in micropores may be estimated using the Brunauer–Emmet–Teller (BET) equation [14] as

$$\frac{n}{n_0} = \frac{1}{1-p/p_0} - \frac{1}{1+p/p_0(Q-1)}. \quad (12)$$

Here, n is the absolute amount of adsorbed gas (expressed in mols); n_0 is the capacity of a monolayer (expressed in mols of adsorbate); $Q \approx \exp[(q_A - q_L)/RT]$, where q_A is the heat of adsorption and q_L is the condensation heat (i.e., $q_A - q_L$ is the net heat of adsorption); R is the universal gas constant; p is pressure; and p_0 is the saturated vapor pressure. Formula (12) describes the process of polymolecular adsorption and specifies the number of monolayers adsorbed under the given pressure.

Capillary condensation is the characteristic mechanism of adsorption for mesopores; this mechanism is described by the Kelvin equation [14]

$$p = p_0\exp\left(\frac{2\sigma V_m}{r_c RT}\right), \quad (13)$$

where p_0 is the saturated-vapor pressure at temperature T, σ is the surface tension of liquid phase (water), V_m is the molar volume of the liquid phase, and r_c is the capillary radius (negative for wetting liquid). According to formula (13), all pores with radii smaller than a certain critical r, which corresponds to a given relative humidity RH = p/p_0, are filled in the layer of porous silicon.

Capillary condensation is prevalent in the processes of the water-vapor adsorption for a relative humidity of 35% and higher, whereas for a lower humidity the main contribution is made by monomolecular and polymolecular adsorption, which leads to volumetric filling of micropores and to the effective decrease in the radii of mesopores [14]. In a broad sense, adsorption in microporous materials involves capillary condensation irrespective of the adsorption mechanism.

We note that only quantity η depends on the relative humidity p/p_0 in formula (6); i.e.,

$$\eta = \frac{S_{\text{fill}}}{S_{por}} = \frac{\int_0^{r_c} f(r)\pi r^2 dr}{S_{por}}. \quad (14)$$

Here, $r_c = r_c(p/p_0)$ is the critical pore radius, which is calculated according to the Kelvin equation and represents the upper boundary for the size of the pores filled with condensate for a given relative humidity, and $f(r)$ is the distribution function for pore sizes.

In the range of high relative humidities, in which case the process of capillary condensation prevails, we can differentiate the dependence $C_{\max}(p/p_0)$ [see (6)] with respect to r taking into account the relation between r and p/p_0 (13) and obtain an "experimental" distribution function for mesopore sizes (in the region of $r > 1.2$ nm) as

$$f^*(r) = \frac{d_{\text{eff}}}{\omega k(\varepsilon_{H_2O}-1)}\frac{2\sigma V_m}{RT}\frac{1}{r^4} \times \exp\left(-\frac{2\sigma V_m}{rRT}\right)\frac{dC_{\max}}{d(p/p_0)}, \quad (15)$$

where the derivative $dC_{\max}/d(p/p_0)$ is obtained by graphical differentiation.

We can find the remaining parts of the function $f(r)$ (for micropores) using model distribution (11) normalized in reference to the total porosity and the BET equation.

Thus, the physical adsorption of water vapor in micropores and capillary condensation in mesopores both result in an effective increase in the dielectric constant of porous layer, which may be used to develop capacitance-type humidity sensors. An analysis of the relative-humidity dependence for the capacitance of such sensors which represents the isothermal curve for adsorption makes it possible to determine the quantitative relation between micropores and mesopores in porous silicon and the size distribution for mesopores [17].

REFERENCES

1. T. G. Plachenov and S. D. Kolosentsev, *Porometry* (Khimiya, Leningrad, 1988).
2. P. G. Cheremskoĭ, *Methods for Researching Porosity of Solids* (Énergoatomizdat, Moscow, 1985).
3. V. V. Petrova, *Microporosity of Anodic Aluminum-Oxide Films* (Petrozavodsk. Univ., Petrozavodsk, 1992).
4. *Properties of Porous Silicon*, Ed. by L. Canham (IEE, London, 1997), EMIS Datareviews Series, No. 18.
5. A. L. McClellan and H. E. Harnsberger, J. Colloid Interface Sci. **23**, 577 (1967).
6. *Tables of Physical Quantities*, Ed. by I. K. Kikoin (Atomizdat, Moscow, 1976).
7. I. A. Myasnikov, V. Ya. Sukharev, L. Yu. Kupriyanov, and S. A. Zav'yalov, *Semiconductor Sensors in Physicochemical Research* (Nauka, Moscow, 1991).
8. L. N. Aleksandrov and P. L. Novikov, Pis'ma Zh. Éksp. Teor. Fiz. **65**, 685 (1997) [JETP Lett. **65**, 714 (1997)].

9. É. Yu. Buchin, A. V. Postnikov, A. V. Prokaznikov, *et al.*, Pis'ma Zh. Tekh. Fiz. **21** (1), 60 (1995) [Tech. Phys. Lett. **21**, 27 (1995)].

10. E. P. Domashevskaya, V. M. Kashkarov, E. Yu. Manukovskii, *et al.*, J. Electron Spectrosc. Relat. Phenom. **88–91**, 958 (1998).

11. L. V. Belyakov, T. L. Makarova, and V. I. Sakharov, Fiz. Tekh. Poluprovodn. (St. Petersburg) **32**, 1122 (1998) [Semiconductors **32**, 1003 (1998)].

12. S. Sze, *Physics of Semiconductor Devices* (Wiley, New York, 1981; Mir, Moscow, 1984).

13. E. A. Tutov, A. Yu. Andryukov, and V. M. Kashkarov, Zh. Prikl. Khim. **73** (7), 1071 (2000).

14. S. J. Gregg and K. S. Sing, *Adsorption, Surface Area, and Porosity* (Academic, New York, 1982; Mir, Moscow, 1984).

15. A. A. Kovalevskiĭ and I. L. Baranov, Mikroélektronika **25** (4), 298 (1996).

16. I. O. Protod'yakonov and S. V. Silarov, *Mechanics of Adsorption in Gas–Solid Systems* (Nauka, Leningrad, 1985).

17. E. A. Tutov and É. P. Domashevskaya, in *Proceedings of the International Workshop "Results of Fundamental Research for Investment" ("IWRFRI 2000"), St. Petersburg, 2000*, p. 182.

Translated by A. Spitsyn

Semiconductors, Vol. 35, No. 7, 2001, pp. 821–826. Translated from Fizika i Tekhnika Poluprovodnikov, Vol. 35, No. 7, 2001, pp. 854–860.

AMORPHOUS, VITREOUS, AND POROUS SEMICONDUCTORS

Structural Transformations and Silicon Nanocrystallite Formation in SiO_x Films

V. Ya. Bratus'*, V. A. Yukhimchuk, L. I. Berezhinsky, M. Ya. Valakh, I. P. Vorona, I. Z. Indutnyi, T. T. Petrenko, P. E. Shepeliavyĭ, and I. B. Yanchuk

Institute of Semiconductor Physics, National Academy of Sciences of Ukraine, Kiev, 03028 Ukraine

** e-mail: endor@div51.semicond.kiev.ua*

Fax: 38(044)2658342

Submitted November 10, 2000; accepted for publication December 19, 2000

Abstract—The results of a comprehensive study by the methods of IR absorption, Raman scattering, photoluminescence (PL), and electron spin resonance (ESR) of SiO_x films prepared by thermal evaporation of SiO in a vacuum are presented. The nature of structural transformations occurring on annealing the films is determined. Annealing in the temperature range 300–600°C gives rise to a PL band at 650 nm, presumably related to structural defects in SiO_x film. Raising the annealing temperature further leads to healing of such defects and quenching of the PL band. Silicon precipitates pass from the amorphous to the crystalline state on being annealed at T_{ann} = 1100°C, which gives rise to a new PL band at 730 nm. ESR spectra of P_b centers were recorded at the interface between randomly oriented silicon nanocrystallites and SiO_2. © *2001 MAIK "Nauka/Interperiodica".*

INTRODUCTION

Nanocrystalline silicon (*nc*-Si) has been extensively studied in the last decade with the aim of creating visible-light emitters on the basis of highly developed low-cost silicon technology. Of particular interest in this respect is a study of the electronic structure and optical properties of *nc*-Si. Nanocrystalline silicon can be prepared by various techniques, e.g., ion implantation and magnetron sputtering [1, 2], laser sputtering of a silicon target [3], and molecular-beam epitaxy [4].

Fabrication of functional light-emitting devices based on structures with nanocrystalline Si has already been reported [5, 6]. The technology of SiO deposition onto various substrates by thermal vacuum evaporation is rather promising for the manufacture of silicon-based large-area displays. In this case, a nonstoichiometric SiO_x layer is formed, with $x < 2$. This unstable phase can be preserved at room temperature for a long time. Two models have been proposed for describing the structure of SiO_x films: the model of (Si + SiO_2) mixture and the random-binding model [7] in which each silicon atom is tetrahedrally coordinated to y silicon atoms and $(4 - y)$ oxygens. Data furnished by optical measurements [7, 8], X-ray photoelectron spectroscopy [9], and ESR spectroscopy of amorphous SiO_x layers [10] are adequately described in terms of the random-binding model. Annealing of SiO_x films may lead to the precipitation of a phase of fine Si particles forming silicon crystallites upon further heating [7–9].

Photoluminescence (PL) spectra of SiO_x films prepared by thermal evaporation of SiO have not been studied in detail. More attention has been given to films obtained by other methods [11], exhibiting PL bands associated with Si nanocrystallite formation. Despite the great number of investigations in this field, the nature of visible light emission by structures containing silicon nanocrystallites remains a matter of discussion. An important point in this regard is the mechanism of emission: is light emitted via the recombination of electron–hole pairs in silicon nanocrystallites themselves, having an electronic structure modified by quantum confinement, or through the transport of carriers toward the Si/SiO_x interface and/or their localization on certain centers with eventual recombination.

In this study, a set of optical and ESR investigations of SiO_x films is deposited by thermal evaporation of SiO in a vacuum and annealed in a wide temperature range. A relationship is established between different PL bands in these films and thermally stimulated changes in their structure.

EXPERIMENTAL

SiO_x films were obtained by thermal evaporation of SiO in a vacuum of ~10^{-3} Pa onto silicon, quartz, and sapphire substrates kept at room temperature. The film thickness was varied between 0.5 and 2.5 μm. In the course of the study, the films were annealed in an atmosphere of nitrogen at temperatures in the range from 100 to 1100°C, with the annealing time ranging from 10 min to 4 h.

PL and Raman spectra were measured at room temperature on a DFS-24 double monochromator in reflec-

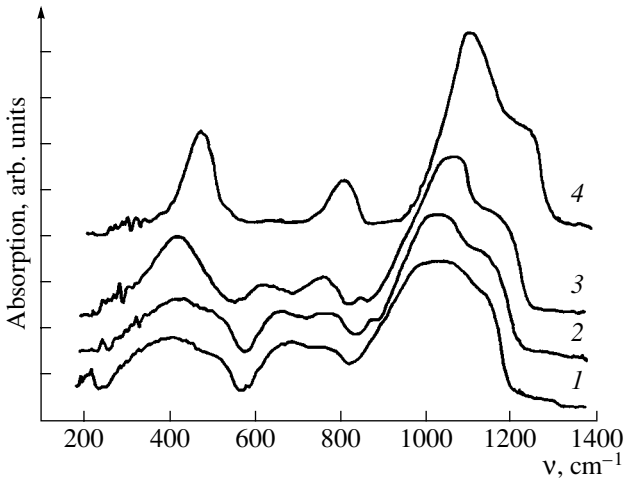

Fig. 1. IR absorption spectra of SiO_x samples on silicon substrates (*1*) immediately after deposition and upon thermal annealing in an atmosphere of nitrogen for 15 min at T_{ann} = (*2*) 500, (*3*) 700, and (*4*) 1100°C.

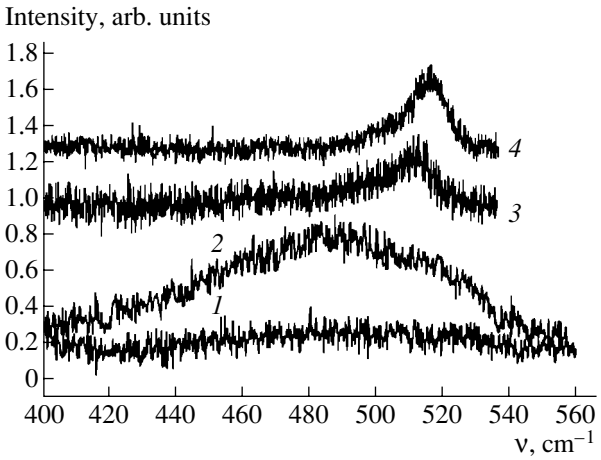

Fig. 2. Raman spectra of SiO_x films on sapphire substrates, measured after annealing for 15 min at T_{ann} = (*1*) 800, (*2*) 900, and (*3*) 1100°C. Spectrum *4* was obtained after annealing a sample at 1100°C for 120 min.

tion arrangement. The spectra were excited by Ar^+ laser radiation with wavelengths of 487.9 and 514.5 nm, respectively. The power of light did not exceed 50 mW in either case. To prevent sample heating during the measurements, the laser light was focused with a cylindrical lens. The signals were recorded with a cooled FÉU-136 photomultiplier in the photon count mode. All the PL spectra were corrected for instrument sensitivity. IR absorption spectra were measured on a Perkin–Elmer 599B double-beam spectrophotometer. The transmission spectra were recorded on a KSVU-23 instrument at room temperature.

ESR studies were done in the *X*-band (9.36 GHz) at room temperature with a magnetic field modulation at a frequency of 100 kHz. The number of paramagnetic defects and *g*-factor values were determined relative to the $MgO:Mn^{2+}$ reference with a known number of spins which was placed in the microwave cavity together with a sample under study. The error in determining the number of defects in these measurements was ±40%, whereas the relative inaccuracy in comparing ESR signals from different samples did not exceed ±15%.

RESULTS AND DISCUSSION

Figure 1 shows the IR absorption spectra of SiO_x films on silicon substrates measured immediately after their deposition (spectrum *1*) and after subsequent thermal annealing in an atmosphere of argon at different temperatures (spectra *2–4*). It can be seen that the spectrum contains a number of strong bands. It is known [12] that, for SiO_2, the band at $\nu \approx 400$ cm^{-1} corresponds to Si–O rocking vibrations and bands at ~800 and ~1100 cm^{-1} correspond to Si–O bending and stretching vibrations, respectively. With increasing annealing temperature, the bands change their shape and their peaks are shifted to higher frequencies. It was established in [8] that the dependence of the peak position of the asymmetric stretching Si–O–Si mode in the region around $\nu \approx 1100$ cm^{-1} and the *x* value in SiO_x is nearly linear. An evaluation of *x* by means of this dependence demonstrated that it varies between 1.3 (immediately after deposition of a film) and 2 (after its thermal annealing at T_{ann} = 1100°C).

The observed changes in the IR spectra may result from a transition of a metastable SiO_x film from a single- to two-phase state. As shown in [13], the following reaction occurs in the annealing of SiO_x films:

$$2SiO_x \longrightarrow xSiO_2 + (2 - x)Si.$$

According to the Raman spectral data, the conversion of SiO_x into SiO_2 and elemental Si also occurs in the case in question. Since a strong Raman signal from the silicon substrate (and a weaker signal from sapphire) are recorded in the spectral region under study (ν = 400–560 cm^{-1}), the spectra were measured with films deposited onto sapphire substrates. The appearance of a broad band peaked at around 490 cm^{-1} in Raman spectra of samples annealed at T_{ann} = 900°C indicates the formation of amorphous silicon clusters in SiO_x films (Fig. 2). According to IR spectral data, the coagulation of Si atoms into clusters starts upon annealing at lower temperatures. However, their detection in the Raman spectra is limited by the sensitivity of this method. Raising the annealing temperature to 1100°C leads to a substantial decrease in the intensity of this band and the appearance of a band peaked at 512.5 cm^{-1} with a half-width of about 10 cm^{-1}, which points to the formation of Si nanocrystallites. The model of "spatial correlation of phonons" [14, 15] was applied to evaluate the average size of silicon crystallites formed upon annealing at

1100°C for 15 min, which turned out to be about 2 nm. Increasing the time of annealing, the average size of the crystallites grows, which is manifested in a shift of the Raman peak to higher frequencies and a decrease in its half-width (Fig. 2, spectrum *4*).

Additional data on film structure obtained by analyzing ESR spectra were found to be identical for samples on silicon and quartz substrates. Spectra of SiO_x films on silicon substrates are presented in Fig. 3. Unannealed samples are characterized by a broad structureless Gaussian-shaped line with $g = 2.0038 \pm 0.0002$ and width $\Delta H_{pp} = 1.0$ mT, whose parameters are close to those of the ESR line observed in amorphous SiO_x layers with $x \approx 1.3$ [10]. On the assumption of a uniform distribution of paramagnetic centers across the film thickness, their volume density is found to be rather high (4×10^{20} cm^{-3}). In the annealing temperature range 200–700°C, the number of paramagnetic centers decreases by more than an order of magnitude, which is accompanied by a narrowing of the ESR line and its shift to higher *g*-factor values. Such a behavior and the asymmetric line shape indicate that the spectra are a superposition of several components. In contrast to SiO_2 layer implanted with Si^+ ions [16], no narrow ESR lines attributable to a certain kind of paramagnetic defects are observed in the SiO_x films under study. Similarly to implanted SiO_2 layers [16], defects with $g \approx 2.0048$ are stablest in this temperature range.

Raising the annealing temperature from 700 to 900°C makes the number of defects nearly four times larger. The observed symmetric ESR line has parameters ($g = 2.0055$ and $\Delta H_{pp} = 0.62$ mT) typical of defects in amorphous silicon (*a*-Si) [17]. Raising the annealing temperature to 1100°C again leads to a decrease in the total number of defects, shape asymmetry, and an apparent broadening of the ESR line because of the appearance of features at $g \approx 2.008$ and $g \approx 2.002$, becoming more pronounced with an increase in the annealing time to 4 h (Fig. 4). Interestingly, the total number of defects remains nearly unchanged in the process. The observed features are characteristic of the so-called P_b centers—dangling bonds of silicon atoms at the Si/SiO_2 interface [18].

The obtained ESR data are readily interpreted in terms of the random-binding model on the assumption that the paramagnetic centers are related to dangling bonds in $Si–Si_yO_{4-y}$ tetrahedra. An ESR spectrum can be regarded as the superposition of several resonance lines with different *g*-factors, whose relative intensities are proportional to the statistical content of the corresponding tetrahedra in the disordered structure of a SiO_x film. As is known, the dangling bonds in *a*-Si, further designated as DB *a*-Si, and oxygen vacancies in SiO_2, called *E*' centers [20], are characterized by the values $g_{DB} = 2.0055$ and $g_{E'} = 2.0005$, respectively. They can be represented as $Si_3{\equiv}Si–$ and $O_3{\equiv}Si–$, where an unpaired electron is shown by a single line. The fact

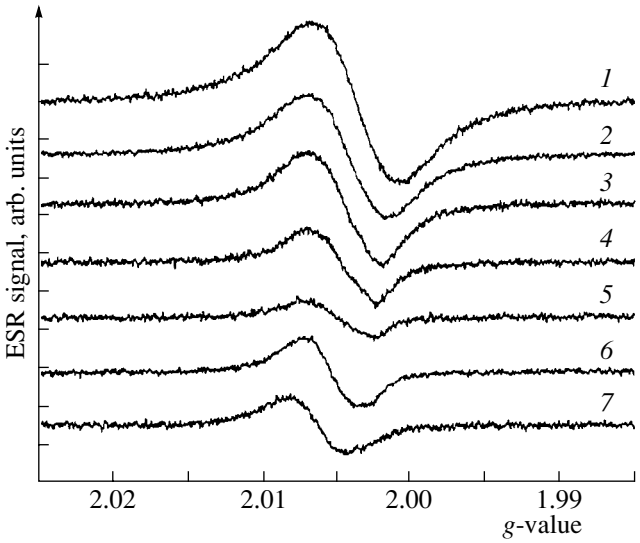

Fig. 3. ESR spectra ($f = 9.363$ GHz, $T = 300$ K) of SiO_x films on silicon substrates (*1*) immediately after deposition and upon thermal annealing in an atmosphere of nitrogen for 15 min at T_{ann} = (*2*) 300, (*3*) 400, (*4*) 500, (*5*) 700, (*6*) 900, and (*7*) 1100°C. The intensities of the spectra are normalized to unit sample area.

that an ESR line with $g = 2.0038$ (intermediate between the resonance positions of DB *a*-Si and *E*' center) is observed in the initial films means that their basic structural elements are $Si–Si_3O$, $Si–Si_2O_2$, and $Si–SiO_3$ tetrahedra. The shift of the ESR line on annealing the films at $T_{ann} = 700$°C indicates that the healing of structural defects begins in regions with a high content of Si–O bonds. It seems natural to assume that the line with $g = 2.0048$, also observed in silicon-enriched SiO_2 powder [20], corresponds to dangling bonds of silicon atoms in $Si–Si_3O$ and $Si–Si_2O_2$ tetrahedra, i.e., to $OSi_2{\equiv}Si–$ structural units.

As follows from the ESR and Raman spectra, the coagulation of Si atoms leads to the formation of their amorphous phase at $T_{ann} = 900$°C. According to Raman data, raising the annealing temperature to 1100°C leads to the formation of Si nanocrystallites. The features appearing in the ESR spectra can be accounted for by the defect formation at the interface between Si and SiO_2 nanocrystallites. P_b centers appear in ESR spectra of single-crystal silicon oxidized by various methods (see, e.g., [21]). To the best of our knowledge, these centers have been clearly recorded in chaotically oriented Si nanocrystallites in SiO_2 for the first time. The observed spectra can be described as a superposition of three components associated with DB *a*-Si and chaotically oriented P_{b1} and P_{b0} centers, with the intensities of these components related as 5.5 : 1 : 1 (Fig. 4). In modeling the ESR line of the dangling bond of silicon, a Lorentzian line with $g = 2.0058$ and $\Delta H_{pp} = 0.60$ mT was chosen. Spectra of chaotically oriented P_b centers

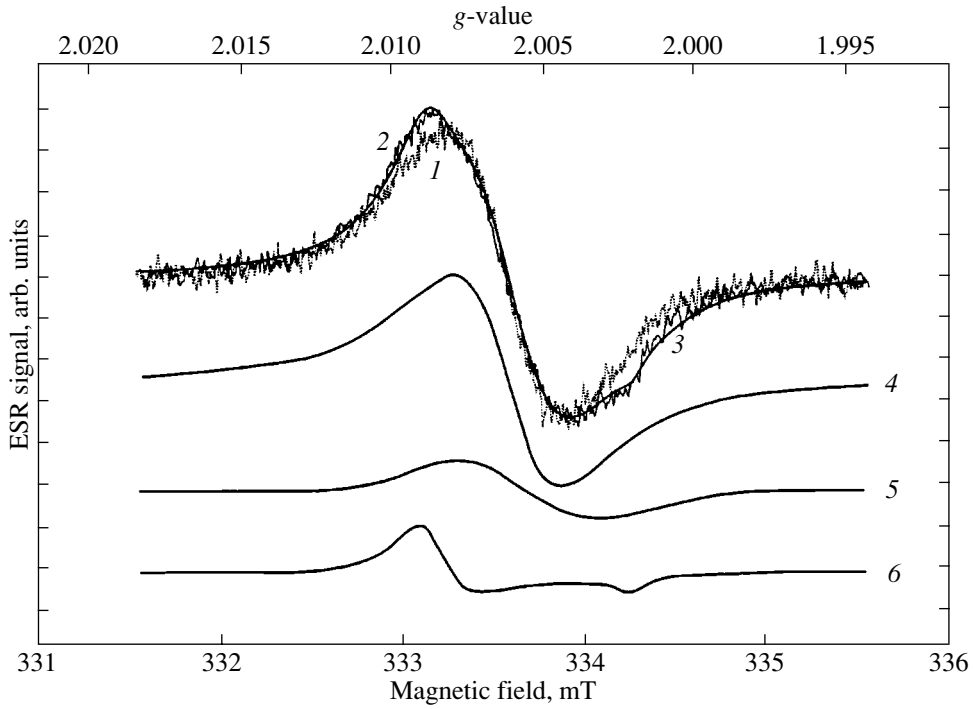

Fig. 4. ESR spectra (f = 9.363 GHz, T = 300 K) of SiO_x film on quartz substrate annealed at 1100°C for (*1*) 15 min and (*2*) 4 h. For convenience of comparing ESR line shapes, the intensity of spectrum *1* is reduced by a factor of 1.2. The calculated spectrum (solid smooth line *3*) is a superposition of three components related to three kinds of defects: the isotropic line of Si dangling bonds in *a*-Si (*4*) and lines of chaotically oriented P_{b1} and P_{b0} centers (spectra *5* and *6*, respectively). The spectroscopic parameters of modeling are given in the text.

were calculated using Lorentzian lines with parameters found for oxidized single-crystal silicon [20]: g_1 = 2.0058, g_2 = 2.0074, g_3 = 2.0022, and ΔH_{pp} = 0.41 mT for the P_{b1} center; and $g_{\|}$ = 2.0019, $g_{\perp}$ = 2.0084, $\Delta H_{pp\|}$ = 0.12 mT, and $\Delta H_{pp\perp}$ = 0.26 mT for the P_{b0} center.

Thus, the structural changes occurring in SiO_x films are manifested in ESR spectra in a wide range of annealing temperatures.

The initial SiO_x films show no photoluminescence in the visible spectrum. On their annealing at temperatures higher than 300°C, a broad band appears in the PL spectrum centered around ~650 nm and modulated with periodic peaks (Fig. 5, spectrum *1*). These peaks originate from the interference of light reflected from the film surface and the SiO_x/substrate interface. The interference origin of the peaks (rather than that associated with superposition of PL bands of varied nature) is shown by the fact that, with the decreasing thickness of SiO_x films in their etching or upon depositing thinner layers, the PL peaks are shifted to higher frequencies. The spacings between the interference peaks are described by the expression [22]

$$2nd = \left(\frac{1}{\lambda_1} - \frac{1}{\lambda_2}\right)^{-1},$$

where n is the refractive index, d is the thickness of a SiO_x film, and λ_1 and λ_2 ($\lambda_1 > \lambda_2$) are the wavelengths corresponding to the peaks in the interference pattern. As is known, the n value for SiO_2 is close to 1.46. At the same time, the refractive index of SiO_x, found using the above formula, is substantially higher (n = 2.25), which is characteristic of SiO_2 films with excess silicon [1].

An important issue of the present study is the mechanism of the appearing PL. As shown in the insert of Fig. 5, its intensity grows with the annealing temperature increasing to 600°C and then falls dramatically. In all probability, the PL is related to defects or complexes of defects, which is evidenced by the correlation between changes in ESR and PL intensities in the annealing temperature range 500–700°C.

Annealing at 1100°C leads to the appearance in the PL spectrum of a broad band peaked at 730 nm (Fig. 5, spectrum *2*). This band is also modulated with interference peaks. Its appearance is attributed to the formation of silicon nanocrystallites at this temperature. The parameters of this luminescence band are similar to those of the PL from SiO_2 samples implanted with Si^+ ions and annealed at T_{ann} = 1100°C [16]. Raising the annealing duration from 10 min to 4 h led, as a rule, to a severalfold increase in PL intensity. As for the P_b centers revealed in ESR spectra and which are assumed to enhance the nonradiative recombination channel [23],

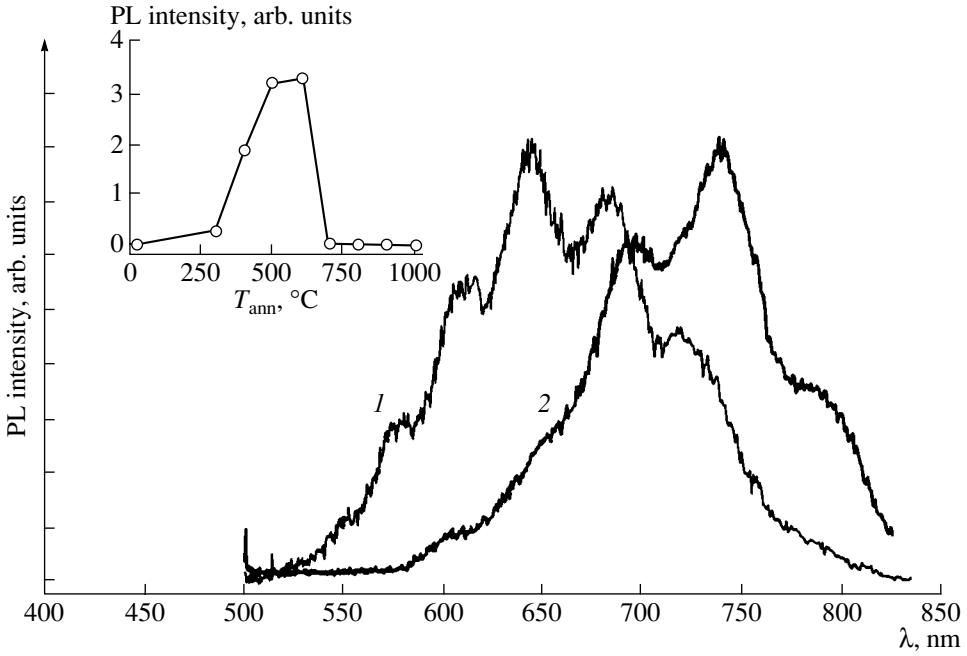

Fig. 5. PL spectra of SiO_x films on silicon substrates annealed for 15 min at T_{ann} = (*1*) 500 and (*2*) 1100°C. Inset: intensity of PL band peaked at 650 nm vs. the annealing temperature.

the situation in SiO_x films is similar to that observed in porous Si [24]. In this material, a qualitative correlation between the number of P_b centers and the fall of the PL intensity is only observed in separate samples at sufficiently high defect concentrations.

It is known that the average size of Si crystallites grows with an increasing duration of annealing [25]. Indeed, annealing for 2 h shifts the Raman peak to higher frequencies, which indicates an increase in the average crystallite size. At the same time, the peak position of the PL band remains unchanged, with only the PL intensity increasing. Such a behavior can be understood in terms of Kanemitsu's interference model [26]. According to this model, the process of radiative recombination in surface-oxidized Si nanocrystallites consists in the following. Electron–hole pairs are photogenerated within nanocrystallites and then diffuse into the interfacial SiO_x layer, whose band gap is narrower than that of *nc*-Si or pure SiO_2. The pairs are localized at the interface and then recombine with light emission. This model accounts for the dependence of the PL intensity on nanocrystallite size at practically any position of the PL band peak.

SiO_x films annealed at different temperatures have color in transmitted light, varying from yellow for T_{ann} = 300°C to dark brown at T_{ann} = 900°C and then again to yellow upon annealing at 1100°C. The corresponding transmission spectra are shown in Fig. 6. It can be seen that, upon annealing at 500°C, the absorption edge is shifted to shorter wavelengths; then, with the annealing temperature raised to 900°C, its pronounced shift to longer wavelengths is observed. Further annealing at 1100°C shifts the transmission band to its original position. Such changes may result from a structural transformation in the SiO_x films. Annealing at temperatures in the range from 100 to 500°C heals the defects and leads to structural ordering of the SiO_x films, which is also manifested in IR absorption band narrowing (Fig. 1). As a result, the absorption edge shifts to shorter wavelengths. It was noted in discussing the results of ESR and Raman measurements that annealing at 500 to 900°C favors the coagulation of Si atoms into amorphous clusters. Since the absorption

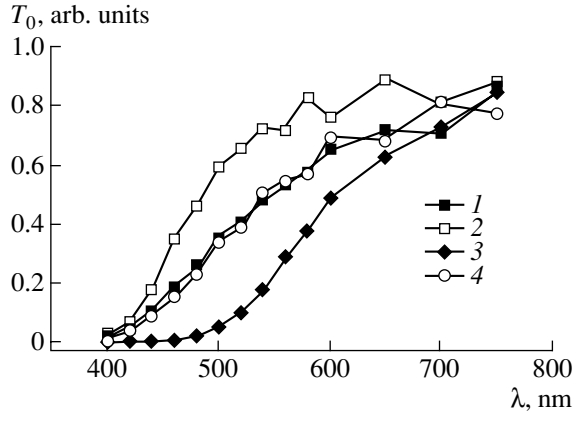

Fig. 6. Transmission spectra of SiO_x films (*1*) after deposition and annealing for 15 min at T_{ann} = (*2*) 500, (*3*) 900, and (*4*) 1100°C.

edge of *a*-Si lies at longer wavelengths than that in SiO_x films, it is the former that plays the decisive role in this two-phase system, which is manifested in its transmission spectrum (Fig. 6, spectrum *3*). In annealing above 900°C, amorphous silicon clusters start to crystallize, producing Si crystallites whose electronic structure is modified by quantum confinement. As a result, the absorption edge is again shifted to shorter wavelengths.

CONCLUSION

Thus, the performed optical and ESR studies revealed the stages and nature of structural transformations that occur in the annealing of SiO_x films obtained by thermal evaporation of SiO in a vacuum. In a transition of the films from the single-phase (SiO_x) to the two-phase (Si + SiO_2) state, the x value steadily grows from 1.3 in the initial films to 2 in those annealed at T_{ann} = 1100°C. The forming silicon precipitates are first amorphous and then become crystalline. This is indicated both by the Raman data and by ESR spectra of P_b centers related to chaotically oriented Si nanocrystallites in SiO_2. Structural changes occurring in SiO_x films in the annealing temperature range 300–700°C are accompanied first by a rise in intensity and then by quenching of the PL band peaked at 650 nm. This band is in all probability related to defects in SiO_x. With the annealing temperature increased, to T_{ann} = 1100°C, a band peaked at 730 nm associated with the forming silicon crystallites appears in the PL spectrum.

ACKNOWLEDGMENTS

We thank B.D. Shanina for her interest in the work and her helpful participation in the discussions.

REFERENCES

1. T. Shimizu-Iwayama, N. Kurumado, D. E. Hole, and P. D. Townsend, J. Appl. Phys. **83**, 6018 (1998).
2. H. Z. Song, X. M. Bao, N. S. Li, and X. L. Wu, Appl. Phys. Lett. **72**, 356 (1998).
3. L. Patrone, D. Nelson, V. I. Safarov, *et al.*, J. Appl. Phys. **87**, 3829 (2000).
4. Y. Ishikawa, N. Shibata, and S. Fukatsu, Appl. Phys. Lett. **68**, 2249 (1996).
5. A. G. Nassiopoulou, V. Ioannou-Sougleridis, P. Photopoulos, *et al.*, Phys. Status Solidi A **165**, 79 (1998).
6. L. Tsybeskov, S. P. Duttagupta, K. D. Hirschman, and P. M. Fauchet, Appl. Phys. Lett. **68**, 2058 (1996).
7. H. R. Philipp, J. Phys. Chem. Solids **32**, 1935 (1971).
8. M. Nakamura, Y. Mochizuki, K. Usami, *et al.*, Solid State Commun. **50**, 1079 (1984).
9. G. Hollinger, Y. Jugnet, and T. M. Duc, Solid State Commun. **22**, 277 (1977).
10. E. Holzenkampfer, F.-W. Richter, J. Stuke, and U. Voget-Grote, J. Non-Cryst. Solids **32**, 327 (1979).
11. T. Inokuma, Y. Wakayama, T. Muramoto, *et al.*, J. Appl. Phys. **83**, 2228 (1998).
12. A. Lehmann, L. Schuman, and K. Hubner, Phys. Status Solidi B **117**, 689 (1983).
13. F. Rochet, G. Dudour, H. Roulet, *et al.*, Phys. Rev. B **37**, 6468 (1988).
14. H. Richter, Z. P. Wang, and L. Ley, Solid State Commun. **39**, 625 (1981).
15. H. Cambell and P. M. Fauchet, Solid State Commun. **58**, 739 (1986).
16. M. Ya. Valakh, V. A. Yukhimchuk, V. Ya. Bratus', *et al.*, J. Appl. Phys. **85**, 168 (1999).
17. M. H. Brodsky and R. S. Title, Phys. Rev. Lett. *23*, 581 (1969).
18. E. H. Poindexter, P. J. Caplan, B. E. Deal, and R. R. Razouk, J. Appl. Phys. **52**, 879 (1981).
19. D. L. Griscom, E. J. Friebele, and G. H. Sigel, Jr., Solid State Commun. **15**, 479 (1974).
20. C. F. Young, E. H. Poindexter, and G. J. Gerardi, J. Appl. Phys. **81**, 7468 (1997).
21. A. Stesmans and V. V. Afanas'ev, J. Appl. Phys. **83**, 2449 (1998).
22. M. Born and E. Wolf, *Principles of Optics* (Pergamon, Oxford, 1969; Nauka, Moscow 1973).
23. D. Goguenheim and M. Lannoo, Phys. Rev. B **44**, 1724 (1991).
24. H. J. von Bardeleben, M. Chamarro, A. Grosman, *et al.*, J. Lumin. **57**, 39 (1993).
25. J. G. Zhu, C. W. White, J. D. Budai, *et al.*, J. Appl. Phys. **78**, 4386 (1995).
26. Y. Kanemitsu, T. Ogawa, K. Shiraishi, and K. Takeda, Phys. Rev. B **48**, 4883 (1993).

Translated by M. Tagirdzhanov

Semiconductors, Vol. 35, No. 7, 2001, pp. 827–834. Translated from Fizika i Tekhnika Poluprovodnikov, Vol. 35, No. 7, 2001, pp. 861–868.

PHYSICS OF SEMICONDUCTOR DEVICES

Luminescence Spectra and Efficiency of GaN-based Quantum-Well Heterostructure Light Emitting Diodes: Current and Voltage Dependence[1]

V. E. Kudryashov*, S. S. Mamakin*, A. N. Turkin*, A. É. Yunovich*,[1], A. N. Kovalev, and F. I. Manyakhin****

** Faculty of Physics, Moscow State University, Vorob'evy gory, Moscow, 119899 Russia*

[1] e-mail: yunovich@scon175.phys.msu.edu

*** Moscow Institute of Steel and Alloys, Leninskiĭ pr. 4, Moscow, 117936 Russia*

Submitted November 27, 2000; accepted for publication November 29, 2000

Abstract—Luminescence spectra and quantum yield in light emitting diodes (LEDs) based on InGaN/AlGaN/GaN heterostructures with multiple quantum wells (MQWs) were studied in the range of currents $J = 10^{-6}$–10^{-1} A. Minor spread in the quantum yield at operating currents (±15% at $J \approx 10$ mA) was observed in these LEDs, which were fabricated by Hewlett–Packard. The spread is due to differences in the current and voltage dependences of the diode emission intensity, caused by differences in the charged center distribution across the space-charge region (SCR) of the structures and in the role of the tunnel current component at low voltages. In the diodes with a thin ($\lesssim$120 nm) SCR, a tunnel emission band was observed for $J \lesssim 100$ μA; the peak energy of this band $\hbar\omega_{max} = 1.92$–2.05 eV corresponds to the voltage applied. At low currents ($J = 0.05$–0.5 mA), the spectral position of the main peak $\hbar\omega_{max} = 2.35$–2.36 eV is independent of the voltage and is determined by the radiative transitions between the localized states. At $J > 1$ mA, this band shifts with the current ($\hbar\omega_{max} = 2.36$–2.52 eV). Its shape corresponds to the model for the occupation of states in the two-dimensional energy band tails, which are caused by the microscopic potential fluctuations. The four parameters in this model are related to the calculated energy band diagram of the MQW structure. © *2001 MAIK "Nauka/Interperiodica"*.

1. INTRODUCTION

Problems related to the recombination mechanisms in light emitting diodes (LEDs) based on complex InGaN/AlGaN/GaN quantum-well (QW) heterostructures [1] have been discussed in detail previously [2–6, 7–9]. The results of studying the single- and multiple-QW LEDs fabricated by Nichia and Toyoda Gosei were reported recently [2–5].

Here, we investigate green LEDs with multiple QWs (MQWs) made by Hewlett–Packard Laboratories. Emission spectra, current–voltage and dynamic capacitance–voltage characteristics were measured in a wide range of currents in order to find a correlation between the emission quantum yield at operating currents ($J \approx 10$ mA), the charged center distribution in the space-charge region (SCR), and the role of the tunneling current component.

To gain insight into the results obtained and to carry out quantitative analysis of the spectra, the energy band diagram of the InGaN/AlGaN/GaN MQW heterostructures was calculated and several models of radiative recombination were considered, in particular, the model of recombination in two-dimensional (2D) systems with the tails of the density of states.

2. EXPERIMENTAL

We investigated green LEDs based on $In_xGa_{1-x}N/Al_yGa_{1-y}N/GaN$ heterostructures [6] grown by metalloorganic chemical vapor deposition onto sapphire substrates. The active layer of the structure is formed by five-period $In_xGa_{1-x}N/GaN$ MQWs ($x \approx 0.30$–0.35) with a period less than 8 nm. The samples were divided into three groups, referred to below as Q, *N*, and *P* (each containing 20 samples) and differing in

[1] Part of this study was reported at the 3rd All-Russia Workshop on Structures and Devices Based on Gallium, Indium, and Aluminum Nitrides (Moscow State University, 1999); the 3rd International Conference on Nitride Semiconductors (Montpellier, 1999); and the 4th European Gallium Nitride Workshop (Nottingham, 2000).

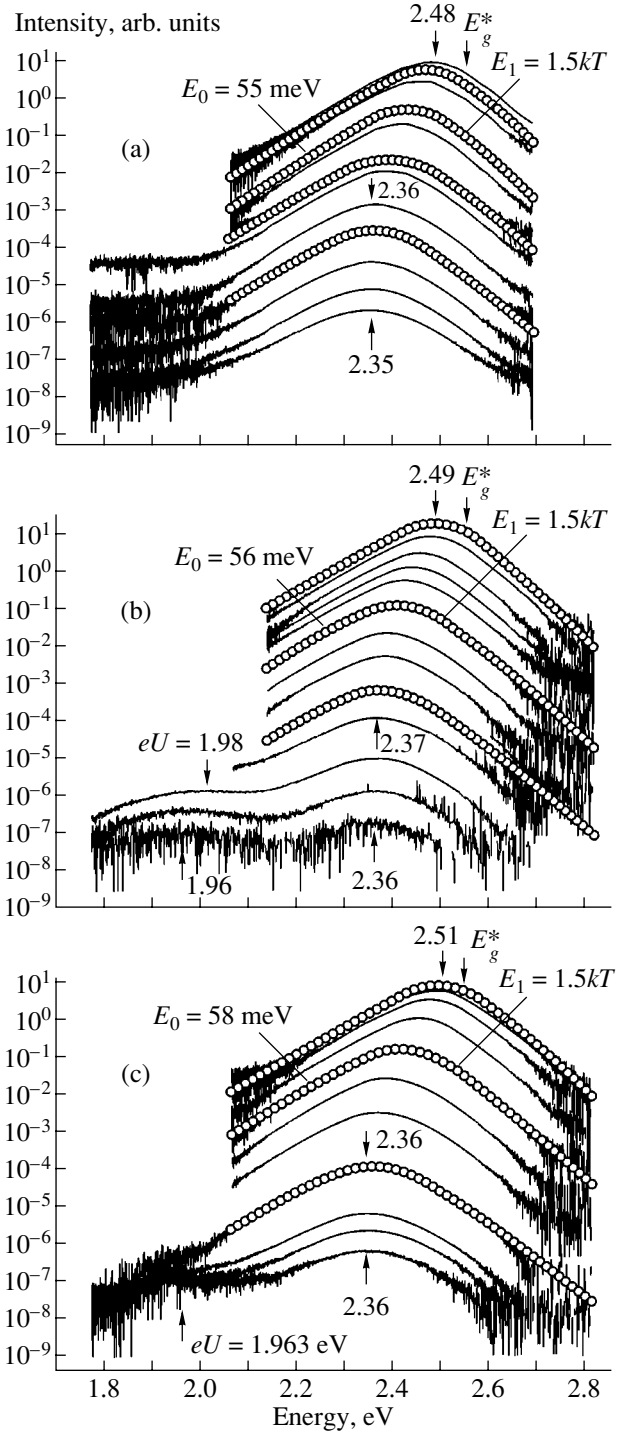

Fig. 1. Measured (solid lines) and calculated (circles) electroluminescence spectra of the MQW LEDs: (a) *Q* LED spectra measured at the currents J = 1.25, 2.5, 5, 10, 20, and 50 μA, and 0.1, 0.5, 1, 5, 10, and 20 mA and calculated for J = 10 μA and 0.1, 1, and 10 mA; (b) *N* LED spectra measured at J = 20, 30, 50, and 100 μA, and 0.15, 0.2, 0.3, 0.5, 1, 2, 3, 5, 10, and 15 mA and calculated for J = 0.15, 1, and 15 mA; and (c) *P* LED spectra measured at J = 60 and 80 μA, and 0.1, 0.2, 0.5, 1, 2, 5, 10, 15, and 20 mA and calculated for J = 0.2, 2, and 20 mA. In each plot, the curves are arranged from top to bottom in order of increasing current. The arrows indicate characteristic energies discussed in the text.

their LED luminous intensity (1.2, 1.0, and 0.9 cd, respectively) at operating current J = 10 mA ± 10%. Several samples from each group were studied; careful room-temperature measurements in the range of currents from 10^{-7} to 3×10^{-2} A were carried out for two LEDs from each group. The techniques used for the spectral and electrical measurements were described in detail elsewhere [2, 4]. The external quantum yield of radiation $\eta_e(J)$ and the efficiency $\eta_P(J)$ of the LEDs were determined by measuring their output power.

3. EXPERIMENTAL RESULTS

3.1. Luminescence Spectra of LEDs at Different Currents

The peak of the room-temperature emission band in *Q*, *N*, and *P* type LEDs appears at $\hbar\omega_{max}$ = 2.35–2.52 eV, and the band width at half-maximum is $\Delta\hbar\omega_{1/2} \approx$ 0.21–0.23 eV (on the wavelength scale, $\Delta\lambda_{1/2}$ = 36–38 nm). In Figs. 1a–1c, the spectra of the *Q*, *N*, and *P* type LEDs are shown for currents higher than 1.25, 20, and 60 μA, respectively.

Depending on J, three regions can be recognized in the spectra. At high currents (J > 1 mA), the spectral peaks shift with the voltage ($\hbar\omega_{max}$ = 2.35–2.52 eV). This was observed previously in green LEDs with single and multiple QWs [2–6]. This main band in the spectra can be described in the context of the model of radiative recombination in the 2D energy band tails originating from potential fluctuations [2–6]. In the current range from 0.1 to 1 mA, the positions of the spectral peaks are independent of the current ($\hbar\omega_{max}$ = 2.35–2.36 eV).

At low currents, emission intensities for the diodes from different groups differ by 2–3 orders of magnitude. In the emission spectra of the diodes of type *N* and *P* at J < 70 μA, we observed a low-intensity band whose peak shifts in approximate correspondence with the voltage applied ($\hbar\omega_{max}$ = 1.92–2.04 eV). This band is similar to the tunnel emission band in SQW blue LEDs in the region $\hbar\omega_{max}$ = 2.1–2.3 eV, which was investigated previously [3].

3.2. Current–Voltage Characteristics and Charge Distribution in the Structures

The distribution of the density of charged acceptor centers N_A^- in the diodes of type *Q*, *N*, and *P* as a function of the coordinate x is shown in Fig. 2 (x is measured from the boundary of the *n*-type region, which thus lies at x < 0). This distribution is determined from the dynamic capacitance measurements (see [5] for details on the technique). One can see that a compensated region and SCRs exist in the heterostructures; this observation is important for the subsequent discussion (see Subsection 4.1.1). The compensated region

(80–150 Å) in the structures under study is wider than that in the SQW diodes [2, 3]. The width of the compensated region at zero voltage ($U = 0$) in the diodes of types *N* and *P* ($\lesssim$120 Å) is smaller than in the diodes of type *Q* (~200 Å). The samples from the groups *P*, *N*, and *Q* differ also in the density of charged impurities in the *p*-region (2×10^{17}, 5×10^{17}, and 10^{18} cm^{-3}, respectively). The charge distribution in the *Q* type LEDs is close to that in the green LEDs fabricated by Toyoda Gosei [5].

The *I–U* curves for the three groups of LEDs are plotted in Fig. 3. Four regions, separated by the characteristic points, can be distinguished in these curves. In the voltage range U = 1.92–2.54 V (region III), the injection mechanism is dominant in all three types of LEDs; the slope of the *I–U* curves $E_J = dU/d(\ln J) \approx$ 70–80 meV. At higher voltages (region IV), the effect of the series resistance $R_s \approx 20\ \Omega$ becomes important. Region II corresponds to the tunnel radiative recombination. In *N* type LEDs it appears in the voltage range from 1.03 to 1.92 V, and in *P* LEDs, in a wider range from 0.3 V (where the current is a fraction of a nanoampere) to 1.92 V; the slope of the *I–U* curves here is $E_{T0} \approx$ 120 meV. In the LEDs from group *Q*, the tunnel emission band is not manifested due to the wider compensated region (see Figs. 1a, 2). At still lower currents, nonradiative tunnel recombination is dominant (region I). In this region, the slope of the *I–U* curve $E_T \approx 85$ meV is the same in the LEDs of all types.

3.3. Emission Quantum Yield: Current and Voltage Dependences

The current dependence of the emission power for three diode samples (one from each of the three groups) is shown in Fig.4. The efficiency $\eta_P(J) = \eta_e(J)\hbar\omega_{max}/eV$, calculated from these data, is plotted in Fig. 5. The $\eta_P(J)$ dependence is not monotonic; the maximum of η_P corresponds to the voltage U = 2.6–3.2 V. It should be noted that in the *Q* LEDs the maximum value of η_P (η_{max} = 1.8–2.4%) is higher and is attained at lower currents ($J \approx$ 0.5–1 mA) than in the *N* and *P* diodes (η_{max} = 1.2–1.4% at $J \approx$ 8–12 mA). The relation between η_e and the parameters of the spectra is discussed below (Section 4.4).

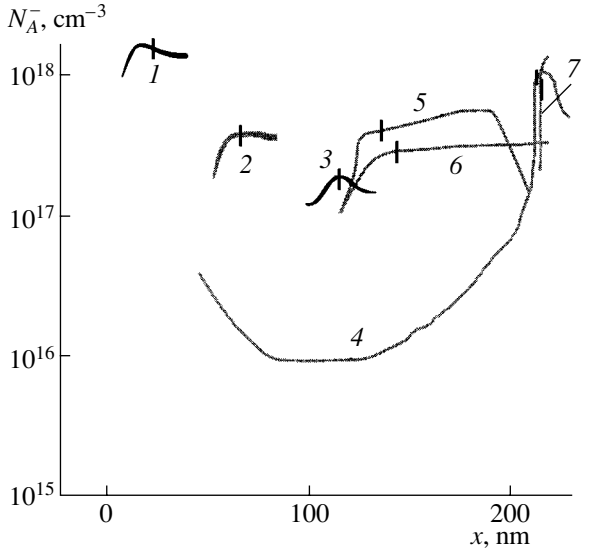

Fig. 2. Distribution of the charged centers in the *p*-type region of the LEDs: curves (*1*) and (*2*) correspond to the blue and the green SQW LEDs fabricated by Nichia; curves (*3*) and (*4*) correspond to the blue and the green MQW LEDs fabricated by Toyoda Gosei; and curves (*5*), (*6*), and (*7*) correspond to the green MQW LEDs of types *N*, *P*, and *Q*, respectively, fabricated by Hewlett–Packard.

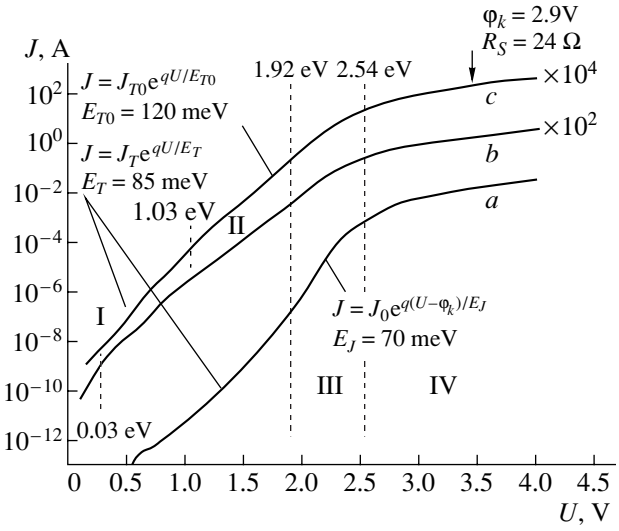

Fig. 3. Current–voltage characteristics of (*a*) *Q*-, (*b*) *P*-, and (*c*) *N*-type LEDs. The ordinate scale is shifted by 2 and 4 orders of magnitude for curves (*b*) and (*c*), respectively. Vertical lines indicate the characteristic voltages discussed in the text.

4. DISCUSSION

4.1. Energy Band Diagram of the Heterostructures

It was shown that heterostructures of the type considered can be strongly nonuniform [7, 8], especially with respect to In distribution in a QW. Decomposition of the solid solution into phases with different In content can take place in InGaN layers. This nonuniformity results in the fluctuations of the potential and the energy band gap in the QW plane (microscopic nonuniformity) or leads to the formation of "quantum dots" and "quantum islands" or to QW segmentation (macroscopic nonuniformity).

The spectra of the LED electroluminescence (EL) can be adequately described by a 2D model taking into account the potential fluctuations [2–6]. Thus, we use this model here to calculate the heterostructure energy band diagram. The potential fluctuations are included

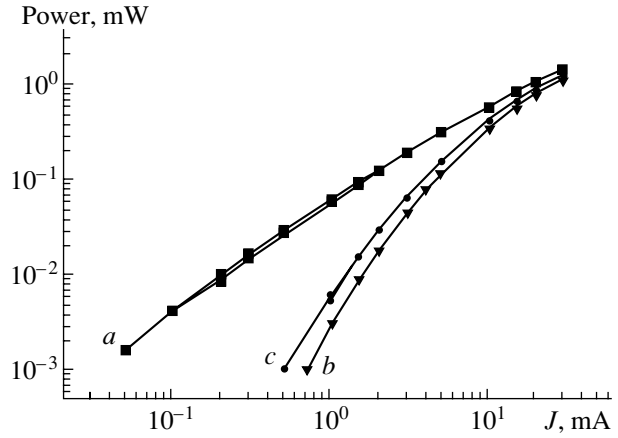

Fig. 4. Current dependence of the emission power for (*a*) *Q*-, (*b*) *P*-, and (*c*) *N*-type LEDs.

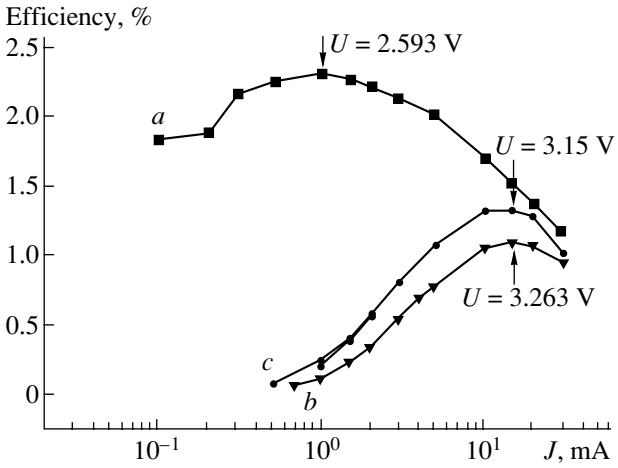

Fig. 5. Current dependence of the efficiency for (*a*) *Q*-, (*b*) *P*-, and (*c*) *N*-type LEDs.

by allowing for variations in the parameters of the 2D band model; in this way, the significant role of microinhomogeneities is taken into consideration.

4.1.1. Potential distribution. When calculating the potential drop across the *p*–*n* junction, we assume that there are SCRs at the *p* and *n* sides of the junction and a compensated *i* region (where the electric field $E_{\max}$ is uniform) between them [4–6]. We assume that the concentrations of the charged donors (Si^+) and acceptors (Mg^-) in both SCRs are constant ($N_d^+ \approx 10^{19}$ cm^{-3} and $N_a^- \approx 10^{18}$ cm^{-3}).

Then, the values of the potential drop φ_n and φ_p in the *n*- and *p*-type regions are inversely proportional to the densities of donors and acceptors, respectively: $\varphi_n/\varphi_p = N_a^-/N_d^+$. Since $N_d^+ \gg N_a^-$, most of the contact potential φ_k drops in the *p*-type region. φ_p corresponds to the barrier that the holes have to overcome to arrive at the active QW region from the *p*-GaN/*p*-AlGaN layers (see Fig. 6).

The Mg ionization energy in GaN is fairly high: $\Delta E_A(\mathrm{Mg}) = 0.22$ eV [1]. Consequently, in the exact calculation, variation in the occupation of the acceptor states with the potential (and, thus, with the coordinate) should be taken into account. Here, we choose the effective acceptor ionization energy ($E_A^* = 0.08$ eV) in such a way that the calculated ionized-acceptor concentration coincides with the value $N_a^- \approx 10^{18}$ cm^{-3} determined from the capacitance measurements.

4.1.2. Heterojunction band offsets. The band gap in $In_xGa_{1-x}N$ and $Al_yGa_{1-y}N$ ternary compounds can be calculated using the following expressions [9]:

$$\begin{aligned} E_g(\mathrm{InGaN}) &= xE_g(\mathrm{InN}) + (1-x)E_g(\mathrm{GaN}) \\ &\quad - b(\mathrm{InGaN})x(1-x), \\ E_g(\mathrm{AlGaN}) &= yE_g(\mathrm{AlN}) + (1-y)E_g(\mathrm{GaN}) \\ &\quad - b(\mathrm{AlGaN})y(1-y). \end{aligned} \tag{1}$$

Here, $E_g(\mathrm{GaN}) = 3.4$ eV, $E_g(\mathrm{InN}) = 1.9$ eV, and $E_g(\mathrm{AlN}) = 6.22$ eV are the band gaps in binary compounds; *x* and *y* stand for the molar content of In and Al, respectively, in the ternary solid solutions; and $b(\mathrm{InGaN}) = 3$ eV and $b(\mathrm{AlGaN}) = 0.5$ eV are the bowing parameters for the dependences $E_g(x)$ and $E_g(y)$. We use the values of *b* that agree most satisfactorily with the latest experimental data [9].

Contradictory data are reported in the available publications on the distribution of the band offsets between the conduction and the valence bands. We assume that the ratios of the conduction and valence band offsets ΔE_c and ΔE_v at the heterointerfaces of GaN with the solid solutions $Al_yGa_{1-y}N$ and $In_xGa_{1-x}N$ can be determined from the data for the AlN/GaN and GaN/InN heterointerfaces [10]; i.e.,

$$\begin{aligned} \Delta E_v(\mathrm{GaN/AlGaN})/\Delta E_c(\mathrm{GaN/AlGaN}) &= 0.3/0.7, \\ \Delta E_v(\mathrm{GaN/InGaN})/\Delta E_c(\mathrm{GaN/InGaN}) &= 0.4/0.6. \end{aligned} \tag{2}$$

The total band gap offsets at the heterointerfaces $Al_yGa_{1-y}N/GaN$ and $GaNIn_xGa_{1-x}N$ are equal to

$$\begin{aligned} &\Delta E_c(\mathrm{GaN/AlGaN}) + \Delta E_v(\mathrm{GaN/AlGaN}) \\ &= \Delta E_g(\mathrm{GaN/AlGaN}) = E_g(\mathrm{AlGaN}) - E_g(\mathrm{GaN}), \\ &\Delta E_c(\mathrm{GaN/InGaN}) + \Delta E_v(\mathrm{GaN/InGaN}) \\ &= \Delta E_g(\mathrm{GaN/InGaN}) = E_g(\mathrm{GaN}) - E_g(\mathrm{InGaN}). \end{aligned} \tag{3}$$

It is also assumed that the band offsets are independent of the order in which materials are deposited; i.e., $\Delta E_{c,v}(\mathrm{AlGaN/GaN}) = \Delta E_{c,v}(\mathrm{GaN/AlGaN})$ and

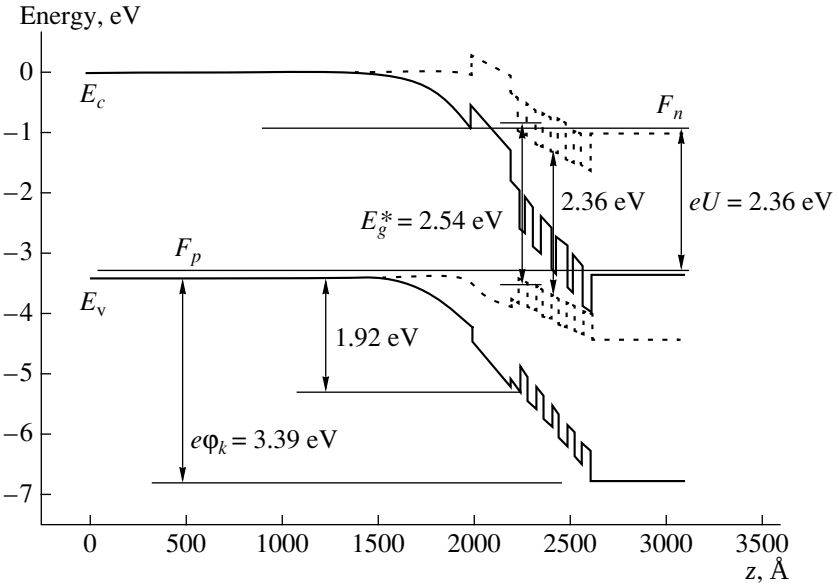

Fig. 6. Energy band diagram of the AlGaN/InGaN/GaN quantum-well heterostructure. The diagram corresponding to the forward bias U = 2.36 V is shown by the dashed line. The arrows indicate characteristic energy spacings discussed in the text.

$\Delta E_{c,v}$(GaN/InGaN) = $\Delta E_{c,v}$(InGaN/GaN). In fact, the band offsets do depend on this order [10]. We assume that this effect can be ignored in solid solutions with a low content of Al (y = 0.1–0.2) and In (x = 0.1–0.3) and, consequently, with relatively small band offsets: ΔE_g(GaN/InGaN) = 0.78–1.08 eV and ΔE_g(GaN/AlGaN) = 0.484 eV. The calculation results are given in the table.

4.1.3. Effective band gap. The heterostructure active layer consists of one or several InGaN QWs (in the samples under study, there are five wells) separated by GaN barriers; the band gap was calculated according to (1).

Thus, at room temperature for the LEDs under consideration (x = 0.2–0.35, T = 300 K) E_g(InGaN) = 2.32–2.62 eV (see table and Fig. 6). In addition to the $E_g(x, T)$ dependence, the effective band gap E_g^* is determined by the energy of the lowest electron and hole quantum-confinement levels in the QWs ΔE_{c1} and ΔE_{v1}, by the strain-induced shift of the energy bands ΔE_P, by the piezoelectric fields ΔE_{pe}, by the random charged-impurity fields ΔE_{DA}, and by the electron–hole Coulomb interaction ΔE_{exc} [2]:

$$E_g^* = E_g(\text{InGaN}) + \Delta E_{c1} + \Delta E_{v1} + \Delta E_P + \Delta E_{pe} + \Delta E_{DA} - \Delta E_{\text{exc}}. \quad (4)$$

The electron and hole quantum-confinement levels in InGaN QWs separated by GaN barriers can be determined from the solution of the one-dimensional Schrödinger equation. Tunneling between the QWs results in the spreading of discrete levels into minibands. However, for the barrier width D_b > 35 Å the miniband width is below 1.5 meV. Within this accuracy, we can use the solution for a single rectangular QW to determine E_g^*. Generally, the shape of the well changes due to the piezoelectric fields [11]; we do not take this effect into account here. Dependences of E_g^* on the well width calculated by formula (4) for x = 0.25, 0.30, and 0.35 are plotted in Fig. 7. For x = 0.3 and the well width D_w = 30 Å, the electron quantum-confinement levels are separated by ΔE_{c1} = 0.17 eV from the bottom of the conduction band. Due to the relatively large hole effective mass, the hole quantum-confinement levels are separated from the valence-band top by a smaller amount ΔE_{v1} = 0.08 eV. Thus, in the active MQW layer E_g^* = 2.52–2.54 eV.

The fluctuations δE_g^* in the effective band gap are mainly determined by the fluctuations δx in In content and by the broadening of the quantum-confinement levels due to the fluctuations δD_w in the QW width (see (1), (4)):

$$\delta E_g^* = \sqrt{\left(\frac{\partial E_g^*}{\partial D_w}\delta D_w\right)^2 + \left(\frac{\partial E_g^*}{\partial x}\delta x\right)^2}. \quad (5)$$

The slopes of the dependence $E_g^*(x, D_w)$ for x = 0.3 and D_w > 35 Å can be calculated using Eq. (1) and Fig. 7: $\partial E_g^*/\partial D_w$ = 9.26 meV/Å and $\partial E_g^*/\partial x$ = 2.377 eV.

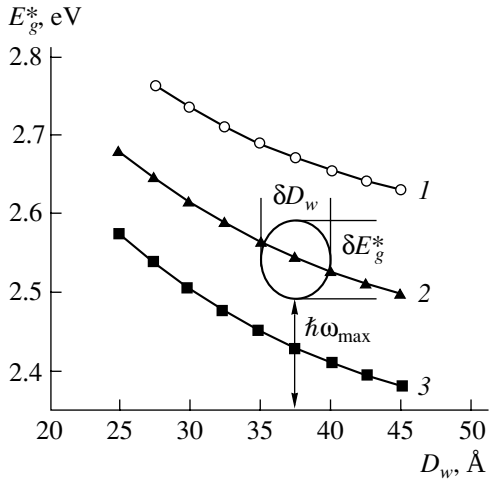

Fig. 7. Dependence of the effective band gap E_g^* on the width of $In_xGa_{1-x}N$ QW calculated by equation (4) with the first three terms taken into account: (*1*) $x = 0.25$, (*2*) $x = 0.30$, and (*3*) $x = 0.35$. The ellipsis describes the spread in E_g^* and D_w. The arrow indicates the peak position $\hbar\omega_{max}$ of the shifting emission band.

The fluctuations of the well width δD_w are governed by the heterointerface roughness and their characteristic scale is given by the lattice constant $a_{\|} = 5.185$ Å [1]. Assuming $\delta D_w = a_{\|}$, we obtain $\delta E_g^* = 48$ meV. Assuming that $\delta x = 1\%$, we obtain $\delta E_g^* = 24$ meV. Thus, the statistical average of the band gap fluctuations amounts to $\delta E_g^* = 53$ meV.

4.2. Recombination in the 2D Energy Band Tails

A model of recombination in the tails of 2D energy bands was considered in detail previously [4]. It is assumed in this model that the spectral intensity of emission is proportional to the joint 2D density of states N^{2D} near the edges of the energy bands (which has tails extending into the band gap) and the occupation numbers f_c and f_v of these states; i.e.,

$$I(\hbar\omega) \propto N^{2D}(\hbar\omega - E_g^*) f_c(\hbar\omega, kT, F_n) \times [1 - f_v(\hbar\omega, kT, F_p)], \quad (6)$$
$$N^{2D} \propto [1 + \exp(\hbar\omega - E_g^*)/E_0]^{-1}.$$

Relation (6) describes adequately the shape of the spectra of the LEDs based on InGaN/AlGaN/GaN heterostructures [2–6], but it includes as many as six parameters.

At operating currents, the electron distribution function $f_c(\hbar\omega, kT, F_n)$ near E_c is close to unity. Under this approximation, we arrive at a four-parameter model describing the shape of the spectra. It is important that the physical meaning of the parameters appearing in expression (6) can be readily understood by considering the correspondence with the parameters of the energy band diagram (Subsection 4.1):

(i) $E_g^* = 2.5$–2.7 eV is the effective band gap, corresponding to the energy spacing between the electron and the hole quantum-confinement levels in the wells.

(ii) $E_0 = 50$–60 meV is the scale of the exponential decay of the joint 2D density of states within the band gap, and its value corresponds to the effective band gap fluctuation: $E_0 \approx \delta E_g^*$.

(iii) $E_1 = mkT = 1.35$–$1.55kT$ is the exponent characterizing the decay of the short-wavelength wing of the spectrum (this parameter is related to the electron and hole distribution functions).

(iv) $\Delta F_p = F_p - E_v$ is the hole quasi-Fermi level.

The results of the calculations of the shape of the EL spectra performed in the context of this model are shown in Fig. 1.

4.3. Shift of the Main Emission-Band Peak with the Current

Energy spacing between the bottom of the conduction band and the top of the valence band in $In_{0.3}Ga_{0.7}N$ QWs is 2.36–2.40 eV. This value corresponds to the position of the peak for the "fixed" spectral band. As long as the voltage U applied to the active region satisfies the condition $\Delta F = F_n - F_p = eU < 2.36$ eV, radiative recombination occurs between the localized levels in

Conduction and valence band offsets at GaN/InGaN and GaN/AlGaN heterointerfaces

E_g(GaN), eV	x	E_g(InGaN), eV	ΔE_g(GaN/InGaN), eV	ΔE_v(GaN/InGaN), eV	ΔE_c(GaN/InGaN), eV
3.40	0.2	2.62	0.78	0.312	0.468
	0.3	2.32	1.08	0.432	0.648
E_g(GaN), eV	y	E_g(AlGaN), eV	ΔE_g(GaN/AlGaN), eV	ΔE_v(GaN/AlGaN), eV	ΔE_c(GaN/AlGaN), eV
3.40	0.2	3.884	0.484	0.145	0.339

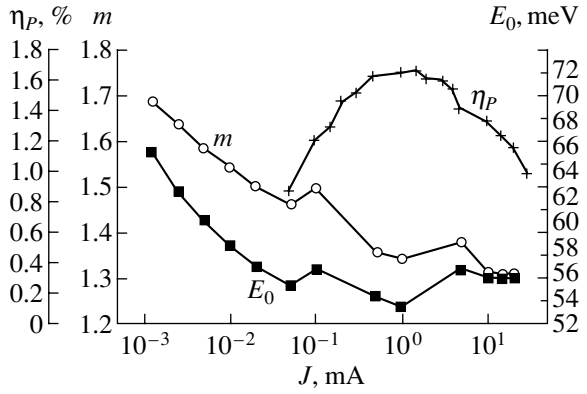

Fig. 8. Correlation between the current dependences of the efficiency η_P and the model parameters E_0 and m for the Q-type LED (sample $Q11$).

the tails of the density of states near the edges of the conduction and the valence bands. At higher voltages, $eU > 2.36$ eV (and, correspondingly, at higher currents), the localized levels are occupied. With increasing current, the peak of the main spectral band shifts linearly with the voltage and, thus, with the position of the hole quasi-Fermi level, since the extended states in the valence-band tail become occupied with the variation in ΔF_p. In the voltage range $U = 2.36$–2.95 V, the current correlates with the hole quasi-Fermi level position ΔF_p (determined from the analysis of the shape of the spectra): $J \propto \exp(\Delta F_p/kT)$. This is due to the fact that the hole distribution function is included in the four-parameter model describing the spectra (it is assumed that $f_c(\hbar\omega, kT, F_n) = 1$). Thus, the current is proportional to the density of holes injected into the active region:

$$\delta p = N_v^{2D} \exp(\Delta F_p/kT). \quad (7)$$

4.4. Emission Efficiency

The parameters E_0 and $E_1 = mkT$ depend only slightly on the current: E_0 varies from 56 to 63 meV, and m varies from 1.35 to 1.55. In Fig. 8, the current dependences of E_0, m, and η_P for one of the Q LEDs are shown. Small variations in E_0 and E_1 reflect the variation in the relative importance of the radiative recombination mechanisms, which can take place either between localized or between extended states. The current flows predominantly through certain microscopic regions characterized by their own values of the parameter E_0, and these regions can vary to some extent with J and U. An increase in E_1 with the current can also be the result of the structure heating [12]. The quantum yield has a maximum at the demarcation line between the regions on the current–voltage characteristic corresponding to the injection and the tunnel recombination mechanisms ($U = 2.54$ V). The current corresponding to the maximum quantum yield decreases upon a decrease in the importance of the tunneling effects.

5. CONCLUSION

(I) Minor spread (±10%) in the quantum yield of investigated LEDs, based on InGaN/AlGaN/GaN heterostructures with MQWs, is related to the differences in the distribution of effective charged centers in the space-charge region and in the role of the tunneling component of the current.

(II) The characteristic energies in the emission spectra and voltages in the current–voltage curves of green LEDs are related to the onset of the tunnel emission ($\hbar\omega = eU = 1.90 \pm 0.05$ eV; to the peak of the "fixed" emission band ($\hbar\omega_{max} = 2.36 \pm 0.01$ eV); to the effective band gap for the "shifting" emission band ($E_g^* = 2.54 \pm 0.01$ eV); and to the contact potential drop, whose value is a parameter in the numerical description of the current–voltage curves ($U = 2.9$–3.1 V).

(III) It follows from the energy band diagram that the value $eU = 1.90 \pm 0.05$ eV corresponds to the barrier that the holes need to overcome to enter the active layer from the p-region. The energies of 2.36 ± 0.01 and 2.54 ± 0.01 eV correspond to the difference $E_c - E_v$ and to the effective band gap in InGaN QWs.

(IV) The proposed phenomenological model provides a quantitative description of the LED spectra. The model has four parameters, whose physical meaning is as follows: E_g^* is the effective band gap, $E_0 = 50$–60 meV is the effective band gap fluctuation, $E_1 = mkT = 1.35$–$1.55kT$, and ΔF_p is the hole quasi-Fermi level.

(V) The fixed luminescence band with a peak at 2.36 eV corresponds to the recombination between the QW near-band-edge localized states; the shifting band corresponds to the recombination between the extended states.

(VI) The maximum in the current dependence of the efficiency correlates with the minima in the dependences of the parameters E_0 and E_1 on the current and is determined by the competition between the injection and the tunnel currents.

ACKNOWLEDGMENTS

We thank Dr. P. Martin (Hewlett–Packard Laboratories) for the LED samples supplied and O.A. Shustin and L.S. Lovinskiĭ for their help in the emission power measurements.

REFERENCES

1. S. Nakamura and G. Fasol, *The Blue Laser Diode* (Springer-Verlag, Berlin, 1999).
2. K. G. Zolina, V. E. Kudryashov, A. N. Turkin, and A. É. Yunovich, Fiz. Tekh. Poluprovodn. (St. Peters-

burg) **31** (9), 1055 (1997) [Semiconductors **31**, 901 (1997)].

3. V. E. Kudryashov, K. G. Zolina, A. N. Kovalev, *et al.*, Fiz. Tekh. Poluprovodn. (St. Petersburg) **31** (11), 1304 (1997) [Semiconductors **31**, 1123 (1997)].
4. F. I. Manyakhin, A. N. Kovalev, V. E. Kudryashov, *et al.*, Fiz. Tekh. Poluprovodn. (St. Petersburg) **32** (1), 63 (1998) [Semiconductors **32**, 54 (1998)].
5. V. E. Kudryashov, A. N. Turkin, A. É. Yunovich, *et al.*, Fiz. Tekh. Poluprovodn. (St. Petersburg) **33** (4), 445 (1999) [Semiconductors **33**, 429 (1999)].
6. A. E. Yunovich, V. E. Kudryashov, S. S. Mamakin, *et al.*, Phys. Status Solidi A **176** (1), 125 (1999).
7. S. F. Chichibu, S. P. DenBaars, K. Wada, *et al.*, Mater. Sci. Eng. B **B59**, 298 (1999).
8. P. G. Eliseev, P. Perlin, J. Lee, and M. Osinski, Appl. Phys. Lett. **71** (5), 569 (1997).
9. B. Monemar, J. P. Bergman, J. Dalfors, *et al.*, MRS Internet J. Nitride Semicond. Res. **4**, 16 (1999).
10. F. Bernardini and V. Fiorentini, Phys. Rev. B **57** (16), R9427 (1998).
11. A. Hangleiter, J. S. Im, H. Kollmer, *et al.*, MRS Internet J. Nitride Semicond. Res. **4S11**, G6.20 (1999).
12. V. Schwegler, S. S. Schad, C. Kirchner, *et al.*, Phys. Status Solidi A **176**, 783 (1999).

Translated by M. Skorikov

Semiconductors, Vol. 35, No. 7, 2001, pp. 835–839. Translated from Fizika i Tekhnika Poluprovodnikov, Vol. 35, No. 7, 2001, pp. 869–873.

PHYSICS OF SEMICONDUCTOR DEVICES

Interaction of Metal Nanoparticles with a Semiconductor in Surface-Doped Gas Sensors

S. V. Ryabtsev*, E. A. Tutov, E. N. Bormontov, A. V. Shaposhnik, and A. V. Ivanov

Voronezh State University, Universitetskaya pl. 1, Voronezh, 394893 Russia

** e-mail: phssd28@main.vsu.ru*

Submitted November 29, 2000; accepted for publication December 6, 2000

Abstract—A capacitance response of semiconductor sensors fabricated on the basis of thin NiO and SnO_2 films with noble-metal nanoparticles deposited on their surface was analyzed. This response was shown to appear due to the solid-phase metal–semiconductor reaction accompanied by the formation of a boundary layer with a fairly high density of surface electron states in its band gap. The chemisorption field effect (the change in work function of the metal after inlet of gases) observed in the capacitance gas sensors not only forms the basis for the sensitive and prompt method of analysis but also represents the basic functional phenomenon responsible for their capacitance response. *© 2001 MAIK "Nauka/Interperiodica".*

INTRODUCTION

Thin films of oxide semiconductors with noble-metal particles deposited on their surface are used as high-sensitive gas sensors. By analogy with a field transistor, the metal nanoparticles deposited on the surface of oxide play the role of microgates, which are controlled due to the fact that analyzed gases are adsorbed on them. This mechanism of controlling the sensor conductivity is referred to as electronic.

Another mechanism is associated with the so-called spillover effect, i.e., with the activation of gas molecules on a metal particle acting as a catalyst and their diffusion to the gas-sensitive semiconductor layer. The adsorption of activated gases leads to charging the surface layer of semiconductor. This mechanism of sensitivity is referred to as chemical.

The disadvantages of the surface-doped sensors include an instability stimulated by their elevated operating temperature (150–200°C) and by the cyclic action of analyzed gases. The instability of surface-doped sensors is mainly caused by the lateral mobility of metal particles and by their physicochemical interaction with a semiconductor substrate. It is possible to prevent the aggregation of particles, for example, by depositing a gas-permeable membrane onto the sensor surface; this membrane plays the role of a matrix for metal particles [1]. The metal–semiconductor interaction can be monitored, for example, by spectroscopic methods [2, 3].

In this study, we investigate the interphase metal–semiconductor interaction using the chemisorption field effect, i.e., the property of noble-metal particles to change their work function as a result of adsorption of gases from the environment [4]. The response of a metal–semiconductor structure to a cyclic action of gases is investigated by measuring its longitudinal low-signal capacitance in the case of the alternate inlet of hydrogen and oxygen.

EXPERIMENTAL

The semiconductor *n*-SnO_2 and *p*-NiO layers were obtained by magnetron deposition of tin and nickel on quartz substrates and the subsequent oxidation of the metal at a temperature of 600°C in air. For electrodes with the oxide layer, we used the In–Ga eutectic with an electron work function approaching that of SnO_2 and NiO (~4.5 eV). This value provided barrier-free contacts with the semiconductor, which is confirmed by the linear current–voltage characteristics of the sensors.

We used vacuum condensation to deposit a Pd or Au layer of 5×10^{16}–10^{17} at/cm^2 onto a thin semiconductor film 20–70 nm thick. The amount of metal deposited was determined by calculations from the temperature and geometry of the evaporator.

The preparation of samples involve the cyclic treatment alternately in oxygen (100%) and hydrogen (5% in air) at a temperature of 150°C. After treatment in the gases, a semicontinuous metal layer, which shunted the semiconductor surface, became dispersed, i.e., separated into small islands of nanometer size. The phenomena of structural degradation of metal catalysts, metal film membranes, etc., during the cyclic exposure in gases have been studied rather well. The fragmentation of metal layers during the cyclic treatment in gases is caused by mechanisms such as the adsorption and desorption on the metals and the reversible formation of bulk chemical compounds of the hydride, carbonyl, and oxide types.

The electric conductivity of samples decreased abruptly in the course of treatment owing to the above reasons, while the gas sensitivity, on the contrary, increased, which is associated with the progressing

1063-7826/01/3507-0835$21.00 © 2001 MAIK "Nauka/Interperiodica"

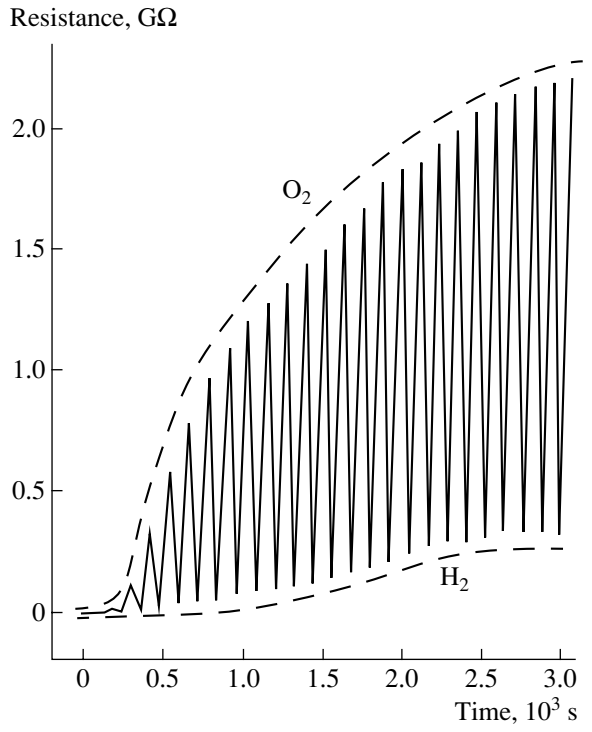

Fig. 1. Resistive response of the Pd/SnO_2 structure under a cyclic action of oxygen (100%) and hydrogen (5% in air) at $T = 473$ K.

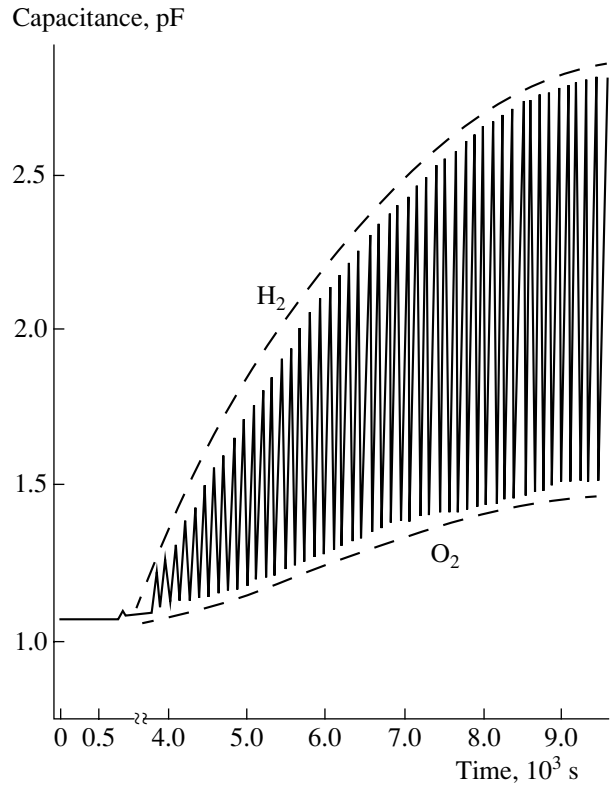

Fig. 2. Capacitance response of the Pd/SnO_2 structure under a cyclic action of oxygen (100%) and hydrogen (5% in air) at a frequency of 1 kHz.

fragmentation of a metal layer under the action of inlet gases. After 20–30 cycles of treatment (~60 min), the resistive response attained its highest value (Fig. 1). According to the data obtained by scanning-tunneling microscopy, a metal was on the treated semiconductor surface in the form of islands of 5–10 nm in size electrically insulated one from another. Such samples are perceived as ready for the subsequent capacitance investigations.

The longitudinal capacitance of the semiconductor SnO_2 and NiO films with deposited islandlike metal particles was measured in the atmosphere of hydrogen and oxygen by E7-8 and E7-15 digital immitance meters at a test-signal frequency of 1 kHz.

RESULTS AND DISCUSSION

The capacitance of undoped sensors is invariant to the action of gases and is virtually equal to the capacitance of the substrate with the system of electrodes (~1 pF). This fact indicates that there are no significant (with $\Delta E > kT$) intercrystal energy barriers in the semiconductor layer or at the interfaces between metal electrodes and the semiconductor.

Immediately after depositing a doping metal onto the semiconductor layer, the capacitance of sensors is also invariant to the action of gases. Only after 60–100 cycles of treatment in the H_2–O_2 medium, a capacitance response of doped sensors appears, with the relative value $\Delta C/C_0$ of this response attaining 500% for certain samples (Fig. 2).

The capacitance effects in semiconductor sensors are routinely related to the following factors: intercrystallite barriers in a semiconductor, barriers between electrodes and a semiconductor, the contribution of ionic conductivity, and the influence of adsorbed water on the permittivity of the sensor. Additionally, we analyzed the possible relation of the observed low-frequency capacitance to "slow" processes of recharging the adsorption-induced surface electron states (SESs) and the background defects (structure defects, impurity and strongly chemisorbed particles, etc.), whose population and parameters are changed as a result of gas adsorption. However, none of the mechanisms considered can explain the time delay (3–4 h) of the capacitance response under the action of gases.

The delay in appearance of the capacitance response is adequately explained in terms of the model of physical and chemical interactions between the metal and semiconductor. The solid-phase interaction requires a certain amount of time and elevated temperatures for forming the boundary layer. The delay time is influenced not only by temperature but also by the cyclic action of gases. The gases adsorbed at metal particles induce a strain in the crystal lattice and generate various structural defects, which promote interphase diffusion processes. The observed capacitance response of Me/NiO and Me/SnO_2 structures is interpreted as fol-

lows. The gas chemisorption leads to variations in the work function of metal particles (the microgates of the corresponding structures). According to the Schottky theory [5], this fact leads to a variation in the height of the metal–semiconductor potential barrier and in the position of the Fermi level in the band gap at the surface of the semiconductor. Thus, the chemisorption of gases on the surface of metal particles manifests itself in the form of the field effect [6]. After 60–100 cycles of treatment in gases, an intermediate layer with surface electron states is formed between the metal and semiconductor. The density of these states must be sufficient for making a marked contribution to the capacitance of the structures, but not too large so that the possibility of controlling the height of potential barrier by the chemisorption effect of the field is retained. In this case, changing the Fermi-level position in the band gap of the semiconductor film by alternating the inlet of hydrogen and oxygen, it is possible to detect the capacitance response of the corresponding structure caused by the SES recharging.

We consider the capacitance response of the Pd/*n*-SnO_2 structure in more detail. The testing ac voltage induces the SES recharge when the Fermi level in the semiconductor-surface band gap coincides with an SES energy level if the signal frequency is sufficiently low so that these states are in equilibrium with the ac signal. The absence of a capacitance response at a frequency of 1 MHz indicates that SESs formed in the band gap of the intermediate layer between a metal and a SnO_2 film are sufficiently slow. The capacitance response appears only at frequencies on the order of 1 kHz, which enables us to estimate the recharge time of these SESs as $\tau \approx 1$ ms.

It is known that the SES energy spectrum in the case of a quasi-continuous distribution over the band gap of a semiconductor has pronounced peaks near the band edges. The Gergel'–Suris fluctuation theory [7] for the surface states yields the U-shaped energy spectrum with a minimum near the midgap:

$$D_{ss}(E) = \frac{1}{\Delta}\frac{(\sigma_0/\pi)^{5/8}}{(4\alpha_n\alpha_p)^{3/8}}\exp\left(-\frac{E_g}{4\Delta}\right)\cosh\left(\frac{E-E_0}{2\Delta}\right),$$

where $E_0 = \frac{3}{4}\Delta\ln\left(\frac{m_n}{m_p}\right)$ is the position of the minimum of the SES density in reference to the midgap of the semiconductor, with this position being shifted from the midgap towards the allowed band with a lower effective mass; σ_0 is the surface density of changed centers at the semiconductor–insulator interface, which initiate the fluctuations of the surface potential; Δ is the characteristic electrostatic energy of fluctuations; α_n and α_p are the Bohr electron and a hole radii; E_g is the band gap of semiconductor; and m_n and m_p are the effective masses of the electron and the hole. The highest SES density in this model is observed near the band-gap edges. In addition to the U-shaped energy spectra, M-shaped spectra with two peaks in the upper and lower halves of the band gap were observed in the experiments [8]. The SES capacitance is proportional to their spectral density D_{ss}: $C = qD_{ss}$, where q is the elementary charge.

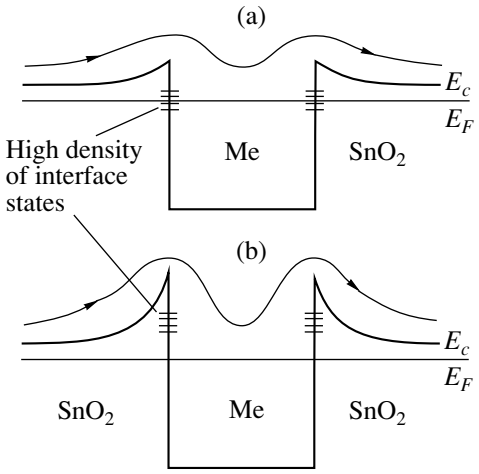

Fig. 3. Model of charge transport in the metal/SnO_2 structure: (a) under the action of hydrogen, (b) under the action of oxygen.

In addition to the quasi-continuous SES spectrum, narrow peaks of density of states caused by monoenergy levels may be observed in the band gap. When the Fermi level coincides with the SES monolevels, the capacitance $C = q^2N_t/(4kT)$ (where N_t is the SES concentration at the monolevel, k is the Boltzmann constant, and T is temperature) corresponds to these states.

A change in the capacitance observed experimentally as a result of the inlet of oxidizing and reducing gases can be explained by a nonuniform distribution of SESs in the band gap of semiconductor, for example, by the distribution with a sharp peak or with the exponential rise of density near the allowed bands. In oxide semiconductors (with a large fraction of ionic bonds), the SES density in the intermediate layer is so low that the Fermi level is not pinned and can shift somewhat relative to SESs under the action of gases. The Fermi-level position relative to the SESs in the region immediately below a metal particle depends mainly on the contact potential difference between the metal and semiconductor (Fig. 3).

As a result of hydrogen inlet, the electron work function for Pd decreases, which leads to a reduction of the Pd/SnO_2 potential barrier. In this case, the Fermi level turns out to be in the region of high density of SESs near the edge of the conduction band (Fig. 3a). For this reason, the capacitance caused by the recharging of the surface states and, correspondingly, the total capacitance of the structure increase with the hydrogen inlet (Fig. 4, curve *2*).

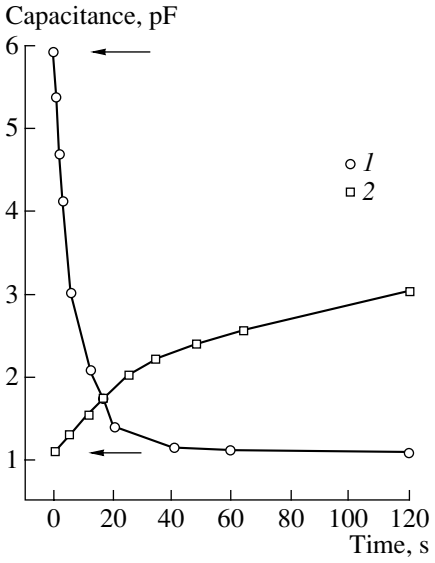

Fig. 4. Change in the capacitance of (*1*) Pd/NiO and (*2*) Pd/SnO_2 doped samples under the action of gases at a frequency of 1 kHz. Arrows indicate the moment of change of oxygen (100%) to hydrogen (5% in air) in the measurement cell.

As a result of oxygen inlet, the electron work function for Pd increases, which leads to a rise in the Pd/SnO_2 potential barrier. In this case, the Fermi level shifts from the conduction-band edge to the region of low-density SES (Fig. 3b); thus, both SES capacitance and total capacitance of the structure decrease with the oxygen inlet. The sensor capacitance decreases to a minimum, i.e., to a value close to the capacitance of undoped samples. Changes in the low-signal capacitance of the Pd/SnO_2 structure in the case of the alternating inlet of hydrogen and oxygen are illustrated in Fig. 2.

The opposite situation is observed in the Me/*p*-NiO samples. In an oxygen atmosphere, they have the highest capacitance because the Fermi level is shifted towards the valence-band edge and is in the high-density SES region. The change of gas atmosphere to hydrogen shifts the Fermi level from the valence-band edge deep into the band gap and forces it out of the region of an SES high density; thus, the capacitance of the Me/NiO samples drops to the minimum after the hydrogen inlet.

A long-time treatment of samples leads to a decrease in their capacitance response; by heating the samples to 350°C, the response disappears completely. This phenomenon can be related to the disappearance of surface doping particles and broadening of the boundary layer due to the diffusion and chemical metal–semiconductor interaction. In this case, the density of electron states decreases in the region of the metal–semiconductor interface.

The suggested model is indirectly confirmed by the published data. Thus, the interaction between Pd and SnO_2 was observed previously [2, 3] by X-ray photoelectron spectroscopy, ultraviolet photoelectron spectroscopy, and ion scattering spectroscopy. It was established that the degree of oxidation of Pd and the profile of its distribution in the semiconductor bulk vary depending on a temperature of this structure. Up to 200°C, Pd exists in the form of compact and neutral islands of metal (Pd^0) on the semiconductor surface. At higher temperatures, Pd is partly oxidized by atmospheric oxygen and is found as Pd^{+2} in the surface layer of the semiconductor. At temperatures higher than 600°C, Pd^0 is totally oxidized to the Pd^{+2} state and is distributed in the semiconductor bulk owing to diffusion. It was noted [9] that PdO is quite active in solid-phase reactions and forms binary oxides with SnO_2 at elevated temperatures and for a reasonably high concentration of Pd. For low concentrations, Pd forms defects in the semiconductor bulk.

Gutman *et al.* [10] investigated the interphase interaction in Pd/SnO_2 by Mössbauer spectroscopy in the high-sensitive mode of detection of conversion electrons using ^{119}Sn nuclei. From the analysis of isomer shifts (δ) and quadrupole splittings (Δ) obtained for the SnO_2 and Pd/SnO_2 samples, it was established that (i) small quantities of tin oxide SnO are present in the SnO_2 film, which can be explained by the partial reduction of oxide in a medium with hydrogen, and (ii) Pd and SnO interact with formation of a new phase O–Sn–Pd–O.

The emergence of SESs as a result of the interaction between a metal and a semiconductor has been noted previously [11]. In the case of the high-vacuum deposition of 2–10 monolayers of Ni and Pd on *n*-Si(111), a reconstruction of the electron spectrum of silicon was observed. The formation of Si–metal chemical bond gives rise to localized SESs in the band gap and valence band of Si.

The methods of capacitance–voltage characteristics, synchrotron spectroscopy, photoelectron spectroscopy, and X-ray spectroscopy were used to study the SES spectra of various metal–semiconductor pairs [12, 13]. A property common to these pairs is the peaks of the SES spectral density located in the band gap of semiconductors, which can be interpreted as the discrete levels. For Si, 3–5 levels are routinely observed, while their number attains to 6–8 for GaAs. The concentration of levels varies within 10^{11}–10^{13} cm^{-2}. The SES spectrum depends on metal properties.

CONCLUSION

These results and the published data enable us to conclude that the gas-induced capacitance response in the structures under investigation is associated with the metal–semiconductor interaction leading to the formation of a new phase near the interface and to the gener-

ation of fairly slow SESs. The delay time of the capacitance response is the time necessary for the solid-phase reaction to proceed. The investigations based on using the chemisorption field effect and measuring the longitudinal capacitance in thin semiconductor layers with the metal nanoparticles deposited on the surface yield information about the physical and chemical processes in the boundary layer between the metal and semiconductor, in particular, about the degradation of doped sensors. The chemisorption field effect represents not only a rather sensitive and prompt method for analysis but also the basic functional phenomenon in chemical gas sensors with a capacitance response.

REFERENCES

1. S. V. Ryabtsev and A. V. Shaposhnik, RF Patent No. 2096775.
2. R. Huck, U. Bottger, D. Kohl, and G. Heiland, Sens. Actuators **17**, 355 (1989).
3. T. B. Fryberger, J. W. Erickson, and S. Semancik, Surf. Interface Anal. **14**, 83 (1989).
4. S. V. Ryabtsev, in *Proceedings of the 13th European Conference on Solid State Transducers "Eurosensors XIII", Hague, 1999*, p. 93.
5. W. Schottky, Naturwissenschaften **26**, 843 (1938).
6. W. H. Brattain and J. Bardeen, Bell Syst. Tech. J. **32**, 1 (1953).
7. V. A. Gergel' and R. A. Suris, Zh. Éksp. Teor. Fiz. **84**, 719 (1983) [Sov. Phys. JETP **57**, 415 (1983)].
8. A. N. Ponomarev and V. G. Prikhod'ko, Fiz. Tekh. Poluprovodn. (Leningrad) **20**, 427 (1986) [Sov. Phys. Semicond. **20**, 270 (1986)].
9. R. W. Clark, J. K. Tien, and P. Wynblatt, Surf. Interface Anal. **6**, 5 (1980).
10. E. E. Gutman, T. V. Belyscheva, S. V. Ryabtsev, and F. H. Chibirova, in *Proceedings of the 6th International Meeting on Chemical Sensors, Gaithersburg, 1999*, p. 75.
11. E. V. Buzaneva and V. I. Strikha, in *Proceedings of the Ninth International Vacuum Congress and Fifth International Conference on Solid Surfaces, Madrid, 1983*, Ed. by J. L. de Segovia, p. 56.
12. V. E. Primachenko and O. V. Snitko, *Physics of Metal Doped Semiconductor Surfaces* (Naukova Dumka, Kiev, 1988).
13. E. V. Buzaneva, G. V. Kuznetsov, and V. I. Strikha, Mikroélektronika **15**, 275 (1986).

Translated by V. Bukhanov

Semiconductors, Vol. 35, No. 7, 2001, pp. 840–846. Translated from Fizika i Tekhnika Poluprovodnikov, Vol. 35, No. 7, 2001, pp. 874–880.

PHYSICS OF SEMICONDUCTOR DEVICES

Cross-Sectional Electrostatic Force Microscopy of Semiconductor Laser Diodes

A. V. Ankudinov, E. Yu. Kotel'nikov, A. A. Kantsel'son, V. P. Evtikhiev, and A. N. Titkov

Ioffe Physicotechnical Institute, Russian Academy of Sciences, St. Petersburg, 194021 Russia

Submitted December 22, 2000; accepted for publication December 27, 2000

Abstract—The possibilities of electrostatic force microscopy in studying semiconductor device structures are considered. A study of the cross sections of a GaAlAs/GaAs laser diode demonstrated that the method yields the position and width of the *n–p* junction in the laser structure, the profile of the voltage drop across the layers constituting the structure, and the distribution of injected carriers in the waveguide. © *2001 MAIK "Nauka/Interperiodica".*

INTRODUCTION

The miniaturization of semiconductor structures to submicrometer dimensions makes precision monitoring of the distribution of composition, dopants, and electrical parameters throughout their bulk necessary. The recent development of various techniques of atomic force microscopy (AFM) meets these requirements ideally, ensuring spatial resolution as good as several nanometers even for operation in air. Data on how the parameters of a structure are distributed can be obtained by studying cross sections of the structures intersecting the regions of interest.

Already the use of the simplest AFM methods—topographic and friction-force—allows the reliable visualization of all structural elements differing in chemical composition. On atomically smooth cross sections oxidized in air, regions of dissimilar compositions commonly differ in height because of being overgrown with oxides of unequal thicknesses [2, 3]. The existence of mechanical stresses at boundaries between dissimilar materials may also contribute to the surface relief, thus visualizing the boundaries [4, 5]. On applying the friction force technique, parts of the surface are distinguished by different friction forces measured in these regions [5, 6]. The development of the method measuring the local capacitance between the tip and the surface [7] enabled the quantitative characterization of a two-dimensional doping profile in the concentration range from 10^{15} to 10^{20} cm^{-3} [8].

In addition, an AFM method detecting the force of electrostatic interaction between the probe tip and the surface under study has been developed. Electrostatic force microscopy (EFM) measures the mechanical response of the probe to the action of an electrostatic force that depends on the local difference of potentials between the tip and the surface below, the surface charge density, and local capacitance [9, 10]. Apparently, the EFM technique is promising for analyzing the distributions of intrinsic and external electric fields in the device structure bulk. In measurements by conventional EFM, the potential distributions are found in relative units, which require additional calibration. However, there already exists a variation of the EFM method (Kelvin mode [10, 11]) measuring the absolute potential differences.

This study is concerned with the application of the EFM method to studying electric field distributions across the layers in semiconductor laser heterostructures. In heterostructures of this kind the external voltage mainly drops across the *n–p* junction created by doping the emitters situated on opposite sides of an undoped waveguide in different ways. Successful laser operation requires that the position of the *n–p* junction should fall exactly on the waveguide region. The position of the *n–p* junction is commonly determined by measuring the current induced by an electron probe scanning the region of a reverse-biased *n–p* junction—an electron beam induced current technique (EBIC) [12, 13]. In this method the recorded current is strongest when the electron beam impinges approximately on the middle of a reverse-biased *n–p* junction. The true position of the *n–p* junction is found by comparing the measured induced current distribution with model dependences. The precision of this comparison depends on quite a number of parameters, such as carrier diffusion length, surface recombination rate, depletion layer thickness, and the shape of the carrier generation function. Therefore, with the EBIC method it is difficult to achieve nanometer precision in determining the position of the *n–p* junction necessary for the fabrication of modern laser heterostructures containing quantum-confinement layers.

The EFM allows direct determination of the electric field distribution over the surface under study (in the case in question, over the cross section of a laser structure). Simultaneously, the voltage profiles obtained are directly related to structural elements of the laser, revealed in topographic AFM images obtained together

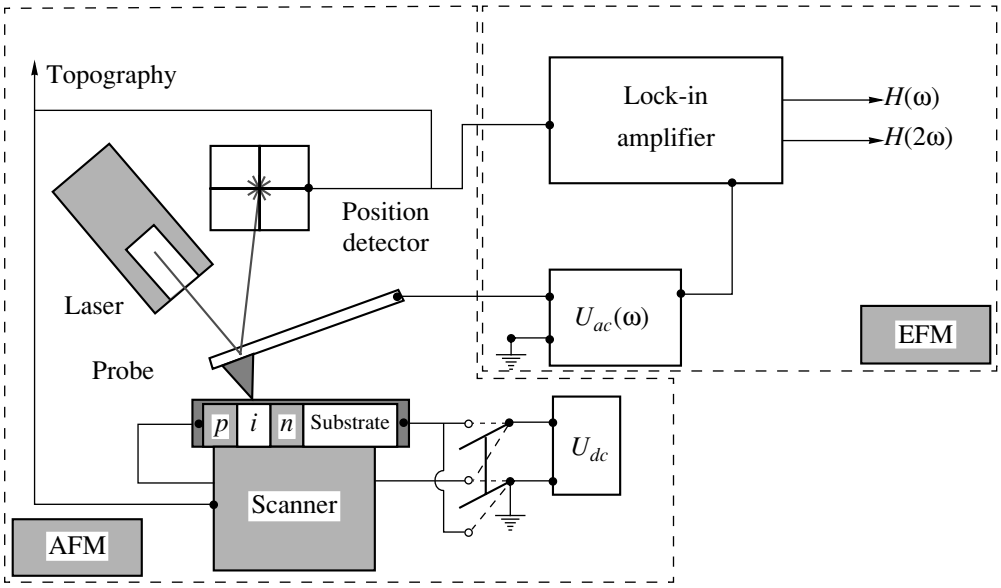

Fig. 1. Experimental setup.

with the EFM data. The method can ensure a nanometer plan-view resolution of about 20–30 nm, determined by the probe tip diameter. As shown below, the EFM technique is also sensitive to local variations of the surface capacitance, whence additional data on the electronic properties of the structures can be obtained.

We investigated the possibilities of using EFM to study a laser heterostructure based on the well-understood GaAlAs/GaAs/GaAlAs system. It should be noted that EFM studies of laser heterostructures have only just started. The first recently reported studies concerned with GaAlSb/GaSb/GaAlSb [14] and InP/InGaAsP/InP laser heterostructures [14, 15] employed a noncontact EFM mode in which the tip performs resonance oscillations at a certain distance from the surface, rather than touching it. We used the recent method relying upon a contact EFM mode [16] in which the tip is in permanent contact with the surface under study. In this case, the tip is the closest to the surface studied, which ensures the simultaneous improvement of the sensitivity and plan-view resolution of the EFM technique. The substantially lower cost of the experiment is also important, the contact mode employing more durable and less expensive tips.

EXPERIMENTAL PROCEDURE

We now briefly consider the basic concepts of the EFM technique [9–11]. Let a tip insulated from the surface under study be at a potential U relative to the surface. Then an electrostatic interaction force arises between the tip and the surface:

$$F_{\text{cl}} = (1/2)[d(CU^2)/dz], \qquad (1)$$

where C is the tip–sample capacitance, and the z-axis is directed normal to the sample surface. Commonly, there exists some initial voltage V_{cp} between the tip and the surface owing to the difference in work function between the different materials. In an experiment, dc (U_{dc}) and ac ($U_{ac}\cos(\omega t)$) voltages can be additionally applied between the tip and the surface. The substitution of the total voltage $V_{cp} + U_{dc} + U_{ac}\cos(\omega t)$ into (1) shows that the resulting force F_{cl} will have three components: one time-independent and two alternating, oscillating at frequencies of ω and 2ω. The oscillating components have the form

$$F_{\text{cl}}(\omega) = (dC/dz)(V_{cp} + U_{dc})U_{ac}\cos(\omega t), \qquad (2)$$

$$F_{\text{cl}}(2\omega) = (1/4)(dC/dz)U_{ac}^2\cos(2\omega t). \qquad (3)$$

The alternating force will cause tip oscillations at frequencies of ω and 2ω, which can be detected. The amplitudes of forced oscillations are commonly small (on the order of a nanometer) and linearly related to force harmonics $F_{\text{cl}}(\omega)$ and $F_{\text{cl}}(2\omega)$ [16]. Thus, by recording amplitudes of tip oscillations at frequencies of ω and 2ω, we can measure the signals $H(\omega)$ and $H(2\omega)$ proportional to the changes in the electrostatic force components $F_{\text{cl}}(\omega)$ and $F_{\text{cl}}(2\omega)$. In this case, the signal $H(2\omega)$ will reflect changes in capacitance at different points of the surface, and the signal $H(\omega)$ will additionally reflect the change in potential difference between the surface and the tip.

The investigations were performed on an NP-MDT P-4 SPM atomic-force microscope (Russia). A schematic of the setup is shown in Fig. 1. The AFM probe is a pyramid of height ~10 μm with a sharpened vertex and base attached to one end of a ~200-μm-long rectangular cantilever with cross section of ~20 × 2 μm^2.

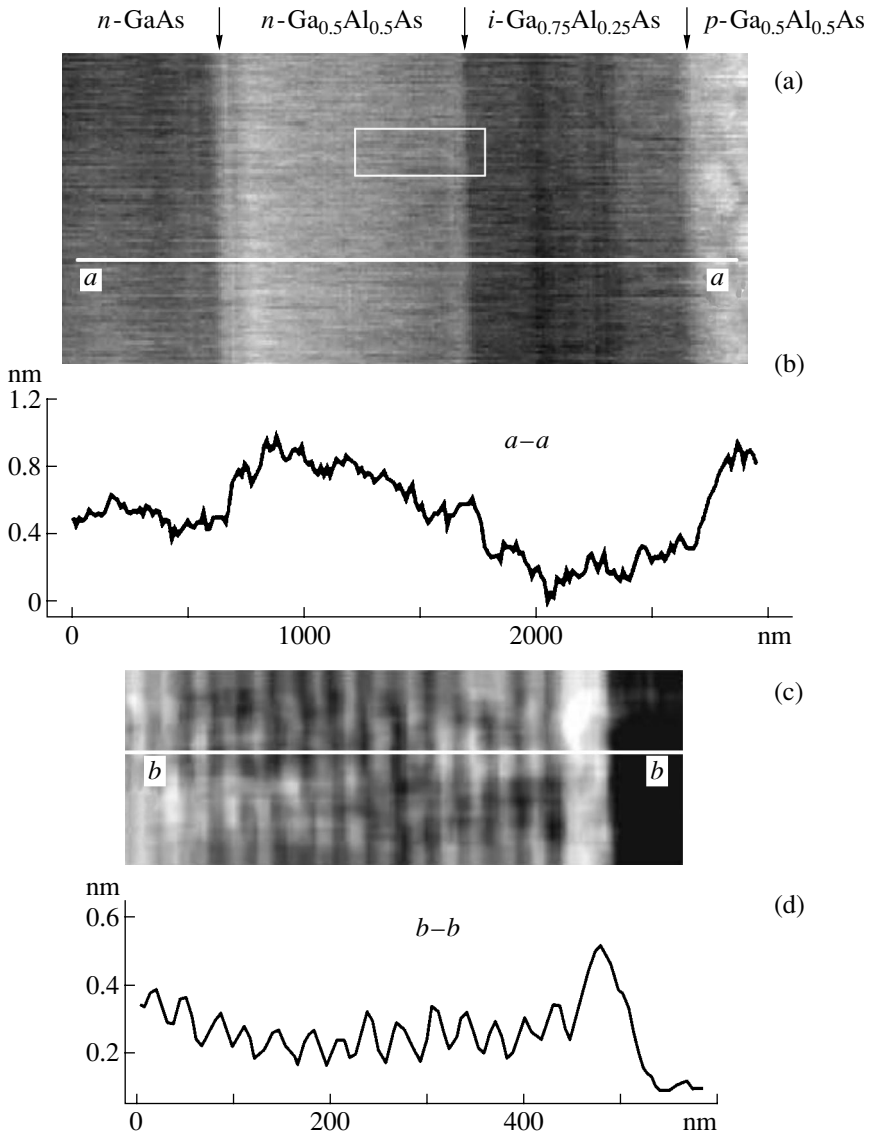

Fig. 2. Surface topography of the 1.5×3.0 μm^2 cross section of a n-GaAs/n-$Ga_{0.5}Al_{0.5}As$/i-$Ga_{0.75}Al_{0.25}As$/p-$Ga_{0.5}Al_{0.5}As$ laser heterostructure, obtained by AFM in the contact mode at tip–surface interaction force $F = 50$ nN: (a) topographic image of the cross section surface; (b) Surface profile along the line *a–a* in image a; (c) topographic image of a part of the n-$Ga_{0.5}Al_{0.5}As$ emitter cross section, marked by a rectangle in image a; and (d) surface profile along the line *b–b* in image c.

The other end of the cantilever is fixed on the support of a laser device monitoring the oscillations of the cantilever end with the pyramid. We used Silicon-MDT CSC12/15 contact-mode tips (Russia) fabricated from heavily doped *p*-silicon. To perform an experiment, a scanner with a semiconductor heterostructure laser attached is moved so as to press the structure's cross-sectional area under study against the pointed vertex of the pyramid. The alternating voltage between the tip and the surface (in the frequency range 200–400 kHz) is supplied by a generator integrated with the resonance-mode unit of the microscope, the dc voltage is applied across the laser heterostructure. The ac voltage generator may share common ground with the *p*- or *n*-contact of the laser. The electrical insulation of the tip from the cross section surface is ensured by oxide layers covering it and the silicon pyramid. The mechanical loading force F can be adjusted and made much stronger than the electrostatic force F_{el}, so that changes in F_{cl} have no effect on the topographic signal measured with the total force maintained constant. The microscope operation mode allows the simultaneous recording of the topographic signal and one of the EFM signals—$H(\omega)$ or $H(2\omega)$—analyzed with a lock-in amplifier of the resonance-mode unit.

We studied an MBE-grown n-GaAs/n-$Ga_{0.5}Al_{0.5}As$/i-$Ga_{0.75}Al_{0.25}As$/p-$Ga_{0.5}Al_{0.5}As$ laser heterostructure. The substrate and the *n*-emitter were

doped with Si to $(1–2) \times 10^{18}$ cm^{-3}. The waveguide was nominally undoped, and the *p*-emitter doped with Be to 3×10^{18} cm^{-3}.

EXPERIMENTAL RESULTS AND DISCUSSION

Figure 2a presents a cross-sectional topographic AFM image of the laser heterostructure under study. The dark stripe in the left side of the image corresponds to the *n*-GaAs substrate. To the right of this stripe lies a lighter one, corresponding to the *n*-$Ga_{0.5}Al_{0.5}As$ region. The higher brightness corresponds to the elevated relief of this part of the surface. Further we again have a dark stripe (*i*-$Ga_{0.75}Al_{0.25}As$ region) followed once more by a lighter stripe (*p*-$Ga_{0.5}Al_{0.5}As$ region). The difference in height between different regions of the laser cross section was as large as 0.6 nm, as can be seen from the profile in Fig. 2b, measured along the *a–a* line in Fig. 2a. The difference in height between regions with unequal Al contents is well established [2, 3], which is accounted for by the higher thickness of the natural oxide on a surface with higher Al content. This circumstance, in particular, made it possible to also resolve the fine structure of the *n*-emitter layer formed as a *n*-$Ga_{0.48}Al_{0.52}As$ (30 nm)/*n*-GaAs (1.5 nm) superlattice and capped with a 50-nm-thick $Ga_{0.5}Al_{0.5}As$ layer. Figure 2c shows at higher magnification a part of the *n*-emitter (marked by a white frame in Fig. 2a). An array of light and dark stripes with a period of 32 nm and a wider light stripe at the extreme right are easily resolved in Fig. 2c and also in the profile in Fig. 2d.

Let us now consider the behavior of the $H(2\omega)$ signal when scanning the layers of the structure with the tip and also on reversing the polarity of the voltage U_{dc} applied to the laser contacts, presented in Fig. 3b. The upper part of the frame was obtained with a reverse-biased *n–p* junction, and the lower, under a forward bias. A change in the image contrast is observed for the $H(2\omega)$ signal from the cross-sectional area, indicating different tip–surface capacitances over different layers and a substantial increase in the capacitance over the waveguide for the forward-biased *n–p* junction. To relate the $H(2\omega)$ signal to the components of the laser heterostructure, Fig. 3a also presents a topographic AFM image of the upper part of the cross-sectional area under study.

To analyze the data in Fig. 3, it is necessary to consider the nature of the tip–semiconductor sample capacitance *C*. To a first approximation, we can distinguish two principal contributions: tip–semiconductor surface capacitance C_1 and a series capacitance of the depletion layer in the semiconductor, C_2. Then we have

$$C = C_1C_2/(C_1 + C_2). \quad (4)$$

Here, $C_1 = \varepsilon_i\varepsilon_0 S/D$ and $C_2(U) = \varepsilon_s\varepsilon_0 S/W(U)$, where ε_i and ε_s are, respectively, the dielectric constants of the surface oxide and semiconductor; ε_0 is the permittivity of free space; *S* is the contact area; *D* is the oxide thickness; and $W(U)$ is the thickness of the surface depletion region in the semiconductor, dependent on the applied voltage. Even in this simplified approximation, the data in Fig.3 find understandable qualitative explanation.

Let us consider changes in capacitance over layers of a reverse-biased *n–p* junction of the laser. The lower capacitance over the *n*-GaAlAs layer, compared with that over the equally heavily doped *n*-GaAs substrate, can be, naturally, attributed to the larger oxide thickness over Al-containing layers already discussed. Let us evaluate the effect. The thickness of natural oxide on GaAs is 1.5 nm [3], and for $Ga_{0.5}Al_{0.5}As$ this parameter can be estimated at 4 nm in view of the fact that the oxide thickness is 2.5 nm at an Al content of 30% [3]. The thickness of natural oxide on silicon, the probe material, is less than 4 nm [17]. Taking into account that the $H(2\omega)$ signal being analyzed is proportional to the first derivative dC/dz, it might be assumed that, with the capacitance C_1 predominating, the decrease in the signal, proportional to the squared oxide thickness, would be 3-to-4-fold. However, the decrease observed is no more than a factor of 2. Therefore, it seems reasonable that the capacitance C_2 plays an important role.

Indeed (see the profile *y–y* in Fig. 3c), for a reverse-biased *n–p* junction the capacitance over the waveguide layer is even lower than that over the emitters containing twice the amount of Al. This fact can be attributed to an expansion of the surface depletion region in the undoped layer. The capacitance C_2 plays a prominent role in the abrupt increase in the signal over the *i*-layer, occurring when the *n–p* junction is forward-biased and a large number of carriers is injected into the *i*-GaAlAs region. In this case, the surface depletion region becomes narrower and the capacitance over the *i*-layer increases.

In Fig. 3b, the much narrower region of pronounced increase in capacitance, observed when the *n–p* junction becomes forward-biased, is noteworthy compared with the waveguide width indicated by the topographic cross-sectional image in Fig. 3a. The same is evidenced by the shape of the *x–x* profile of the $H(2\omega)$ signal in Fig. 3c. The capacitance increases steeply at the left-hand boundary of the waveguide, and much more slowly on the right-hand boundary side. In our opinion, the observed protraction indicates that the concentration of injected carriers in the waveguide decreases on the *p*-emitter side.

Let us now analyze EFM images of a laser heterostructure, obtained in the $H(\omega)$ signal measurement mode. Figure 4b presents a set of images obtained for a laser heterostructure with grounded *n*-contact, biased in the range from +1 V at the *p*-contact (the *n–p* junction is nearly forward-biased) to –5 V (reverse-biased *p–n* junction). The left-hand sides of all the images show a step associated with a decrease in capacitance on passing from the *n*-GaAs substrate to the *n*-emitter. This step allows independently relating features in the image to exist in the layer positions in the laser (see also the

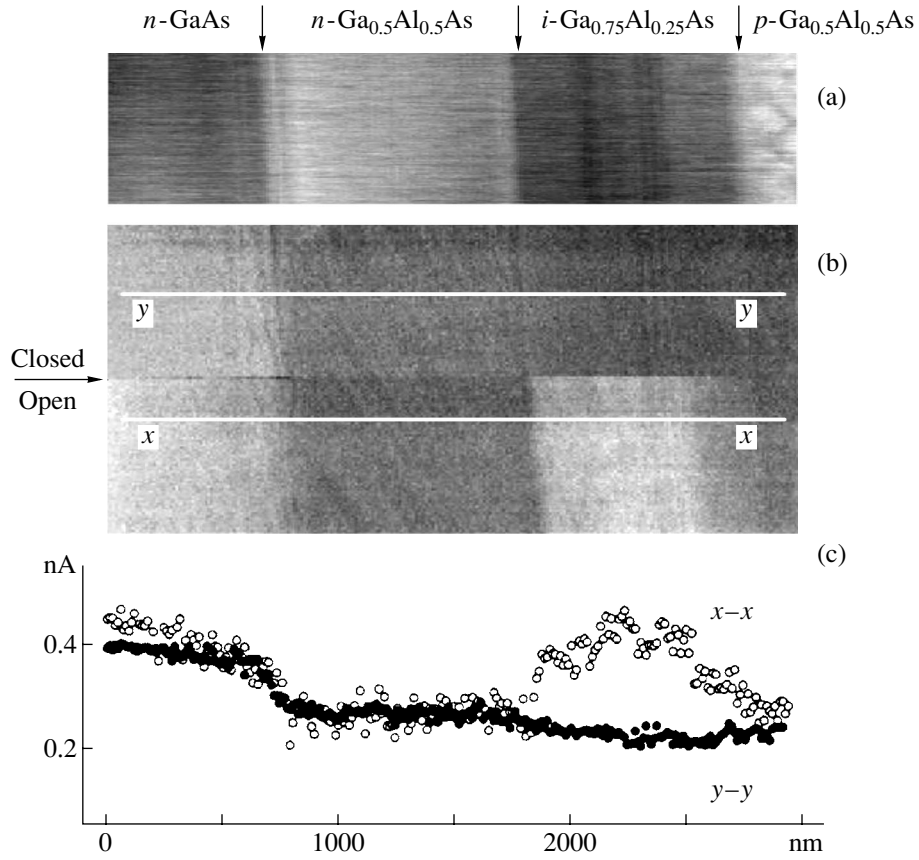

Fig. 3. Behavior of the EFM signal $H(2\omega) \propto dC/dz$ on the surface of a 1.5×3.0 μm^2 cross section of the laser heterostructure: (a) topographic AFM image of the upper part (0.75×3.0 μm^2) of the cross-sectional area under study; (b) continuous-tone image illustrating the variation of the $H(2\omega)$ signal, $U_{ac} = 3$ V, the arrow shows the instant when the *n*–*p* junction goes from reverse- to forward-biased on reversing the polarity of the dc bias U_{dc} at the *p*-contact of the laser from –5 to +1.2 V with a grounded *n*-contact; (c) *x*–*x* and *y*–*y* profiles of the $H(2\omega)$ signal for the *n*–*p* junction in, respectively, reverse-biased (along the *x*–*x* line in image b) and forward-biased *n*–*p* junction (along the *y*–*y* line in image b).

topographic AFM image in Fig. 4a). The light regions in the $H(\omega)$ images correspond to larger signal values and indicate higher surface potential. For example, at a zero bias the *n*-side of the laser looks dark, which points to an expected decrease in the sample–tip contact potential difference on moving from the *p*- to the *n*-region.

Changes in the $H(\omega)$ signal are better seen in Fig. 4c, which shows the signal profiles. The profiles were not corrected for capacitance changes and, therefore, reflect the overall dependences of $H(\omega)$ on $(dC/dz)(V_{cp} + U_{dc})$. However, the changes occurring in the capacitance (see Fig. 3) do not hinder the analysis of the voltage distribution pattern in the structure. For example, without any bias the capacitance in the waveguide region remained practically unchanged, being, in addition, only slightly different from the capacitance values of the *n*- and *p*-emitters. Therefore, the recorded increase in potential in the waveguide region under a zero bias must adequately reflect the position and width of the *p*–*n* junction. Further, we observed that applying a reverse voltage has no noticeable effect on the surface capacitance of all layers of the structure. Therefore, the change occurring in the behavior of the potential in the waveguide region (a decrease instead of the prior rise) objectively reflects the process of the *n*–*p* junction becoming reverse-biased (U_{dc} = 0…–5 V). A certain influence of the capacitance change over the waveguide would be only expected if the *n*–*p* junction becomes forward-biased ($U_{dc} = +1$ V), with the capacitance growing noticeably. However, the capacitance changes by only a factor of 1.5–2 relative to the $H(2\omega)$ level over the *n*-GaAs substrate (see the relationship between the capacitances in Fig. 3c), whereas the actual rise in the $H(\omega)$ signal on forward-biasing the *n*–*p* junction is much more pronounced.

Thus, we obtained an objective pattern of voltage distribution across a laser heterostructure. No voltage drop across the *n*-substrate and *n*- and *p*-emitters was observed under any biases. As can be seen from the branching points of the $H(\omega)$ profiles in Fig. 4c, a

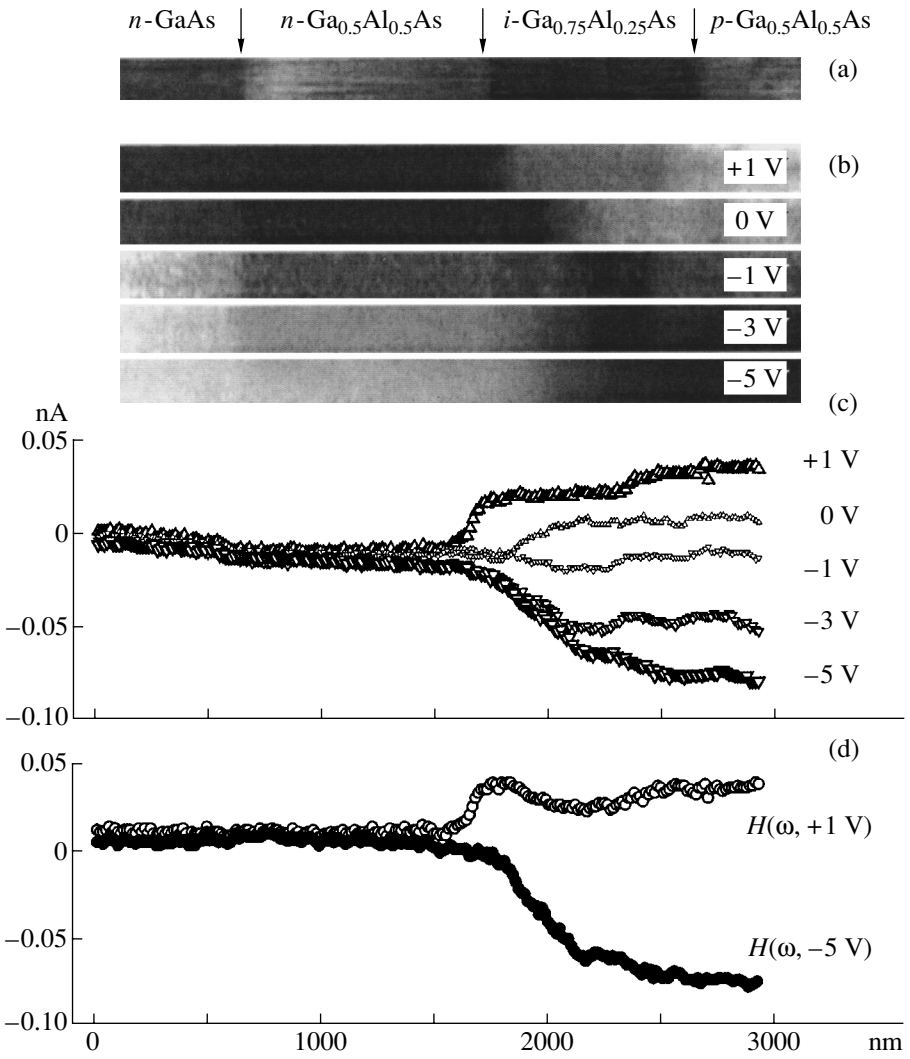

Fig. 4. Behavior of the EFM signal $H(2\omega) \propto (V_{cp} + U_{dc})dC/dz$ on the surface of a $0.2 \times 3.0\ \mu m^2$ cross section of the laser heterostructure; $U_{ac} = 3$ V; dc bias U_{dc} applied to the *p*-contact of the laser, *n*-contact grounded, lock-in amplifier phase tuned to the maximum positive signal from the *p*-region of forward-biased laser. (a) Topographic image of the investigated region of the cross section; (b) continuous-tone images illustrating the variation of the $H(\omega)$ signal with voltage U_{dc} across the laser structure; (c) $H(\omega)$ signal profiles plotted using the respective continuous-tone images b; and (d) the run of $H(\omega, +1\ V)$ and $H(\omega, -5\ V)$ signals minus the background signal $H(\omega, 0\ V)$, defining the profile of the voltage U_{dc} in the laser heterostructure for forward- and reverse-biased *n–p* junction, respectively.

noticeable voltage drop starts to be observed only beginning at the *n*-emitter–waveguide interface. The distribution of the external voltage U_{dc} for the forward- and reverse-biased *n–p* junctions of the laser are shown in Fig. 4d, where the $H(\omega, +1\ V)$ and $H(\omega, -5\ V)$ profiles minus the $H(\omega, 0\ V)$ signal obtained at a zero bias are plotted. It can be seen that, with the reverse-biased *n–p* junction, the potential in the waveguide falls nonlinearly, and in the case of a forward-biased *n–p* junction the potential increases stepwise. It is noteworthy that in all the cases we studied a voltage drop mainly across the first two thirds of the waveguide in the laser structure.

To conclude, it should be noted that the investigations performed demonstrated the considerable opportunities offered by contact EFM for diagnostics of semiconductor device structures. For the laser heterostructure studied here, the application of EFM made it possible to reveal all characteristic layers of the structure on its cross sections, to determine the position and extension of the *n–p* junction, to obtain profiles of the voltage drop across the forward- and reverse-biased laser, and also to describe, on the basis of capacitance measurements, the distribution of injected carriers in the waveguide.

ACKNOWLEDGMENTS

We thank M.S. Dunaevskiĭ for his assistance in experiments and N.M. Shmidt for helpful participation in discussions.

This study was supported by the Russian Foundation for Basic Research (project no. 00-02-16948) and the Ministry of Science (grant no. 97-1035).

REFERENCES

1. G. Binnig, Ch. Gerber, E. Stell, *et al.*, Europhys. Lett. **3**, 1281 (1987).
2. P. Moriarty and G. Hughes, Ultramicroscopy **42–44**, 956 (1992).
3. A. V. Ankudinov, V. P. Evtikhiev, V. E. Tokranov, *et al.*, Fiz. Tekh. Poluprovodn. (St. Petersburg) **33**, 594 (1999) [Semiconductors **33**, 555 (1999)].
4. I. Suemune and M. Hoshiyama, Jpn. J. Appl. Phys., Part 1 **33**, 3748 (1994).
5. A. V. Ankudinov, A. N. Titkov, T. V. Shubina, *et al.*, Appl. Phys. Lett. **75**, 2626 (1999).
6. G. Bratina, L. Vanzetti, and A. Franciosi, Phys. Rev. B **52**, R8625 (1995).
7. C. C. Williams, J. Slinkman, W. P. Hough, and H. K. Wickramasinghe, Appl. Phys. Lett. **55**, 1662 (1989).
8. V. V. Zavyalov, J. S. McMurray, and C. C. Williams, Rev. Sci. Instrum. **70**, 158 (1999).
9. Y. Martin, D. W. Abraham, and H. K. Wickramasinghe, Appl. Phys. Lett. **52**, 1103 (1988).
10. D. Sarid, *Scanning Force Microscopy* (Oxford Univ. Press, Oxford, 1992).
11. B. D. Terris, J. E. Stern, D. Rugar, and H. J. Mamin, Phys. Rev. Lett. **63**, 2669 (1989).
12. H. J. Leamy, J. Appl. Phys. **53**, R51 (1982).
13. S. G. Konnikov, V. A. Solov'ev, V. E. Umanskiĭ, *et al.*, Fiz. Tekh. Poluprovodn. (Leningrad) **21**, 1648 (1987) [Sov. Phys. Semicond. **21**, 997 (1987)].
14. G. Leveque, P. Girard, E. Skouri, and D. Yareka, Appl. Surf. Sci. **157**, 251 (2000).
15. F. Robin, H. Jacobs, O. Homan, *et al.*, Appl. Phys. Lett. **76**, 2907 (2000).
16. J. W. Hong, K. H. Noh, Sang-il Park, *et al.*, Phys. Rev. B **58**, 5078 (1998).
17. G. D. Wilk, Yi. Wei, Hal Edwards, and R. M. Wallace, Appl. Phys. Lett. **70**, 2288 (1997).

Translated by M. Tagirdzhanov

Semiconductors, Vol. 35, No. 7, 2001, pp. 847–853. Translated from Fizika i Tekhnika Poluprovodnikov, Vol. 35, No. 7, 2001, pp. 881–888.

PHYSICS OF SEMICONDUCTOR DEVICES

Comparative Analysis of Long-Wavelength (1.3 μm) VCSELs on GaAs Substrates

N. A. Maleev, A. Yu. Egorov, A. E. Zhukov, A. R. Kovsh, A. P. Vasil'ev, V. M. Ustinov, N. N. Ledentsov, and Zh. I. Alferov

Ioffe Physicotechnical Institute, Russian Academy of Sciences, Politekhnicheskaya ul. 26, St. Petersburg, 194021 Russia

Submitted December 29, 2000; accepted for publication January 10, 2001

Abstract—Two designs of vertical-cavity surface-emitting lasers (VCSELs) for the 1.3 μm spectral range on GaAs substrates with active regions based on InAs/InGaAs quantum dots and InGaAsN quantum wells are considered. The relationship between the active region properties and optical microcavity parameters required for lasing has been investigated. A comparative analysis is made of VCSELs with active regions based on InAs/InGaAs quantum dots or on InGaAsN quantum wells, which are fabricated by MBE and demonstrate room-temperature CW operation. Optimization of the vertical microcavity design provides single-pass internal optical losses lower than 0.05%. *© 2001 MAIK "Nauka/Interperiodica".*

Semiconductor vertical-cavity surface-emitting lasers (VCSELs) are finding increasingly wide application in high-speed fiber-optic links for information transmission. Compared with the conventional stripe lasers, in which the optical beam is emitted through one of the mirrors formed by the laser structure edges, VCSELs possess an emission directional pattern with higher symmetry, thus enabling a more effective input of the optical radiation into the fiber. Among other important advantages of VCSELs are the higher temperature stability of the lasing wavelength and the applicability of batch technologies in fabrication and testing [1].

Presently, VCSELs for λ = 850 and 980 nm wavelengths are available commercially. High-quality distributed Bragg reflectors (DBRs) formed by alternating AlGaAs and GaAs layers with a thickness equal to 1/4 resonance wavelength (taking into account the refractive index of the material) are used as mirrors. The VCSEL structures are grown on GaAs substrates by molecular-beam epitaxy (MBE) or by metal-organic chemical vapor deposition (MOCVD).

Despite the evident success in developing the technology of VCSEL manufacture for the λ = 850 and 980 nm spectral ranges, several fundamental problems must be resolved to create similar devices for the λ = 1.3 and 1.55 μm ranges [1]. The basic limitations of the InGaAsP/InP system traditionally employed for these spectral ranges result from the relatively poor DBR characteristics. This is associated with the smaller (compared with the AlGaAs/GaAs system) difference between the refractive indices of InGaAsP, InAlGaAs, and InP and also with the low thermal conductivity of quaternary compounds. Furthermore, the relatively poor thermal stability of the basic characteristics is typical of laser diodes on InP substrates. The above problems stimulate a search for new semiconductor materials applicable in designing 1.3 and 1.55 μm optical radiation sources on GaAs substrates. Since the modern technology of device fabrication on GaAs substrates outperforms that for InP substrates in all basic technical and commercial aspects, solving this problem could substantially extend the application area of fiber-optic communication systems.

A number of new semiconductor heterostructures that emit in the λ = 1.2–1.5 μm wavelength range and can be synthesized on GaAs substrates have been proposed in recent years [2]. These include InGaAsN [3] and GaAsSb [4] quantum well (QW) structures and also In(Ga)As structures with arrays of quantum dots (QDs) [5, 6]. Although long-wavelength lasing has been obtained at room temperature in conventional stripe lasers based on all of the systems listed above, the maximal lasing wavelength for VCSELs on GaAs substrates did not exceed, until recently, 1.23 μm [7]. Lately, lasing at λ = 1.3 μm has been demonstrated for the first time with the participation of the authors of this communication for InAs/InGaAs QD VCSELs on GaAs substrates [8], and record-breaking parameters have obtained for CW long-wavelength VCSELs based on InGaAsN QWs [9]. For the latter system, VCSEL lasing at about λ = 1.3 μm has also been achieved in other studies, by using MBE [10] and MOCVD [11]. Thus, the problem of optimizing the active region parameters and the VCSEL design on GaAs substrates in order to obtain device parameters satisfying the basic requirements imposed by commercial applications in fiber-optic communication lines is now coming to the forefront.

In this paper, we discuss the specifics of fabricating long-wavelength (λ = 1.3 μm) VCSELs on GaAs substrates, with active regions based on InAs/InGaAs QDs

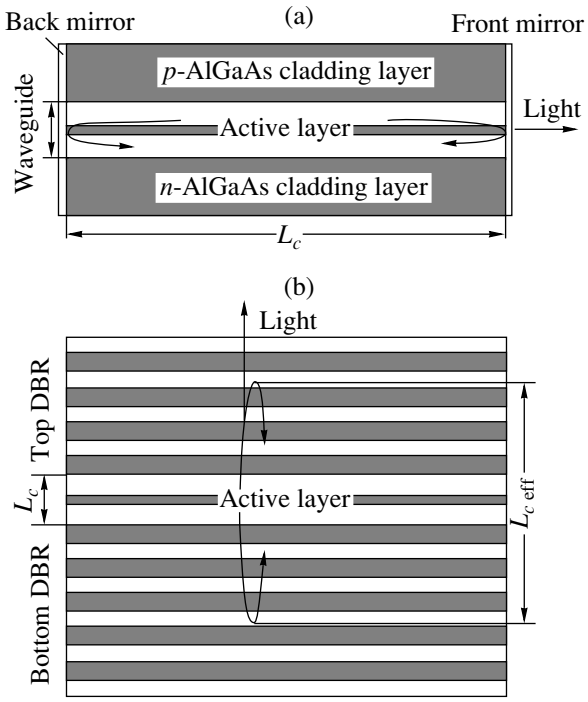

Fig. 1. Schematic of laser structures: (a) conventional stripe laser; (b) VCSEL.

and InGaAsN QWs. The influence of the optical microcavity and active region parameters on the device characteristics is analyzed.

Let us consider the basic factors determining the design choice of long-wavelength VCSELs based on InAs/InGaAs QDs and InGaAsN QWs. The necessary condition for the onset of lasing is the balance between the optical gain and total optical losses, including the output emission losses and the internal losses in the laser structure. In the general case, this condition can be represented for each optical mode as

$$\Gamma g_{\mathrm{th}} = \langle \alpha_i \rangle + \alpha_m, \tag{1}$$

where g_{th} is the optical gain of the active material at the lasing threshold, $\langle \alpha_i \rangle$ is the internal optical loss for a given mode, α_m is the emission output loss associated with the mirrors, and Γ is the 3D optical confinement factor characterizing the interaction of the electromagnetic field of a given mode with the active (amplifying) medium. The product (Γg_{th}) determines the modal optical gain at the lasing threshold.

In conventional stripe lasers, the mirrors confining the optical Fabry–Perot cavity are formed by the structure edges, and, as a rule, the cavity itself is long in comparison to the period of the standing wave of the optical field (Fig. 1a). The optical wave propagates in the active layer plane, and the length of the active (amplifying) region usually coincides with the cavity length L_c, equal in this case to the geometrical distance between the cleaved mirrors. The 3D optical confinement factor can be represented as a product of the optical confinement factor (Γ_z) in the direction of the epitaxial structure growth, z, and the optical confinement factor (Γ_{xy}) in the xy plane parallel to the structure surface [1]. For a conventional laser with a stripe several tens of micrometers wide and several hundred micrometers long, $\Gamma_{xy} \approx 1$. In this case, condition (1) is usually written in the form

$$\Gamma_z g_{\mathrm{th}} = \langle \alpha_i \rangle + \frac{1}{L_c} \ln\left(\frac{1}{R}\right), \qquad R = \sqrt{R_1 R_2}, \tag{2}$$

where R_1, R_2 are the reflectivities of the front (output) and back mirrors.

If the active layer is very thin (as in QW or QD cases) and is situated at the center of the waveguide layer with symmetric emitter layers, the optical confinement factor for the zeroth mode can be approximately calculated using the relation

$$\Gamma_z \equiv \frac{n_{\mathrm{act}} \int_{\mathrm{act}} |E(z)|^2 dz}{n_{\mathrm{eff}} \int_{\mathrm{tot}} |E(z)|^2 dz} \approx \frac{|E_{\max}|^2 L_{\mathrm{act}}}{\int_{\mathrm{tot}} |E(z)|^2 dz} = K L_{\mathrm{act}}. \tag{3}$$

Here, E is the optical wave amplitude, $E_{\max}$ is its maximal value at the center of the cavity layer, L_{act} is the active layer thickness, n_{act} is the refractive index of the active layer, and n_{eff} is the effective refractive index for the mode in question. The indices "total" and "act" refer to integration over the entire structure or only within the active region, respectively.

Some important specific features of VCSEL structures, compared with conventional edge-emitting lasers, are as follows (Fig. 1b):

(i) DBRs are used as top and bottom mirrors.

(ii) The optical cavity is comparatively short (i.e., we have the microcavity mode corresponding to a substantially nonuniform distribution of the amplitude of the optical emission standing wave).

(iii) The light wave propagates in a direction perpendicular to the active layer plane.

(iv) The active layer thickness in VCSELs based on QWs or QDs is much shorter than the cavity length.

To write condition (1) for a VCSEL, account should be taken in the first place of the fact that the optical wave penetrates into the DBR to some depth; i.e., the effective cavity length $L_{c\,\mathrm{eff}}$ differs from the geometrical distance between the mirrors (Fig. 2). Further, for thin active layers, we should take into account the position of the active layer relative to the space distribution of the standing wave amplitude inside the microcavity, with the standing wave factor ξ introduced for this purpose. If the active region of thickness L_{act} lies between

the two cavity mirrors, the standing wave factor can be calculated using the expression [1]:

$$\zeta = 1 + \cos 2\beta Z_s \frac{\sin \beta L_{act}}{\beta L_{act}},$$

where $\beta = 2\pi n_{eff}/\lambda_c$ is the propagation constant for the given optical emission mode, λ_c is the resonance wavelength, and Z_s is the shift between the position of the active layer and the antinode of the standing wave. Evidently, for a thin active region ($\beta L_{act} \ll 1$) the values of the standing wave factor may be in the range from 0 ($Z_s = \lambda_c/4n_{eff}$) to 2 ($Z_s = 0$). For devices of relatively large lateral dimensions (the optical aperture diameter exceeding 3–5 μm), $\Gamma_{xy} \approx 1$, since the scattering of the light wave on edges is negligible and a uniform distribution of the emission intensity over the device area can be assumed. Then, taking into account (3), relation (1) takes the form [1]:

$$\xi g_{th} \frac{L_{act}}{L_{ceff}} = \langle \alpha_i \rangle + \frac{1}{L_{ceff}} \ln\left(\frac{1}{R}\right). \quad (4)$$

The possibility of designing a VCSEL with a given kind of optical resonator can be assessed on the basis of experimental characteristics of stripe lasers with the same active region. From Eqs. (2) and (3) we obtain an expression for calculating the material gain of a stripe laser at the generation threshold

$$g_{th} = \frac{g_{mod}}{KL_{act}}, \quad (5)$$

where g_{mod} is the measured modal gain.

If the thickness of the active material in VCSEL is the same as that in the stripe laser, the fundamental possibility of lasing can be assessed by transforming Eq. (4). The result is as follows:

$$\frac{\xi g_{mod}}{K} = \langle \alpha_i \rangle L_{ceff} + \ln\left(\frac{1}{R}\right). \quad (6)$$

It is worth noting that the active layer thickness L_{act} does not appear in (6). This is particularly important in analyzing QD structures, where the active layer thickness is not clearly defined. Once the threshold modal gain for the stripe laser is measured, and the K value, the distribution of the optical field amplitude, and the corresponding reflectivities of the top and bottom mirrors for are calculated for a given cavity, we can assess the possibility of lasing at the given level of internal losses.

Previously, we showed that the optimization of MBE conditions allows the fabrication of structures with several InAs/InGaAs QD layers with high surface density of the array, exhibiting bright photoluminescence (PL) in the $\lambda = 1.3$ μm wavelength range, and without broadening of the line half-width relative to single-layer QD structures [12]. Stripe lasers with this active region demonstrate a low lasing threshold

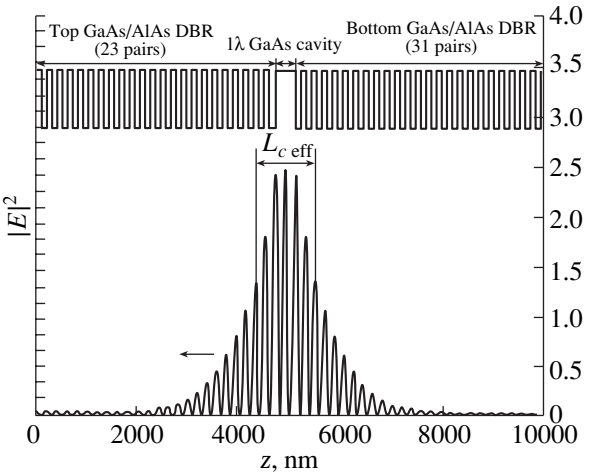

Fig. 2. Distribution of the squared optical field amplitude and the refractive index profile for a typical VCSEL structure on a GaAs substrate.

(<80 A/cm^2) and a high output power of CW generation (>2.5 W) [13]. However, for InGaAs QD structures the gain levels off at high injection currents, due to the finite QD surface density [2]. The measured modal optical gain for long-wavelength InAs/InGaAs QD edge lasers is 10–12 cm^{-1} (Fig. 3), with internal optical losses (1.5 ± 0.3) cm^{-1} [14] (laser structures with three QD layers, $Al_{0.8}Ga_{0.2}As$ emitters, and 0.4 μm thick GaAs waveguide have $\Gamma_z = 0.017$ and $K = 3.4 \times 10^4$ cm^{-1} at 5-nm effective thickness of the active layer).

The optical gain achieved in InGaAsN QW structures exceeds that in InAs/InGaAs QD structures [15, 16] (Fig. 3). The dependence of the modal optical gain g on the injection current density J for QW structures can be approximated by the expression

$$g_{mod} = g_0 \ln(J/J_{tr}), \quad (7)$$

where J_{tr} is the transparency current density, and g_0 is a numerical parameter.

For InGaAsN structures with two QWs ($Al_{0.3}Ga_{0.7}As$ n- and p-emitters, a 0.4-μm-thick GaAs waveguide, 6.5-nm-thick QWs, $\Gamma_z \approx 0.014$ and $K = 2.15 \times 10^4$ cm^{-1}), the measured values are $g_0 = 30$ cm^{-1} and $J_{tr} = 290$ A/cm^2, with internal optical losses (7.0 ± 0.5) cm^{-1} [16].

Let us now discuss the standard VCSEL design with AlAs/GaAs top and bottom DBRs and a GaAs cavity of thickness $L_{cGaAs} = \lambda_c/n_{GaAs}$ and a thin active layer located precisely at its center (here n_{GaAs} is the GaAs refractive index at the resonance wavelength λ_c = 1300 nm). The calculated distribution of the squared optical field amplitude for this structure is presented in Fig. 2. In calculating the effective cavity length, we can

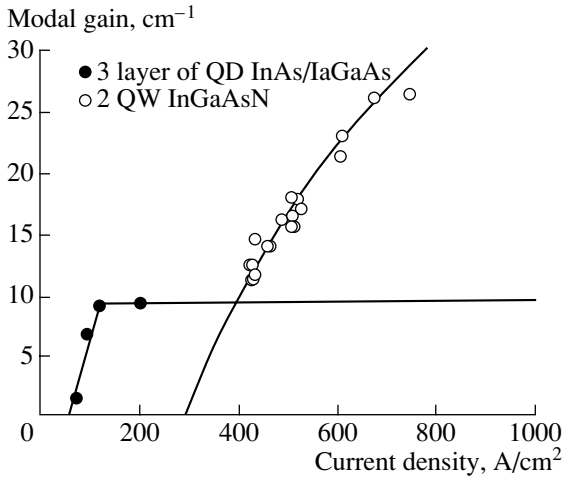

Fig. 3. Modal optical gain vs. current density for stripe lasers whose active region comprises 3 InAs/InGaAs QD layers [14] and 2 InGaAsN QWs [16].

use an approximate relation for the depth of optical field penetration into the DBR [1]:

$$L_{\text{pen}} \approx \frac{h_{\text{high}} + h_{\text{low}}}{4} \frac{n_{\text{high}} + n_{\text{low}}}{n_{\text{high}} - n_{\text{low}}},$$

where n_{high} and n_{low} are the optical refractive indices for the layers forming a DBR; $h_{\text{high}} = \lambda_c n_{\text{high}}$, $h_{\text{low}} = \lambda_c / n_{\text{low}}$. In the case of a AlAs/GaAs DBR ($n_{\text{nigh}} = n_{\text{GaAs}} = 3.44$, $n_{\text{low}} = n_{\text{AlAs}} = 2.91$ for $\lambda_c = 1300$ nm), the effective cavity length

$$L_{c\,\text{eff}} = L_{c\,\text{GaAs}} + 2L_{\text{pen}} = 377.6 + 2 \times 617.3 \approx 1600 \text{ nm}.$$

For an active region comprising three InAs/InGaAs QD layers ($\xi \approx 1.85$, maximal modal gain 12 cm^{-1} at $K = 3.4 \times 10^4$ cm^{-1}), we obtain, using Eq. (6) and assuming zero internal losses, $R > 0.9994$ as the value necessary for the onset of lasing. At internal losses of 2 cm^{-1}, $R > 0.9997$ is already necessary, which corresponds to a mirror reflectivity of no less than 0.9998 (for symmetrical top and bottom DBRs).

The estimated values for an InGaAsN layer with two QWs are $R > 0.994$ (at zero internal losses) and $R > 0.995$ (at internal losses of 2 cm^{-1}). In performing these calculations, a threshold current density of 3 kA/cm^2 was assumed. Thus, the higher optical gain of the InGaAsN QW structures renders the requirements for the microcavity quality somewhat less stringent. Nevertheless, in both cases extremely high mirror reflectivity is required for lasing to occur.

Let us assess the possibility of using the traditional VCSEL design with top and bottom contacts on doped mirrors with *n*- and *p*-type conduction. One of the principal mechanisms of losses in AlGaAs/GaAs mirrors is absorption in *p*-GaAs layers (both by free carriers and via intersubband transitions in the valence band). The maximum possible DBR reflectivity can be calculated using the expression [17]:

$$R_{\max} = 1 - \lambda_c \alpha \frac{n_{\text{high}}^2 + n_{\text{low}}^2}{n_{\text{GaAs}}(n_{\text{high}}^2 - n_{\text{low}}^2)},$$

where α is the free-carrier absorption coefficient. Calculations and experimental studies show that for *p*-GaAs/*p*-AlAs DBRs with an average doping level of $(1–2) \times 10^{18}$ cm^{-3}, the maximum reflectivity is limited by 0.995. At lower doping levels, the series resistance of the device increases dramatically because of the additional voltage drop across the heterointerfaces [1]. Recent studies have shown that for *n*-AlAs/*n*-GaAs DBRs doped to ~10^{18} cm^{-3}, the maximal reflectivity also does not exceed 0.997 [18]. Therefore, it is unlikely that long-wavelength VCSELs can be fabricated on GaAs substrates in the traditional design.

Our analysis shows that the optimal design of long-wavelength VCSELs on GaAs substrates is a configuration with undoped top and bottom AlAs/GaAs or Al_xO_y/GaAs DBRs. Mirrors of the latter type can be fabricated by the selective oxidation of AlGaAs layers in an atmosphere saturated with water vapor [19]. The large difference between the refraction indices of layers in oxidized mirrors ($n_{\text{GaAs}} = 3.44$, $n_{\text{Al}_x\text{O}_y} = 1.61$ for $\lambda =$ 1300 nm) ensures high optical reflectivity in a wide spectral range, thus reducing the sensitivity to calibration errors. At the same time, the use of nonconducting mirrors somewhat complicates device fabrication because of the necessity to deposit *p*- and *n*-contacts onto the conducting layers inside the cavity and the possible increase in the series resistance. In our study, we used AlAs/GaAs DBR for InGaAsN QW devices and oxidized mirrors for InAs/InGaAs QD VCSELs.

The VCSEL structures with InAs/InGaAs QD active layers were grown by MBE with a solid-state As_4 source in a Riber 32P installation at the Ioffe Institute, and the InGaAsN QW structures, in a VG Semicon MBE machine with an RF plasma source of atomic nitrogen at Infineon Technologies Co., Germany. The specifics of active region formation have been described previously [6, 12, 16].

Figure 4 shows the design and principal characteristics of a VCSEL whose active region comprises two InGaAsN QWs. Devices with an oxidized aperture of size 3×7 μm^2 have a threshold current of 3.3 mA at external quantum efficiency $\eta_d = 18\%$ (emission output through the top mirror) [9]. The maximal CW output power at a temperature of 10°C exceeds 1 mW, which is the best result reported for long-wavelength VCSELs on GaAs substrates.

In designing the optical cavity, account was taken of the fact that a contact *p*-layer must be comparatively thick because of the relatively low hole mobility in GaAs. To diminish internal optical losses, primarily associated with free-carrier absorption in the *p*-layer, a comparatively thick AlGaAs aperture layer is used,

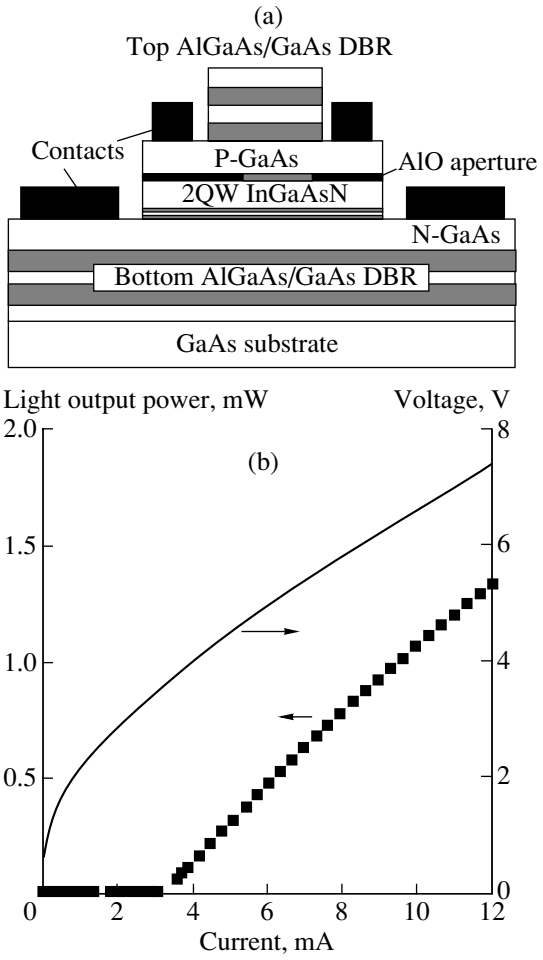

Fig. 4. (a) Schematic of cross section and (b) characteristics of a VCSEL whose active region comprises two InGaAsN QWs. $\lambda = 1.29$ μm, pulse mode.

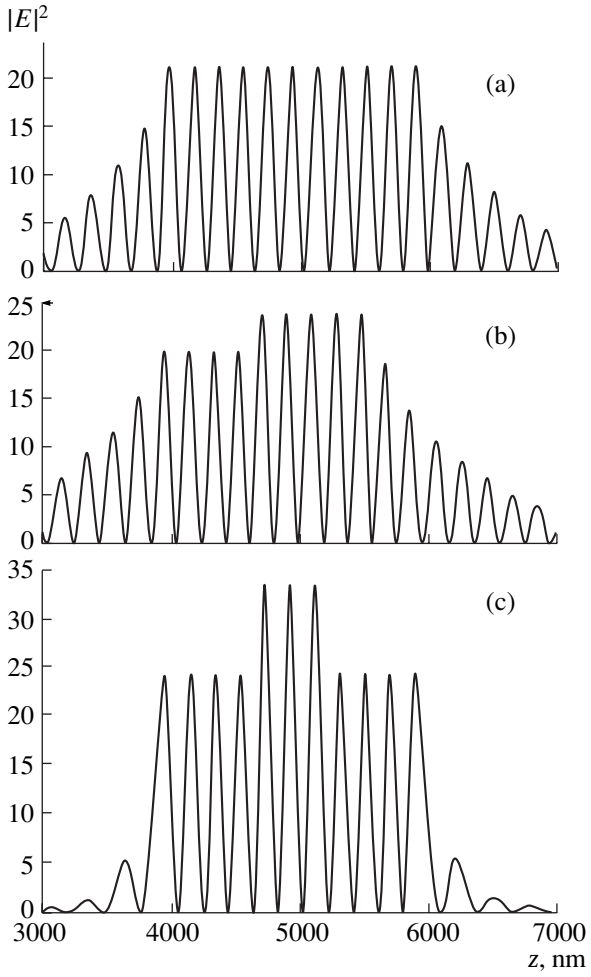

Fig. 5. Normalized spatial distributions of a squared optical field amplitude for three types of microcavities: (a) AlAs/GaAs DBR, $5\lambda_c/n_{GaAs}$-thick GaAs cavity; (b) AlAs/GaAs DBR, $4\lambda_c/n_{GaAs}$-thick GaAs cavity with a single oxidized aperture; (c) AlGaO/GaAs DBR, $5\lambda_c/n_{GaAs}$-thick GaAs cavity with two oxidized apertures.

which allows partial redistribution of the optical field in the cavity, compared with a structure without an aperture (Figs. 5a and 5b). At a nominal cavity length $L_{cGaAs} = 4\lambda_c/n_{GaAs}$, we have $L_{ceff} \approx 2750$ nm.

The calculated reflectivities for both mirrors at the resonance wavelength are 0.9977, which yields the estimated optical output losses of ~8 cm^{-1}. Assuming a uniform current distribution across the active region (aperture) and that relation (7) is valid, we obtain that the modal optical gain of a stripe laser of ~140 cm^{-1} corresponds to a threshold current density of ~15 kA/cm^2. It follows from Eq. (6) that the condition for lasing onset corresponds to internal losses of ~35 cm^{-1}. Such a value of internal losses makes it possible to estimate, at given emission output losses, the internal quantum efficiency: $\eta_i \approx 1$. Thus, the results obtained confirm the high quality of the active material and give reason to expect a substantial improvement of the device characteristics upon further optimization of the microcavity design.

Since the optical gain of QD structures is limited, we used, for the InAs/InGaAs QD VCSELs, an optical microcavity with Al_xO_y/GaAs DBRs, preliminarily optimized to suppress the optical losses. Figure 6 presents a schematic of the VCSEL cross section and its principal characteristics. For devices with an oxidized aperture of 8×8 μm, the threshold current is 1.8 mA at an external quantum efficiency of 41% (with emission output through the top mirror) [8], which is the best result reported for VCSELs on GaAs substrates operating in the $\lambda = 1.3$ μm range. In the CW mode at room temperature, the output power exceeds 0.6 mW at an external quantum efficiency of 39% [20]. The threshold current densities of VCSEL exceed the characteristic values at which the gain of the QD ground state levels off. This may be due to nonuniform current distribution over the aperture area.

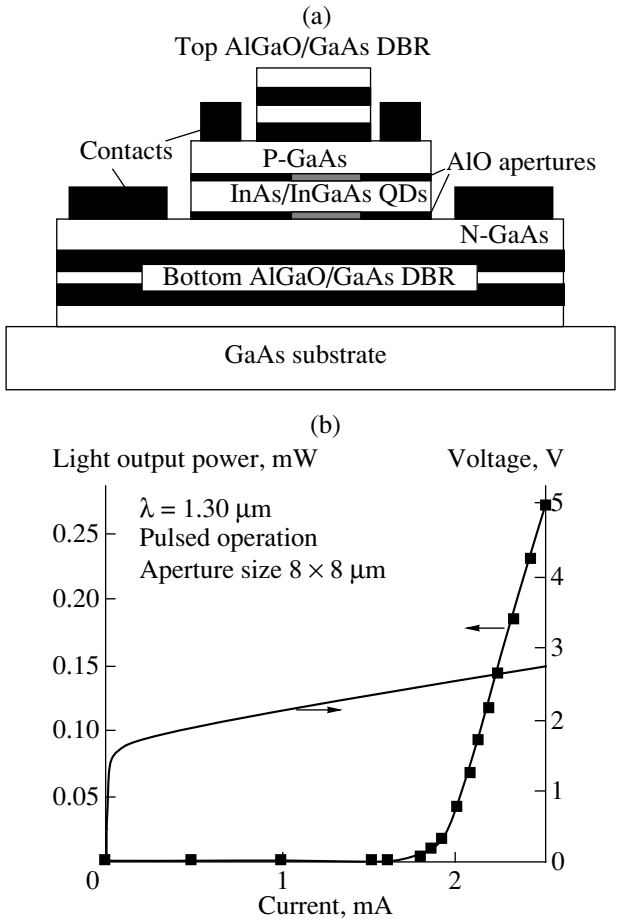

Fig. 6. (a) Schematic of cross section and (b) characteristics of a VCSEL whose active region comprises 3 InGaAsN QD layers. $\lambda = 1.30$ μm, pulse mode.

Two Al_xO_y apertures obtained by partially oxidizing AlGaAs layers provide for not only current confinement but also additional redistribution of the optical field in the cavity. Compared with semiconductor cavities, the optical field amplitude in the active region increases substantially, and the penetration depth of the optical field into the mirrors decreases (Fig. 5c). The calculated values $L_{ceff} \approx 2300$ nm and $R = 0.9996$ yield output losses of optical emission equal to ~1.5 cm^{-1}. Applying the method described above, we obtain that the level of internal optical losses consistent with the condition for lasing onset should not exceed 1.5 cm^{-1}. On the other hand, the internal optical losses can be estimated using the formulae relating the external and internal quantum efficiencies of VCSEL to the dissimilar mirror reflectivities [21]:

$$\eta_d^1 = \eta_d \frac{(1-R_1)}{(1-R_1)+(1-R_2)\sqrt{R_1/R_2}},$$

$$\eta_d = \eta_i \frac{\ln(1/R)}{\langle\alpha_i\rangle L_{ceff} + \ln(1/R)}.$$

Here, η_d^1 is the external quantum efficiency for emission through the top mirror with reflectivity R_1. It can be shown that, for the measured quantum efficiency of 41%, the internal optical losses in the structure must not exceed 2.6 cm^{-1} (at internal quantum efficiency $\eta_i = 1$) and 1.6 cm^{-1} (at $\eta_i = 0.7$, a value typical of stripe lasers with similar active regions [13]). Thereby, we have a good coincidence between the values of internal optical losses calculated from the experimental data for edge lasers and directly from measured VCSEL parameters. The achieved level of single-pass optical losses $\langle\alpha_i\rangle L_{ceff} = 0.04$–$0.05\%$ corresponds to the best results reported for all types of VCSELs [1, 21, 22]. It is worth noting that the level of internal optical losses for VCSELs operating in the $\lambda = 1.3$ μm range is significantly lower than that for a VCSEL of the same design with an active region of vertically coupled InGaAs QDs, emitting in the $\lambda = 1$ μm range [23]. In the latter case, the losses measured by the method proposed in [21] are ~8 cm^{-1}. Interestingly, smaller optical losses, compared with vertically coupled InGaAs QD stripe lasers, are also regularly observed for stripe lasers with InAs/InGaAs QDs.

The electrical parameters of the fabricated devices indicate good possibilities for further improvement. The relatively high (300–400 Ω) series resistance is far from the best data reported for optimized VCSELs of similar design [24], and causes additional overheating of the active region.

Summarizing the experimental data obtained and differences observed between InAs/InGaAs QD and InGaAsN QW VCSELs, we make the following conclusions:

(i) The high optical gain achieved in InGaAsN QW structures enables the operation of VCSELs based on semiconductor microcavities with relatively high internal losses.

(ii) To produce VCSELs based on QD arrays, it is advisable to use cavities with Al_xO_y reflectors, with optical properties, in general, much exceeding those of cavities with semiconductor mirrors.

In this paper, we analyzed the specifics of designing long-wavelength VCSELs on GaAs substrates, and performed a comparative study of the parameters of devices based on InAs/InGaAs QDs and InGaAsN QWs. The analysis demonstrated a significantly higher level of electrical and internal optical losses in the structures of the second type, which is due to the nonoptimal design of the vertical semiconductor microcavity. Nevertheless, by virtue of the high optical gain in the active region, InGaAsN QW VCSELs demonstrate the highest output power (>1 mW in CW mode) among all the VCSELs on GaAs substrates. The design optimization must substantially improve their parameters. As for QD VCSELs, it is advisable to use microcavities with Al_xO_y/GaAs DBRs, since they ensure the lowest level of single-pass optical losses (0.04–0.05%), low

threshold currents (<2 mA), and high differential efficiency (~40%). We believe that QD VCSELs will be preferable in creating devices with small (less than 1–2 μm) emitting regions because of the suppression of the lateral carrier diffusion.

ACKNOWLEDGMENTS

We are indebted to Prof. D. Bimberg, Prof. J. A. Lott, and Dr. H. Riechert. This study was supported by the Russian Foundation for Basic Research, Programs "Physics of Solid-State Nanostructures," NanOp, and CRDF (grant no. RE1-2221).

REFERENCES

1. *Vertical-Cavity Surface-Emitting Lasers*, Ed. by C. W. Wilmsen, H. Temkin, and L. A. Coldren (Cambridge Univ. Press, Cambridge, 1999).
2. V. M. Ustinov and A. E. Zhukov, Semicond. Sci. Technol. **15**, R41 (2000).
3. K. Nakahara, M. Kondow, T. Kitatani, *et al.*, IEEE Photonics Technol. Lett. **10**, 487 (1998).
4. T. Anan, K. Nishi, S. Sugou, *et al.*, Electron. Lett. **34**, 2127 (1998).
5. D. L. Huffaker, G. Park, Z. Zhou, *et al.*, Appl. Phys. Lett. **73**, 2564 (1998).
6. V. M. Ustinov, N. A. Maleev, A. E. Zhukov, *et al.*, Appl. Phys. Lett. **74**, 2815 (1999).
7. M. Yamada, T. Anan, K. Kurihara, *et al.*, Electron. Lett. **36**, 637 (2000).
8. J. A. Lott, N. N. Ledentsov, V. M. Ustinov, *et al.*, Electron. Lett. **36**, 1384 (2000).
9. G. Steinle, A. Yu. Egorov, and H. Riechert, Electron. Lett. **37**, 92 (2001).
10. K. D. Choquette, J. F. Klem, A. J. Fisher, *et al.*, Electron. Lett. **36**, 1388 (2000).
11. S. Sato, N. Nishiyama, T. Miyamoto, *et al.*, Electron. Lett. **36**, 2018 (2000).
12. N. A. Maleev, A. E. Zhukov, A. R. Kovsh, *et al.*, Fiz. Tekh. Poluprovodn. (St. Petersburg) **34**, 612 (2000) [Semiconductors **34**, 594 (2000)].
13. A. E. Zhukov, A. R. Kovsh, V. M. Ustinov, *et al.*, IEEE Photonics Technol. Lett. **11**, 1345 (1999).
14. M. V. Maximov, Yu. M. Shernyakov, I. N. Kaiander, *et al.*, Electron. Lett. **35**, 2038 (1999).
15. A. Yu. Egorov, D. Bernklau, D. Livshits, *et al.*, Electron. Lett. **35**, 1643 (1999).
16. A. Yu. Egorov, D. Bernklay, B. Borchert, *et al.*, in *Proceedings of MBE XI, Beijing, 2000*, J. Cryst. Growth (2001) (in press).
17. D. I. Babic, J. Piprek, K. Streubel, *et al.*, IEEE J. Quantum Electron. **33**, 1369 (1997).
18. S. Mogg, F. Salomonsson, C. Asplund, *et al.*, in *Proceedings of the International Conference on Indium Phosphide and Related Materials, Williamsburg, 2000*, p. 388.
19. M. H. MacDougal, P. D. Dapkus, A. E. Bond, *et al.*, IEEE J. Sel. Top. Quantum Electron. **3**, 905 (1997).
20. J. A. Lott, N. N. Ledentsov, V. M. Ustinov, *et al.*, in *Proceedings of the LEOS 2000 Conference: IEEE Lasers and Electro-Optics Society Annual Meeting, Rio Grande, Puerto Rico, 2000*, Vol. 1, p. 304.
21. G. M. Yang, M. H. MacDougal, V. Pudikov, and P. D. Dapkus, IEEE Photonics Technol. Lett. **7**, 1228 (1995).
22. D. L. Huffuker and D. G. Deppe, IEEE Photonics Technol. Lett. **11**, 934 (1999).
23. J. A. Lott, N. N. Ledentsov, V. M. Ustinov, *et al.*, Electron. Lett. **33**, 1150 (1997).
24. M. H. MacDougal, J. Geske, C.-K. Lin, *et al.*, IEEE Photonics Technol. Lett. **10**, 9 (1998).

Translated by D. Mashovets

Semiconductors, Vol. 35, No. 7, 2001, pp. 854–859. Translated from Fizika i Tekhnika Poluprovodnikov, Vol. 35, No. 7, 2001, pp. 889–895.

PHYSICS OF SEMICONDUCTOR DEVICES

1.3 μm Vertical Microcavities with InAs/InGaAs Quantum Dots and Devices Based on Them

A. V. Sakharov*, I. L. Krestnikov*, N. A. Maleev*, A. R. Kovsh*, A. E. Zhukov*, A. F. Tsatsul'nikov*, V. M. Ustinov*, N. N. Ledentsov*, D. Bimberg, J. A. Lott***, and Zh. I. Alferov***

** Ioffe Physicotechnical Institute, Russian Academy of Sciences, St. Petersburg, 194021 Russia*

*** Institut für Festkörperphysik, Technische Universität Berlin, D-10623 Berlin, Germany*

**** Air Force Institute of Technology, Department of Electrical and Computer Engineering, Wright-Patterson AFB, Ohio, USA 45433*

Submitted December 29, 2000; accepted for publication January 10, 2001

Abstract—Various structures with optical microcavities and active layers based on InGaAs/GaAs quantum dots MBE-grown on GaAs substrates were studied theoretically and experimentally. LEDs for the 1.3 μm spectral range with narrow spectral characteristics and low light beam divergence were fabricated. Vertical lasing at 1.3 μm was obtained in a structure with oxidized AlO/GaAs mirrors under injection pumping. © *2001 MAIK "Nauka/Interperiodica".*

1. INTRODUCTION

In recent years, light-emitting optoelectronic devices for 1.3- and 1.55-μm spectral ranges have comprised more than two-thirds of the entire semiconductor laser market, their production increasing annually by 60%. Nowadays, the overwhelming majority of these lasers are made in the stripe configuration. At the same time, vertical cavity surface-emitting lasers (VCSELs) offer good prospects for telecommunication applications owing to their better integration with optical fibers and higher temperature stability. The best VCSEL structures operating at 1.3 μm are fabricated by sintering the InGaAs/InP active region with AlGaAs distributed Bragg reflectors (DBRs) [1, 2]. These devices can find only a rather limited application because of their complexity and high production cost. Along with VCSELs, vertical cavity light-emitting diodes (VC LEDs) could find wide application [3] by virtue of their relatively simple fabrication and absence of threshold characteristics.

All this has stimulated attempts to produce light-emitting devices for this spectral range on GaAs substrates, both in conventional configuration [4–8] and with vertical cavities [9–12]. In the present study, we analyzed the possibilities of fabricating VCSELs and VC LEDs for the 1.3 μm spectral range on the basis of InAs/InGaAs heterostructures with quantum dots (QDs).

2. EXPERIMENTAL

2.1. Growth and Optical Properties of Structures with InAs/InGaAs QDs

All the structures studied in this work were grown by MBE on (001) GaAs substrates. For test structures, one or several layers of InAs/InGaAs QDs were deposited onto the GaAs surface and confined on both sides by short-period AlAs/GaAs superlattices. Each QD layer was formed by depositing 2.5–2.75 InAs monolayers overgrown with a $In_{0.15}Ga_{0.85}As$ layer 5.5–7.5 nm thick [13]. The QD layers were separated with 25-nm-thick GaAs. Photoluminescence (PL) was excited either by an Ar-ion (100 W/cm^2, 515 nm) or semiconductor AlGaAs (5 W/cm^2, 782 nm) laser. Optical reflection (OR) was studied under illumination with a halogen lamp. A germanium photodiode connected to a lock-in amplifier was placed at the monochromator output.

The main problem in using QDs as an active region is their low surface density (especially for the 1.3-μm spectral range) [4]. On the other hand, the stacking of QDs can dramatically enhance the amount of nonradiative recombination centers [14]. However, the optimization of the growth process for InAs/InGaAs QDs by carefully adjusting the growth rate and the layer thickness and composition and also by using thick (20–25 nm) GaAs spacers grown at elevated temperatures [15] made it possible to obtain QD arrays with relatively high density—(3–4) × 10^{10} cm^{-2}—for all the QD layers. Figure 1 presents the PL spectra of test sam-

ples with varied In content of the QDs and different numbers of QD layers (m). The radiation wavelength can be controlled within the 1.15- to 1.3-μm range without impairing the emission properties. At a low excitation level, the PL intensities for a single QD layer and for a structure with three QD layers are equal. On raising the optical excitation level, linear dependences of the PL integral intensity on the excitation density are observed for structures with different numbers of QD layers (m = 1, 3, 5). This indicates that radiative recombination is the main channel of nonequilibrium carrier relaxation. Therefore, with MBE conditions optimized, the stacking of QD layers does not impair the optical properties of the structures.

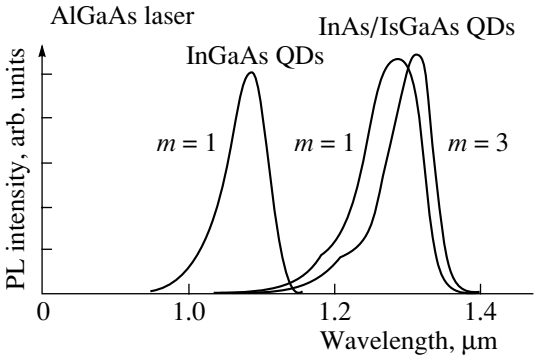

Fig. 1. Room temperature PL spectra of test structures (m is the number of QD layers).

2.2. Structures with Vertical Microcavities

The preliminarily optimized InAs/InGaAs QDs were used as the active region in cavity structures. Both the structures for optical studies and the VC LED structures included bottom 33-period AlAs/GaAs DBRs. In the optical structures, three InAs/InGaAs QD layers were placed at the center of the undoped GaAs cavity with a thickness equal to the wavelength of light in the crystal (1λ cavity). For the VC LED structures, we used 2λ cavity with the same active region, confined from both sides with short-period $Al_{0.25}Ga_{0.75}As$/GaAs superlattices (SL) with λ/4 effective thickness serving as emitters. The last two pairs of the AlAs/GaAs DBRs and the lower part of the cavity (including the SL) were doped with silicon; the upper part of the cavity (including the SL), with beryllium. The VC LED structure was completed with two pairs of $Al_{0.25}Ga_{0.75}As$:Be/GaAs:Be DBRs, which are necessary for the formation of a p-contact and better current spreading in the device. Top mirrors were formed by depositing ZrO_2/SiO_2 DBRs both for optical and for VC LED structures.

The mirrors used in VCSELs were AlO/GaAs DBRs (5 and 7.5 periods for top and bottom DBRs, respectively) fabricated by selective oxidation of epitaxial AlAs layers in water vapor. The symmetrical 5λ cavity consisted of GaAs:(Si or Be) (7λ/4) layers adjacent to the DBR, aperture AlAs:(Si or Be) (λ/4) layers, and a central undoped GaAs layer; three QD layers were placed between these layers.

For VC LEDs and VCSELs, we used n- and p-contacts to directly the doped layers inside the cavity. The carrier confinement layers in the VC LEDs were fabricated by proton implantation of the passive regions of the device [16], whereas in VCSELs the apertures were formed by partial oxidation of the AlAs layers of the cavity [17].

2.3. Calibration of the Microcavity Structures

The main problem in MBE fabrication of vertical-microcavity structures is that even a minor (~1–2%) error in the thickness of the DBR layers and/or the cavity itself may impair the device parameters. In our case, the growth chamber was not equipped with devices for monitoring the growing layer thickness *in situ*. Therefore, a preliminary calibration was necessary. A special calibration structure was designed, comprising six pairs of Al(Ga)As/GaAs DBRs and a GaAs-(λ/2) cavity. OR spectra were measured both for the whole structure and after selectively etching off the GaAs cavity and the top Al(Ga)As layer. A comparative analysis of the obtained and simulated OR spectra allowed us to determine the thicknesses of GaAs and Al(Ga)As layers. Thus, only one additional structure is necessary for calibrating the GaAs and Al(Ga)As growth rates. However, an additional epitaxial process is usually required for a more precise calibration of microcavities with several QD layers.

3. RESULTS AND DISCUSSION

3.1. Photoluminescence and Optical Reflectivity of Structures with QDs in Microcavity

Before fabricating optoelectronic devices based on QD microcavities, we performed preliminary studies of optical structures. Figure 2a shows a typical room temperature PL spectrum of a test QD structure without DBRs (upper curve). Analysis shows that the PL spectrum is a superposition of two peaks corresponding to the ground (long-wavelength peak) and excited (short-wavelength peak) states of QDs (the result of numerical analysis for the peaks is represented by dashed lines in Fig. 2a). The full width at half-maximum (FWHM) of the ground state peak is 55 nm (40 meV) because of the inhomogeneous broadening. The arrangement of QDs inside the microcavity drastically modifies the PL spectra. Depending on the microcavity quality, the FWHM of the PL spectra decreases; it is only 4 nm (Fig. 2d) with top dielectric DBR of 13 ZrO_2/SiO_2 pairs.

Although the PL line is appreciably narrowed (from 55 to 4 nm), the calculations show that for ideal DBRs consisting of 33 AlAs/GaAs pairs and 13 ZrO_2/SiO_2 pairs, the FWHM of the PL spectrum must be substantially narrower (0.005 nm). This means that the reflec-

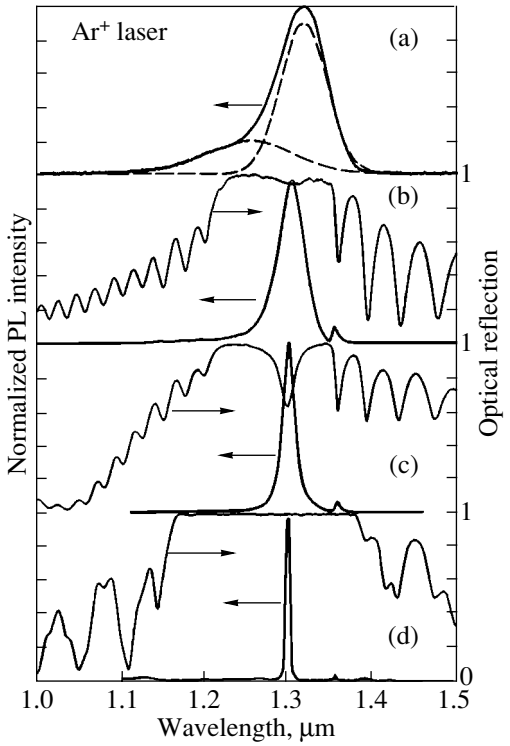

Fig. 2. Room temperature PL (thick solid lines) and OR (thin solid lines) spectra of structures with different numbers of ZrO_2/SiO_2 pairs in the top DBR. (a) Satellite sample without top and bottom DBRs. Number of pairs in the top DBR: (b) 0; (c) 2; (d) 13. Dashed lines in Fig. 2a represent the results of a numerical analysis of the PL peaks.

tivity of real mirrors does not reach the predicted level. If the top DBR is absent, the GaAs–air interface serves as a top mirror, providing a reflectivity of ~30%. In this case, the cavity becomes strongly asymmetrical owing to the high reflectivity of the bottom AlAs/GaAs DBR and the dip in the OR spectrum must be practically unobservable. However, the experiment (Fig. 2b) shows a noticeable dip, which can be related to the insufficient reflectivity of the bottom AlAs/GaAs DBR. This is confirmed by the fact that, for a structure with high-reflectivity top DBR consisting of 13 ZrO_2/SiO_2 pairs, no spectral dip is observed because of the microcavity asymmetry (Fig. 2d).

The reflectivity of mirrors can be evaluated numerically from the FWHM of the PL spectrum. Indeed, the product of reflectivities of the top (R_t) and bottom (R_b) mirrors equals [18]

$$R_t R_b = \left[1 - \pi\frac{N_{\lambda/2}}{Q}\right]^2, \qquad (1)$$

where $N_{\lambda/2}$ is the effective microcavity length (in half-wavelength units) and Q is the microcavity quality factor ($Q = \lambda/\Delta\lambda$, λ is the resonance wavelength, and $\Delta\lambda$ the FWHM of the PL line or of the dip in the OR spectrum). Since an electromagnetic wave penetrates into the DBR (see below, Sec. 3.2), we have $N_{\lambda/2} = 6$. Substituting this value and $Q = 430$ into Eq. (1), we obtain $R_t R_b = 0.91$. Taking into account the above considerations and the fact that the FWHM of the PL line remains practically unchanged when the number of pairs in the top ZrO_2/SiO_2 DBR is raised to more than 5–6, we may suppose that the key contribution to the transmission is made by the bottom AlAs/GaAs DBR. Thus, because of the fluctuations of the AlAs and GaAs layer thicknesses in the semiconductor DBR and the calibration uncertainties, the available MBE equipment enables the reliable fabrication of AlAs/GaAs DBRs with a reflectivity of only up to 91%.

3.2. Choice of the Device Design

QD structures emitting in the 1.3-μm range are characterized by low modal gain, the gain of the QD ground state being limited. Below, we discuss the different types of microcavities with regard to their possible application in optoelectronic devices based on InGaAs/GaAs QDs and, in particular, in VCSELs.

Dependences of the electroluminescence (EL) intensity on the current density are presented in Fig. 3. These dependences were obtained at room temperature for an ordinary nonresonant LED. The ground-state EL intensity levels off with increasing current density, although the integral EL intensity grows linearly. Not only is the ground state clearly visible in the EL spectra, but two excited states as well. The difference from the PL spectra presented in the preceding section, where only one excited state was observed, consists in a substantially higher level of QD excitation at a current density of ~0.8 kA/cm^2 as compared with the PL excitation by an argon laser.

We have observed the same effect, i.e., the leveling off of the ground state intensity, in stripe lasers with several InGaAs/GaAs QD layers in the active region [19]. As follows from the data obtained, the material gain (g_{mat}) does not exceed 1000 cm^{-1} for three QD layers [20]. To apply these data to the case of vertical microcavities, we assumed that the QD material gain is nearly direction-independent. This is true if the wave function of an exciton in the QD is nearly spherical. Then the necessary condition for the onset of lasing is [18]

$$g_{mat}\Gamma_{xy}\xi\frac{L_{act}}{L_{eff}} \geq \alpha_{int} + \alpha_{ext}, \qquad (2)$$

where Γ_{xy} is the optical confinement factor in the plane perpendicular to the growth direction [$\Gamma_{xy} \approx 1$ for large (>5 μm) apertures]; ξ is the standing wave factor ($\xi \approx 2$); L_{act} is the active region thickness; L_{eff} is the effective microcavity thickness (which may differ substantially from the nominal microcavity thickness owing to the electromagnetic wave penetration into the DBR, Figs. 4 and 5); α_{int} and α_{ext} are the internal and external (output) losses, respectively. Substituting numerical

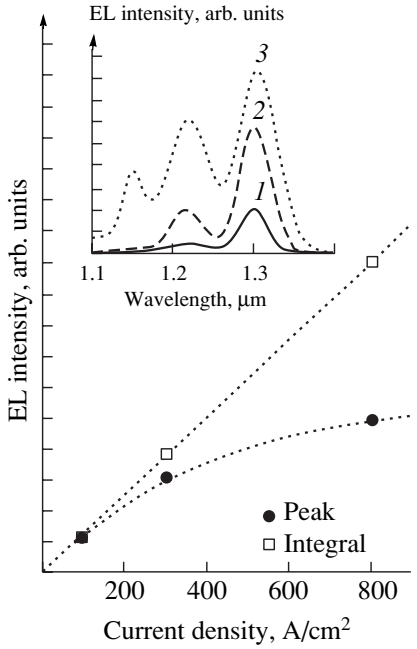

Fig. 3. Room temperature EL intensity vs current density for a standard QD LED. Solid circles: intensity in the peak of the EL spectrum, squares: integral intensity. Insert: luminescence spectra at current densities: (*1*) 100, (*2*) 300, and (*3*) 800 A/cm^2.

values into the left-hand side of Eq. (2), we find that the modal gain for the devices with vertical microcavities does not exceed 4 cm^{-1}. Therefore, the external emission losses, which can be calculated using the formula

$$\alpha_{ext} = \frac{1}{L_{eff}} \ln\left(\frac{1}{\sqrt{R_t R_b}}\right), \quad (3)$$

must also be lower than this value. Calculation for a structure with 33-period AlAs/GaAs bottom DBR and 13-period ZrO_2/SiO_2 top DBR shows that R_tR_b = 0.99995 and α_{ext} = 0.12 cm^{-1}. This value is substantially lower than the maximal modal gain (4 cm^{-1}), but we know from the preceding section that the real α_{ext} value is 0.91, which yields the external losses of 250 cm^{-1}. In this case, no lasing can be obtained. To overcome this difficulty, we used AlO/GaAs DBRs obtained by oxidation of epitaxial AlAs layers. The large difference between the refractive indices of Al_xO_y and GaAs compounds (1.7 and 3.45 for Al_xO_y and GaAs, respectively, at 1.3 μm) makes it possible to use a small number of periods in the DBR and leads to less stringent requirements to the control of the epitaxial layer thickness. For a structure with a 7.5-period bottom and a 5-period top AlO/GaAs DBRs, the calculated values are R_tR_b = 0.999 and α_{ext} = 2.5 cm^{-1}. These values are substantially worse than those calculated for AlAs/GaAs and ZrO_2/SiO_2 DBRs. Nevertheless, as shown below, they are quite sufficient for lasing.

3.3 Vertical Cavity LEDs

Since the operation of VC LED does not require a high-quality resonator with low output losses, we used a simpler device design based on a semiconductor and a dielectric DBRs as top and bottom mirrors, respectively. Figure 6 presents a light–current characteristic of a VC LED with light window of 34 × 37 μm and a current aperture of 40 × 40 μm. This characteristic shows a linear portion at a low current but levels off to an output power of ~10 μW. This leads to a decrease in the quantum efficiency of the device at high current densities (Fig. 6) from its value of ~0.16% at low current densities. This value is in good agreement with the results obtained for nonresonant QD LEDs for the 1.3-μm range [21], thus indicating that the emission output in our QD LED structure has not been improved. This is presumably accounted for by nonoptimal com-

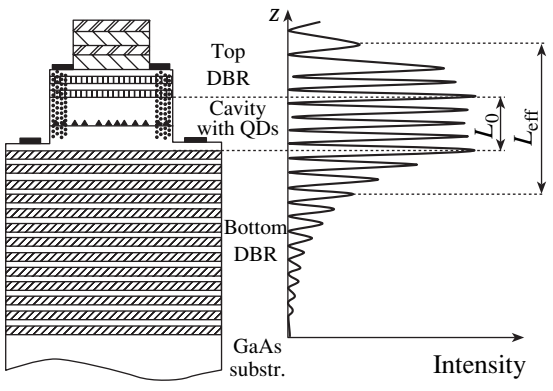

Fig. 4. VC LED design and distribution of the electromagnetic field intensity at the resonance wavelength.

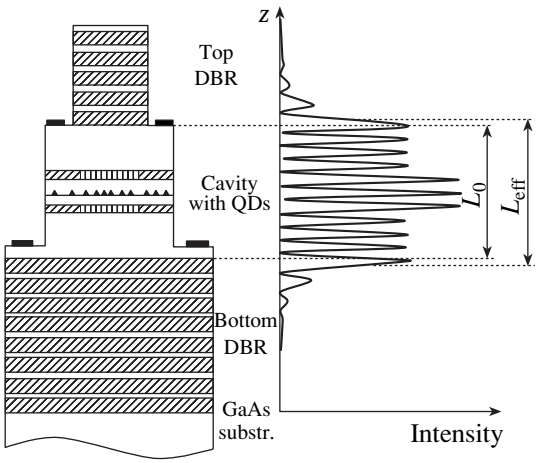

Fig. 5. VCSEL design and distribution of the electromagnetic field intensity at the resonance wavelength.

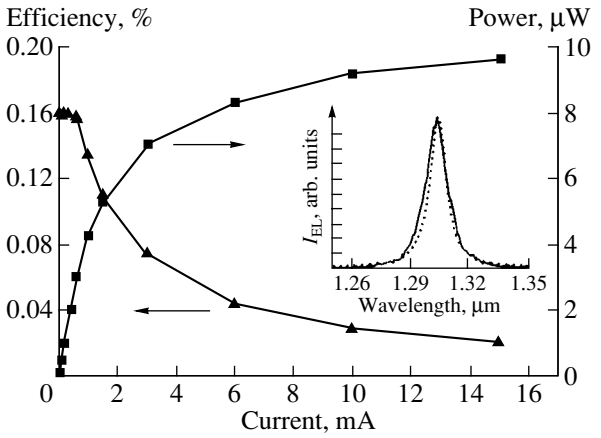

Fig. 6. Light–current characteristic (squares) and quantum efficiency vs current (triangles) for a VC LED. Inset: experimental (solid line) and calculated (dotted line) EL spectra.

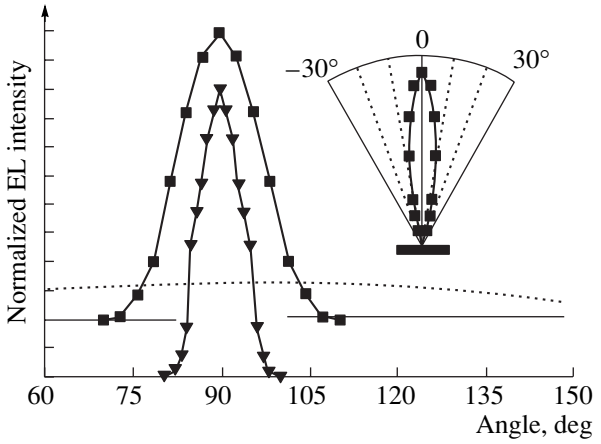

Fig. 7. Far-field distribution for a VC LED, integrated over wavelength (squares) and at peak wavelength (triangles); dotted line represents the far-field distribution for on ordinary non-resonant LED. Insert: the same data in polar coordinates.

bination of a high-quality cavity with a wide emission spectrum of the QDs [22].

Nevertheless, the VC LEDs under study demonstrate some other properties typical of microcavity structures, namely, a narrow spectral characteristic and low light-beam divergence. The insert of Fig. 6 shows an EL spectrum of a VC LED with a peak at 1.303 μm and FWHM of 13 nm, which remain unchanged when the current is raised. The dotted line in the same figure represents a simulated spectrum practically coinciding with the experimental curve. The far-field distribution of power integrated over wavelength, shown by squares in Fig. 7, has a FWHM of 17°, which is substantially narrower than the far-field distribution for ordinary nonresonant diode (dotted line). The structure of the far-field distribution at the resonance wavelength (Fig. 7, triangles) is more complicated, which is due to the influence of various transverse modes.

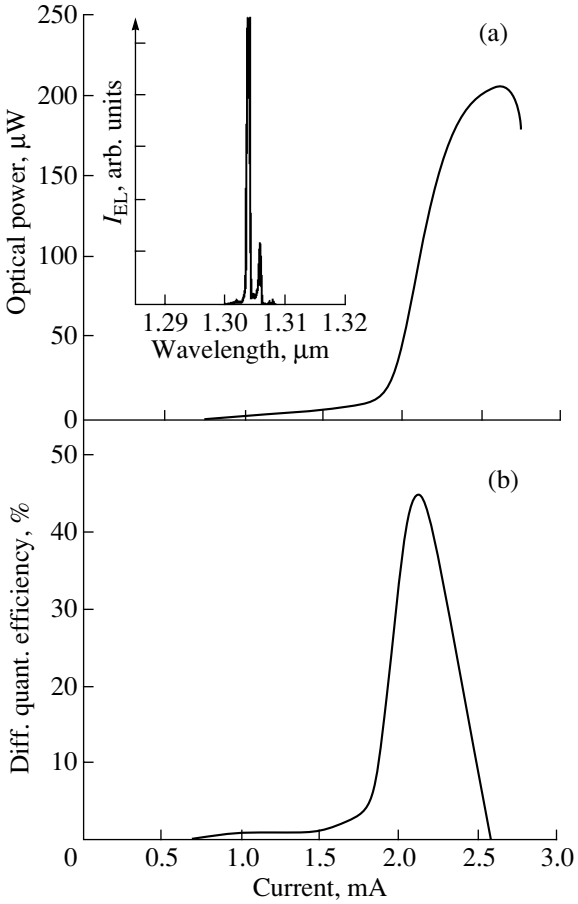

Fig. 8. (a) Light–current characteristic of VCSEL and (b) differential quantum efficiency vs drive current. Insert: lasing spectrum for a current exceeding the threshold value by 5%.

3.4. Vertical Lasing with Injection Pumping

As shown in Section 3.2, the use of only a few pairs of AlO/GaAs DBRs leads to sufficiently high reflectivity and reduces the optical losses to 2.5 cm^{-1}. This allowed us to obtain vertical lasing in structures fabricated by AlAs layer oxidation. Figure 8a presents a light–current characteristic of a VCSEL. The lasing threshold is 1.8 mA, corresponding to the current density of 2.8 kA/cm^2 [23]. The lasing spectrum measured at a current exceeding the threshold value by 5% contains, along with the main peak at 1.304 μm, a satellite peak on the long-wavelength side (see the insert of Fig. 8a). The emergence of this satellite peak can be attributed to the lateral confinement of the light wave in the 8×8 μm aperture. In spite of the low external optical losses in this structure (2–3 cm^{-1}), the differential quantum efficiency is high enough, reaching a value of 45% (Fig. 8b), which is possible in the case of low internal losses. Indeed, low internal losses (1–2 cm^{-1}) are typical of 1.3-μm stripe lasers with InAs/InGaAs QDs as the active region [24]. The use of an aperture

exceeding 5 μm and low doping levels (~10^{18} cm^{-3}) in VCSELs allowed us to attain low diffraction losses and low free-carrier absorption losses. In this case, the internal losses are comparable with the external losses, which accounts for the so high differential efficiency. By contrast, the internal losses are higher in the case of InGaAs QDs emitting in the 1-μm spectral range; the attainment of high-efficiency lasing becomes difficult and requires that reflectors with lower reflectivity should be used. For example, a differential quantum efficiency of 30% was achieved in a 1-μm VCSEL with three AlO/GaAs pairs in the top DBR, whereas with five pairs the efficiency decreased to 4% [25].

Devices with AlO/GaAs DBRs fabricated by oxidation of AlAs layers exhibit a tendency toward exfoliation in the course of time. Introduction of a minor amount (~2%) of Ga stabilizes Al(Ga)O/GaAs DBRs. The use of Al(Ga)O/GaAs DBRs allowed us to obtain a long-term CW lasing at 1.3 μm at a temperature of 35°C (the structures have operated for more than 700 h, without any noticeable degradation of the threshold current). The maximal output power was 0.65 mW; the maximal external differential quantum efficiency, 39–40%; and the wall-plug efficiency, 10–15% [26].

4. CONCLUSION

In the present study, we analyzed theoretically and investigated experimentally various types of VC LEDs and VCSELs for the 1.3-μm spectral range, based on heterostructures with InAs/InGaAs QDs, grown on GaAs substrates. A high-precision control of the layer thickness is necessary when semiconductor AlAs/GaAs DBRs are used, since even a minor (~1–2%) error leads to a substantial deterioration of the device characteristics. VC LEDs with narrow spectral characteristic (~13 nm) and low light beam divergence (<20%) have been fabricated. The use of AlO/GaAs oxide reflectors allowed fabrication of injection VCSELs for the 1.3-μm range, with active region based on InAs/InGaAs QDs, demonstrating low threshold current (<2 mA) and high external differential quantum efficiency (>40%).

ACKNOWLEDGMENTS

The study was supported by the Ministry of Science of the Russian Federation (the program "Physics of Solid-State Nanostructures"), the Russian Foundation for Basic Research, and the programs NanOp and INTAS.

REFERENCES

1. Y. Qian, Z. H. Zhu, and Y. H. Lo, Appl. Phys. Lett. **71**, 25 (1997).
2. V. Jayaraman, J. C. Geske, M. H. MacDougal, *et al.*, in *Proceedings of the 11th Annual Meeting IEEE Lasers and Electro-Optics Society, Orlando, 1998*, p. 210.
3. N. E. J. Hunt, E. F. Schubert, R. A. Logan, and G. J. Zydzik, Appl. Phys. Lett. **61**, 2287 (1992).
4. D. L. Huffaker, G. Park, Z. Zou, *et al.*, Appl. Phys. Lett. **73**, 2564 (1998).
5. Yu. M. Shernyakov, D. A. Bedarev, E. Yu. Kondrat'eva, *et al.*, Electron. Lett. **35**, 898 (1999).
6. K. Nakahara, M. Kondow, T. Kitatani, *et al.*, IEEE Photonics Technol. Lett. **10**, 487 (1998).
7. A. Yu. Egorov, D. Bernklau, D. Livshits, *et al.*, Electron. Lett. **35**, 1643 (1999).
8. K. Nishi, T. Anan, and S. Sugou, in *Proceedings of the IEEE/LEOS Summer Topical Meeting, Workshop on Nanostructures and Quantum Dots, San Diego, 1999*, p. 39.
9. T. Anan, K. Nishi, S. Sugou, *et al.*, Electron. Lett. **34**, 2127 (1998).
10. M. C. Larson, M. Kondow, T. Kitatani, *et al.*, IEEE Photonics Technol. Lett. **10**, 188 (1998).
11. G. Steinle, A. Yu. Egorov, and H. Riechert, in *Proceedings of the Summer School and European Optical Society Topical Meeting on Semiconductor Microcavity Photonics, Ascona, 2000.*
12. K. D. Choquette, J. F. Klem, A. J. Fisher, *et al.*, Electron. Lett. **36**, 1388 (2000).
13. V. M. Ustinov, N. A. Maleev, A. E. Zhukov, *et al.*, Appl. Phys. Lett. **74**, 2815 (1999).
14. K. Mukai, Y. Nakata, K. Otsubo, *et al.*, IEEE J. Quantum Electron. **36**, 472 (2000).
15. N. A. Maleev, A. E. Zhukov, A. R. Kovsh, *et al.*, Fiz. Tekh. Poluprovodn. (St. Petersburg) **34**, 612 (2000) [Semiconductors **34**, 594 (2000)].
16. N. A. Maleev, I. L. Krestnikov, A. R. Kovsh, *et al.*, in *Proceedings of the International Conference on Semiconductor Quantum Dots, Munich, 2000*, Phys. Status Solidi (in press).
17. N. N. Ledentsov, D. Bimberg, V. M. Ustinov, *et al.*, Semicond. Sci. Technol. **14**, 99 (1999).
18. *Vertical Cavity Surface–Emitting Lasers*, Ed. by C. Wilmsen, H. Temkin, and L. A. Coldren (Cambridge Univ. Press, Cambridge, 1999).
19. A. E. Zhukov, A. R. Kovsh, N. A. Maleev, *et al.*, Appl. Phys. Lett. **75**, 1926 (1999).
20. M. V. Maximov, Yu. M. Shernyakov, I. N. Kaiander, *et al.*, Electron. Lett. **35**, 2038 (1999).
21. D. L. Huffuker and D. G. Deppe, Appl. Phys. Lett. **73**, 520 (1998).
22. H. Benisty, H. De Neve, and C. Weisbuch, IEEE J. Quantum Electron. **34**, 1612 (1998).
23. J. A. Lott, N. N. Ledentsov, V. M. Ustinov, *et al.*, Electron. Lett. **36**, 1384 (2000).
24. A. E. Zhukov, A. R. Kovsh, V. M. Ustinov, *et al.*, IEEE Photonics Technol. Lett. **11**, 1345 (1999).
25. J. A. Lott, N. N. Ledentsov, V. M. Ustinov, *et al.*, Electron. Lett. **33**, 1150 (1997).
26. J. A. Lott, N. N. Ledentsov, V. M. Ustinov, *et al.*, in *Proceedings of the LEOS 2000 Conference: IEEE Lasers and Electro-Optics Society Annual Meeting, Rio Grande, Puerto Rico, 2000*, p. 304.

Translated by D. Mashovets